

# **Designing Nanocrystal Interfaces to Improve Charge Transport for Photo- and Electro- Catalytic Solar Energy Applications**

*A thesis  
submitted in partial fulfilment  
of the requirements for the*

*Doctorate of Philosophy*

By

**G Shiva Shanker**

**(20133269)**



**Department of Chemistry,  
Indian Institute of Science Education and Research (IISER),  
Pune, India - 411008**

**December 2018**

## **DECLARATION**

I declare that this written submission represents my ideas in my own words and wherever other's ideas have been included, I have adequately cited and referenced the original sources. I also declare that I have adhered to all principles of academic honesty and integrity and have not misrepresented or fabricated or falsified any idea / data / fact / source in my submission. I understand that violation of the above will cause for disciplinary action by the Institute and can also evoke penal action from the sources which have thus not been properly cited or from whom proper permission has not been taken when needed.

**Date: 19<sup>th</sup> March 2019**

**Mr. G Shiva Shanker**  
**(Reg. No: 20133269)**

## **CERTIFICATE**

This is to certify that this dissertation entitled “**Designing Nanocrystal Interfaces to Improve Charge Transport for Photo- and Electro-Catalytic Solar Energy Applications**” towards the partial fulfilment of the Integrated PhD dual degree programme at the Indian Institute of Science Education and Research, Pune represents original research carried out by G Shiva Shanker at IISER Pune under my supervision. The work presented here or any part of it has not been included in any other thesis submitted previously for the award of any degree or diploma from any other university or institution.

**Date: 19<sup>th</sup> March 2019**

**Dr. Angshuman Nag**  
**(Research Supervisor)**

## **Acknowledgements**

On successful completion of this thesis, it is my pleasure to acknowledge all those who have contributed towards it, be it through encouragement, guidance and/or support.

I would first like to express my sincere gratitude towards my research supervisor Dr. Angshuman Nag for his excellent guidance throughout the course of my doctoral studies. His understanding behavior, emphasis on rigorousness of concepts and constant encouragement at every step of the research has allowed me to mold into an independent researcher. I also thank him for permitting me to work on this research problem and encouraging me to cultivate my own understanding of the literature.

I want to thank my RAC Members, Dr. B. L. V. Prasad and Dr. Pramod Pillai for their valuable comments during our annual RAC meetings. Their criticality and attention to detail encouraged me to investigate my claims and understanding of concepts more thoroughly before presenting, whether in written or oral form.

I want to thank all my lab mates in Dr. Angshuman's group for reviewing my work critically, suggesting me with experiments and comforting me during several roadblocks during this long tenure of 5 years.

I can't imagine my Ph.D. with the constant love and support of my family and friends. They have played a very significant role in ensuring that I am always in the best mental health to conduct my research and cope with the failures therein.

I would like to also thank CSIR-NCL-Pune and University of Mumbai where a lot of the experiments were carried out and all the agencies that have funded me during the tenure of my doctoral studies particularly, UGC for Research fellowship.



## Synopsis

This thesis mainly focuses on improving the charge transport of nanocrystalline solids through its interface connection, and their ascertainment of efficiency of catalytic activity in electrochemical hydrogen evolution reaction (HER) and photoelectrochemical (PEC) water splitting. In this regard, TiN - N-doped few-layer graphene (TiN-NFG) nanocomposite, Sn-doped  $\text{In}_2\text{O}_3$  (ITO) and PbX (X = S and Se) nanocrystals (NCs) are synthesized and characterized. Then, the charge transport properties of these nanocrystalline solids are studied in detail. Subsequently, electrocatalytic and co-catalytic activity of TiN-NFG nanocomposites are determined in HER, dye sensitized solar cell (DSSC) and PEC water splitting. Mechanistic origin of localized surface plasmon resonance (LSPR) band of ITO NCs and their co-catalyst efficiency are evaluated in PEC water splitting. In the end, electronic grade semiconductor films are made from colloidal PbS and PbSe NCs by employing oriented attachment. More details of different chapters of this thesis are discussed below.

**Chapter 1. Introduction:** This chapter gives a brief introduction of the work carried out in this thesis. To begin with, the recent progress of hydrogen energy production is discussed briefly. Subsequently, basic principles of the experimental methods such as HER and PEC water splitting are discussed. The fundamentals of widely used protocols of colloidal synthesis and solid state reactions are described. NCs provide more surface to volume ratio yielding more active sites for catalytic reactions. But this large contribution of surface sites hinders charge transport in NC solids, which often reduces catalytic processes in HER and PEC water splitting. Therefore, approaches to improve the charge transport properties of nanocrystalline solids are discussed. In the approach-1, the basis of choosing of TiN-NFG nanocomposite is discussed. Owing to metallic nature of TiN and good charge transport property of NFG, TiN-NFG nanocomposite is prepared with large surface area for catalysis. Moreover, activity of counter electrode in DSSC and principles of solar cells are described briefly since some of the electrocatalyst for HER has the potential to act as counter electrode in DSSC. In the approach-2, we describe another strategy to achieve electronic grade semiconductor film from colloidal PbS and PbSe NCs by employing oriented attachment. In the end, we discuss the scope of present thesis work, where the charge transport of nanocrystalline solids is improved through their interface connection to enhance the efficiency of electrochemical HER and PEC water splitting.

**Chapter 2. Colloidal Nanocomposite of TiN and N-Doped Few-Layer Graphene for Solar Cell and Electrochemical Hydrogen Evolution:** In this chapter, we report the

synthesis of colloidal TiN-NFG nanocomposite starting from molecular precursors. Thus, we establish a stable chemically bound interface between TiN and NFG providing colloidal stability and improved charge transfer across the interface. Interesting properties such as LSPR band arising from TiN NCs, colloidal stability, high surface area ( $270 \text{ m}^2/\text{g}$ ) and electrical conductivity ( $0.3 \text{ ohm cm}$ ) of both colloidal nanocomposite and their films are explored. Owing to the combination of these properties, we evaluate the counter electrode efficiency of TiN-NFG nanocomposite in DSSC. The DSSCs prepared using TiN-NFG counter electrode exhibit high power conversion efficiency of 8.9 % which are comparable to our DSSC prepared using Pt counter electrode. The nanocomposite also exhibits stable electrocatalytic HER with reasonably low overpotential of 161 mV at  $10 \text{ mA}/\text{cm}^2$  current density. Overall, our TiN-NFG nanocomposite is an alternative of expensive noble metals like Pt, for electrocatalytic applications.

**Chapter 3. 2D Nanocomposite of g-C<sub>3</sub>N<sub>4</sub> Nanosheet and TiN - N-Doped Graphene for Photoelectrochemical Reduction of Water using Sunlight:** In this chapter, we introduce a 2D co-catalyst, TiN-NFG nanocomposite for improving the PEC water splitting performance of 2D g-C<sub>3</sub>N<sub>4</sub> nanosheet (photocatalyst). 2D/2D layered hetero-junctions are constructed between g-C<sub>3</sub>N<sub>4</sub> nanosheet and TiN-NFG nanocomposite. The extended interface of 2D g-C<sub>3</sub>N<sub>4</sub>:TiN-NFG nanocomposite suppresses recombination of photo-excited electron-hole by separating the charge carriers and also reduces the charge transfer resistance ( $R_{ct}$ ) across the electrode/electrolyte interface. Subsequently, the enhancement in the overall PEC performance is observed for the 2D g-C<sub>3</sub>N<sub>4</sub>:TiN-NFG nanocomposite. The nanocomposite shows ~16 times enhancement in the PEC activity of g-C<sub>3</sub>N<sub>4</sub> nanosheet at 0.11 V versus reversible hydrogen electrode (RHE) under simulated solar light illumination. The nanocomposites exhibit good stability under experimental conditions and are cost-effective without involving any noble metal. This study establishes TiN-NFG as a promising 2D co-catalyst for PEC water splitting.

**Chapter 4. Plasmonic Properties of Sn-Doped In<sub>2</sub>O<sub>3</sub> Nanocrystals and Their Co-catalytic Activity with g-C<sub>3</sub>N<sub>4</sub> Nanosheets for Photoelectrochemical Reduction of Water**

In this chapter, we synthesize colloidal Sn-doped In<sub>2</sub>O<sub>3</sub> (ITO) NCs following reported protocol. ITO NCs showing LSPR band in the near infrared region suggests the presence of metallic free electrons in ITO NCs, similar to TiN NCs studied in previous chapters.

Mechanistic origin of generation of free electrons in ITO NCs during our synthesis is studied. These free electrons can promote the electrical conductivity required for co-catalytic application for PEC reduction of water. We prepare nanocomposite of g-C<sub>3</sub>N<sub>4</sub> nanosheets (photocatalyst) and ITO NCs co-catalyst for PEC reduction of water. The ITO NCs as a co-catalyst suppress the photoluminescence intensity and also reduce the  $R_{ct}$  at electrode/electrolyte interface. Consequently, the enhancement in the PEC performance is observed for the g-C<sub>3</sub>N<sub>4</sub>:ITO (2%) nanocomposite. The nanocomposite shows ~6 times enhancement in the PEC activity of g-C<sub>3</sub>N<sub>4</sub> nanosheets at 0.11 V vs RHE under simulated solar light illumination.

### **Chapter 5. Electronic Grade and Flexible Semiconductor Film Employing Oriented Attachment of Colloidal Ligand-Free PbS and PbSe Nanocrystals at Room**

**Temperature:** In this chapter, electronic grade semiconductor thin films are prepared using colloidal ligand-free PbS and PbSe NCs at room temperature. The sintering temperature of NCs is decreased to room temperature by employing two strategies: (i) synthesis of ligand-free colloidal PbS and PbSe NCs, and (ii) oriented attachment of NCs. Dipole moment of PbS and PbSe NCs encourages oriented attachment of NCs, decreasing the activation energy for the fusion of NCs. Therefore, the organic-free surface and the oriented attachment of NCs help the easier fusion of NCs forming larger crystal of PbS and PbSe during the precipitation process of NCs. Larger sized solution processed crystals provide better charge transport by making NC film at room temperature. Current (I) vs voltage (V) plots of PbS and PbSe NC films exhibit linear ohmic behavior with electrical conductivities 0.03 S/m and 0.08 S/m respectively after processing the film at room temperature. The electrical conductivities increase to 1.1 S/m and 137 S/m for PbS and PbSe respectively, after annealing the film on glass substrate at 150 °C. The grain boundary effect on the films of PbS and PbSe NCs is studied using AC impedance spectroscopy. Our study suggests that a combination of oriented attachment and organic-free colloidal NCs can be explored for other NC systems as well in future for preparing a semiconductor film at room temperature.

**Thesis Summary and Future Outlook:** In this section we summarize the major findings of the thesis work, and discuss about possible future directions.

## List of Abbreviations

**AFM:** Atomic Force Microscopy

**BET:** Brunauer-Emmett-Teller

**CB:** Conduction Band

**CE:** Counter Electrode

**CV:** Cyclic Voltammetry

**DLS:** Dynamic Light Scattering

**DMF:** N, N-Dimethyl Formamide

**DMSO:** Dimethyl Sulfoxide

**DSSC:** Dye Sensitized Solar Cell

**EDAX:** Energy Dispersive X-ray Analysis

**EDS:** Energy Dispersive X-ray Spectroscopy

**EIS:** Electrochemical Impedance Spectroscopy

**FA:** Formamide

**FESEM:** Field Emission Scanning Electron Microscopy

**FFT:** Fast Fourier Transform

**FTIR:** Fourier Transformed Infrared

**FTO:** F-Doped Tin Oxide

**FWHM:** Full Width Half Maximum

**GC:** Glassy Carbon or Gas Chromatography

**GO:** Graphene Oxide

**HER:** Hydrogen Evolution Reaction

**ICP-OES:** Inductively Coupled Plasma Optical Emission Spectrometry

**ITO:** Sn-Doped Indium Oxide

**IPCE:** Incident Photon to Current Efficiency

**LSPR:** Localized Surface Plasmon Resonance

**LSV:** Linear Sweep Voltammetry

**MVRH:** Mott Variable Range Hopping

**NCs:** Nanocrystals

**NFG:** N-Doped Few-Layer Graphene

**NNH:** Nearest neighboring Hopping

**OER:** Oxygen Evolution Reaction

**PCE:** Power Conversion Efficiency

**PEC:** Photo-Electro-Catalysis

**PET:** Polyethylene Terephthalate

**PXRD:** Powder X-ray Diffraction

**PEM:** Proton Exchange Membrane

**PPMS:** Physical Property Measurement System

**RHE:** Reversible Hydrogen Electrode

**RPM:** Revolution Per Minute

**SC:** Semiconductor

**STP:** Standard Temperature and Pressure

**TCD:** Thermal Conductivity Detector

**TEM:** Transmission Electron Microscopy

**TEOA:** Triethanolamine

**TGA:** Thermo Gravimetric Analysis

**TiN-NFG:** Titanium Nitride - N-Doped Few-layer Graphene

**HRTEM:** High Resolution Electron Microscopy

**VB:** Valance Band

**XPS:** X-ray Photoelectron Spectroscopy

## Table of Contents

### 1. Introduction

<b>1.1 Energy and Civilization</b> .....	<b>2</b>
<b>1.2 Basic Principle of Electrochemical Hydrogen Evolution Reaction (HER)</b> .....	<b>4</b>
1.2.1 Mechanism of Electrochemical Hydrogen Evolution Reaction (HER) .....	6
1.2.2 Tafel Slope .....	8
1.2.3 Stability of Catalyst .....	8
1.2.4 Faraday Efficiency .....	9
1.2.5 Some Known Efficient Electrocatalysts from Literature .....	9
<b>1.3 Basic Principle of Photoelectrochemical (PEC) Water Splitting</b> .....	<b>10</b>
1.3.1 Stability of Photoelectrodes .....	12
1.3.2 Solar to Energy Conversion Efficiency .....	12
1.3.3 Incident Photon to Current Efficiency (IPCE) .....	12
<b>1.4 Counter Electrodes in Dye Sensitized Solar Cell (DSSC)</b> .....	<b>15</b>
1.4.1 Characterization of Solar Cell .....	16
<b>1.5 Synthesis of Semiconductor and Metal Nanocrystals (NCs)</b> .....	<b>17</b>
1.5.1 Colloidal Synthesis .....	18
1.5.2 Solid State Synthesis .....	19
<b>1.6 Improving the Charge Transport of Films</b> .....	<b>20</b>
1.6.1 Approach 1: Decoration of TiN Nanocrystals on N-Doped Graphene .....	20
1.6.2 Approach 2: Through Interconnection of Nanocrystals .....	21
<b>1.7 Scope of This Ph.D. Work</b> .....	<b>22</b>

#### References

### 2. Colloidal Nanocomposite of TiN and N-Doped Few-Layer Graphene for Solar Cell and Electrochemical Hydrogen Evolution

<b>Summary</b> .....	<b>32</b>
<b>Graphical Presentation</b> .....	<b>32</b>
<b>2.1 Introduction</b> .....	<b>33</b>
<b>2.2 Experimental Section</b> .....	<b>33</b>
2.2.1 Chemicals .....	33

2.2.2 Synthesis of TiN-N-Doped Few-Layer Graphene (TiN-NFG) Nanocomposite .....	34
2.2.3 Preparation of N-Doped Few-Layer Graphene (NFG) .....	34
2.2.4 Characterization .....	35
2.2.5 Fabrication of Dye Sensitized Solar Cell (DSSC) .....	35
2.2.6 Solar Cell, Cyclic Voltammetry and Impedance Measurements .....	36
2.2.7 Electrochemical Measurements for Hydrogen Evolution Study .....	36
<b>2.3 Results and Discussion .....</b>	<b>37</b>
2.3.1 Synthesis of TiN-NFG Nanocomposite .....	37
2.3.2 Microscopic Analysis of TiN-NFG Nanocomposite .....	37
2.3.3 Structural Analysis of TiN-NFG Nanocomposite .....	38
2.3.4 Proposed Mechanism for the Formation of TiN-NFG Nanocomposite .....	41
2.3.5 Colloidal Stability of TiN-NFG Nanocomposite .....	42
2.3.6 Properties of TiN-NFG Nanocomposite .....	43
2.3.7 Counter Electrode Efficiency of TiN-NFG Nanocomposite .....	46
2.3.8 Electrochemical Hydrogen Evolution Reaction Using TiN-NFG Nanocomposite .....	52
<b>2.4 Conclusions .....</b>	<b>56</b>
<b>References</b>	
<b>3. 2D Nanocomposite of g-C<sub>3</sub>N<sub>4</sub> and TiN Embedded N-Doped Graphene for Photoelectrochemical Reduction of Water using Sunlight</b>	
<b>Summary .....</b>	<b>65</b>
<b>Graphical Presentation .....</b>	<b>65</b>
<b>3.1 Introduction .....</b>	<b>66</b>
<b>3.2 Experimental Section .....</b>	<b>67</b>
3.2.1 Chemicals .....	67
3.2.2 Synthesis of Graphitic Carbon Nitride (g-C <sub>3</sub> N <sub>4</sub> ) Nanosheets .....	67
3.2.3 Synthesis of Titanium Nitride – N-Doped Few-Layer Graphene (TiN-NFG) .....	67
3.2.4 Synthesis of N-Doped Few-Layer Graphene (NFG) .....	68



3.2.5 Characterization .....	68
3.2.6 Preparation g-C <sub>3</sub> N <sub>4</sub> :TiN-NFG Nanocomposite Photoelectrodes .....	69
3.2.7 Photoelectrochemical (PEC) Measurements .....	69
<b>3.3 Results and Discussion .....</b>	<b>70</b>
3.3.1 Preparation g-C <sub>3</sub> N <sub>4</sub> :TiN-NFG Nanocomposite .....	70
3.3.2 Microscopic and Structural Analysis of g-C <sub>3</sub> N <sub>4</sub> :TiN-NFG Nanocomposite .....	71
3.3.3 Finding of Possible Interaction between g-C <sub>3</sub> N <sub>4</sub> and TiN-NFG in g-C <sub>3</sub> N <sub>4</sub> :TiN-NFG Nanocomposite .....	75
<b>3.4 Conclusions .....</b>	<b>89</b>
<b>References</b>	
<b>4. Plasmonic Properties of Sn-Doped In<sub>2</sub>O<sub>3</sub> (ITO) Nanocrystals and Their Co-catalytic Activity with g-C<sub>3</sub>N<sub>4</sub> Nanosheets for Photoelectrochemical Reduction of Water</b>	
<b>Summary .....</b>	<b>95</b>
<b>Graphical Presentation .....</b>	<b>95</b>
<b>4.1 Introduction .....</b>	<b>96</b>
<b>4.2 Experimental Section .....</b>	<b>97</b>
4.2.1 Chemicals .....	97
4.2.2 Synthesis of Graphitic Carbon Nitride (g-C <sub>3</sub> N <sub>4</sub> ) Nanosheets .....	97
4.2.3 Synthesis of Sn-Doped In <sub>2</sub> O <sub>3</sub> Nanocrystals (NCs) .....	97
4.2.4 Characterization .....	98
4.2.5 Preparation of g-C <sub>3</sub> N <sub>4</sub> :ITO Nanocomposite Photoelectrodes .....	98
4.2.6 Photoelectrochemical (PEC) Measurements .....	99
<b>4.3 Results and discussion .....</b>	<b>99</b>
4.3.1 Mechanistic Insight about the Generation of Free electron in Colloidal ITONCs .....	99
4.3.2 Electrical Conductivity .....	103
4.3.3 Preparation of g-C <sub>3</sub> N <sub>4</sub> :ITO Nanocomposite .....	104
4.3.4 Microscopic Analysis of g-C <sub>3</sub> N <sub>4</sub> Nanosheets and g-C <sub>3</sub> N <sub>4</sub> :ITO (2%) Nanocomposite .....	105

4.3.5 Properties of g-C <sub>3</sub> N <sub>4</sub> Nanosheet and g-C <sub>3</sub> N <sub>4</sub> :ITO (2%) Nanocomposite .....	106
4.3.6 Photoelectrochemical Activity of g-C <sub>3</sub> N <sub>4</sub> :ITO (2%) Nanocomposite .....	109
<b>4.4 Conclusions .....</b>	<b>112</b>
<b>References</b>	
<b>5. Electronic Grade and Flexible Semiconductor Film Employing Oriented Attachment of Colloidal Ligand-Free PbS and PbSe Nanocrystals at Room Temperature</b>	
<b>Summary .....</b>	<b>118</b>
<b>Graphical Presentation .....</b>	<b>118</b>
<b>5.1 Introduction .....</b>	<b>119</b>
<b>5.2 Experimental Section .....</b>	<b>120</b>
5.2.1 Chemicals .....	120
5.2.2 Synthesis of Ligand-Free PbS Nanocrystals (NCs) .....	120
5.2.3 Synthesis of Ligand-Free PbSe NCs .....	120
5.2.4 Characterization .....	121
5.2.5 Deposition of NC Film .....	121
5.2.6 DC and AC Electrical Measurements .....	121
<b>5.3 Results and Discussion .....</b>	<b>122</b>
5.3.1 Colloidal Ligand-Free PbS NCs .....	122
5.3.2 Larger NCs at Room Temperature through Oriented Attachment .....	123
5.3.3 DC and AC Electrical Properties of NC Film .....	129
5.3.4 PbSe NCs .....	133
<b>5.4 Conclusions .....</b>	<b>137</b>
<b>References</b>	
<b>Thesis Summary and Future Outlook .....</b>	<b>144</b>
<b>List of Publications .....</b>	<b>148</b>



# **Chapter 1**

## **Introduction**

## 1.1 Energy and Civilization

In the beginning of 1970's, hydrogen fuel was considered as energy source.<sup>1-2</sup> Hydrogen is the most abundant element in the earth.<sup>3</sup> However, it does not exist in the form of molecular hydrogen. Thus, for the production of molecular hydrogen, efficient technologies are needed. Presently, fossil fuels are major source for the production of hydrogen fuel through steam reforming process.<sup>4</sup> In this process steam reacts with hydrocarbons at high temperature (700 - 1100 °C) giving the products of hydrogen fuel and carbon dioxide. This is efficient method to produce hydrogen fuel in large scale but disadvantage is that the fossil fuels are non-renewable sources. Also in this reaction, along with molecular hydrogen, carbon dioxide get emitted into environment which leads the environmental pollution.<sup>5</sup>

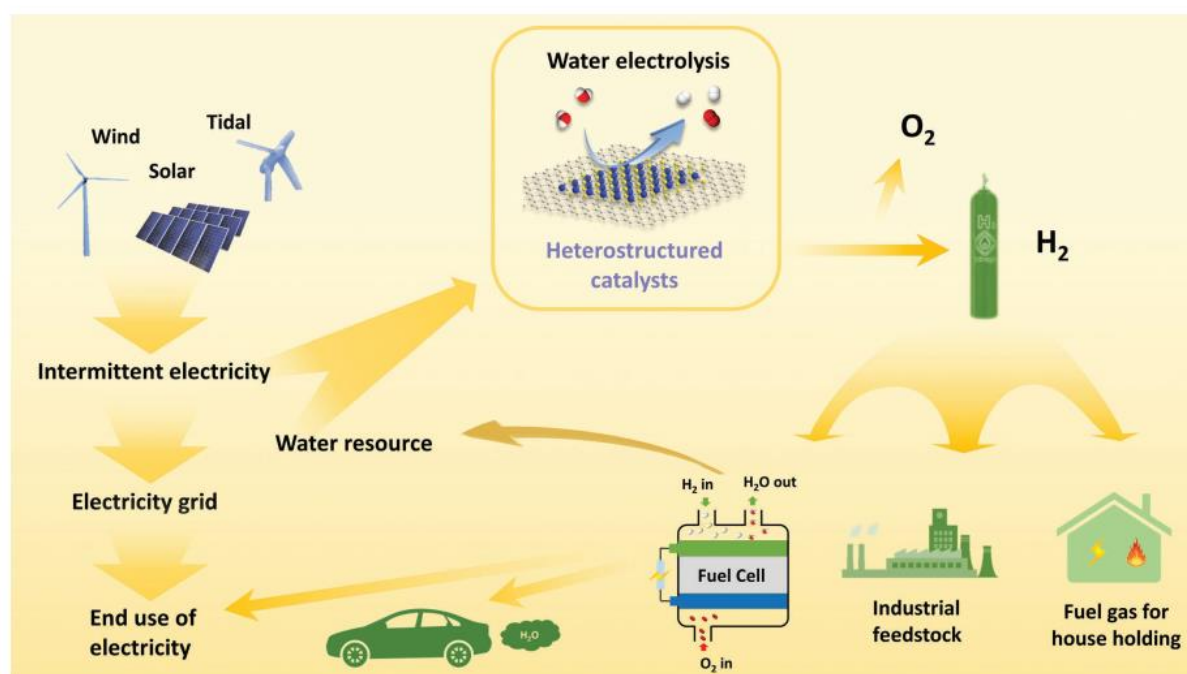


**Figure 1.1:** Schematics showing hydrogen fuel production from clean and renewable energy sources and, hydrogen utility in various aspects. Reprinted with permission from ref.<sup>6</sup> Copyright 2018, Wiley-VCH Verlag GmbH & Co.

Recently, International Energy Agency has given a report on global energy demand. The data suggest that the global energy demand will be increased by 30% in the year 2040 and, carbon dioxide emissions will be reached by 35% Gt/year in 2040.<sup>6-7</sup> In this context, production of sustainable energy in large scale with low-cost, and from clean and renewable energy sources is one of the top priorities in front of the scientists and engineers. To this end, scientific community has been taken initiative to produce energy from renewable sources such as solar,

hydropower and wind energy.<sup>8-9</sup> Significant contribution of energy production has been achieved through these sources. However, these energy sources still include problems like low energy delivery efficiency and non-transportable sources. In addition to this, there is other alternative and promising methods for production of energy in large-scale with low-cost is conversion of renewable energy into chemical fuel. The obtained chemical energy through this method is high in purity and, can be easily stored and transported. In this regard, production of hydrogen fuel from water is considered as the best strategy which significantly reduces the environmental pollution because this kind of reaction does not involve in the production of any carbon based harmful gases in to the environment.

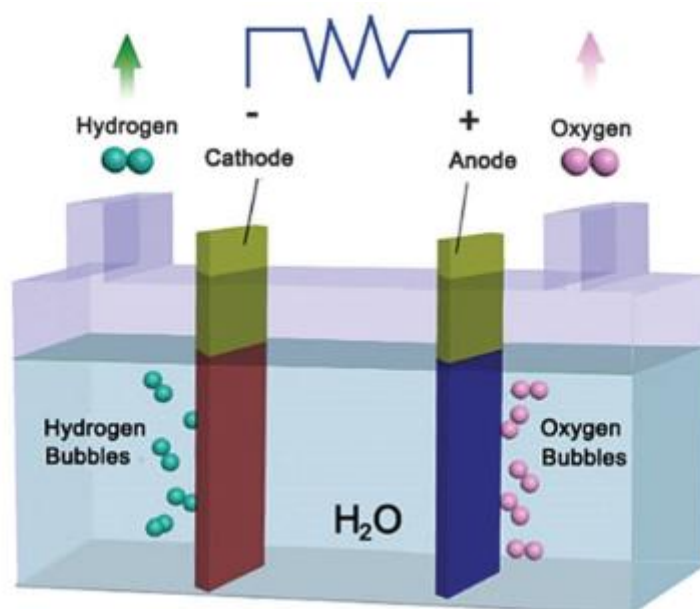
Figure 1.1 shows the hydrogen fuel production from renewable energy sources through electrochemical water splitting process, and hydrogen fuel utility in various aspects. To convert water into hydrogen fuel and oxygen, in the present context, electrochemical water splitting (HER) and photo electrochemical (PEC) water splitting methods have received great attention from scientific community. Hydrogen fuel production from these methods require only water and electricity,<sup>10-11</sup> and importantly no carbon based harmful gases are released in these reactions as byproducts. Additionally, the produced hydrogen through these methods is high in purity. So that, it can be directly used in proton exchange membrane (PEM) fuel cell which is one of the potential system to use in electronic vehicle as a power system. Furthermore, hydrogen fuel can be used directly in industrial feedstock and in house hold as a cooking gas.

Therefore, it is necessary to develop efficient, cost-effective and environment friendly water electrolysis system which produces non-polluting hydrogen fuel for fulfilling sustainable and clean energy demand of society. Typically, in a water electrolysis system, oxygen gas and hydrogen gas is evolved at anode and cathode through oxygen evolution reaction (OER) and hydrogen evolution reaction (HER), respectively. To overcome the energy barrier (1.23 V) of the water splitting reaction, an external voltage applied to the system. At present, hydrogen production through water splitting contributes about 4% of the total production of H<sub>2</sub> worldwide.<sup>12-13</sup> This is really a small fraction, and mainly due to high cost of electrocatalysts and photoelectrocatalysts. Practically, the energy conversion efficiency of hydrogen production through water splitting is about 50 - 70%.<sup>14</sup> To further enhance the energy conversion efficiency it is necessary to develop proper catalysts. At present, the excellent energy conversion efficiency has been achieved by noble-metal based catalysts for HER.<sup>15</sup> Particularly, Pt is state of the art electrocatalyst for HER.<sup>16-18</sup> However, Pt is not abundant

materials in the earth. Therefore, the development of earth abundant catalysts with comparable activity to the noble metal catalysts is an immediate requirement. In this regard, scientists have been putting enormous efforts to synthesize different kinds of non-noble metal based catalysts with different types of conceptual designs. Here, first I discuss the experimental techniques for the production of hydrogen from water.

1. Electrochemical hydrogen evolution reaction
2. Photoelectrochemical water splitting

## 1.2 Basic Principle of Electrochemical Hydrogen Evolution Reaction (HER)



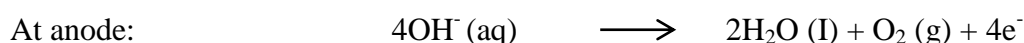
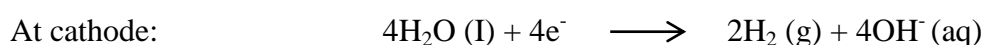
**Figure 1.2:** Schematic representation of electrolyser. Reprinted with permission from ref.<sup>19</sup> Copyright 2015, Royal Society of Chemistry.

Figure 1.2 shows the typical electrolyser consists of three components such as a cathode, an anode and electrolyte ( $\text{H}_2\text{O}$ ). HER occurs at cathode and OER occurs at anode, respectively. When we apply external voltage to the electrodes, the water molecules are decomposed into hydrogen gas and oxygen gas at cathode and anode, respectively. Thus, oxygen gas released into environment and hydrogen gas is stored for application as fuel. In this way, water splitting reaction divided into two half reactions such as water oxidation reaction or OER and water reduction reaction or HER. Conversion of water into hydrogen and oxygen reaction can be expressed in the following reactions in acidic, neutral and basic media.

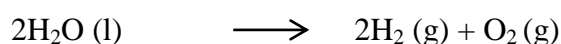
In acidic solution:



In neutral and alkaline medium:



Overall reaction:



Irrespective of the acidic, alkaline and neutral, at standard temperature and pressure (STP) condition, the thermodynamic potential is required for converting one molecule of water into hydrogen and oxygen is 1.23 V. This value corresponds to the reversible electrolysis cell voltage. To start water splitting process, the potential 1.23 V would be sufficient. However, to expand the produced gases from electrochemical cell, the voltage must be supplied higher than the thermodynamic potential (i.e., 1.23 V at 25 °C) by using an external source. The excess potential is known as over potential ( $\eta$ ) which is mainly useful to overcome the energy barriers at cathode ( $\eta_c$ ), anode ( $\eta_a$ ), and also some other energy barriers ( $\eta_{\text{others}}$ ), like solution resistance and contact resistance. Thus, practically, the operational voltage of electrolyser described as<sup>20</sup>

$$E_{\text{op}} = 1.23 \text{ V} + \eta_a + \eta_c + \eta_{\text{other}}$$

The job of electrocatalysts is to reduce  $\eta$ , in detail, the external potential helps to the formation of reaction intermediates on surface of the catalyst, which drives the electron transfer process with significant rates to overcome the kinetic energy barriers of high activation energy. Efficient electrocatalyst materials are those that form the reaction intermediates at lower overpotential values.

From the above equation we can understand that, there is a possibility to improve the water splitting reaction efficiency through the reduction of overpotentials by employing suitable



approaches.  $\eta_a$  and  $\eta_c$  can be reduced through the introduction of highly active oxygen evolution and hydrogen evolution catalysts, respectively.  $\eta_{\text{other}}$  can be reduced through optimized design of electrolytic cell. Increasing the active surface area of the electrode by introducing the nanostructure based catalysts is a useful strategy to reduce the overpotential. Likewise, bubbling effect cannot be ignored. During the electrolysis of water, large number of bubbles generated on active surface area of electrode, some of them do not leave from the electrode surface which reduces the active surface area of the electrode which leads to increase of an overpotential.

### 1.2.1 Mechanism of Electrochemical Hydrogen Evolution Reaction (HER)

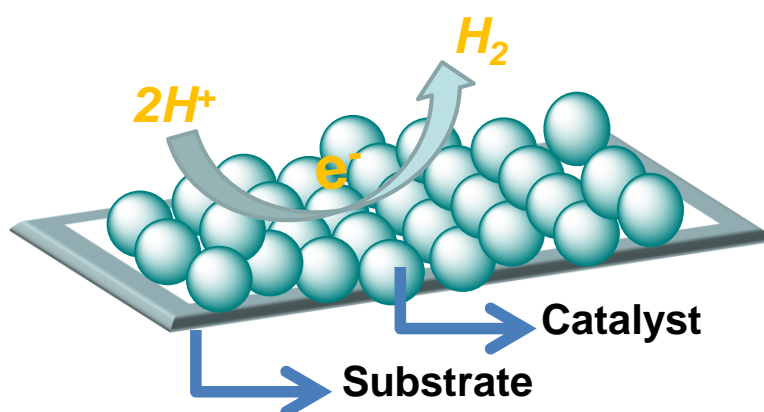


**Figure 1.3:** Hydrogen evolution reaction on the catalyst surface in acidic media.

Figure 1.3 shows the HER on the catalyst surface in acidic media. Typically, in acidic media, the HER involves two major reaction steps during the production hydrogen fuel through the water splitting. These reactions take place on the surface of electrode via multiple reaction intermediate pathways. In the reaction step 1, the formation of adsorption of hydrogen on the electrode surface through the reaction between an electron and proton. And, this reaction termed as Volmer reaction.<sup>21</sup>

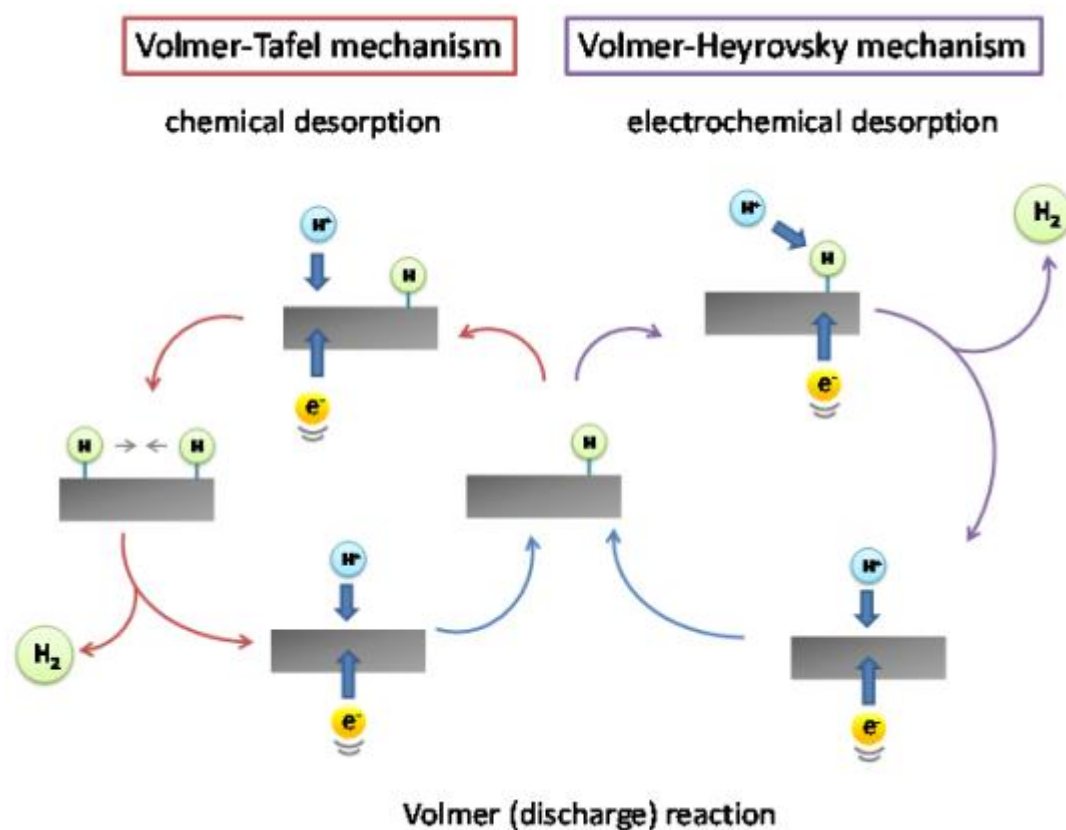
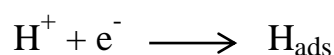
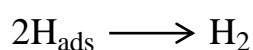


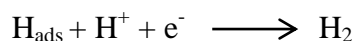
**Figure 1.4:** The mechanism of electrochemical hydrogen evolution reaction in acidic medium. Reprinted with permission from ref.<sup>21</sup> Copyright 2014, Royal Society of Chemistry.



In the reaction step 2, the electrochemical hydrogen evolution reaction occurs. In this step, hydrogen evolution takes place through possibly two different kinds of reaction intermediate pathways. As shown in the Figure 1.4, in the reaction intermediate path 1, adsorbed hydrogen atoms ( $\text{H}_{\text{ads}}$ ) on the electrode surface couple each other, leading to the formation of a hydrogen molecule. This kind of reaction is termed as the Tafel reaction, and the overall mechanism is termed as the Tafel - Volmer mechanism.<sup>21</sup>



In the reaction intermediate path 2, an adsorbed hydrogen atom and a proton in a solution react with an electron or both reaction intermediate 1 and 2, leading to the formation of a hydrogen molecule. This kind of reaction is named as the Heyrovsky reaction, and the mechanism is termed as the Volmer - Heyrovsky mechanism.<sup>21</sup> Regardless of the method by which HER takes place,  $\text{H}_{\text{ads}}$  is always present in the HER process.



$\Delta G_{\text{H}}$  is the free energy change for adsorption of hydrogen on hydrogen evolution catalyst. For instance,  $\Delta G_{\text{H}}$  for Pt is approximately zero, hence Pt is known as ideal electrocatalyst for HER. If  $\Delta G_{\text{H}}$  is large negative value, the  $\text{H}_{\text{ads}}$  strongly bound to catalyst surface which lead to initial Volmer step easy but the Tafel or Hyrovsky steps will become difficult to take place. Likewise, if  $\Delta G_{\text{H}}$  is more positive, the  $\text{H}_{\text{ads}}$  have a weak interaction with catalyst surface as a result Volmer step become slower which limits the overall HER activity.

To design a new efficient noble metal free electrocatalyst for HER both the reaction intermediate steps such as hydrogen adsorption and hydrogen evolution should be taken into account. Therefore, the electrocatalyst expected to show approximately zero  $\Delta G_{\text{H}}$  value.

### 1.2.2 Tafel Slope

To know the predominant HER mechanism which takes place on the electrocatalyst surface, Tafel slopes are estimated. Typically, Tafel slope defined as overpotential ( $\eta$ ) is logarithmically related to the current density ( $J$ ), and the linear portion of Tafel plot fit with the Tafel equation.<sup>21</sup>

$$\eta = a + b \log (J/J_0)$$

where,  $b$  denotes the Tafel slope and  $J_0$  denotes the exchange current density.

From above Tafel equation, we can get the information about two parameters such as; (1) Tafel slope ( $b$ ) which typically related to catalytic mechanism on electrode surface, and (2) exchange current density ( $J_0$ ) which denotes the current density at zero over potential. The exchange current density describes the intrinsic catalytic activity of catalyst under equilibrium conditions. Typically, an efficient electrocatalyst shows high exchange current density ( $J_0$ ) and small Tafel slope ( $b$ ).

### 1.2.3 Stability of Catalyst

To the point of practical application purpose, along with good HER activity, stability of electrocatalyst is another crucial parameter. Particularly, in the case of HER catalyst, mostly works is often done in either extreme acidic solution or in extreme basic solution (i.e., pH = 0 or 14). There are two methods known to characterize the stability of HER catalyst.<sup>6</sup> The first method is to measure the current density with time (I - T curve). For this experiment, the set current density would be greater than 10 mA/cm<sup>2</sup> for a long time (> 10 hours). And, the second method is related cycling stability. In this experiment, repeating the cycles of cyclic

voltammetry curves or linear sweep voltammetry curves by performing the cyclic voltammetry and the number of cycles should be maintained greater than 5000 to evaluate the stability of electrocatalyst.

### 1.2.4 Faraday Efficiency

In an electrochemical system, faraday efficiency gives the information about the efficiency of electrons participate in a desired reaction. In HER experiment, the faraday efficiency defined as the ratio between the experimentally observed H<sub>2</sub> amount and theoretical estimated H<sub>2</sub> amount.<sup>6</sup>

$$\text{Faraday efficiency (\%)} = \frac{\text{Experimental gas evolution}}{\text{Theoretical gas evolution}} \times 100$$

### 1.2.5 Some Efficient Electrocatalysts from Literature

So far, noble metal based catalysts showed the efficient activity towards electrochemical HER. Pt metal is state of the art catalyst for HER. However, these noble metal based electrocatalysts are very expensive. In this context, the designing of earth abundant catalysts with comparable activity similar to noble metals is necessary. Up to now, different electrocatalysts have been reported, which showed reasonable activity towards HER which includes different class of materials such as transition metal dichalcogenides,<sup>22-23</sup> transition metal phosphides,<sup>24-25</sup> carbides<sup>26-27</sup> and nitrides.<sup>28-29</sup> Further, recently, heterostructured based catalysts showed excellent electrochemical water splitting activity. For example, heterostructure of MoS<sub>2</sub>/CoSe<sub>2</sub> showed excellent HER activity in 0.5 M H<sub>2</sub>SO<sub>4</sub> with an over potential of 68 mV at 10 mA/cm<sup>2</sup> and Tafel slope 36 mV/dec.<sup>30</sup> Another, heterostructured catalyst of metallic core/amorphous shell of Co/Co<sub>3</sub>O<sub>4</sub> showed the lower overpotential 90 mV at 10 mA/cm<sup>2</sup> in 1M KOH electrolyte solution.<sup>31</sup> However, till date, the synthesized catalysts showed remarkable performance towards to HER activity but still there is scope to improve the HER activity close to the activity of noble metal based electrocatalysts by designing or optimizing of various conceptual architectures.

## 1.3 Basic Principle of Photoelectrochemical (PEC) Water Splitting

Photoelectrochemical (PEC) water splitting is another experimental technique to achieve hydrogen production by utilization of renewable solar energy. The conversion of water into hydrogen fuel using solar energy through PEC water splitting is an efficient approach. In

recent times, this method has attracted greatly the hydrogen fuel research community due to high purity of hydrogen production, and the sources required in this method is water and sunlight. Thus, this is low-cost method for the production hydrogen fuel.

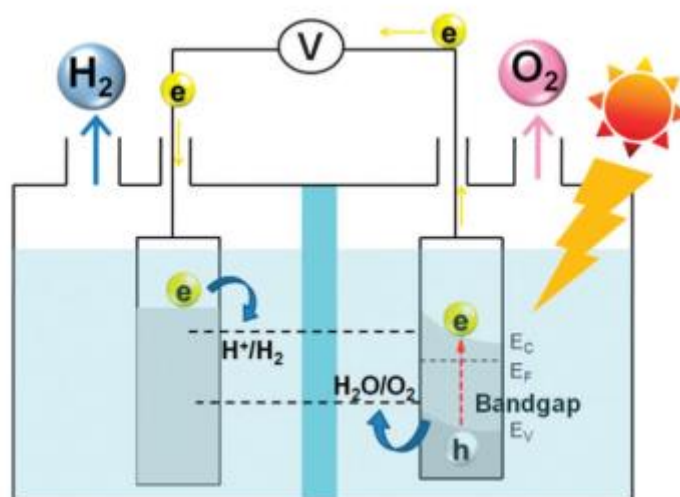


**Figure 1.5:** Schematic representation for basic principle of PEC water splitting. A n-type semiconductor is photoanode where oxygen is evolved, and hydrogen is evolved at photocathode (Pt sheet). Reprinted with permission from ref.<sup>32</sup> Copyright 2012, Royal Society of Chemistry.

The PEC water splitting method is depicted in Figure 1.5. This system involves three major components such as anode, cathode and electrolyte solution. The anode is made by coating of semiconductor material which is illuminated under solar light during the water splitting process. Usually, Pt sheet is used as a cathode, and also called as counter electrode. To begin PEC water splitting process, the photoanode must absorb solar light, and create potential higher than 1.23 V. Consequently, water molecules get oxidised to  $O_2$  and protons. These protons can be reduced to  $H_2$  at cathode. Due to the sluggish nature of water splitting reaction, during the transfer of electrons at photoanode/electrolyte interface the energy is lost. Hence, the energy required for PEC water splitting is mentioned in the range of 1.7 – 2.4 eV. The light induced process must generate four electron - hole pairs at photoanode to generate  $O_2$  molecule. If the energy of solar light is higher than the bandgap of photoactive material then the electrons will be excited in to conduction band (CB) from valence band (VB). Afterward, the photogenerated electrons will move through the external circuit, and reach the photocathode, where these electrons react with protons, and lead to the formation of  $H_2$  molecule. Likewise, holes at photocathode will oxidize the  $H_2O$  to  $O_2$ . In addition to band

gap, the band edges are other important parameters which usually play crucial role in water splitting process. The water splitting essentially need that the conduction band minimum must be more positive than the reduction potential of  $\text{H}^+/\text{H}_2$ . Similarly, the valence band maximum is required to be more negative than the oxidation potential of  $\text{H}_2\text{O}/\text{O}_2$ . There are some metal oxide materials that can able to oxidize the water but not able to reduce it. For this type of materials, external bias is essential for the reduction of protons.

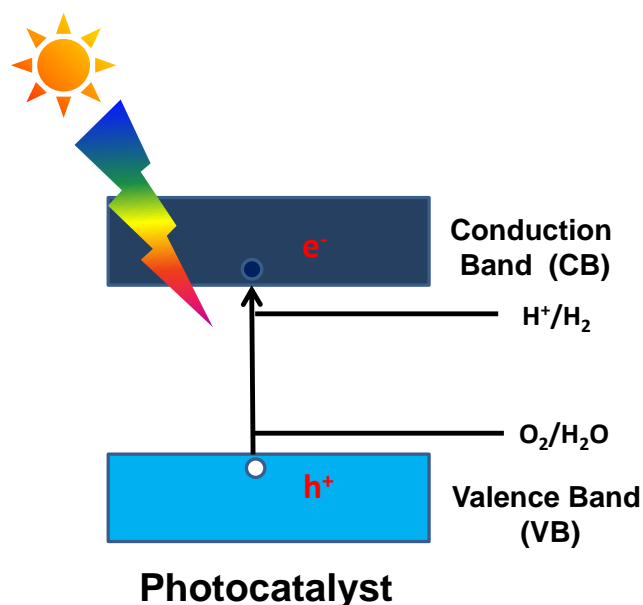


**Figure 1.6:** Schematic representation of n - type semiconductor for PEC water splitting.

As shown in Figure 1.6, typically, PEC water splitting method mainly consists of three major processes such as (1) photogenerated charge carriers in a semiconductor with suitable band gap for absorption of solar light, (2) separation and transportation of charge carriers to the surface of semiconductor, and (3) initiation of redox reaction on the surface of semiconductor by photogenerated charge carriers. The above mentioned properties strongly determined by the properties of semiconductors such as electronic structure, band gap and band edge positions.

However, the energy conversion efficiency of semiconductor material alone is too low in comparison of practical application due to the recombination of electron - hole pair, and low electrical conductivity.<sup>33</sup> Hence, to further enhance the PEC water splitting efficiency, various designs of photoelectrocatalysts have been introduced such as semiconductor/semiconductor and semiconductor/metal hetero-junctions.<sup>34-35</sup>

### 1.3.1 Stability of Photoelectrodes

Stability of photoelectrode is crucial parameter for practical application. The photoelectrocatalyst should maintain the stability under the light illumination and in electrolyte solution for long period of time (at least 10 hours). Therefore, the development of stable catalyst of semiconductors and various type hetero-junction based materials with high efficiency and durability is a challenge in front of the scientific community.

### 1.3.2 Solar to Energy Conversion Efficiency

Another important parameter in PEC water splitting is solar to energy conversion efficiency. The overall solar energy conversion efficiency can be evaluated by using the following equation.<sup>32</sup>

$$\eta (\%) = J \times (1.23 - |V|/I) \times 100$$

Where  $\eta$  denotes the solar energy conversion efficiency,  $J$  denotes the photocurrent density ( $\text{mA}/\text{cm}^2$ ) at measured potential,  $I$  is the incident light intensity ( $\text{mW}/\text{cm}^2$ ), and  $V$  denotes the bias potential versus reversible hydrogen electrode (RHE).

### 1.3.3 Incident Photon to Current Efficiency

For the evaluation of photoelectrocatalyst, the incident photon to current efficiency (IPCE) of the catalyst can be estimated experimentally. IPCE defined as photoresponse as the function of wavelength of incident light. By using the following equation, we estimate the IPCE at a given voltage.

$$\text{IPCE} (\%) = \frac{\text{Total energy of converted electrons}}{\text{Total energy of incident photons}}$$

$$\text{IPCE} (\%) = \left( \frac{1240 \times J}{\lambda} \times I \right) \times 100$$

Where  $J$  is the photocurrent density ( $\text{mA}/\text{cm}^2$ ),  $\lambda$  is wavelength of incident light (nm) and  $I$  is intensity of incident light ( $\text{mW}/\text{cm}^2$ ).

In 1970's, Fujishima and Honda first introduced the production of hydrogen through PEC water splitting where they used  $\text{TiO}_2$  semiconductor under illumination of UV - light.<sup>36</sup> Large number of semiconductor based photocatalysts have been developed due to their suitable bandgap to absorb the large amount solar light. These photocatalysts consists of different class of materials such as metal oxides, metal sulfides, and metal-free semiconductors.<sup>37</sup>

These semiconductor based materials have been showed reasonable efficiencies for the production of hydrogen from water by using solar light.

However, hydrogen generation using pristine semiconductor based photocatalysts suffers from faster recombination of photogenerated charge carriers before they could participate in redox reactions occurring on the surface.<sup>38</sup> Therefore, a new design of composite of semiconductor photocatalyst with other semiconductor or co-catalyst material having a suitable band alignment to facilitate charge separation (transfer) at the interface is beneficial.

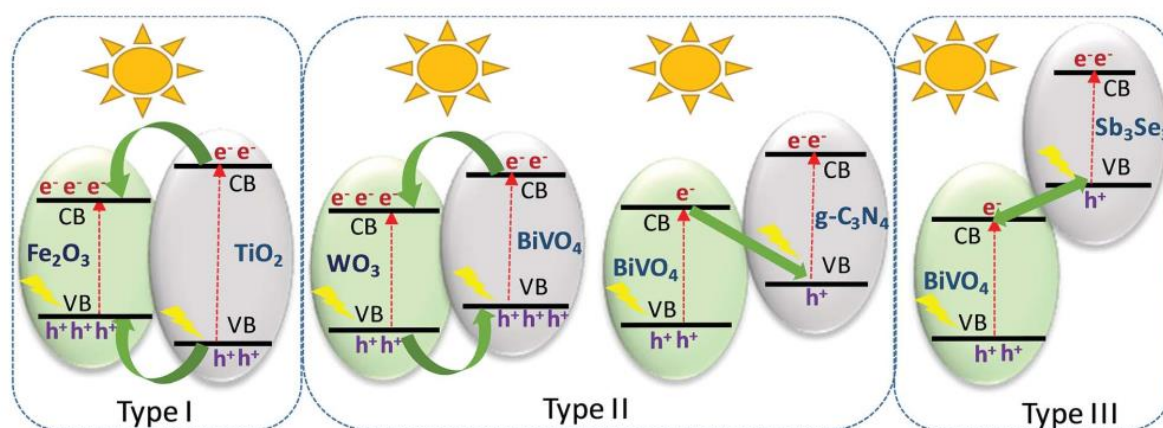


**Figure 1.7:** Schematic presentation of band alignment diagram of different semiconductor/semiconductor hetero-junctions for PEC water splitting. Reprinted with permission from ref.<sup>34</sup> Copyright 2018, Royal Society of Chemistry.

Towards this end, various types of semiconductor/semiconductor hetero-junctions<sup>34</sup> have been made to facilitate the charge transfer or charge separation at interface, as shown in Figure 1.7. For example, according to type I hetero-junction,  $\text{Fe}_2\text{O}_3$  has a smaller band gap compared that of  $\text{TiO}_2$ . Due to a more negative CB and a more positive VB of  $\text{TiO}_2$ , the electrons and holes transfer from  $\text{TiO}_2$  to  $\text{Fe}_2\text{O}_3$ . In the type II hetero-junction, the CB position of  $\text{WO}_3$  is more negative than that of  $\text{BiVO}_4$ , and the VB position is more positive than that of  $\text{BiVO}_4$ . Consequently, holes and electrons transfer opposite way. From this type of band alignment, we can also derive the Z scheme type hetero-junction by decreasing the gap between CB of (left side material) and VB of (right side material), as shown hetero-junction between  $\text{BiVO}_4$  and  $\text{g-C}_3\text{N}_4$ . Furthermore, in type III hetero-junction, the photogenerated electron from  $\text{BiVO}_4$  transfer to hole of  $\text{Sb}_3\text{Se}_3$ , and the electron from  $\text{Sb}_3\text{Se}_3$  and the hole from  $\text{BiVO}_4$  involves in the water reduction and oxidation process, respectively. All these different types of hetero-junctions will help to enhance the PEC water splitting efficiency. Likewise, metal free semiconductor/inorganic semiconductor hetero-junction



architecture between the semiconductors like  $g\text{-C}_3\text{N}_4/\text{TiO}_2$ ,  $g\text{-C}_3\text{N}_4/\text{BiVO}_4$  and  $g\text{-C}_3\text{N}_4/\text{CdS}$ <sup>39</sup> have accelerated the charge separation through built-in electric field at the interface.<sup>40</sup>

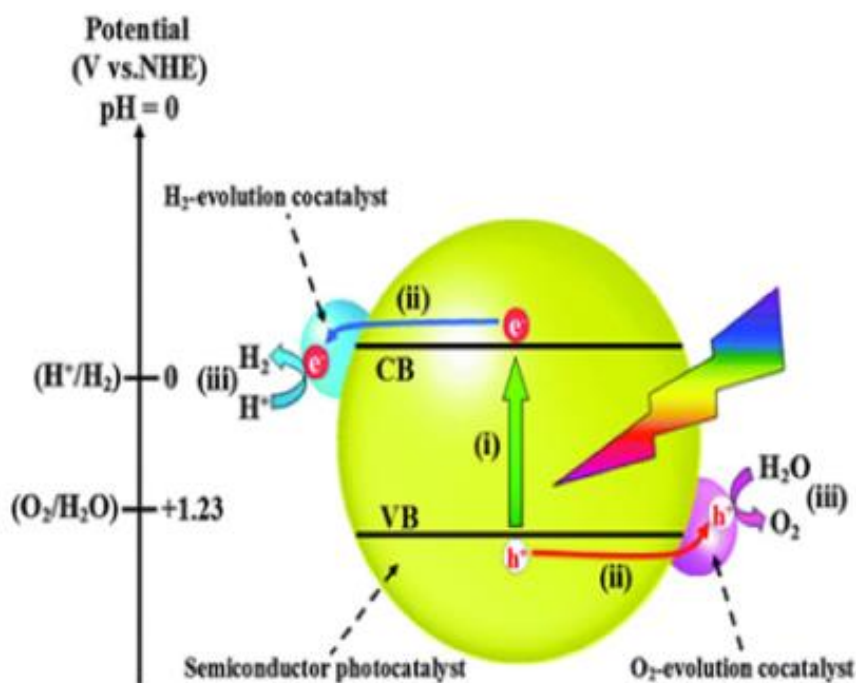


**Figure 1.8:** Schematic representation of band alignment diagram of semiconductor/co-catalyst hetero-junctions for PEC water splitting. Reprinted with permission from ref.<sup>35</sup> Copyright 2018, Elsevier.

As showed in Figure 1.8, the hetero-junctions of semiconductor photocatalysts (Pt, Pd and Au) and noble metal oxides ( $\text{IrO}_2$  and  $\text{RuO}_2$ ) have been employed for water reduction and oxidation, respectively.<sup>41-42</sup> In principle, the efficacy of charge transfer can be improved further by increasing the interfacial area per unit weight of the composite, and therefore, the possibilities of 2D co-catalyst with high surface area are also being explored. For example, Han et al.<sup>43</sup> showed that 2D/2D hetero-junction of  $g\text{-C}_3\text{N}_4/\text{graphdiyne}$  significantly enhances the separation of photogenerated carriers because of excellent hole transfer nature of graphdiyne at the extended interface, eventually displaying a three-fold enhancement in PEC activity. Che et al.<sup>44</sup> fabricated a hetero-junction of  $g\text{-C}_3\text{N}_4$  with planar carbon ring for efficient photoexcited electron transfer with six times enhancement in photocatalytical performance. In the similar direction the PEC efficiency of  $g\text{-C}_3\text{N}_4$  can be achieved to greater

extent if 2D carbon containing electrocatalyst is employed as a co-catalyst which not only reduces interfacial resistance but also provides lower overpotential.

## 1.4 Counter Electrode in Dye Sensitized Solar Cell (DSSC)

Solar cell is a device which converts solar energy into electrical energy. Figure 1.9 shows the schematic representation of dye sensitized solar cell. A DSSC possesses several major components, which includes titanium dioxide photoanode, a dye (photo absorber), an electrolyte solution, and counter electrode (CE). The generated photoexcited electrons from dye, transfer to the  $\text{TiO}_2$  photoanode and eventually reach to the counter electrode through the external circuit. Usually, counter electrode consists of platinum (Pt) sputtered onto a fluorine-doped tin oxide (FTO) glass. The Pt as a counter electrode helps in the regeneration of dyes by catalysing the I regeneration from the  $\text{I}_3^-$  species in the redox couple. Some of the required properties of electrocatalysts of electrochemical water reduction are also desired properties of CE of DSSC. Therefore, certain aspects of research for water reduction reaction and CE are rather common in nature.

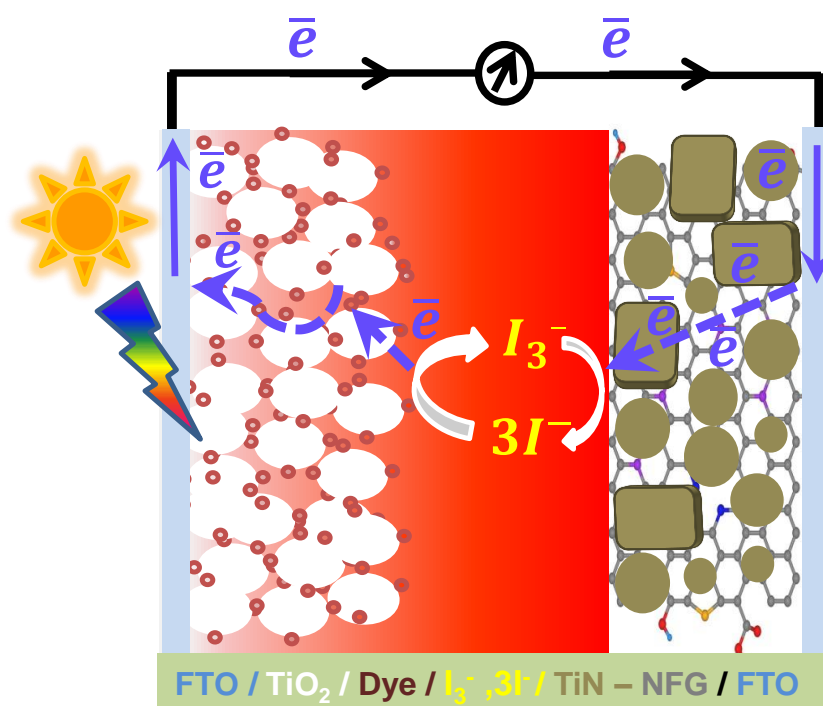


**Figure 1.9:** Schematic representation of dye sensitized solar cell (DSSC).

### 1.4.1 Characterization of Solar Cell

Figure 1.9 shows the current density ( $J$ ) versus voltage ( $V$ ) curves of a solar cell under solar light illumination. Current density ( $J$ ) is defined as current per unit area of the cell. Generally,

the power conversion efficiency (PCE) of a solar cell is mainly dependent on three parameters such as short circuit current ( $I_{sc}$ ), open circuit voltage ( $V_{oc}$ ), and fill factor (FF).  $I_{sc}$  is the maximum current that can be generated from a solar cell at  $V = 0$ . Similarly,  $V_{oc}$  is a maximum voltage which can be obtained from a solar cell at  $I_{sc} = 0$ . The product of current and voltage gives the power of a solar cell. The product of current  $I_{sc}$  and voltage  $V_{oc}$  gives the maximum power ( $P_T$ ) that can be obtained theoretically from a solar cell. However, practically, product of  $I_{sc}$  and  $V_{oc}$  will become zero. Thus, the maximum power ( $P_m$ ) obtained from a solar cell is the product of current ( $I_m$ ) and voltage ( $V_m$ ), as shown in the Figure 1.9.

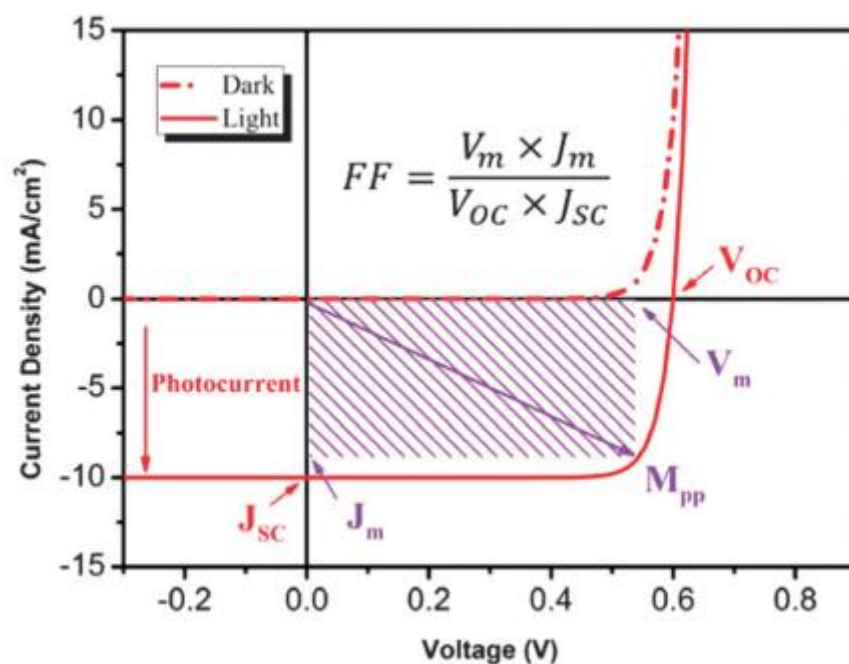


**Figure 1.10:** Typical, J-V characteristics of solar cell under dark and light illumination. Reprinted with permission from ref.<sup>45</sup> Copyright 2013, Royal Society of Chemistry.

$$FF = \frac{P_m}{P_T} = \frac{V_m \times I_m}{V_{oc} \times I_{sc}} \quad (1.1)$$

FF is the ratio between maximum powers ( $P_m$ ) obtained from solar cell and theoretically calculated power ( $P_T$ ).

$$\eta = \frac{P_m}{P_{in}} \quad (1.2)$$

The PCE ( $\eta$ ) of solar cell obtained from the ratio of maximum power ( $P_m$  or  $M_{pp}$ ) from solar cell to power of incident solar light ( $P_{in}$ ). Typically, solar lamp which used for these experiments is illumination of 1 sun intensity with power density of  $100 \text{ mW/cm}^2$ .

The PCE ( $\eta$ ) of solar cell of equation (1.3) is obtained by the substitution of  $P_m$  value of equation (1.1), in equation (1.2).

$$\eta = \frac{P_m}{P_{in}} = \frac{FF \times V_{oc} \times I_{sc}}{P_{in}} \quad (1.3)$$

Where, the solar cell efficiency ( $\eta$ ) depends on the product of FF,  $V_{oc}$  and  $I_{sc}$ , and the value of  $P_{in}$  considered as 1 owing to its 1sun intensity.

Gratzel and O' Regan's work on DSSC by using  $TiO_2$  particles as photoanode and ruthenium dye as a photoabsorber was a breakthrough in the field of DSSC.<sup>46</sup> In this design of DSSC, Pt metal electrode used as a CE mainly for two reasons: (1) the efficient collection of electrons from the external circuit, and (2) it acts as an efficient catalyst for the regeneration of I<sup>-</sup> from  $I_3$ . Pt metal as a CE showed an efficient activity in DSSC.<sup>47</sup> However, Pt is an expensive noble metal and diminishing in its availability. To overcome scarcity of Pt metal, there is an initiation to explore Pt-free materials for the CEs in DSSC. According to various researchers, there are different promising alternatives to Pt have been reported, mainly which includes carbon materials<sup>48</sup> and transition metal carbides and nitrides due to metallic electronic structure similar to that of Pt.<sup>49-50</sup> In addition to that, some composite materials have been developed such as composite of metal nitride/graphene<sup>51</sup> and metal sulphide/graphene<sup>52</sup> like materials. However, still there is significant opportunity and requirement to find new counter electrode materials with high activity comparable to Pt, and good durability in electrolyte solution and under light illumination with low-cost (through solution processability of fabrication). Therefore, certain electrocatalysts developed for water reduction can be explored as CE in DSSC.

## 1.5 Synthesis of Semiconductor and Metal Nanocrystals (NCs)

For the synthesis of semiconductor or metal nanocrystals (NCs), there are different types synthetic methods known in the literature. Among them, few popularly known synthetic methods are listed here such as electron beam lithography, molecular beam epitaxy, colloidal synthesis,<sup>53</sup> and solid state synthesis.<sup>54</sup> The first two synthetic methods involve highly complex instrumentation and need highly controlled atmosphere, high vacuum and also high voltage. On the other hand, colloidal synthesis of NCs is cost effective due to chemical synthesis take place in solution phase.<sup>55</sup> Solid state synthesis is also convenient method which

allows synthesizing samples in large scale. But in this method, we need a furnace, and the reactions take place at high temperatures.

### 1.5.1 Colloidal Synthesis

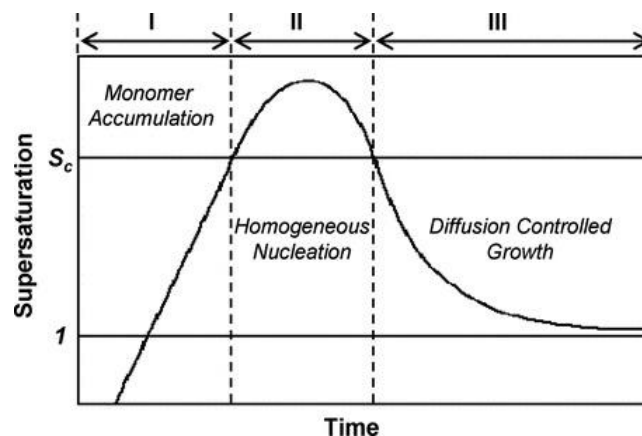


**Figure 1.11:** LaMer diagram.  $S_c$  is the critical supersaturation, the minimum supersaturation level for the homogeneous nucleation. Reprinted with permission from ref.<sup>56</sup> Copyright 2011 Wiley-VCH Verlag GmbH & Co.

Colloidal synthesis is well known method to synthesize good quality semiconductor and metal NCs. Murray et al. introduced for the first time, the synthesis of cadmium chalcogenide NCs through a specific kind of colloidal synthesis, termed as hot injection method.<sup>57</sup> Generally, the synthesis of semiconductor NCs has multiple major steps. First, the metal ion precursors in the form of metal complexes and metal salts are dissolved in high boiling solvents such as 1-octadecene or trioctyl phosphine oxide. The dissolved metal precursors are then heated to a high temperature like  $\sim 300$  °C. Afterward, the anion precursors such as sulphur or selenium are dissolved in trioctyl phosphine and maintained at room temperature are then quickly injected into the reaction mixture of metal precursors kept at high temperature (Figure 1.11). As per LaMer mechanism, after the injection of anion precursor into the hot metal precursor solution, concentration of free monomers in the solution increases rapidly and reaches the critical value or above. Afterward, the monomers undergo instant nucleation, subsequently reducing the free monomer concentration in the solution. Thereafter, there is almost no nucleation occurring due to the low concentration of monomers. Then, begins the growth when the nucleated small clusters grow into bigger sized NCs. All these stages have been showed in Figure 1.11. Further, high surface to volume ratio of small NCs re-dissolved into solution and which lead to continuous growth of larger NCs at

the expense of small ones. As a result, the size distribution NCs become narrower as well as decreases free energy of the overall system. This phenomenon is known as Ostwald refining.<sup>58</sup>

Somewhat different kind of colloidal synthesis was carried out to synthesize the organic ligand free inorganic nanocrystals such as CdS and AgInS<sub>2</sub>.<sup>59</sup> Films of these organic ligand-free NC systems exhibit better charge transport properties compared to films of capped inorganic NCs. However, some other materials like metal nitrides and metal carbides are difficult synthesize by employing colloidal synthesis. These metal nitrides and metal carbides received great attention in the research area of electrocatalysis and photoelectrocatalysis due to metallic electronic band structure,<sup>60-61</sup> and high durability in electrolyte solution. Solid state method is widely used experimental technique for the synthesis of metal nitrides, metal carbides and other different materials which requires high temperature.

### **1.5.2 Solid State Synthesis**

Solid state synthesis is a widely used experimental technique to synthesize various polycrystalline samples such as semiconductors, metals and dielectrics. In this method, the precursor materials are solids which mostly do not react together at room temperature. Hence, to drive the reaction between them, it is necessary to apply much higher temperature often in the range (500 - 1500 °C).<sup>54,62</sup> The factors which mainly effect on feasibility of solid state reactions are: (1) increasing the contact area between the reactant solids, (2) the slow rate of nucleation of product, and (3) the diffusion of the ions through various phases and particularly, through product phase. The fine grinded reactant material or pellet of reactant materials increases the contact area between the solids, and the rate of nucleation possibly increased by choosing the reactants and products have similar structural properties. The rate diffusion of ions can be increased by using two processes. The first one is the increasing the temperature, and second one introducing the defects prior or during the reaction.

Further to carry out the reaction at high temperatures, it is necessary to choose a suitable sample holder which does not react with both the reactant and product solids under the heating conditions used during the synthesis. Typically, the alumina and quartz based crucibles or boats are used. Likewise, noble metal based sample holders are used such as platinum and gold. The last step is the heat treatment process by using a furnace. The heating programme is used depending on the reactivity of reactant solids under the control of required atmosphere. Finally, the obtained product samples are characterized using various

experimental techniques. Using solid state synthesis method, g-C<sub>3</sub>N<sub>4</sub> nanosheets and TiN-NFG nanocomposites were synthesized, detailed of which was discussed in the chapters.

## 1.6 Improving the Charge Transport Properties of Films

Finally, to produce hydrogen fuel from water by following electrochemical HER and PEC water splitting method, we need efficient catalyst materials. In this regard, catalyst material should possess the properties like high electrical conductivity, large number of active sites on the surface of NCs and efficient transfer properties. NCs provide large number of active sites because of large surface to volume ratio. But the same aspect of NCs is also responsible for reducing charge transport in NCs films. To improve the charge transport properties of the NCs catalyst materials, we have adopted two different approaches.

### 1.6.1 Approach 1: Decoration of TiN Nanocrystals on N-Doped Graphene

As shown in Figure 1.12, to improve the charge transport property, we have prepared the nanocomposite of TiN NCs decorated on N-doped graphene through in-situ method where the TiN NCs provides charge carriers or active sites and N-doped graphene improves the charge transport.

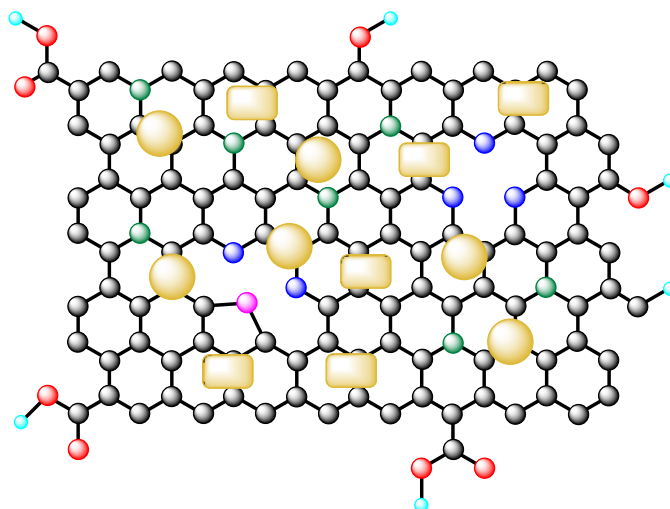


**Figure 1.12:** Schematic representation shows the decoration TiN NCs on N-doped graphene.

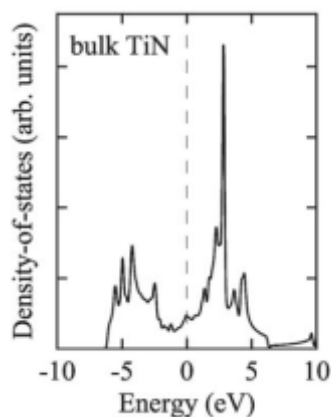


**Figure 1.13:** Total density of states for bulk TiN, and vertical line drawn at Fermi level. Reprinted with permission ref.<sup>63</sup> Copyright, 2012. Royal Society of Chemistry.

As shown in Figure 1.13, it has been realized that incorporation of nitrogen in the lattice of transition metal form interstitial alloys like TiN, exhibiting metallic electronic structure.<sup>60-61,</sup><sup>63</sup> A high ( $0.87 \text{ states eV}^{-1}$ ) density of states have been observed at the Fermi level of TiN, which mainly arise from contribution of Ti  $3d$ -levels.<sup>64</sup> This metallic electronic band structure of TiN similar to the noble metals is motivated us to explore the TiN as catalyst for different electrocatalytic applications.<sup>65-66</sup> TiN NCs have been studied as an alternative material for the noble metal NCs such as Pt and Au catalysts.<sup>67-72</sup> However, films of TiN NCs displayed poor charge transport properties due to the presence of large number of grain boundaries among the adjacent NCs. On the other hand,  $sp^2$  hybridized carbons in N-doped graphene offers good charge transport properties. Hence, we have synthesized nanocomposite of TiN and N - doped graphene like material where TiN NCs offers carrier density or active sites and N - doped graphene enhances charge transport. Furthermore, the composite offers large surface area which required in catalysis. In addition to, we prepared both TiN NC and N-doped graphene in-situ method using molecular precursor. This synthesis method is allows the chemical connectivity at the interface between TiN and N-doped graphene.

### 1.6.2 Approach 2: Through Interconnection of Nanocrystals

In approach 2, we developed a method to achieve electronic grade semiconductor (SC) thin film at room temperature from colloidal ligand-free lead chalcogenide (PbS and PbSe) NCs (Figure 1.13). We decreased temperature which required for the sintering of NCs by using two strategies: (i) synthesis of ligand-free colloidal PbS and PbSe NCs, and (ii) oriented attachment of NCs. Along with this, dipole moment of PbS and PbSe NCs support the



oriented attachment of NCs, therefore, decreasing the activation energy for the fusion of NCs, lead to formation of single-crystalline larger size NCs at room temperature. The organic-free surface of NCs also probably helps the easier fusion of NCs.

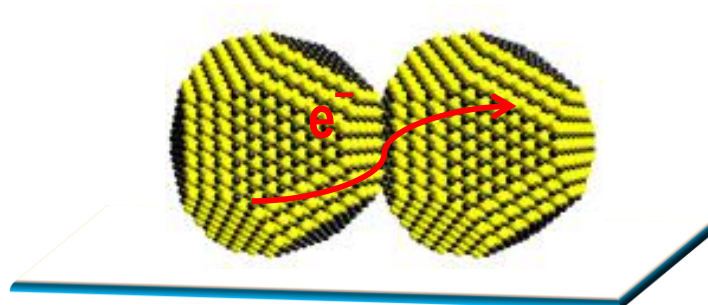


**Figure 1.13:** Interconnection of organic ligand-free PbS NCs.

## 1.7 Scope of This Ph.D. Work

Production of a clean fuel using renewable energy sources has been considered as the solution to our over-dependence on fossil fuels that are harmful to the environment. Consequently, production of hydrogen through water splitting has received great attention from the scientific community. The methods, electrocatalysis, and photoelectrocatalysis are known to assist the production of hydrogen from water. In this context, noble metals such as Pt, Au, and Pd became benchmark materials to drive such water splitting. In this thesis, we develop non-noble metal catalysts in the nanocrystalline form. Owing to high surface-to-volume ratio, NCs can exhibit more active surface sites for such catalytic applications. But these NCs suffer from poor charge transport compared to their bulk counterpart. Improving the charge transport in NC solids to achieve better catalytic performance is one of the key aspects of this thesis.

We developed titanium nitride - N-doped few-layer graphene (TiN-NFG) nanocomposite as an efficient electrocatalyst. The employed synthesis method produced a stable chemically bound interface between TiN and NFG providing colloidal stability, and enhanced electrocatalytic activities. Colloidal nanocomposite exhibit localized surface plasmon resonance (LSPR) band arising from metal-like TiN NCs. NFG provide colloidal stability, large surface area, and a medium charge transport. These properties motivated us to study the electrocatalytic activity of TiN-NFG nanocomposites for both HER and as counter electrode

in DSSC. This study is shown in chapter 2 of this thesis, showing superior activity of TiN-NFG nanocomposite as cost-effective and stable electrocatalyst.

It is known that electrocatalyst can be act as a co-catalyst with a photocatalyst in photocatalytic and photoelectrochemical water splitting for the production of hydrogen. Due to the impressive electrocatalytic activity of our TiN-NFG nanocomposite, we have studied in chapter 3, the co-catalyst efficiency of TiN-NFG with g-C<sub>3</sub>N<sub>4</sub> nanosheet (photo absorber) for photoelectrochemical reduction of water using solar light. The photocurrent density for H<sub>2</sub> production enhances by 16 times after using TiN-NFG co-catalyst. TiN-NFG nanocomposites synthesized through solid state method which require high temperature. Therefore, to reduce the cost of catalyst material we have chosen another material namely Sn-doped In<sub>2</sub>O<sub>3</sub> NCs, popularly known as ITO NCs. These ITO NCs were synthesized through colloidal route. Then, we studied the origin of LSPR band in Sn-doped In<sub>2</sub>O<sub>3</sub> NCs by carrying out reaction in different atmosphere like N<sub>2</sub>, Air and in a mixture of 90% N<sub>2</sub> and 10% H<sub>2</sub>. Further, we explored ITO NCs as a co-catalyst in PEC water splitting (chapter 4) by making g-C<sub>3</sub>N<sub>4</sub>:ITO nanocomposite.

In the chapter 5, we have discussed the synthesis and fabrication of electronic grade and flexible semiconductor film from solution processed PbS and PbSe semiconductor NCs by improving charge transport through oriented attachment of NCs. Finally, a summary and future outlook has been provided at the end of the thesis.

## References

1. Bockris, J. O. M. Science and Policy for Sustainable Development. *Environment* **1971**, *13*, 50-51.
2. Bockris, J. O. M. The Origin of Ideas on a Hydrogen Economy and Its Solution to the Decay of the Environment. *Int. J. Hydrog. Energy* **2002**, *27*, 731-740.
3. Fleischer, M. Recent Estimates of the Abundances of the Elements in the Earth's Crust; **1953**, 285.
4. Rostrup-Nielsen, J. R. Fuels and Energy for the Future: The Role of Catalysis. *Catal. Rev.* **2004**, *46*, 247-270.
5. Chu, S.; Majumdar, A. Opportunities and Challenges for a Sustainable Energy Future. *Nature* **2012**, *488*, 294.

6. Zhao, G.; Rui, K.; Dou, S. X.; Sun, W. Heterostructures for Electrochemical Hydrogen Evolution Reaction: A Review. *Adv. Funct. Mater.* **2018**, *28*, 1803291.
7. International Energy Agency, World Energy Outlook, <https://webstore.iea.org/world-energy-outlook-2017> (accessed: May 2018).
8. Cheng, Q.; Yi, H. Complementarity and Substitutability: A Review of State Level Renewable Energy Policy Instrument Interactions. *Renewable and Sustainable Energy Reviews* **2017**, *67*, 683-691.
9. Binz, C.; Gosens, J.; Hansen, T.; Hansen, U. E. Toward Technology-Sensitive Catching-Up Policies: Insights from Renewable Energy in China. *World Development* **2017**, *96*, 418-437.
10. Kreuter, W.; Hofmann, H. Electrolysis: The Important Energy Transformer in a World of Sustainable Energy. *Int. J. Hydrog. Energy* **1998**, *23*, 661-666.
11. C. A. Grimes, O. K. Varghese, S. Ranjan, Light, Water, Hydrogen: The Solar Generation of Hydrogen by Water Photoelectrolysis, Springer, Berlin. **2008**.
12. Tee, S. Y.; Win, K. Y.; Teo, W. S.; Koh, L. D.; Liu, S.; Teng, C. P.; Han, M. Y., Recent Progress in Energy-Driven Water Splitting. *Adv. Sci.* **2017**, *4*, 1600337-1600337.
13. Konieczny, A.; Mondal, K.; Wiltowski, T.; Dydo, P. Catalyst Development for Thermocatalytic Decomposition of Methane to Hydrogen. *Int. J. Hydrog. Energy* **2008**, *33*, 264-272.
14. Turner, J.; Sverdrup, G.; Mann, M. K.; Maness, P. C.; Kroposki, B.; Ghirardi, M.; Evans, R. J.; Blake, D. Renewable Hydrogen Production. *Int. J. Energy Research* **2008**, *32*, 379-407.
15. Lim, J.; Park, D.; Jeon, S. S.; Roh, C.-W.; Choi, J.; Yoon, D.; Park, M.; Jung, H.; Lee, H. Ultrathin IrO<sub>2</sub> Nanoneedles for Electrochemical Water Oxidation. *Adv. Funct. Mater.* **2018**, *28*, 1704796.
16. Zhang, L.; Han, L.; Liu, H.; Liu, X.; Luo, J. Potential-Cycling Synthesis of Single Platinum Atoms for Efficient Hydrogen Evolution in Neutral Media. *Angew. Chem. Int. ed.* **2017**, *56*, 13694-13698.
17. Shen, J.; Li, Z.; Yu, J.; Ding, B. Humidity-Resisting Triboelectric Nanogenerator for High Performance Biomechanical Energy Harvesting. *Nano Energy* **2017**, *40*, 282-288.

18. Wang, P.; Zhang, X.; Zhang, J.; Wan, S.; Guo, S.; Lu, G.; Yao, J.; Huang, X. Precise Tuning in Platinum-Nickel/Nickel Sulfide Interface Nanowires for Synergistic Hydrogen Evolution Catalysis. *Nat. Commun.* **2017**, *8*, 14580.
19. Zou, X.; Zhang, Y. Noble Metal-Free Hydrogen Evolution Catalysts for Water Splitting. *Chem. Soc. Rev.* **2015**, *44*, 5148-5180.
20. Cook, T. R.; Dogutan, D. K.; Reece, S. Y.; Surendranath, Y.; Teets, T. S.; Nocera, D. G. Solar Energy Supply and Storage for the Legacy and Nonlegacy Worlds. *Chem. Rev.* **2010**, *110*, 6474-6502.
21. Morales-Guio, C. G.; Stern, L. A.; Hu, X. Nanostructured Hydrotreating Catalysts for Electrochemical Hydrogen Evolution. *Chem. Soc. Rev.* **2014**, *43*, 6555-6569.
22. Voiry, D.; Yamaguchi, H.; Li, J.; Silva, R.; Alves, D. C. B.; Fujita, T.; Chen, M.; Asefa, T.; Shenoy, V. B.; Eda, G.; Chhowalla, M. Enhanced Catalytic Activity in Strained Chemically Exfoliated WS<sub>2</sub> Nanosheets for Hydrogen Evolution. *Nat. Mater.* **2013**, *12*, 850.
23. Feng, J. X.; Wu, J. Q.; Tong, Y. X.; Li, G. R. Efficient Hydrogen Evolution on Cu Nanodots-Decorated Ni<sub>3</sub>S<sub>2</sub> Nanotubes by Optimizing Atomic Hydrogen Adsorption and Desorption. *J. Am. Chem. Soc.* **2018**, *140*, 610-617.
24. Wang, A. L.; Lin, J.; Xu, H.; Tong, Y. X.; Li, G. R. Ni<sub>2</sub>P-CoP Hybrid Nanosheet Arrays Supported on Carbon Cloth as an Efficient Flexible Cathode for Hydrogen Evolution. *J. Mater. Chem. A* **2016**, *4*, 16992-16999.
25. Zhang, Z.; Lu, B.; Hao, J.; Yang, W.; Tang, J. FeP Nanoparticles Grown on Graphene Sheets as Highly Active Non-Precious-Metal Electrocatalysts for Hydrogen Evolution Reaction. *Chem. Commun.* **2014**, *50*, 11554-11557.
26. Wan, C.; Regmi, Y. N.; Leonard, B. M. Multiple Phases of Molybdenum Carbide as Electrocatalysts for the Hydrogen Evolution Reaction. *Angew. Chem.* **2014**, *126*, 6525-6528.
27. Ang, H.; Wang, H.; Li, B.; Zong, Y.; Wang, X.; Yan, Q. 3D Hierarchical Porous Mo<sub>2</sub>C for Efficient Hydrogen Evolution. *Small* **2016**, *12*, 2859-2865.
28. Yan, H.; Tian, C.; Wang, L.; Wu, A.; Meng, M.; Zhao, L.; Fu, H., Phosphorus-Modified Tungsten Nitride/Reduced Graphene Oxide as a High-Performance, Non-Noble-Metal Electrocatalyst for the Hydrogen Evolution Reaction. *Angew. Chem. Int. Ed.* **2015**, *54*, 6325-6329.

29. Chen, W.-F.; Sasaki, K.; Ma, C.; Frenkel, A. I.; Marinkovic, N.; Muckerman, J. T.; Zhu, Y.; Adzic, R. R. Hydrogen-Evolution Catalysts Based on Non-Noble Metal Nickel-Molybdenum Nitride Nanosheets. *Angew. Chem. Int. Ed.* **2012**, *51*, 6131-6135.
30. Gao, M. R.; Liang, J. X.; Zheng, Y. R.; Xu, Y. F.; Jiang, J.; Gao, Q.; Li, J.; Yu, S. H. An Efficient Molybdenum Disulfide/Cobalt Diselenide Hybrid Catalyst for Electrochemical Hydrogen Generation. *Nat. Commun.* **2015**, *6*, 5982.
31. Yan, X.; Tian, L.; He, M.; Chen, X. Three-Dimensional Crystalline/Amorphous Co/Co<sub>3</sub>O<sub>4</sub> Core/Shell Nanosheets as Efficient Electrocatalysts for the Hydrogen Evolution Reaction. *Nano Lett.* **2015**, *15*, 6015-6021.
32. Chen, H. M.; Chen, C. K.; Liu, R. S.; Zhang, L.; Zhang, J.; Wilkinson, D. P. Nano-Architecture and Material Designs for Water Splitting Photoelectrodes. *Chem. Soc. Rev.* **2012**, *41*, 5654-5671.
33. Hisatomi, T.; Kubota, J.; Domen, K., Recent Advances in Semiconductors for Photocatalytic and Photoelectrochemical Water Splitting. *Chem. Soc. Rev.* **2014**, *43*, 7520-7535.
34. Afroz, K.; Moniruddin, M.; Bakranov, N.; Kudaibergenov, S.; Nuraje, N. A. Heterojunction Strategy to Improve the Visible Light Sensitive Water Splitting Performance of Photocatalytic Materials. *J. Mater. Chem. A* **2018**, *6*, 21696-21718.
35. Saraswat, S. K.; Rodene, D. D.; Gupta, R. B. Recent Advancements in Semiconductor Materials for Photoelectrochemical Water Splitting for Hydrogen Production Using Visible Light. *Renewable and Sustainable Energy Reviews* **2018**, *89*, 228-248.
36. Fujishima, A.; Honda, K. Electrochemical Photolysis of Water at a Semiconductor Electrode. *Nature* **1972**, *238*, 37.
37. Xiang, Q.; Yu, J.; Jaroniec, M. Preparation and Enhanced Visible-Light Photocatalytic H<sub>2</sub>-Production Activity of Graphene/C<sub>3</sub>N<sub>4</sub> Composites. *J. Phys. Chem. C* **2011**, *115*, 7355-7363.
38. Baumgardner, W. J.; Whitham, K.; Hanrath, T. Confined-but-Connected Quantum Solids via Controlled Ligand Displacement. *Nano Lett.* **2013**, *13*, 3225-3231.
39. Tonda, S.; Kumar, S.; Gawli, Y.; Bhardwaj, M.; Ogale, S. B. g-C<sub>3</sub>N<sub>4</sub> (2D)/CdS (1D)/rGO (2D) Dual-Interface Nano-Composite for Excellent and Stable Visible Light Photocatalytic Hydrogen Generation. *Int. J. Hydrogen Energy* **2017**, *42*, 5971-5984.

40. Ong, W. J.; Tan, L. L.; Ng, Y. H.; Yong, S. T.; Chai, S. P. Graphitic Carbon Nitride (g-C<sub>3</sub>N<sub>4</sub>)-Based Photocatalysts for Artificial Photosynthesis and Environmental Remediation: Are We a Step Closer To Achieving Sustainability? *Chem. Rev.* **2016**, *116*, 7159-7329.
41. Chai, B.; Liu, C.; Yan, J.; Ren, Z.; Wang, Z. j. In-situ synthesis of WO<sub>3</sub> Nanoplates Anchored on g-C<sub>3</sub>N<sub>4</sub> Z-Scheme Photocatalysts for Significantly Enhanced Photocatalytic Activity. *Appl. Surf. Sci.* **2018**, *448*, 1-8.
42. Zhang, G.; Lan, Z. A.; Lin, L.; Lin, S.; Wang, X. Overall Water Splitting by Pt/g-C<sub>3</sub>N<sub>4</sub> Photocatalysts without Using Sacrificial Agents. *Chem. Sci.* **2016**, *7*, 3062-3066.
43. Ying-Ying, H.; Xiu-Li, L.; Shang-Feng, T.; Xue-Peng, Y.; Zhen-Wei, W.; Tong-Bu, L. Metal-Free 2D/2D Hetero-junction of Graphitic Carbon Nitride/Graphdiyne for Improving the Hole Mobility of Graphitic Carbon Nitride. *Adv. Energy Mater.* **2018**, *8*, 1702992.
44. Che, W.; Cheng, W.; Yao, T.; Tang, F.; Liu, W.; Su, H.; Huang, Y.; Liu, Q.; Liu, J.; Hu, F.; Pan, Z.; Sun, Z.; Wei, S. Fast Photoelectron Transfer in (C<sub>ring</sub>) - C<sub>3</sub>N<sub>4</sub> Plane Heterostructural Nanosheets for Overall Water Splitting. *J. Am. Chem. Soc.* **2017**, *139*, 3021-3026.
45. Qi, B.; Wang, J. Fill factor in Organic Solar Cells. *Phys. Chem. Chem. Phys.* **2013**, *15*, 8972-8982.
46. O'Regan, B.; Grätzel, M. A Low-cost, High-Efficiency Solar Cell Based on Dye-Sensitized Colloidal TiO<sub>2</sub> Films. *Nature* **1991**, *353*, 737.
47. Lee, Y. L.; Chen, C. L.; Chong, L. W.; Chen, C.-H.; Liu, Y. F.; Chi, C. F., A. Platinum Counter Electrode with High Electrochemical Activity and High Transparency for Dye-Sensitized Solar Cells. *Electrochem. Commun.* **2010**, *12*, 1662-1665.
48. Murakami, T. N.; Grätzel, M. Counter Electrodes for DSSC: Application of Functional Materials as Catalysts. *Inorganica Chim. Acta* **2008**, *36*, 572-580.
49. Li, G. R.; Song, J.; Pan, G. L.; Gao, X. P. Highly Pt-Like Electrocatalytic Activity of Transition Metal Nitrides for Dye-Sensitized Solar Cells. *Energy Environ. Sci.* **2011**, *4*, 1680-1683.
50. Wu, M.; Lin, X.; Wang, Y.; Wang, L.; Guo, W.; Qi, D.; Peng, X.; Hagfeldt, A.; Grätzel, M.; Ma, T. Economical Pt-Free Catalysts for Counter Electrodes of Dye-Sensitized Solar Cells. *J. Am. Chem. Soc.* **2012**, *134*, 3419-3428.

51. Balamurugan, J.; Thanh, T. D.; Kim, N. H.; Lee, J. H. Nitrogen-Doped Graphene Nanosheets with FeN Core-Shell Nanoparticles as High-Performance Counter Electrode Materials for Dye-Sensitized Solar Cells. *Adv. Mater. Interfaces* **2016**, *3*, 1500348.
52. Bi, E.; Chen, H.; Yang, X.; Peng, W.; Grätzel, M.; Han, L. A Quasi Core-Shell Nitrogen-Doped Graphene/Cobalt Sulfide Conductive Catalyst for Highly Efficient Dye-Sensitized Solar Cells. *Energy Environ. Sci.* **2014**, *7*, 2637-2641.
53. Murray, C. B.; Kagan, C. R.; Bawendi, M. G. Synthesis and Characterization of Monodisperse Nanocrystals and Close-Packed Nanocrystal Assemblies. *Ann. Rev. Mater. Sci.* **2000**, *30*, 545-610.
54. Allnatt, A. R.; Jacobs, P. W. M. Theory of Nucleation in Solid State Reactions. *Can. J. Chem.* **1968**, *46*, 111-116.
55. Park, J.; An, K.; Hwang, Y.; Park, J. G.; Noh, H. J.; Kim, J. Y.; Park, J. H.; Hwang, N.-M.; Hyeon, T. Ultra-Large-Scale Syntheses of Monodisperse Nanocrystals. *Nat. Mater.* **2004**, *3*, 891.
56. Kwon, S. G.; Hyeon, T. Formation Mechanisms of Uniform Nanocrystals via Hot-Injection and Heat-Up Methods. *Small* **2011**, *7*, 2685-2702.
57. Murray, C. B.; Norris, D. J.; Bawendi, M. G. Synthesis and Characterization of Nearly Monodisperse CdE (E = sulfur, selenium, and tellurium) Semiconductor Nanocrystallites. *J. Am. Chem. Soc.* **1993**, *115*, 8706-8715.
58. Kershaw, S. V.; Susa, A. S.; Rogach, A. L. Narrow Bandgap Colloidal Metal Chalcogenide Quantum Dots: Synthetic Methods, Heterostructures, Assemblies, Electronic and Infrared Optical Properties. *Chem. Soc. Rev.* **2013**, *42*, 3033-3087.
59. Kadlag, K. P.; Rao, M. J.; Nag, A. Ligand-Free, Colloidal, and Luminescent Metal Sulfide Nanocrystals. *J. Phys. Chem. Lett.* **2013**, *4*, 1676-1681.
60. Chen, J. G. Carbide and Nitride Overlayers on Early Transition Metal Surfaces: Preparation, Characterization, and Reactivities. *Chem. Rev.* **1996**, *96*, 1477-1498.
61. Chen, W. F.; Muckerman, J. T.; Fujita, E., Recent Developments in Transition Metal Carbides and Nitrides as Hydrogen Evolution Electrocatalysts. *Chem. Commun.* **2013**, *49*, 8896-8909.
62. West, A. R. Solid State Chemistry and its Applications, John Wiley and Sons, Student edn, **1998**, ch. 5.

63. Lee, T.; Delley, B.; Stampfl, C.; Soon, A. Environment-Dependent Nanomorphology of TiN: The Influence of Surface Vacancies. *Nanoscale* **2012**, *4*, 5183-5188.
64. Zhang, R. Q.; Lee, T. H.; Yu, B. D.; Stampfl, C.; Soon, A. The Role of Titanium Nitride Supports for Single-Atom Platinum-Based Catalysts in Fuel Cell Technology. *Phys. Chem. Chem. Phys.* **2012**, *14*, 16552-16557.
65. Zheng, P.; Zhao, J.; Zheng, J.; Ma, G.; Zhu, Z. Non-equilibrium Partial Oxidation of TiN Surface for Efficient Visible-Light-Driven Hydrogen Production. *J. Mater. Chem.* **2012**, *22*, 12116-12120.
66. Lu, X.; Wang, G.; Zhai, T.; Yu, M.; Xie, S.; Ling, Y.; Liang, C.; Tong, Y.; Li, Y. Stabilized TiN Nanowire Arrays for High-Performance and Flexible Supercapacitors. *Nano Lett.* **2012**, *12*, 5376-5381.
67. Ottakam Thotiyl, M. M.; Ravikumar, T.; Sampath, S. Platinum Particles Supported on Titanium Nitride: An Efficient Electrode Material for the Oxidation of Methanol in Alkaline Media. *J. Mater. Chem.* **2010**, *20*, 10643-10651.
68. Li, G. R.; Wang, F.; Jiang, Q. W.; Gao, X. P.; Shen, P. W. Carbon Nanotubes with Titanium Nitride as a Low-Cost Counter-Electrode Material for Dye-Sensitized Solar Cells. *Angew. Chem. Int. Ed.* **2010**, *49*, 3653-3656.
69. Guler, U.; Ndukaife, J. C.; Naik, G. V.; Nnanna, A. G. A.; Kildishev, A. V.; Shalaev, V. M.; Boltasseva, A. Local Heating with Lithographically Fabricated Plasmonic Titanium Nitride Nanoparticles. *Nano Lett.* **2013**, *13*, 6078-6083.
70. Yun, S.; Hagfeldt, A.; Ma, T. Pt-Free Counter Electrode for Dye-Sensitized Solar Cells with High Efficiency. *Adv. Mater.* **2014**, *26*, 6210-6237.
71. Xia, W.; Mahmood, A.; Liang, Z.; Zou, R.; Guo, S. Earth-Abundant Nanomaterials for Oxygen Reduction. *Angew. Chem. Int. Ed.* **2016**, *55*, 2650-2676.
72. Xie, J.; Xie, Y. Transition Metal Nitrides for Electrocatalytic Energy Conversion: Opportunities and Challenges. *Chem. – A Euro. J.* **2016**, *22*, 3588-3598.





## Chapter 2

# Colloidal Nanocomposite of TiN and N-Doped Few-Layer Graphene for Solar Cell and Electrochemical Hydrogen Evolution

---

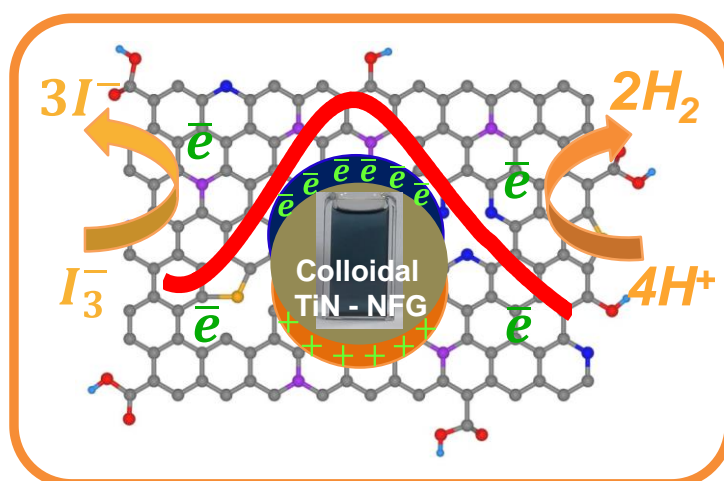
The following paper has been published based on the work documented in this chapter.

Shanker, G. S.; Markad, G. B.; Rao, M. J.; Bansode, U.; Nag, A. Colloidal Nanocomposite of TiN and N-Doped Few-Layer Graphene for Plasmonics and Electrocatalysis. *ACS Energy Lett.* **2017**, *2*, 2251-2256. Copyright permission has been obtained for complete article from American Chemical Society.

## Summary

A combination of high carrier density, high surface area, solution processibility, and low-cost are desired in a material for electrocatalytic applications including  $H_2$  evolution and counter electrode of a solar cell. Also, plasmonic based applications in biological systems can be derived from such material. In this regard, colloidal nanocomposite of TiN and N-doped few-layer graphene (TiN-NFG) is synthesized from molecular precursors. TiN nanocrystals (NCs) provide free electrons for electrical conductivity and plasmonics, whereas NFG is responsible for charge transport, high surface area and colloidal stability. Colloidal TiN-NFG nanocomposites exhibit localized surface plasmon resonance band around 700 nm. Coatings of the nanocomposite forms counter electrode for efficient (8.9 %) dye sensitized solar cells. Furthermore, the nanocomposite acts as an efficient electrocatalyst for hydrogen evolution reaction exhibiting overpotential  $\sim 161$  mV at a current density of  $10 \text{ mA/cm}^2$ . A rigid chemically and electronically connected interface between TiN and NFG components of the nanocomposite is the reason for the improved performance of nanocomposite.

## Graphical Presentation



## 2.1 Introduction

It is known that incorporation of nitrogen in the lattice of early transition metal form interstitial alloys like TiN, exhibiting metal-like electronic structure.<sup>1-2</sup> A high (0.87 states  $ev^{-1}$ ) density of states is observed at the Fermi level of TiN, mainly contributed by Ti 3d-levels.<sup>3</sup> This similarity of relevant part of electronic band structure of TiN with noble metal is the reason for using TiN as catalyst for various electrocatalytic processes.<sup>4-5</sup> Therefore, TiN nanocrystals (NCs) have been explored as an alternative of expensive noble metal NCs such as Pt and Au for catalysis and plasmonic applications.<sup>6-11</sup> However, prior reports of TiN NCs do not show colloidal stability, required for biological applications,<sup>12</sup> and solution processed device fabrication. The problem here is the reaction temperature of TiN is  $\sim 800$  °C.<sup>13</sup> Organic capping molecules and solvents required for colloidal synthesis of NCs are not stable at such high temperatures. Furthermore, such ligands often inhibits charge transport.<sup>14</sup> But films of TiN NCs exhibit poor charge transport because the adjacent nanocrystals in the film are separated by insulating (air) barriers.

On the other hand, in NFG, 2D network of  $sp^2$  hybridized carbons provides good charge transport properties, but does not have the metal-like free electron density required for electrocatalysis. To overcome these problems, we prepared nanocomposite of TiN and N-doped few-layer graphene (TiN-NFG), at a reaction temperature of 900 °C. TiN provides carrier density and NFG provides charge transport. Furthermore, functional groups of NFG provide colloidal stability. Also, NFG provides large surface area required for catalysis. Unlike prior reports,<sup>15-16</sup> we prepared both TiN NC and NFG simultaneously starting from molecular precursors. This method is expected to provide a better chemical connectivity between the two components at the interface, facilitating charge-transfer.

These colloidal TiN-NFG nanocomposites combines properties of TiN NCs and NFG exhibiting localized surface plasmon resonance (LSPR), low electrical resistivity (0.3 ohm cm), and high surface area (270  $m^2/g$ ). These properties were then utilized for applications of TiN-NFG nanocomposites as both counter electrode in dye sensitized solar cells (DSSC) and electrocatalyst for hydrogen evolution reaction (HER).

## 2.2 Experimental Sections

### 2.2.1 Chemicals

Urea (AR, 99.0 %, VETEC), lithium iodide (99.99 %, anhydrous, Aldrich), iodine (99.99% , Aldrich), N719 dye (Aldrich), F-doped  $SnO_2$  (FTO) coated glass ( $\sim 7$  ohm/sq, Aldrich),

dimethyl sulfoxide (DMSO, 99.9 %, Rankem), distilled water, chloroform (99.4%, Rankem), ethylene glycol (98.4%, Rankem), toluene (99.5 %, Rankem), hydrochloric acid (HCl, 33.4%, Rankem), acetonitrile (99.8 %, Rankem), N,N dimethylformamide (DMF, 99.5%, SDFCL), hexane (99.9 % AR, SDFCL), ethanol (99.9% AR, SDFCL), n-butanol (99.95%, Rankem), sulfuric acid (98.0%, Rankem), Pt/C (10 wt%, Aldrich), titanium tetrachloride (anhydrous, 99.0%, Merck), titanium nitride (Nanopowder size ~20 nm Sisco Reasearch Pvt. Ltd.), nafion (5 wt%, Aldrich), transparent titania paste (DSL-18NR-T, diameter ~20 nm), scattering titania paste (WER2-O, diameter ~400 nm) from Dyesol. All these chemicals used directly as received from the sources.

### **2.2.2 Synthesis of TiN and N-Doped Few-Layer Graphene (TiN-NFG) Nanocomposite**

5 mmol (580  $\mu$ L) titanium tetrachloride was added to 3 mL ethanol. The metal chloride reacted with alcohol releasing chlorine and hydrochloric acid, and forming titanium ethoxide. Then, 75 mmol (4.7 g) urea was added slowly (for about 30 min) to the above alcoholic solution, followed by stirring for about 2 hours to solubilize the urea completely, forming titanium-urea viscous solution.<sup>13</sup> This titanium-urea viscous solution was transferred into an alumina crucible, and kept inside a tubular furnace. This reaction mixture was heated to 900 °C using a heating rate of 3 °C/min, followed by calcinated at 900 °C for 5 hours. Then the sample was cooled to room temperature using a cooling rate ~ 2 °C/min. This whole process of heating and cooling was carried out under N<sub>2</sub> atmosphere. The obtained powder at room temperature can be dispersed into polar solvents like water and DMSO after ultra-sonication for about 30 min.

### **2.2.3 Preparation of N-Doped Few-Layer Graphene (NFG)**

N-doped few-layer graphene was prepared using previously reported synthetic protocol.<sup>17</sup> First graphene oxide (GO) was prepared. The mixture of GO and melamine with 1:5 ratio was taken in 100 mL deionized water which was ultrasonicated for 10 min, followed by stirred for 24 hours at 80 °C, resulting into dried uniform mixture. The obtained dried mixture of GO and melamine was calcinated at 800 °C for 4 hours under argon atmosphere, followed by natural cooling to room temperature. Black colored powder was obtained after the reaction.

### 2.2.4 Characterization

Powder x-ray diffraction (XRD) patterns of TiN-NFG nanocomposite were recorded using a Bruker D8 Advance X-ray diffractometer equipped with Cu K $\alpha$  radiation (1.54 Å). Raman spectra of nanocomposites were carried out using LabRAM HR800 from JY Horiba. X-ray photoelectron spectroscopy (XPS) was measured using Phi 5000 Versa Probe II, Physical Electronics, ULVAC PHI spectrometer, equipped with a Al K $\alpha$  ( $\lambda = 1486.6$  eV) x-ray source and a hemispherical analyzer. Fourier transform infrared spectroscopy (FTIR) measurements were carried out on the pellet of nanocomposite and KBr using Thermo scientific NICOLET 6700 FTIR spectrophotometer.  $\zeta$ -Potential data of colloidal TiN-NFG nanocomposite was measured using a Nano-ZS90 from Malvern Instruments, U.K. N<sub>2</sub> adsorption-desorption isotherms were carried out at 77 K, using a BelSorp-max instrument from Bel Japan. Surface area was calculated following Brunauer-Emmett-Teller (BET) method using Belmaster software. UV-visible-NIR absorption spectra of colloidal nanocomposites were measured using PerkinElmer Lambda-950 UV/vis spectrometer. Four probe temperature-dependent electrical resistivity measurements were performed on physical property measurement system from quantum design (PPMS-VSM). Transmission electron microscopy (TEM) images were taken using a JEOL JEM 2100 F field emission transmission electron microscope at 200 kV. High-resolution transmission electron microscopy images were obtained on a UHR FEG-TEM, JEOL JEM-2100 F electron microscope using a 200 kV electron source. Atomic force microscopy (AFM) data were collected using Keysight atomic force microscope (model: AFM 5500) by using tapping mode technique.

### 2.2.5 Fabrication of Dye Sensitized Solar Cell (DSSC)

Mesoporous TiO<sub>2</sub> electrodes have been prepared using a standard protocol.<sup>18</sup> TiO<sub>2</sub> nanoparticles with size 20 nm were coated on FTO glass as active layer. A scattering layer coated by using TiO<sub>2</sub> nanoparticles with size 400 nm on top of active layer. After coating of each layer, films were annealed at 450 °C for 30 min to form anatase phase of TiO<sub>2</sub> nanocrystals. Then the TiO<sub>2</sub> electrode was cooled to room temperature. To get rid of pinholes, the obtained TiO<sub>2</sub> electrodes were dipped in (40 mM) TiCl<sub>4</sub> aqueous solution at room temperature followed by heating at 70 °C for 30 min. After that, the above films were allowed to cool to room temperature, then films were cleaned with water and ethanol followed by annealing at 450 °C for 30 min. The thickness of the resultant active and scattering layers were optimized to ~ 11  $\mu$ m and ~ 5  $\mu$ m, respectively. In the following step, the obtained TiO<sub>2</sub> films were dipped in N719 dye solution for about 24 hours for the

sensitization. Dye solution was made by dissolving 0.012 mmol N719 dye in a mixture of 1:1 acetonitrile and tert-butanol.

For the preparation of counter electrode, 100 mg TiN-NFG nanocomposite was ground using a mortar and pestle to make fine powder. 20  $\mu\text{L}$  n-butanol was added drop-wise to the powder and grounded further to make a thick paste. This process of adding n-butanol (20  $\mu\text{L}$ ) while grinding was repeated for 15 times to obtain a homogeneous paste. This paste was doctor-bladed onto cleaned FTO glass, forming films of TiN-NFG nanocomposite of thickness  $\sim 11$   $\mu\text{m}$ . The composite films were annealed at 200  $^{\circ}\text{C}$  for 2 hour inside a  $\text{N}_2$  filled glove box, before using it as counter electrodes in DSSC and four-probe electrical conductivity measurements. DSSCs were assembled by sandwiching the dye sensitized  $\text{TiO}_2$  electrode with TiN-NFG nanocomposite counter electrode, spatially separated by using  $\sim 80$   $\mu\text{m}$  thick parafilm spacer and electrically connected through 20  $\mu\text{L}$  iodide/triiodide electrolyte. Iodide/triiodide electrolyte was prepared by using 0.6 M 1-propyl-2,3-dimethyl-imidazolium iodide, 0.05 M LiI, 0.05 M  $\text{I}_2$  and 0.5 M 4-tert-butylpyridine in acetonitrile/valeronitrile solution (1:1 v/v).

### 2.2.6 Solar Cell, Cyclic Voltammetry and Impedance Measurements

Current-voltage (I-V) characteristics of solar cells were measured using 150 W xenon lamp fitted with AM1.5 filter (Oriel Instruments) with intensity of 1 sun ( $100 \text{ mW cm}^{-2}$ ). The active area of all the cells was  $0.2 \text{ cm}^2$ . Cyclic voltammetry (CV) measurements were performed with the help of PAR Potentiostat/Galvanostat (PARSTAT 2273), using a typical three electrode system. TiN-NFG nanocomposite and Pt coated on FTO glass were used as working electrodes. Platinum wire loop and  $\text{Ag}/\text{Ag}^+$  (10 mM  $\text{AgNO}_3$  in acetonitrile) were used as counter and reference electrodes, respectively. Acetonitrile containing 1 mM LiI, 0.1 mM  $\text{I}_2$  and 100 mM  $\text{LiClO}_4$  used as electrolyte solution for  $\text{I}^{3-}$  reduction. CV measurements were carried out at scan rate of 50 mV/s. Electrochemical impedance spectroscopy (EIS) measurements were carried out in the frequency range of 100 kHz to 100 mHz. Experimental EIS results were fitted using ZSwimpWin software.

### 2.2.7 Electrochemical Measurements for Hydrogen Evolution Study

All the electrochemical measurements were carried out with the help of PAR Potentiostat/Galvanostat (PARSTAT 2273) using typical three electrode system. Graphite rod and  $\text{Ag}/\text{AgCl}$  (3 M KCl) were used as counter and reference electrodes, respectively. Glassy carbon electrode loaded with catalyst was used as working electrode. Typically, TiN-NFG

(20 mg) and 10  $\mu\text{L}$  nafion were added in 2 mL ethanol and sonicated (at least 2 hours) to prepare the catalyst ink. 2  $\mu\text{L}$  catalyst ink was carefully drop casted on the glassy carbon electrode of 3 mm diameter and dried under vacuum. All the measurements were performed in 0.5 M  $\text{H}_2\text{SO}_4$  solution. Linear sweep voltammetry (LSV) measurements were carried out at a scan rate of 5 mV/s and polarization curves were corrected for  $iR$  contribution with in the cell. Potentials were converted and reported with respect to reversible hydrogen electrode (RHE) using equation;  $E_{\text{RHE}} = E \text{ vs Ag/AgCl} + 0.059\text{pH} + E^0 (\text{Ag/AgCl})$ . Geometric surface areas of electrodes were used to calculate current density.

## 2.3 Results and Discussion

### 2.3.1 Synthesis of TiN-NFG Nanocomposite

TiN-NFG nanocomposites were synthesized by calcination of urea and titanium tetrachloride at 900  $^\circ\text{C}$  and schematic representation shown in Figure 2.1. Details of the synthesis methodology have been given in the experimental section (section 2.2.2).

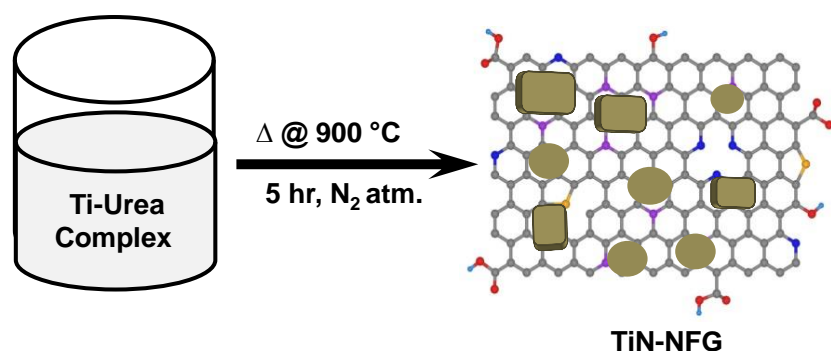


**Figure 2.1:** Schematic representation of synthesis of TiN-NFG nanocomposite.

### 2.3.2 Microscopic Analysis of TiN-NFG Nanocomposite

Transmission electron microscopy (TEM) image in Figure 2.2a shows darker NCs attached to a low-contrast layered material. The size distribution plot for NCs in Figure 2.2b show NCs with a size of  $14 \pm 5$  nm. A high resolution TEM (HRTEM) image (Figure 2.2c) of a single NC and corresponding fast Fourier transformed (FFT) pattern in Figure 2.2d, confirm cubic phase of TiN NCs. Interplanar distances of 0.24, 0.21 and 0.15 nm correspond to (111), (200) and (022) planes, respectively. Atomic force microscopy (AFM) image in Figure 2.3a again show  $\sim 14$  nm sized NCs (height profile-I in Figure 2.3b) are attached to a layered material with  $\sim 1.5$  nm thickness (height profile-II in Figure 2.3c).



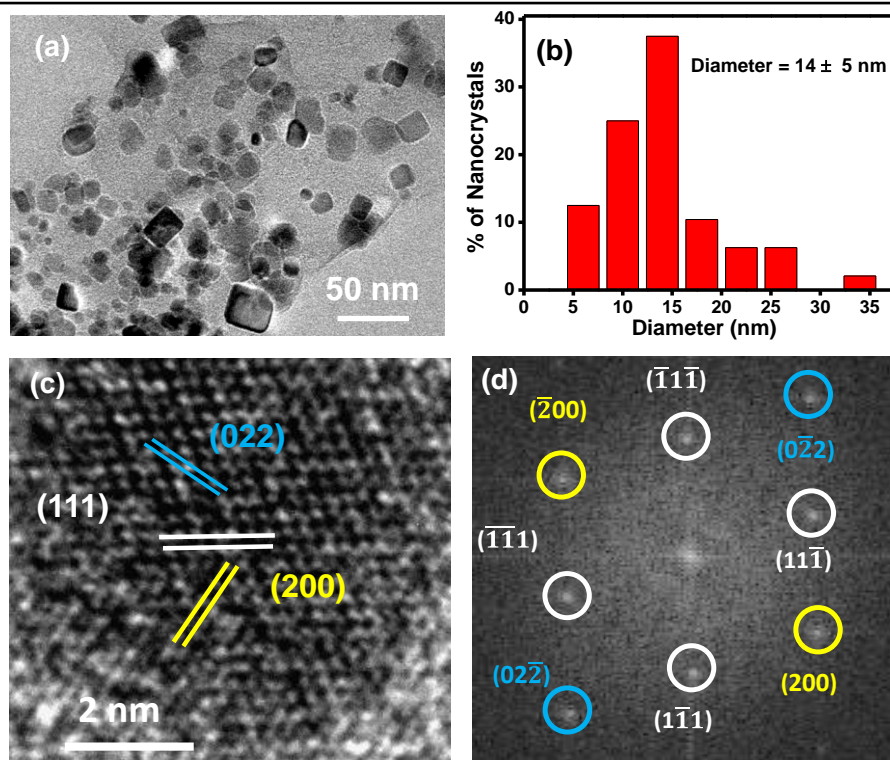


**Figure 2.2:** Morphology of TiN-NFG nanocomposite. (a) TEM, (b) size distribution plot of TiN nanocrystals present in the TiN-NFG nanocomposites. (c) HRTEM image of single TiN NC present in the TiN-NFG nanocomposites and (d) FFT pattern of HRTEM image in (c).

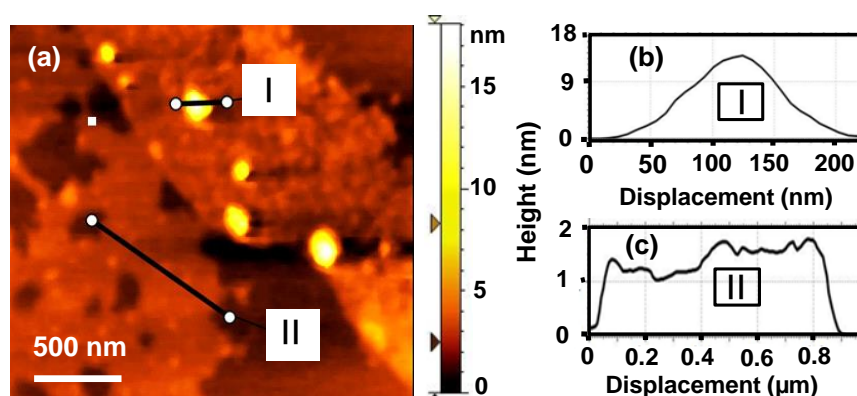
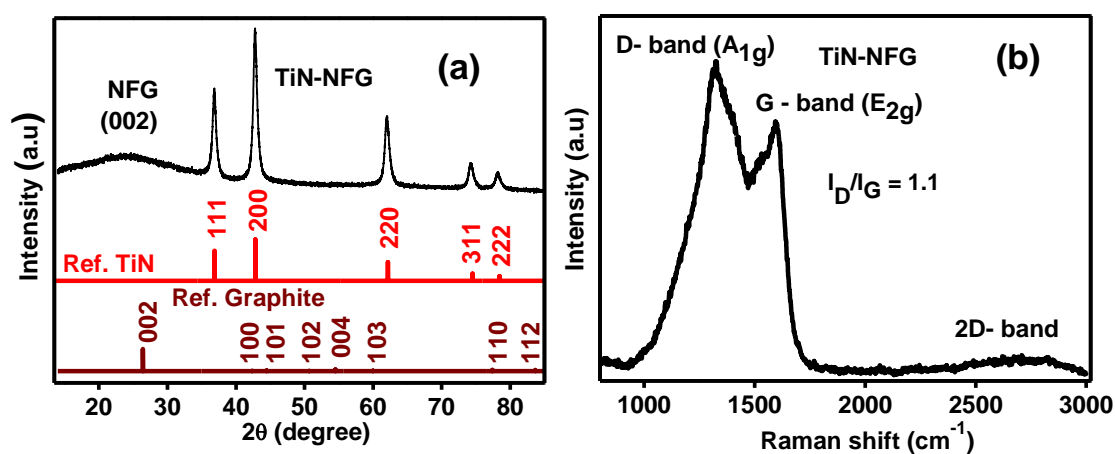


**Figure 2.3:** (a) AFM image of TiN-NFG nanocomposite. Height profiles for line I and II in the AFM image (a) are shown in (b) and (c), respectively.

### 2.3.3 Structural Analysis of TiN-NFG Nanocomposite

Powder x-ray diffraction (XRD) pattern in Figure 2.4a agrees with the formation of TiN NCs along with an additional broad peak at  $2\theta = 24.5^\circ$ . This broad peak may arise due to the few-layer graphene-like material.<sup>19</sup> Preliminary estimation using Scherer equation<sup>20</sup> suggests 3 to

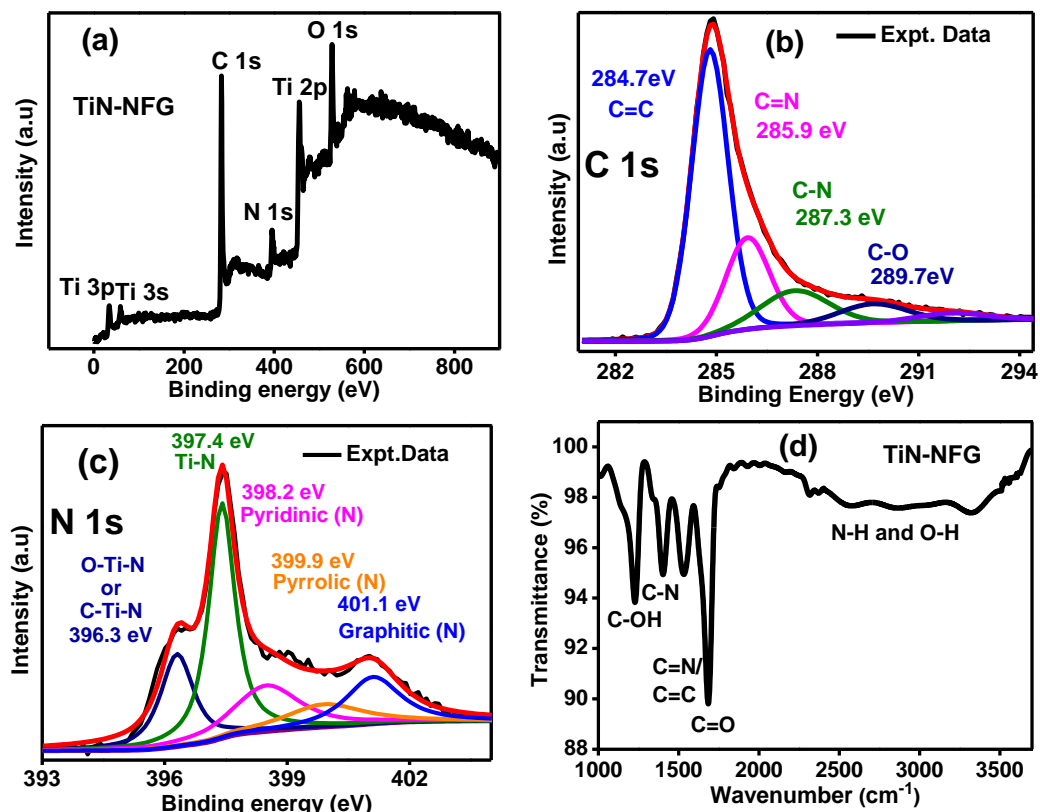
4 layers of graphene-like material, which is in accordance with 1.5 nm thick layer observed by AFM. Under our reaction conditions, there is a possibility of formation of N-doping in few-layer graphene. To explore such possibilities, we used Raman, Fourier transform infrared (FTIR) and X-ray photo electron spectroscopy (XPS) spectroscopy. Three peaks in the Raman spectrum (Figure 2.4b) can be assigned to D-band at  $1327\text{ cm}^{-1}$ , G-band at  $1593\text{ cm}^{-1}$  and the broad 2D band at  $2710\text{ cm}^{-1}$  of a graphene-like material.<sup>21-24</sup> Ratio of peak intensities between D-and and G-band ( $I_D/I_G$ ) is 1.1, suggesting existence of defects/disorders in the few-layer graphene.<sup>21</sup> Such defects may originate from N-doping, however, other possibilities such as amorphous carbon and broken edges cannot be ruled out.



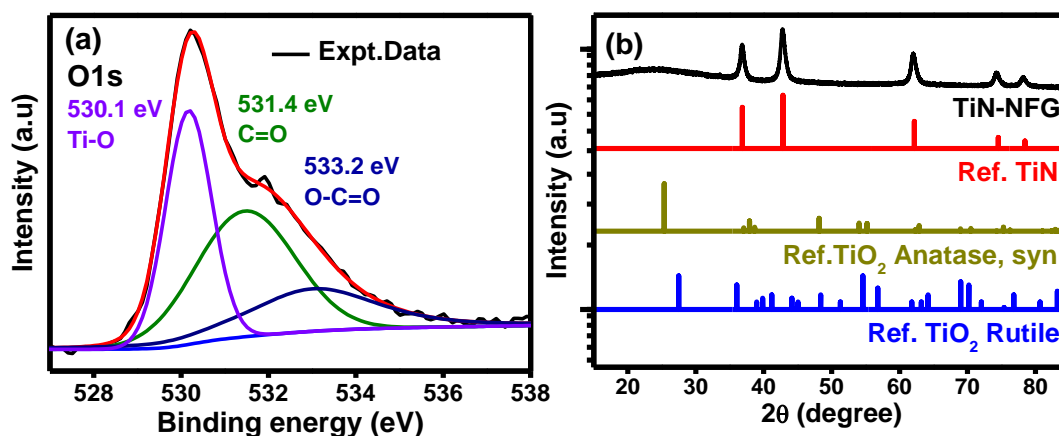
**Figure 2.4:** (a) Powder XRD data, and (b) Raman spectrum of TiN-NFG nanocomposite.

XPS spectra in Figure 2.5a-c show presence of multiple chemical environments around both C and N in the sample. De-convolution of the experimental N 1s spectrum (Figure 2.5c) suggests contributions from TiN NC, pyridinic (N), pyrrolic (N) and graphitic (N) nitrogen at binding energies 397.4, 398.4, 399.9 and 401.1 eV, respectively, suggesting the possibility of N-doping in few-layer graphene.<sup>25-27</sup> Furthermore, N 1s contribution from O-Ti-N and/or C-Ti-N at 396.3 eV,<sup>27</sup> suggests the possibility of chemical binding at the interface of TiN and NFG. Likewise, FTIR spectrum (Figure 2.5d) comprises of the vibrations corresponding to C=O, C–N, C–O, and C=C/C=N functional groups. The broad peak  $\sim 3000\text{ cm}^{-1}$  can be assigned to superposition of N–H and O–H stretching vibrations. XPS data for O 1s spectrum in Figure 2.6a suggest the presence of Ti–O bonds probably because of O–Ti–N interface or some minor surface oxidation of TiN NCs, along with C=O and O–C=O functional groups present in the NFG. XRD data plotted in logarithmic scale in Figure 2.6b rules out the presence of measurable crystalline TiO<sub>2</sub> impurities in the product.

Raman, XPS, and FTIR results together suggest the formation of N-doped graphene in the TiN-NFG nanocomposite.

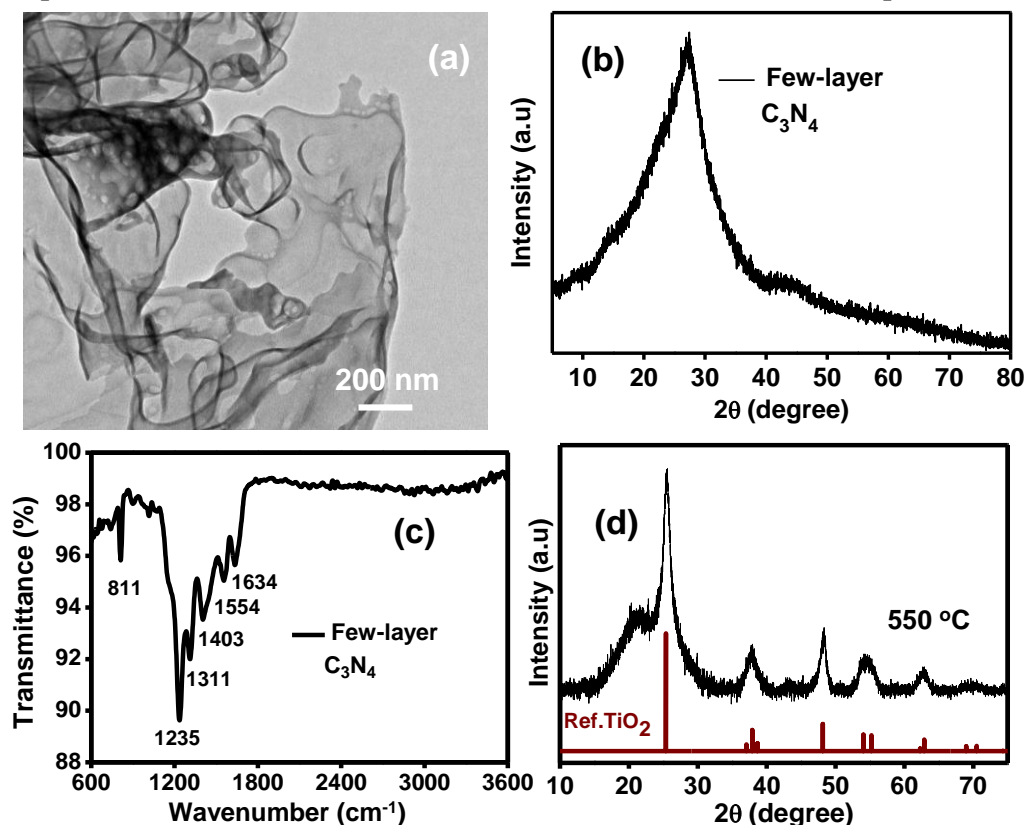


**Figure 2.5:** (a) XPS survey spectrum, (b) C 1s and (c) N 1s spectra of TiN-NFG nanocomposite. Black lines are experimental spectra and red lines are overall fit to the experimental spectra. Other colored lines are de-convoluted component spectra giving the overall fit. This fitting includes a background component violet in color. (d) FTIR spectrum of TiN-NFG nanocomposite.



**Figure 2.6:** (a) XPS for O 1s core level of TiN-NFG nanocomposite, and de-convolution of the experimental data to different component spectra. (b) Comparison of XRD data with different phases of bulk TiO<sub>2</sub> and TiN, when the intensity axis is plotted in logarithmic scale.

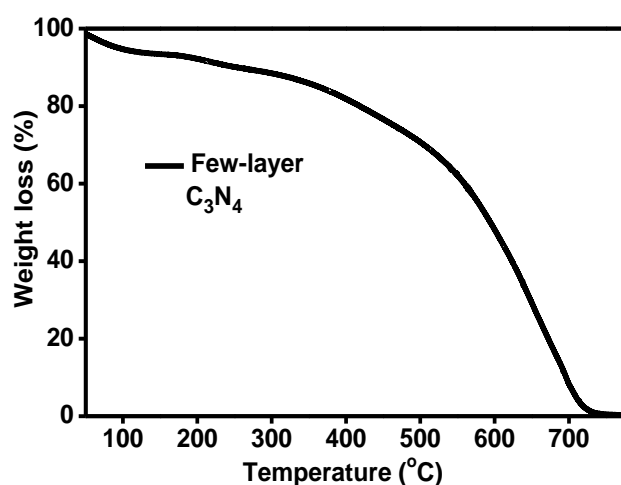
### 2.3.4 Proposed Mechanism for the Formation of TiN-NFG Nanocomposite



**Figure 2.7:** (a) TEM image, (b) powder XRD pattern and (c) FTIR spectrum of carbon nitride (few-layer  $C_3N_4$ ), prepared by decomposing urea at 550 °C. (d) Powder XRD pattern of the product by heating Ti-urea complex (mixture of urea, ethanol and  $TiCl_4$ ) at 550 °C.

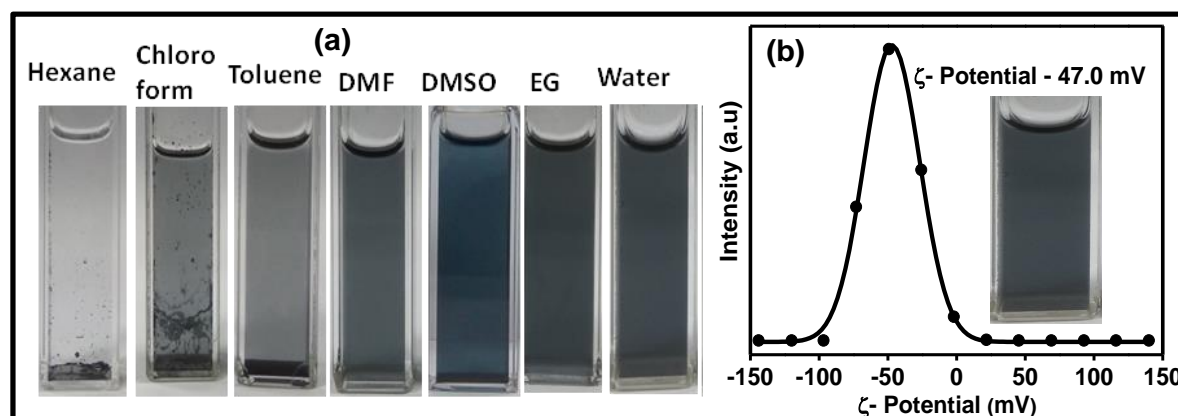
To understand mechanistic pathways involved in this reaction of formation of TiN-NFG nanocomposite, we have studied various intermediate steps of the reaction. As a control reaction, when urea was heated at 900 °C in the absence of  $TiCl_4$ , it decomposes into gaseous products without leaving behind any solid product. However, when the above reaction was carried out at 550 °C, a pale yellow color powder was obtained, which was characterized (Figure 2.7a-c) as few-layer  $C_3N_4$ , similar to the report of Liu et al.<sup>28</sup> This suggests that in the reaction of TiN-NFG nanocomposite, probably  $C_3N_4$  forms first at ~550 °C. Next, the Ti-urea complex shown in Figure 2.1 was reacted at 550 °C, and the product was characterized (Figure 2.7d) as a mixture containing  $TiO_2$  and carbon nitride (or carbon) compounds. This finding again suggests the formation of  $C_3N_4$  but TiN is not formed at ~550 °C. Instead  $TiO_2$  is formed. Interestingly, > 650 °C reaction temperature, we get TiN-NFG nanocomposite as the product. This temperature 650 °C, at which TiN starts forming also coincide with the decomposition temperature of few-layer  $C_3N_4$  (Thermo gravimetric analysis (TGA) data in

Figure 2.8), suggesting that probably the gaseous product formed by decomposition of  $C_3N_4$  act as a major nitrogen source for the formation of TiN. Then the reaction temperature was increased further to 900 °C to facilitate the formation of TiN, yielding the final product TiN-NFG nanocomposite. Overall, these results suggest that, during the heating of Ti-urea complex, few-layer  $C_3N_4$  and  $TiO_2$  are formed at ~ 550 °C, which then react subsequently at higher temperatures yielding TiN-NFG nanocomposite. Similar possibilities have also been discussed in prior literature,<sup>29-30</sup> but further studies are required to confirm the proposed mechanism of formation of TiN-NFG nanocomposite.



**Figure 2.8:** TGA data of few-layer  $C_3N_4$  under  $N_2$  environment.

### 2.3.5 Colloidal Stability of TiN-NFG Nanocomposite



**Figure 2.9:** (a) Digital photograph of TiN-NFG colloidal dispersion in different solvents. (b)  $\zeta$ -potential data and inset in (b) shows digital photograph of colloidal dispersion of TiN-NFG nanocomposite in water.

Photographs in Figure 2.9a shows that the TiN-NFG nanocomposite exhibit colloidal stability in various polar solvents like water, DMSO, N,N-dimethylformamide (DMF), and ethylene glycol (EG).  $\zeta$ -potential value of - 47.0 mV (Figure 2.9b) for the dispersion in water suggests that the nanocomposite maintains colloidal stability by electrostatically repelling each other. This negative charge and colloidal stability is attributed to functional groups in NFG. Colloidal stability again suggests TiN NCs are bound to the NFG.

Colloidal stability, XPS, and TEM (Figure 2.5a-c and Figure 2.2a) suggest TiN NCs form chemically stable interfaces with NFG. We could not find TiN NCs separated from layered material in TEM images, even after sonicating the sample for a long time. This strong interface connecting the TiN and NFG in the TiN-NFG nanocomposites is important for charge-transfer across the interface. Such charge-transfer will improve electrocatalytic performance of the nanocomposite.

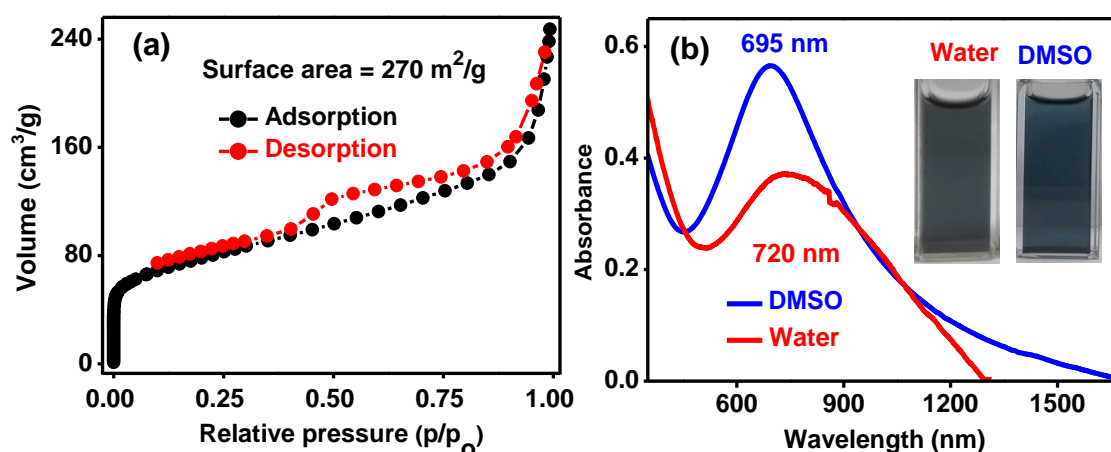


**Figure 2.10:** Surface area and LSPR. (a) N<sub>2</sub> adsorption - desorption isotherm from the powder sample, and (b) UV-visible-NIR absorption spectra showing LSPR from the colloidal TiN-NFG nanocomposite dispersed in DMSO and water. Photographs of corresponding colloidal dispersions are shown in the inset.

### 2.3.6 Properties of TiN-NFG Nanocomposite

After synthesis and characterization, we explore properties such as surface area, LSPR and electrical resistivity. LSPR provides information about the availability of free electrons, resistivity indicates about charge transport behavior, and surface area shows the availability of sites for electrocatalysis. Combination of these properties determines the suitability of a material for photo and electrocatalytic applications.<sup>31-33</sup> BET specific surface area was measured from N<sub>2</sub> adsorption-desorption isotherms shown in Figure 2.10a. BET specific



surface area of TiN-NFG nanocomposite is high ( $270 \text{ m}^2/\text{g}$ ) compared to reported values of similar composites.<sup>15, 34</sup> Such high surface area is desired for electrocatalysis. UV-vis-NIR absorption spectra (Figure 2.10b) of colloidal TiN-NFG nanocomposites show LSPR band with peak  $\sim 700 \text{ nm}$ , arising from metal-like free electrons in TiN NCs.<sup>8</sup> To the best of our knowledge, this is first report of LSPR from TiN NCs (in our composite) in the solution form. Minor red-shift in LSPR peak of the composite dispersed in water compared to that in DMSO is probably because of the higher dielectric constant of water. Such red-shift based on dielectric constant of medium is a characteristic of LSPR band. Interestingly, the LSPR band lies in biologically transparent second window ( $650 \text{ nm}$  to  $950 \text{ nm}$ ), so one can explore this water soluble composite for biological applications.

LSPR suggest high electron density of TiN NCs in the nanocomposite. Now if the interface between NFG and TiN is electronically connected, then the carrier density of TiN should result in electrical conductivity of the nanocomposite. Therefore we made the pellets of TiN-NFG nanocomposites and measured electrical resistivity. Four probe electrical resistivity of the pellet of TiN-NFG nanocomposites at  $300 \text{ K}$  is  $0.3 \text{ ohm cm}$  shown in Figure 2.11. This low value of resistivity agrees with the LSPR data, suggesting the high density of free electrons arising from TiN NCs. Resistivity increases with decreasing temperature (Figure 2.11). Such non-metallic behavior arises from NFG transport layer separating metallic TiN NCs.<sup>35</sup>

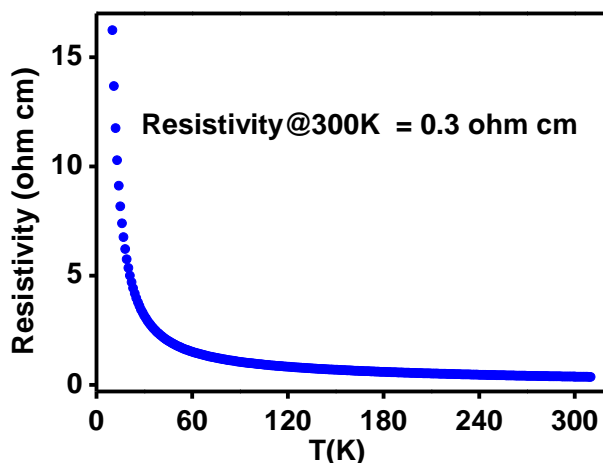


**Figure 2.11:** Temperature dependent electrical resistivity from a pellet of TiN-NFG nanocomposite.

The resistivity data in the temperature range of  $300 - 220 \text{ K}$  was fitted (Figure 2.12a) with nearest neighbour hopping (NNH),<sup>36</sup> whereas at lower temperatures ( $220 - 10 \text{ K}$ ), Mott

variable range hopping (MVRH)<sup>37</sup> mechanism can fit the data (Figure 2.12b). Resistivity of sample increases due to the number of unoccupied states reduces for a particular given occupied state, so that leading to freezing of NNH mechanism. In the NNH mechanism, the electron hops nearest neighbor unoccupied states from below the Fermi level  $E_F$ , of occupied states, this kind of conduction also required activation energy here the obtained activation energy is  $\sim 40.0$  meV. Further, low temperature region follows with MVRH mechanism. Since TiN-NFG nanocomposites exhibit low electrical resistivity and high surface area, along with metallic TiN component, we explore their efficacy as counter electrode in a DSSC, and electrocatalytic HER.

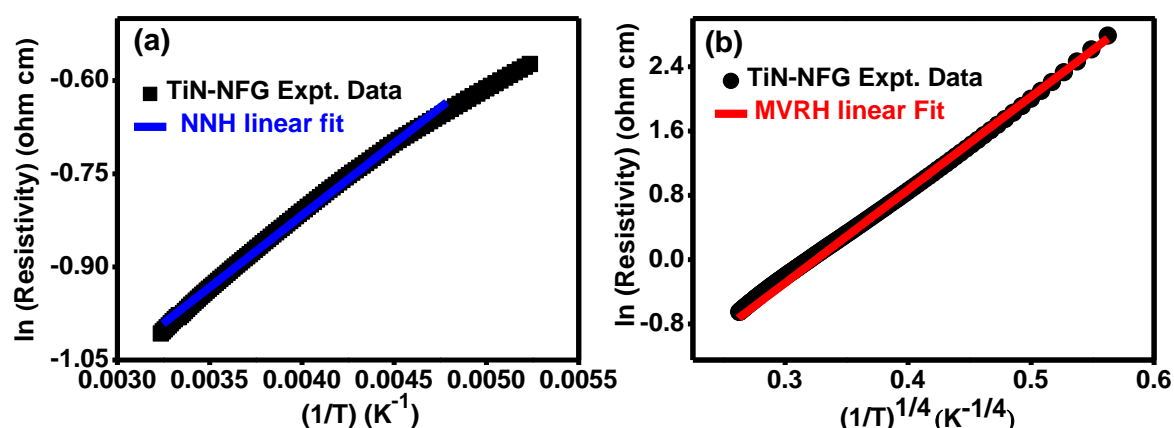


**Figure 2.12:** Fitting of temperature dependent electrical resistivity data with nearest neighbor hopping (NNH), and Mott variable range hopping (MVRH) models.  $\ln(\text{resistivity})$  versus  $(1/T)^{1/x}$  data were fitted using (a)  $x = 1$ , for NNH model, and (b)  $x = 4$ , for MVRH.

Figure 2.13a shows schematic representation of our DSSC. The photoanode was prepared by sensitizing porous  $\text{TiO}_2$  film casted on fluorine doped tin oxide (FTO) glass (Figure 2.13b), using commercially available N719 dye. A film of  $11.5 \mu\text{m}$  thick TiN-NFG nanocomposite on FTO surface (Figure 2.13c) was used as cathode (counter electrode) material, along with tri-iodide redox couple ( $I^-/I_3^-$ ) in acetonitrile as electrolyte. DSSCs were measured using illumination of  $100 \text{ mW/cm}^2$  on  $0.20 \text{ cm}^2$  active area. Details of the device fabrication are given in the experimental section (section 2.2.5). For comparisons, control devices were also fabricated using different counter electrodes, namely, Pt, TiN NCs and NFG instead of TiN-NFG. Use of Pt electrode is the most conventional one.<sup>38</sup> NFG were synthesized following literature<sup>39-41,42</sup>, and  $\sim 20 \text{ nm}$  TiN NCs were procured commercially from Sisco Research Laboratories Pvt. Ltd. Detailed characterizations of both samples are provided in Figure 2.14.



### 2.3.7 Counter Electrode Efficiency of TiN-NFG Nanocomposite

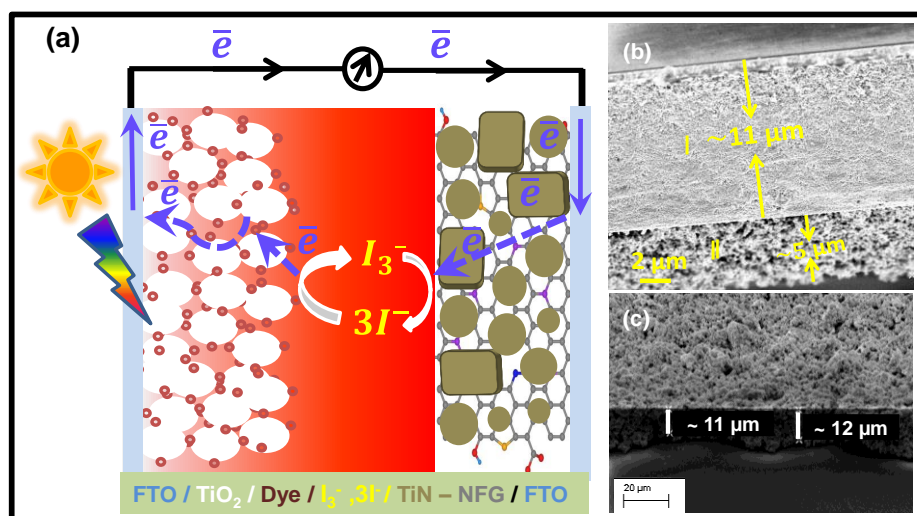


**Figure 2.13:** (a) Schematic representation of our DSSC using TiN-NFG nanocomposite as a counter electrode. (b) FESEM image of TiO<sub>2</sub> electrode where region I and II show thickness of active layer and scattering layer, respectively and (c) thickness of TiN-NFG counter electrode, used for DSSC.

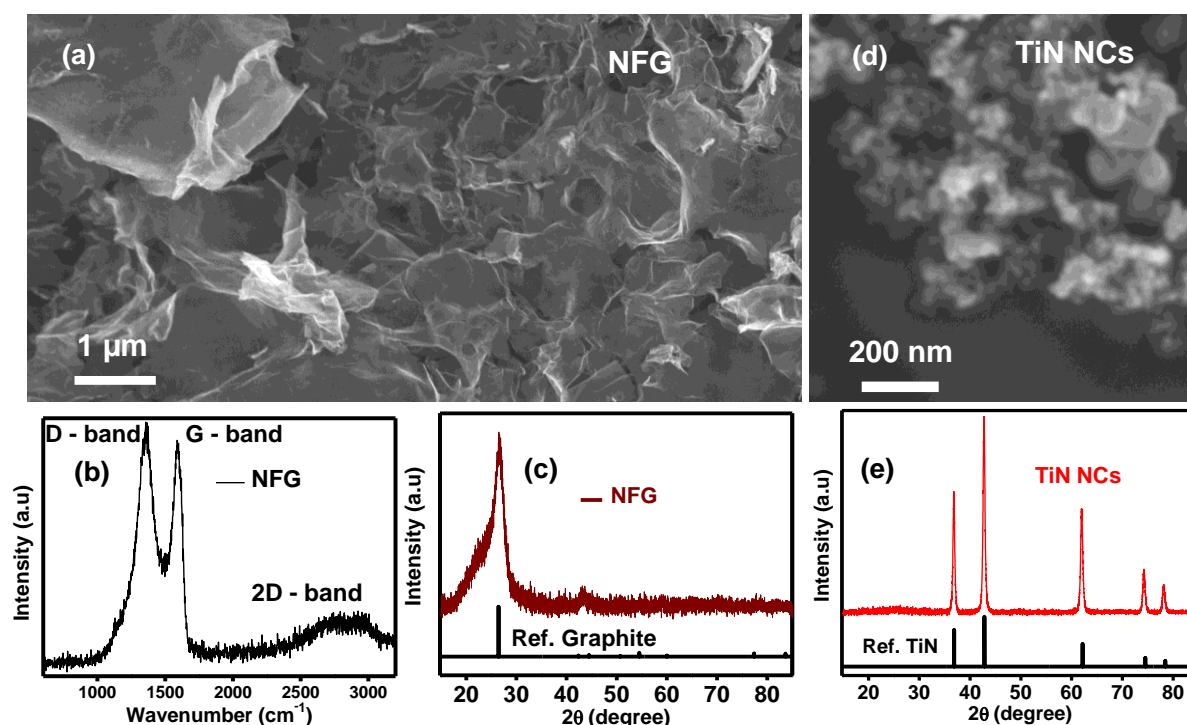


**Figure 2.14:** (a) FESEM image, (b) Raman spectrum, and (c) powder XRD pattern of NFG. (d) FESEM image of TiN NCs shows the nearly spherical morphology. (e) Powder XRD pattern of commercially available TiN NCs where the XRD peaks were matched with bulk TiN reference (JCPDS-38-1420). Diameter of NCs estimated from FWHM of XRD peaks using Scherer equation is ~20 nm.

For making the counter electrodes, films of NFG and TiN NCs were prepared with thicknesses  $\sim 14 \mu\text{m}$  and  $\sim 13 \mu\text{m}$  respectively, as shown in Figure 2.15 and 2.16. Doctor blading technique was used to make the films.

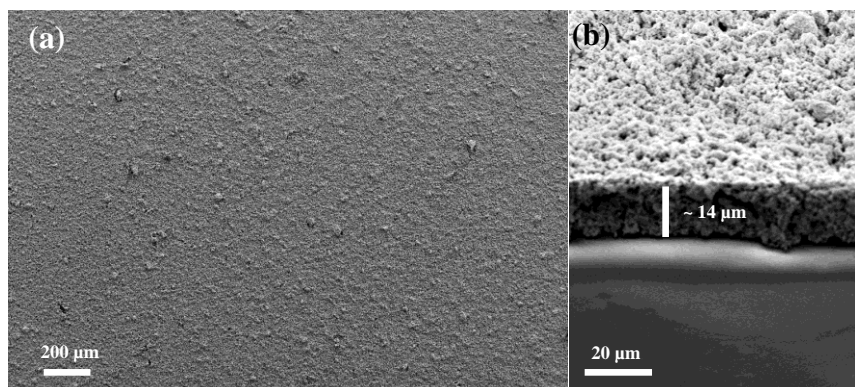


**Figure 2.15:** FESEM images show (a) morphology and (b) thickness of NFG film on FTO coated glass.

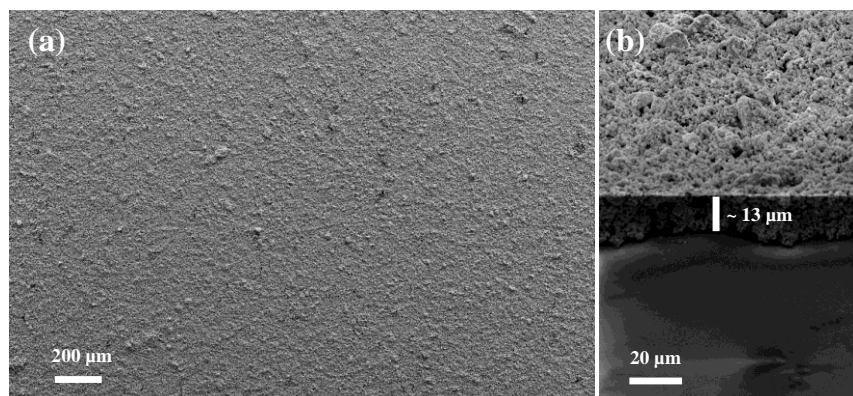


**Figure 2.16:** FESEM images show (a) morphology and (b) thickness of TiN NC film on FTO coated glass.

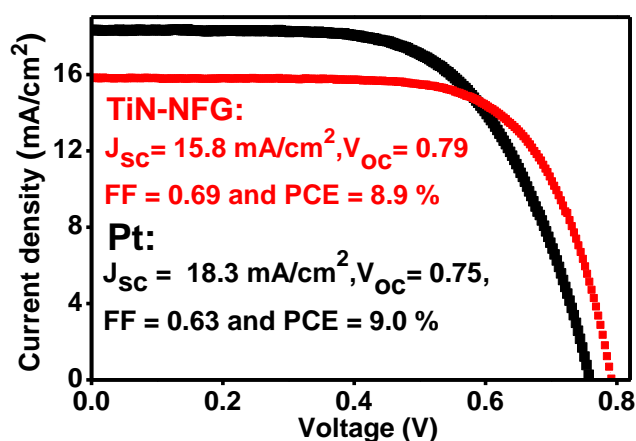


**Figure 2.17:** Current density ( $J$ ) versus voltage ( $V$ ) plots of DSSCs using TiN-NFG or Pt counter electrodes.

Current density (J) versus voltage (V) curves of two best DSSCs, with TiN-NFG or Pt as counter electrode exhibit comparable solar cell parameters. Similar values of short circuit current ( $J_{SC}$ ), fill factor (FF) and open circuit voltage ( $V_{OC}$ ) are shown in Figure 2.17. Power conversion efficiency (PCE) obtained using TiN-NFG counter electrode is 8.9 %, whereas PCE for Pt electrode is 9.0 %. Statistics of solar cell parameters on multiple DSSCs using both TiN-NFG nanocomposite and Pt electrodes are shown in the Figure 2.18. These data show that the overall  $\eta$  is similar using both TiN-NFG and Pt counter electrodes. The average  $V_{OC}$  obtained using TiN-NFG is slightly higher than that of Pt, whereas,  $J_{SC}$  for Pt electrode is slightly higher compared to TiN-NFG electrode.

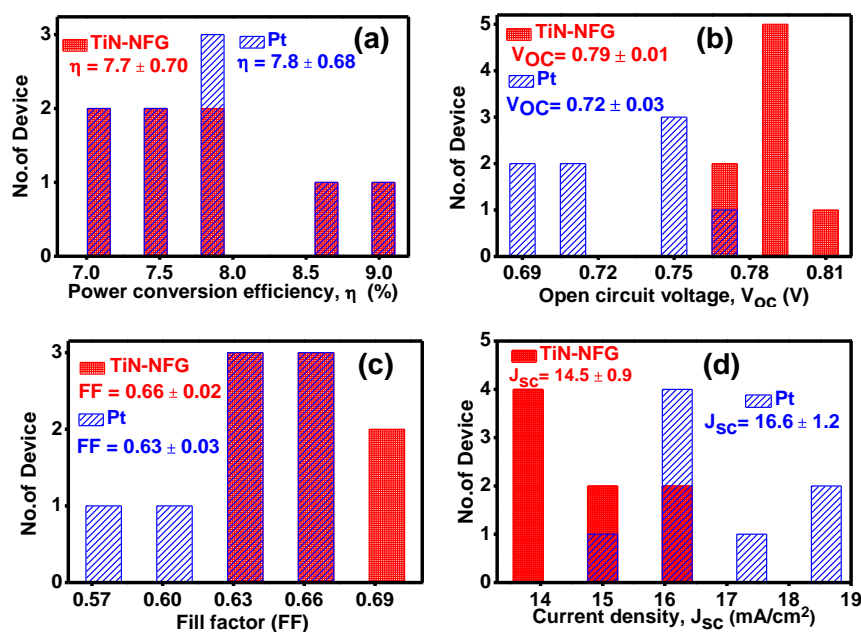


**Figure 2.18:** Statistical comparison of solar cell parameters. (a) Power conversion efficiency ( $\eta$ ), (b) open circuit voltage ( $V_{oc}$ ), (c) fill factor (FF), and (d) short circuit current density ( $J_{sc}$ ), of DSSCs prepared using Pt or TiN-NFG counter electrodes.

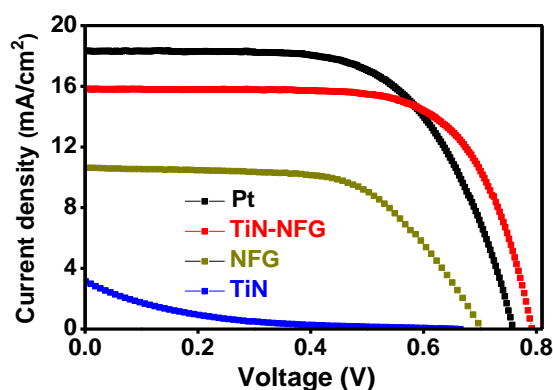


**Figure 2.19:** Comparison of current density (J) vs voltage (V) plot of DSSCs with different counter electrodes, namely, Pt, TiN-NFG nanocomposite, NFG and TiN NCs.

J-V plots in Figure 2.19 and the obtained solar cell parameters in Table 2.1 show that DSSCs prepared using both TiN NCs and NFG as counter electrodes exhibit lower PCE values of 0.2% and 4.6 %, respectively. This poor performance might arise from the higher electrical resistivity values of films of TiN NCs ( $11 \times 10^3$  ohm cm) and NFG (10 ohm cm), at 300 K (Figure 2.20). DSSC parameters obtained using our TiN-NFG counter electrode are among the best ones compared to previously reported non-platinum based counter electrodes, as shown in Table 2.2.

**Table 2.1:** Solar cell parameters of DSSCs with different counter electrodes corresponding to J-V plots shown in Figure 2.19.

Counter electrode	Jsc (mA/cm <sup>2</sup> )	Voc (V)	FF	PCE (%)
Pt	18.3	0.75	0.63	9.0
TiN-NFG	15.8	0.79	0.69	8.9
TiN	3.1	0.66	0.09	0.2
NFG	10.6	0.7	0.61	4.7

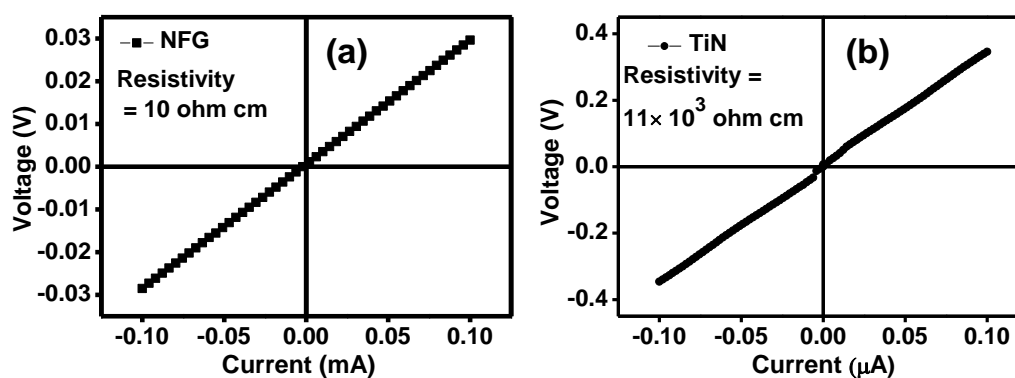


**Figure 2.20:** Voltage vs current plots for (a) NFG films and (b) TiN NC films measured using four-probe method at 300 K.

**Table 2.2:** Comparison of DSSC parameters obtained using our TiN-NFG counter electrode, with other counter electrodes reported in literature. Also, surface area and resistivity of our TiN-NFG counter electrode has been compared with other reported electrodes.

Counter electrode (CE)	$J_{sc}$ (mA/cm <sup>2</sup> )	$V_{oc}$ (V)	Fill factor (FF)	Power conversion efficiency (PCE)	Surface area (m <sup>2</sup> /g)	Resistivity(oh m cm)	References
TiN-NFG	15.8	0.79	0.69	8.9	270	0.3	Present Work
OMC- TiN - C <sup>a</sup>	14.3	0.69	0.67	6.7	389.2	--	<sup>43</sup>
NG - TiN <sup>b</sup>	12.3	0.72	0.64	5.8	136.2	--	<sup>15</sup>
TiN - Carbon nanotubes (CNTS)	12.7	0.75	0.57	5.1	61.2	--	<sup>7</sup>
TiN-3	16.5	0.75	0.62	7.8	76	--	<sup>44</sup>
TiN(P)- PEDOT:PSS	14.4	0.72	0.67	7.0	---	--	<sup>45</sup>
TiN - Carbon Fiber (CF )	19.3	0.64	0.54	7.2	----	--	<sup>46</sup>
TiN/TiO <sub>2</sub>	12.6	0.78	0.72	7.3	25.6	0.00047	<sup>47</sup>
TiN	12.8	0.79	0.61	6.2	--	---	<sup>48</sup>
Pt	20.2	0.69	0.69	9.7	--	--	<sup>49</sup>
NDG – CoS <sup>c</sup>	20.4	0.71	0.74	10.7	---	--	
Pt	17.0	0.75	0.78	9.9	----	--	<sup>50</sup>
NG – FeN <sup>d</sup>	18.8	0.74	0.78	10.9	---	--	
Carbon – Fe <sub>3</sub> O <sub>4</sub>	16.0	0.75	0.68	8.1	---	---	<sup>51</sup>
MoN - N-Doped GO	14.6	0.77	0.70	7.8	---	--	<sup>52</sup>

a: OMC - TiN - C = ordered mesoporous carbon - TiN - carbon; b: NG - TiN = N-Doped graphene - TiN; c: NDG - CoS = N-Doped graphene - CoS and d: NG - FeN = N-Doped graphene - FeN.

To understand the reason behind the impressive DSSC performance, we studied the electrocatalytic activity of both the electrodes towards  $I_3^-$  reduction using cyclic voltammetry (CV) and electrochemical impedance spectroscopy (EIS). Cyclic voltammograms in Figure 2.21a shows two oxidation ( $A_1$  and  $A_2$ ) and two reduction ( $C_1$  and  $C_2$ ) peaks. Pair of peaks  $A_1/C_1$  correspond to  $I_3^- + 2e^- \leftrightarrow 3I^-$  reaction, whereas pair  $A_2/C_2$  corresponds to

$3I_2 + 2e^- \leftrightarrow 2I_3^-$ .<sup>53</sup> TiN-NFG exhibits a lower peak to peak separation ( $E_{pp}$ ) of 133 mV for  $A_1/C_1$  pair, compared to the Pt electrode. Furthermore, TiN-NFG electrode shows stable shape of voltammograms even after 500 cycles (Figure 2.21b).

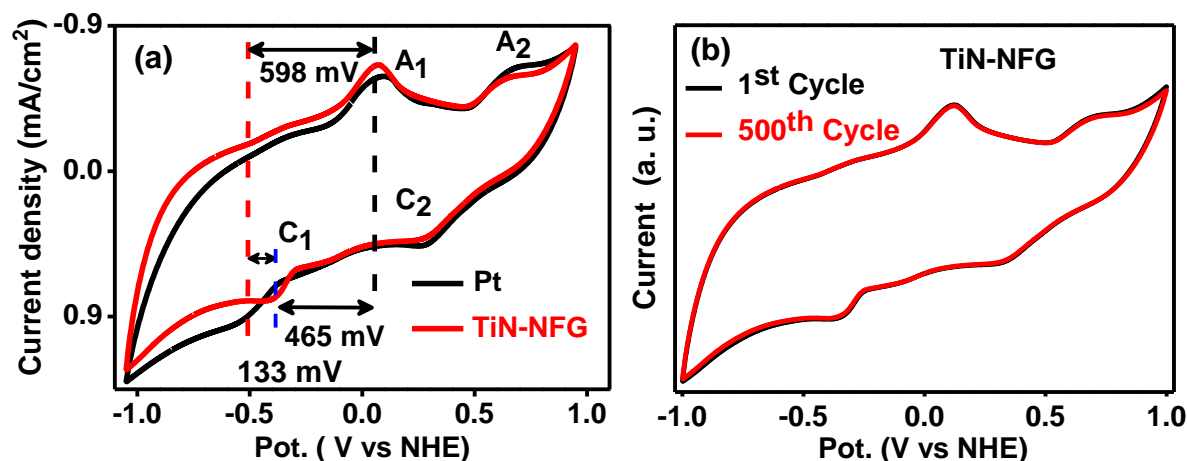


**Figure 2.21:** (a) Cyclic voltammograms using 50 mV/s scan rate and (b) 1<sup>st</sup> and 500<sup>th</sup> cycle of repeated cyclic voltammograms recorded on TiN-NFG electrode in acetonitrile containing 1 mM LiI, 0.1 mM  $I_2$ , and  $LiClO_4$  electrolyte.

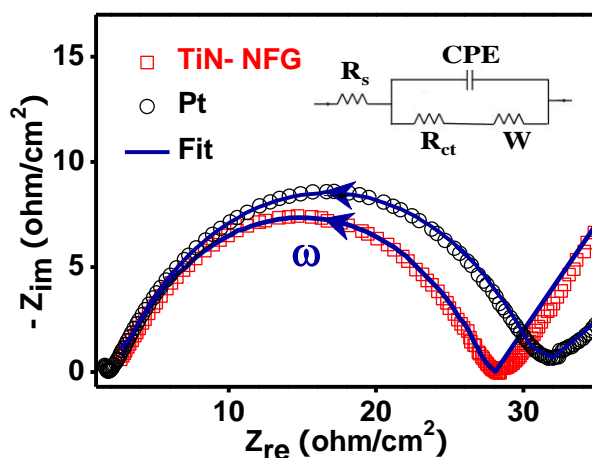


**Figure 2.22:** EIS Nyquist plots (100 kHz to 100 mHz) for TiN-NFG and Pt electrode in acetonitrile containing 1 mM LiI, 0.1 mM  $I_2$ , and 100 mM  $LiClO_4$  electrolyte. Inset shows equivalent circuit used for fitting the experimental EIS data.  $R_s$ : ohmic internal resistance;  $R_{ct}$ : charge-transfer resistance; CPE: constant phase element; and W: Warburg impedance.

EIS in the frequency range of 100 kHz to 100 mHz has been used to study charge transfer kinetics at electrode/electrolyte interface. Nyquist plots in Figure 2.22 were fitted using a model equivalent circuit shown in the inset. Best fit parameters in Table 2.3 show similar



ohmic resistance ( $R_s$ ) for both electrodes but the charge-transfer resistance ( $R_{ct}$ ) values for TiN-NFG (25.2 ohm/cm<sup>2</sup>) is smaller compared to that for Pt (28.8 ohm/cm<sup>2</sup>). Lower values of both  $R_{ct}$  and  $E_{pp}$  suggest an efficient reduction of  $I_3^-$  at TiN-NFG electrode, explaining observed high efficacy DSSC using TiN-NFG counter electrode.<sup>15, 50</sup>

**Table 2.3:** Best fit parameters obtained by fitting EIS data in Figure 2.22, with the equivalent circuit shown in the inset of Figure 2.22.

Counter electrode	$R_s$ , ohm	$R_{ct}$ , ohm /cm <sup>2</sup>	CPE, (Seimens sec <sup>n</sup> /cm <sup>2</sup> )	W, ohm
TiN-NFG	2.4	25.2	$6 \times 10^{-4}$	0.68
Pt	2.3	28.8	$7 \times 10^{-4}$	0.69

### 2.3.8 Electrochemical Hydrogen Evolution Reaction (HER) Using TiN-NFG Nanocomposite

Now we discuss HER, using a typical three electrode system. Working electrode was prepared by drop casting 0.28 mg/cm<sup>2</sup> TiN-NFG nanocomposite on glassy carbon (GC) electrode (Figure 2.23a). Ag/AgCl (3 M KCl) and graphite rod were used as reference and counter electrode, respectively. Linear sweep voltammograms (LSV) of TiN-NFG and Pt/C electrodes are compared in Figure 2.23b. For TiN-NFG, potential at a given current density decreases systematically with increasing number of cycles till ~90 cycles, above which the potential remains unchanged. This decrease in potential with increasing number of cycles might occur because of the liberation of H<sub>2</sub> gas exfoliating NFG layers, which in turn might increase both accessibility and overall surface area.<sup>54</sup> The final overpotential after 90 cycles at current density 1 mA/cm<sup>2</sup> is 93 mV, and that at 10 mA/cm<sup>2</sup> is 161 mV. Figure 2.23c shows that control samples NFG and TiN NCs show higher overpotentials 410 and 227 mV at 10 mA/cm<sup>2</sup>, respectively.

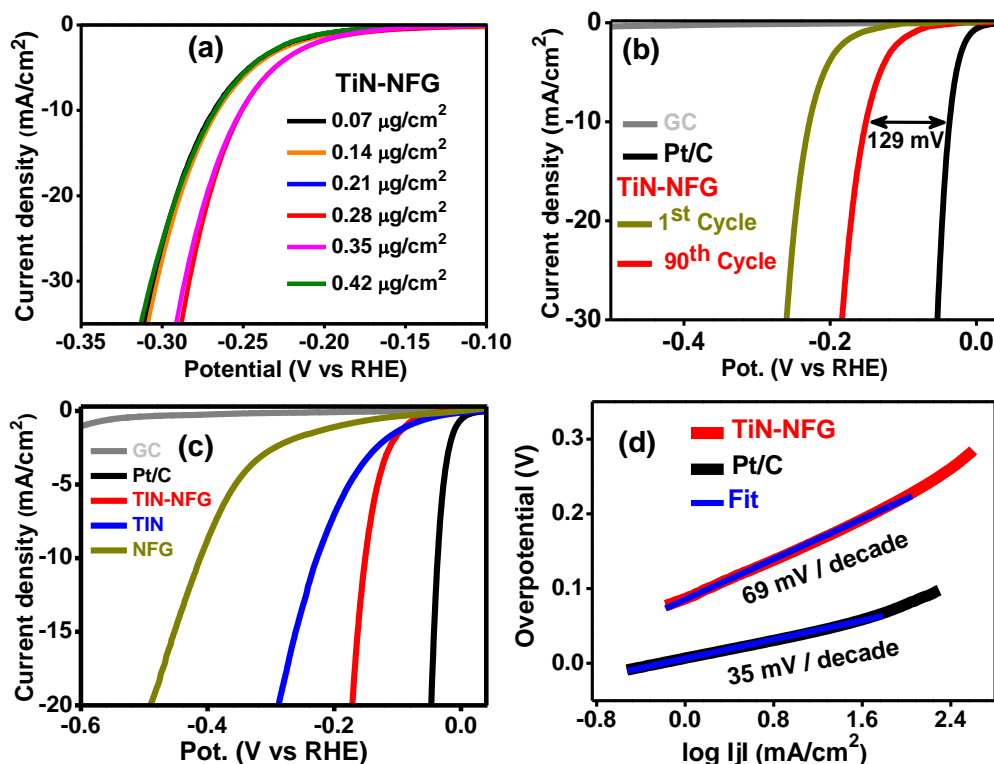


**Figure 2.23:** (a) LSV polarization curves of TiN-NFG electrodes prepared by using different loading amount of TiN-NFG on glassy carbon (GC) electrode. Based on these data, we used 0.28  $\text{mg}/\text{cm}^2$  loading amount for preparing working electrodes for HER experiments in this chapter. (b) LSV polarization curves for TiN-NFG nanocomposite and Pt/C and (c) Comparison of LSV polarisation curves for Pt/C, TiN-NFG nanocomposite, NFG, TiN NC and glassy carbon (GC) electrodes in 0.5 M  $\text{H}_2\text{SO}_4$ . (d) Tafel plots of TiN-NFG nanocomposite and Pt/C in 0.5 M  $\text{H}_2\text{SO}_4$ .

Tafel plots (Figure 2.23d) of TiN-NFG nanocomposite and Pt/C catalyst gives Tafel slopes of 66 and 35  $\text{mV dec}^{-1}$  along with exchange current densities of  $4.36 \times 10^{-2}$  and  $4.8 \times 10^{-1}$   $\text{mA}/\text{cm}^2$ , respectively. This Tafel slope and exchange current density of Pt/C agrees well with known activity and mechanism of Pt/C catalyst.<sup>55-56</sup> Tafel slope for TiN-NFG fall in the range of 42 to 118 suggesting that the HER follows the Volmer-Heyrovsky mechanism.<sup>2, 56</sup> In this mechanism, desorption of  $\text{H}_2$  molecules is the rate determining step. Furthermore, activity of catalyst was retained >95 % (Figure 2.24) after 5000 cycles. Table 2.4 shows that the HER parameters obtained for TiN-NFG electrodes are among the best ones, compared to parameters reported in prior literature of transition metal nitrides. Our TiN-NFG nanocomposite with a suitable interface that facilitate charge transfer between both components of the composite, combines both high carrier density and reasonably good charge



transport properties. Consequently, the TiN-NFG nanocomposites exhibit better electrocatalytic properties both as counter electrodes in DSSC and also in HER, compared to the controlled samples of TiN NCs and NFG.

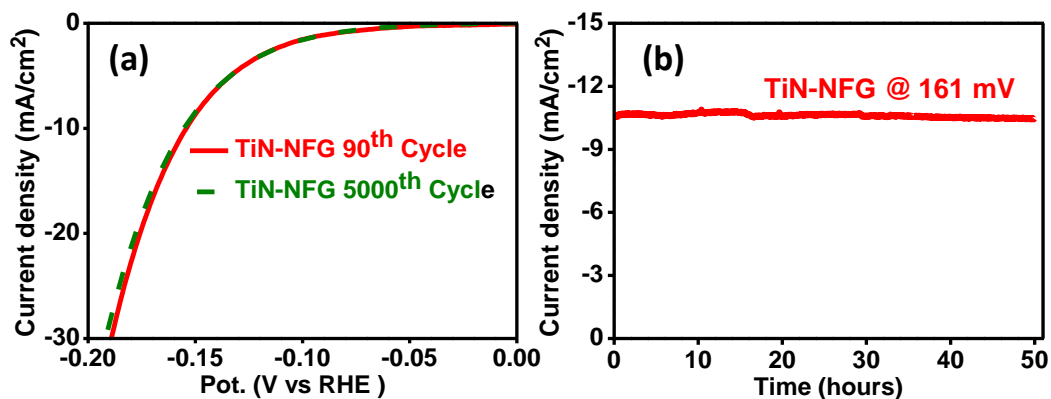


**Figure 2.24:** Stability test of TiN-NFG nanocomposite as HER catalyst. (a) 90<sup>th</sup> and 5000<sup>th</sup> LSV curves of repeated measurements, and (b) time dependent cathodic current density over 50 hours, where potential was held at 161 mV. As shown in figure 2.23b and discussed in the section 2.3.7, overpotential improves from 1<sup>st</sup> cycle to 90<sup>th</sup> cycle. Therefore, for a consistent comparison, initial 90 cycles of LSV were not included in this stability test.

\*Declaration: HER, CV and EIS experiments were carried out by Dr. Ganesh B. Markad (postdoctoral fellow in our group) along with my participation.

**Table 2.4:** Comparison of HER performance of TiN-NFG nanocomposite with different catalysts from literature.

S.No.	Catalyst	Electrolyte	Overpotential mV @ mA /cm <sup>2</sup>			Tafel slope mV dec <sup>-1</sup>	Reference
			1/ onset	10	20		
1.	TiN-NFG	0.5 M H <sub>2</sub> SO <sub>4</sub>	93	161	171	66	Present work
2.	Single-crystalline TiN NWs	1 M HClO <sub>4</sub>	92	--	--	54	57
3.	Ni-C-N NSs	0.5 M H <sub>2</sub> SO <sub>4</sub>	--	60.9	--	32	58
		1.0 M PBS	--	92.1	--	--	
		1.0 M KOH	--	30.8	--	--	
4.	WN NA/CC <sup>a</sup>	0.5 M H <sub>2</sub> SO <sub>4</sub>	--	198	--	92	59
5.	g-Mo <sub>2</sub> N	0.5 M H <sub>2</sub> SO <sub>4</sub>	--	381		100	60
		1 M KOH	240	353		100	
6.	MoCN	P <sup>H</sup> 1 (H <sub>2</sub> SO <sub>4</sub> + Na <sub>2</sub> SO <sub>4</sub> )	50	140		46	61
7.	P-WN/rGO <sup>b</sup>	0.5 M H <sub>2</sub> SO <sub>4</sub>	46	85		54	62
8.	WON@NC NAs/CC <sup>c</sup>	0.5 M H <sub>2</sub> SO <sub>4</sub>	--	106	172	65	63
9.	MoN nanosheets	0.5 M H <sub>2</sub> SO <sub>4</sub>	100		--	90	64
10.	Mo <sub>2</sub> N/CNT-graphene	0.5 M H <sub>2</sub> SO <sub>4</sub>	118	186		72	65
11.	MoN	0.5 M H <sub>2</sub> SO <sub>4</sub>	100			90	64
12.	Fe-WCN	1M H <sub>2</sub> SO <sub>4</sub>	120	250	--		66
13.	Ta <sub>3</sub> N <sub>5</sub>	0.05 MH <sub>2</sub> SO <sub>4</sub>	160	--	--	103	67
14.	Co <sub>0.6</sub> Mo <sub>1.4</sub> N <sub>2</sub>	0.1 M HClO <sub>4</sub>	--	200	--	--	68
	δ-MoN	0.1 M HClO <sub>4</sub>	--	300	--	--	
15.	NiMoN <sub>x</sub> /C	0.1 M HClO <sub>4</sub>	78	--	--	35.9	69
	MoN/C	0.1 M HClO <sub>4</sub>	157	--	--	54.5	
16.	NiMoN <sub>x</sub> /C	0.1 M HClO <sub>4</sub>	78	--	---	35	69

a: WN NA/CC = tungsten nitride nanorods array/carbon cloth; b: P-WN/rGO = phosphorus-modified tungsten nitride/reduced graphene oxide; c: WON@NC NAs/CC = three-dimensional N-doped carbon-coated tungsten oxynitride nanowire arrays on carbon cloth.

## 2.4 Conclusions

In conclusion, we have synthesized colloidal TiN-NFG nanocomposite starting from molecular precursors. This method of synthesis produced a stable chemically bound interface between TiN and NFG providing colloidal stability, and enhanced electrocatalytic activities. Colloidal nanocomposite exhibit LSPR band arising from metal-like TiN NCs. NFG part provide colloidal stability, large surface area ( $270 \text{ m}^2/\text{g}$ ), and a medium for charge transport. Electrical resistivity of  $0.3 \text{ ohm cm}$  is observed for the nanocomposite. This combination of low resistivity and high surface area was then utilized for electrocatalytic applications. DSSC prepared using TiN-NFG counter electrode resulted into high PCE of 8.9 %. The nanocomposite also exhibit stable electrocatalytic HER with reasonably low overpotential of  $161 \text{ mV}$  at  $10 \text{ mA/cm}^2$  current density. Overall, our TiN-NFG nanocomposite is an alternative of expensive noble metals like Pt, for electrocatalytic applications. It is known that electrocatalyst can be act as a co-catalyst with a photocatalyst in photocatalytic and photoelectrochemical water splitting for the production of hydrogen. Due to the impressive electrocatalytic activity of our TiN-NFG nanocomposite, in the next chapter we would be study the co-catalyst efficiency of TiN-NFG with graphitic carbon nitride ( $\text{g-C}_3\text{N}_4$ ) (photo absorber) for photoelectrochemical reduction of water using solar light.

## References:

1. Chen, J. G. Carbide and Nitride Overlayers on Early Transition Metal Surfaces: Preparation, Characterization, and Reactivities. *Chem. Rev.* **1996**, *96*, 1477-1498.
2. Chen, W. F.; Muckerman, J. T.; Fujita, E. Recent Developments in Transition Metal Carbides and Nitrides as Hydrogen Evolution Electrocatalysts. *Chem. Commun.* **2013**, *49*, 8896-8909.
3. Zhang, R. Q.; Lee, T. H.; Yu, B. D.; Stampfl, C.; Soon, A. The Role of Titanium Nitride Supports for Single-Atom Platinum-Based Catalysts in Fuel Cell Technology. *Phys. Chem. Chem. Phys.* **2012**, *14*, 16552-16557.
4. Zheng, P.; Zhao, J.; Zheng, J.; Ma, G.; Zhu, Z. Non-Equilibrium Partial Oxidation of TiN Surface for Efficient Visible-Light-Driven Hydrogen Production. *J. Mater. Chem.* **2012**, *22*, 12116-12120.
5. Lu, X.; Wang, G.; Zhai, T.; Yu, M.; Xie, S.; Ling, Y.; Liang, C.; Tong, Y.; Li, Y. Stabilized TiN Nanowire Arrays for High-Performance and Flexible Supercapacitors. *Nano Lett.* **2012**, *12*, 5376-5381.

6. Ottakam Thotiyl, M. M.; Ravikumar, T.; Sampath, S. Platinum Particles Supported on Titanium Nitride: An Efficient Electrode Material for the Oxidation of Methanol in Alkaline Media. *J. Mater. Chem.* **2010**, *20*, 10643-10651.
7. Li, G. R.; Wang, F.; Jiang, Q. W.; Gao, X. P.; Shen, P. W. Carbon Nanotubes with Titanium Nitride as a Low-Cost Counter-Electrode Material for Dye-Sensitized Solar Cells. *Angew. Chem. Int. Ed.* **2010**, *49*, 3653-3656.
8. Guler, U.; Ndukaife, J. C.; Naik, G. V.; Nnanna, A. G. A.; Kildishev, A. V.; Shalaev, V. M.; Boltasseva, A. Local Heating with Lithographically Fabricated Plasmonic Titanium Nitride Nanoparticles. *Nano Lett.* **2013**, *13*, 6078-6083.
9. Yun, S.; Hagfeldt, A.; Ma, T. Pt-Free Counter Electrode for Dye-Sensitized Solar Cells with High Efficiency. *Adv. Mater.* **2014**, *26*, 6210-6237.
10. Xia, W.; Mahmood, A.; Liang, Z.; Zou, R.; Guo, S. Earth-Abundant Nanomaterials for Oxygen Reduction. *Angew. Chem. Int. Ed.* **2016**, *55*, 2650-2676.
11. Xie, J.; Xie, Y. Transition Metal Nitrides for Electrocatalytic Energy Conversion: Opportunities and Challenges. *Chem. – A Euro. J.* **2016**, *22*, 3588-3598.
12. Yang, L.; Tseng, Y. T.; Suo, G.; Chen, L.; Yu, J.; Chiu, W. J.; Huang, C. C.; Lin, C. H. Photothermal Therapeutic Response of Cancer Cells to Aptamer-Gold Nanoparticle-Hybridized Graphene Oxide under NIR Illumination. *ACS Appl. Mater. Interfaces* **2015**, *7*, 5097-5106.
13. Giordano, C.; Erpen, C.; Yao, W.; Milke, B.; Antonietti, M. Metal Nitride and Metal Carbide Nanoparticles by a Soft Urea Pathway. *Chem. Mater.* **2009**, *21*, 5136-5144.
14. Talapin, D. V.; Lee, J. S.; Kovalenko, M. V.; Shevchenko, E. V. Prospects of Colloidal Nanocrystals for Electronic and Optoelectronic Applications. *Chem. Rev.* **2010**, *110*, 389-458.
15. Wen, Z.; Cui, S.; Pu, H.; Mao, S.; Yu, K.; Feng, X.; Chen, J. Metal Nitride/Graphene Nanohybrids: General Synthesis and Multifunctional Titanium Nitride/Graphene Electrocatalyst. *Adv. Mater.* **2011**, *23*, 5445-5450.
16. Dong, Y.; Deng, Y.; Zeng, J.; Song, H.; Liao, S. A High-Performance Composite ORR Catalyst Based on the Synergy between Binary Transition Metal Nitride and Nitrogen-Doped Reduced Graphene Oxide. *J. Mater. Chem. A* **2017**, *5*, 5829-5837.
17. Singh, S. K.; Dhavale, V. M.; Kurungot, S. Surface-Tuned Co<sub>3</sub>O<sub>4</sub> Nanoparticles Dispersed on Nitrogen-Doped Graphene as an Efficient Cathode Electrocatalyst for Mechanical Rechargeable Zinc-Air Battery Application. *ACS Appl. Mater. Interfaces* **2015**, *7*, 21138-21149.

18. Nazeeruddin, M. K.; De Angelis, F.; Fantacci, S.; Selloni, A.; Viscardi, G.; Liska, P.; Ito, S.; Takeru, B.; Grätzel, M. Combined Experimental and DFT-TDDFT Computational Study of Photoelectrochemical Cell Ruthenium Sensitizers. *J. Am. Chem. Soc.* **2005**, *127*, 16835-16847.
19. Tonda, S.; Kumar, S.; Gawli, Y.; Bhardwaj, M.; Ogale, S. B. g-C<sub>3</sub>N<sub>4</sub> (2D)/CdS (1D)/rGO (2D) Dual-Interface Nano-Composite for Excellent and Stable Visible Light Photocatalytic Hydrogen Generation. *Int. J. Hydrog. Energy* **2017**, *42*, 5971-5984.
20. Patterson, A. L. The Scherrer Formula for X-Ray Particle Size Determination. *Phys. Rev.* **1939**, *56*, 978-982.
21. Indrawirawan, S.; Sun, H.; Duan, X.; Wang, S. Low Temperature Combustion Synthesis of Nitrogen-Doped Graphene for Metal-Free Catalytic Oxidation. *J. Mater. Chem. A* **2015**, *3*, 3432-3440.
22. Sahasrabudhe, A.; Kapri, S.; Bhattacharyya, S. Graphitic Porous Carbon Derived from Human Hair as 'Green' Counter Electrode in Quantum Dot Sensitized Solar Cells. *Carbon* **2016**, *107*, 395-404.
23. Shui, J.; Lin, Y.; Connell, J. W.; Xu, J.; Fan, X.; Dai, L. Nitrogen-Doped Holey Graphene for High-Performance Rechargeable Li-O<sub>2</sub> Batteries. *ACS Energy Lett.* **2016**, *1*, 260-265.
24. He, J.; Chen, Y.; Lv, W.; Wen, K.; Li, P.; Wang, Z.; Zhang, W.; Qin, W.; He, W. Three-Dimensional Hierarchical Graphene-CNT@Se: A Highly Efficient Freestanding Cathode for Li-Se Batteries. *ACS Energy Lett.* **2016**, *1*, 16-20.
25. Liu, M.; Dong, Y.; Wu, Y.; Feng, H.; Li, J. Titanium Nitride Nanocrystals on Nitrogen-Doped Graphene as an Efficient Electrocatalyst for Oxygen Reduction Reaction. *Chem. Eur. J.* **2013**, *19*, 14781-14786.
26. Zheng, F.; Yang, Y.; Chen, Q. High Lithium Anodic Performance of Highly Nitrogen-Doped Porous Carbon Prepared from a Metal-Organic Framework. *Nat. Commun.* **2014**, *5*, 5261.
27. Zgrabik, C. M.; Hu, E. L. Optimization of Sputtered Titanium Nitride as a Tunable Metal for Plasmonic Applications. *Opt. Mater. Exp.* **2015**, *5*, 2786-2797.
28. Liu, J.; Zhang, T.; Wang, Z.; Dawson, G.; Chen, W. Simple Pyrolysis of Urea into Graphitic Carbon Nitride with Recyclable Adsorption and Photocatalytic Activity. *J. Mater. Chem.* **2011**, *21*, 14398-14401.

29. Jun, Y. S.; Hong, W. H.; Antonietti, M.; Thomas, A. Mesoporous, 2D Hexagonal Carbon Nitride and Titanium Nitride/Carbon Composites. *Adv. Mater.* **2009**, *21*, 4270-4274.
30. Li, J.; Zhang, Y.; Zhang, X.; Han, J.; Wang, Y.; Gu, L.; Zhang, Z.; Wang, X.; Jian, J.; Xu, P.; Song, B. Direct Transformation from Graphitic C<sub>3</sub>N<sub>4</sub> to Nitrogen-Doped Graphene: An Efficient Metal-Free Electrocatalyst for Oxygen Reduction Reaction. *ACS Appl. Mater. Interfaces* **2015**, *7*, 19626-19634.
31. Maitra, U.; Gupta, U.; De, M.; Datta, R.; Govindaraj, A.; Rao, C. N. R. Highly Effective Visible-Light-Induced H<sub>2</sub> Generation by Single-Layer 1T-MoS<sub>2</sub> and a Nanocomposite of Few-Layer 2H-MoS<sub>2</sub> with Heavily Nitrogenated Graphene. *Angew. Chem. Int. Ed.* **2013**, *52*, 13057-13061.
32. Kamat, P. V. Graphene-Based Nanoarchitectures. Anchoring Semiconductor and Metal Nanoparticles on a Two-Dimensional Carbon Support. *J. Phys. Chem. Lett.* **2010**, *1*, 520-527.
33. Seger, B.; Kamat, P. V. Electrocatalytically Active Graphene-Platinum Nanocomposites. Role of 2D Carbon Support in PEM Fuel Cells. *J. Phys. Chem. C* **2009**, *113*, 7990-7995.
34. Han, P.; Yue, Y.; Wang, X.; Ma, W.; Dong, S.; Zhang, K.; Zhang, C.; Cui, G. Graphene Nanosheet-Titanium Nitride Nanocomposite for High Performance Electrochemical Capacitors without Extra Conductive Agent Addition. *J. Mater. Chem.* **2012**, *22*, 24918-24923.
35. Jagadeeswararao, M.; Pal, S.; Nag, A.; Sarma, D. D. Electrical and Plasmonic Properties of Ligand-Free Sn<sup>4+</sup>-Doped In<sub>2</sub>O<sub>3</sub> (ITO) Nanocrystals. *ChemPhysChem* **2016**, *17*, 710-716.
36. Lu, C.; Quindeau, A.; Deniz, H.; Preziosi, D.; Hesse, D.; Alexe, M. Crossover of Conduction Mechanism in Sr<sub>2</sub>IrO<sub>4</sub> Epitaxial Thin Films. *Appl. Phys. Lett.* **2014**, *105*, 082407.
37. Huang, Y. L.; Chiu, S. P.; Zhu, Z.-X.; Li, Z. Q.; Lin, J. J. Variable-Range-Hopping Conduction Processes in Oxygen Deficient Polycrystalline ZnO Films. *J. Appl. Phys.* **2010**, *107*, 063715.
38. Wu, J.; Lan, Z.; Lin, J.; Huang, M.; Huang, Y.; Fan, L.; Luo, G.; Lin, Y.; Xie, Y.; Wei, Y. Counter Electrodes in Dye-Sensitized Solar Cells. *Chem. Soc. Rev.* **2017**, *46*, 5975-6023.

39. Marcano, D. C.; Kosynkin, D. V.; Berlin, J. M.; Sinitiskii, A.; Sun, Z.; Slesarev, A.; Alemany, L. B.; Lu, W.; Tour, J. M. Improved Synthesis of Graphene Oxide. *ACS Nano* **2010**, *4*, 4806-4814..
40. Singh, S. K.; Dhavale, V. M.; Kurungot, S. Surface-Tuned  $\text{Co}_3\text{O}_4$  Nanoparticles Dispersed on Nitrogen-Doped Graphene as an Efficient Cathode Electrocatalyst for Mechanical Rechargeable Zinc-Air Battery Application. *ACS Appl. Mater. Interfaces* **2015**, *7*, 21138-21149.
41. Illathvalappil, R.; Dhavale, V. M.; Bhange, S. N.; Kurungot, S. Nitrogen-Doped Graphene Anchored with Mixed Growth Patterns of CuPt Alloy Nanoparticles as a Highly Efficient and Durable Electrocatalyst for the Oxygen Reduction Reaction in an Alkaline Medium. *Nanoscale* **2017**, *9*, 9009-9017.
42. The NFG control sample was prepared by Mr. Santhosh Kumar Singh in the labortaory of Dr. Sreekumar Kurungot, in CSIR-NCL, India.
43. Ramasamy, E.; Jo, C.; Anthonysamy, A.; Jeong, I.; Kim, J. K.; Lee, J. Soft-Template Simple Synthesis of Ordered Mesoporous Titanium Nitride-Carbon Nanocomposite for High Performance Dye-Sensitized Solar Cell Counter Electrodes. *Chem. Mater.* **2012**, *24*, 1575-1582.
44. Zhang, X.; Chen, X.; Dong, S.; Liu, Z.; Zhou, X.; Yao, J.; Pang, S.; Xu, H.; Zhang, Z.; Li, L.; Cui, G. Hierarchical Micro/Nano-Structured Titanium Nitride Spheres as a High-Performance Counter Electrode for a Dye-Sensitized Solar Cell. *J. Mater. Chem.* **2012**, *22*, 6067-6071.
45. Xu, H.; Zhang, X.; Zhang, C.; Liu, Z.; Zhou, X.; Pang, S.; Chen, X.; Dong, S.; Zhang, Z.; Zhang, L.; Han, P.; Wang, X.; Cui, G. Nanostructured Titanium Nitride/PEDOT:PSS Composite Films As Counter Electrodes of Dye-Sensitized Solar Cells. *ACS Appl. Mater. Interfaces* **2012**, *4*, 1087-1092.
46. Chen, L.; Dai, H.; Zhou, Y.; Hu, Y.; Yu, T.; Liu, J.; Zou, Z. Porous, Single Crystalline Titanium Nitride Nanoplates Grown on Carbon Fibers: Excellent Counter Electrodes for Low-Cost, High Performance, Fiber-Shaped Dye-Sensitized Solar Cells. *Chem. Commun.* **2014**, *50*, 14321-14324.
47. Li, C. T.; Li, S. R.; Chang, L. Y.; Lee, C. P.; Chen, P. Y.; Sun, S. S.; Lin, J. J.; Vittal, R.; Ho, K. C. Efficient Titanium Nitride/Titanium Oxide Composite Photoanodes for Dye-Sensitized Solar Cells and Water Splitting. *J. Mater. Chem. A* **2015**, *3*, 4695-4705.

48. Wu, M.; Lin, X.; Wang, Y.; Wang, L.; Guo, W.; Qi, D.; Peng, X.; Hagfeldt, A.; Grätzel, M.; Ma, T. Economical Pt-Free Catalysts for Counter Electrodes of Dye-Sensitized Solar Cells. *J. Am. Chem. Soc.* **2012**, *134*, 3419-3428.
49. Bi, E.; Chen, H.; Yang, X.; Peng, W.; Gratzel, M.; Han, L. A Quasi Core-Shell Nitrogen-Doped Graphene/Cobalt Sulfide Conductive Catalyst for Highly Efficient Dye-Sensitized Solar Cells. *Energy Environ. Sci.* **2014**, *7*, 2637-2641.
50. Balamurugan, J.; Thanh, T. D.; Kim, N. H.; Lee, J. H. Nitrogen-Doped Graphene Nanosheets with FeN Core-Shell Nanoparticles as High-Performance Counter Electrode Materials for Dye-Sensitized Solar Cells. *Adv. Mater. Interfaces* **2016**, *3*, 1500348.
51. Wang, L.; Shi, Y.; Wang, Y.; Zhang, H.; Zhou, H.; Wei, Y.; Tao, S.; Ma, T. Composite Catalyst of Rosin Carbon/Fe<sub>3</sub>O<sub>4</sub>: Highly Efficient Counter Electrode for Dye-Sensitized Solar Cells. *Chem. Commun.* **2014**, *50*, 1701-1703.
52. Zhang, X.; Chen, X.; Zhang, K.; Pang, S.; Zhou, X.; Xu, H.; Dong, S.; Han, P.; Zhang, Z.; Zhang, C.; Cui, G. Transition-Metal Nitride Nanoparticles Embedded in N-Doped Reduced Graphene Oxide: Superior Synergistic Electrocatalytic Materials for the Counter Electrodes of Dye-Sensitized Solar Cells. *J. Mater. Chem. A* **2013**, *1*, 3340-3346.
53. Popov, A. I.; Geske, D. H. Studies on the Chemistry of Halogen and of Polyhalides. XIII. Voltammetry of Iodine Species in Acetonitrile. *J. Am. Chem. Soc.* **1958**, *80*, 1340-1352.
54. Liu, Y.; Wu, J.; Hackenberg, K. P.; Zhang, J.; Wang, Y. M.; Yang, Y.; Keyshar, K.; Gu, J.; Ogitsu, T.; Vajtai, R.; et al. Self-Optimizing Layered Hydrogen Evolution Catalyst with High Basal-Plane Activity. arXiv:1608.05755v1 [cond-mat.mtrl-sci], 2016.
55. Zeng, Z.; Tan, C.; Huang, X.; Bao, S.; Zhang, H. Growth of Noble Metal Nanoparticles on Single-Layer TiS<sub>2</sub> and TaS<sub>2</sub> Nanosheets for Hydrogen Evolution Reaction. *Energy Environ. Sci.* **2014**, *7*, 797-803.
56. Durst, J.; Simon, C.; Hasché, F.; Gasteiger, H. A. Hydrogen Oxidation and Evolution Reaction Kinetics on Carbon Supported Pt, Ir, Rh, and Pd Electrocatalysts in Acidic Media. *J. Electrochem. Soc.* **2015**, *162*, F190-F203.
57. Han, Y.; Yue, X.; Jin, Y.; Huang, X.; Shen, P. K. Hydrogen Evolution Reaction in Acidic Media on Single-Crystalline Titanium Nitride Nanowires as an Efficient Non-Noble Metal Electrocatalyst. *J. Mater. Chem. A* **2016**, *4*, 3673-3677.



58. Yin, J.; Fan, Q.; Li, Y.; Cheng, F.; Zhou, P.; Xi, P.; Sun, S. Ni–C–N Nanosheets as Catalyst for Hydrogen Evolution Reaction. *J. Am. Chem. Soc.* **2016**, *138*, 14546-14549.
59. Shi, J.; Pu, Z.; Liu, Q.; Asiri, A. M.; Hu, J.; Sun, X. Tungsten Nitride Nanorods Array Grown on Carbon Cloth as an Efficient Hydrogen Evolution Cathode at all pH values. *Electrochim. Acta.* **2015**, *154*, 345-351.
60. Ma, L.; Ting, L. R. L.; Molinari, V.; Giordano, C.; Yeo, B. S. Efficient Hydrogen Evolution Reaction Catalyzed by Molybdenum Carbide and Molybdenum Nitride Nanocatalysts Synthesized via the Urea Glass Route. *J. Mater. Chem. A* **2015**, *3*, 8361-8368.
61. Zhao, Y.; Kamiya, K.; Hashimoto, K.; Nakanishi, S. In Situ CO<sub>2</sub>-Emission Assisted Synthesis of Molybdenum Carbonitride Nanomaterial as Hydrogen Evolution Electrocatalyst. *J. Am. Chem. Soc.* **2015**, *137*, 110-113.
62. Yan, H.; Tian, C.; Wang, L.; Wu, A.; Meng, M.; Zhao, L.; Fu, H. Phosphorus-Modified Tungsten Nitride/Reduced Graphene Oxide as a High-Performance, Non-Noble-Metal Electrocatalyst for the Hydrogen Evolution Reaction. *Angew. Chem. Int. Ed.* **2015**, *54*, 6325-6329.
63. Li, Q.; Cui, W.; Tian, J.; Xing, Z.; Liu, Q.; Xing, W.; Asiri, A. M.; Sun, X. N-Doped Carbon-Coated Tungsten Oxynitride Nanowire Arrays for Highly Efficient Electrochemical Hydrogen Evolution. *ChemSusChem* **2015**, *8*, 2487-2491.
64. Xie, J.; Li, S.; Zhang, X.; Zhang, J.; Wang, R.; Zhang, H.; Pan, B.; Xie, Y. Atomically-Thin Molybdenum Nitride Nanosheets with Exposed Active Surface Sites for Efficient Hydrogen Evolution. *Chem. Sci.* **2014**, *5*, 4615-4620.
65. Youn, D. H.; Han, S.; Kim, J. Y.; Kim, J. Y.; Park, H.; Choi, S. H.; Lee, J. S. Highly Active and Stable Hydrogen Evolution Electrocatalysts Based on Molybdenum Compounds on Carbon Nanotube-Graphene Hybrid Support. *ACS Nano* **2014**, *8*, 5164-5173.
66. Zhao, Y.; Kamiya, K.; Hashimoto, K.; Nakanishi, S. Hydrogen Evolution by Tungsten Carbonitride Nanoelectrocatalysts Synthesized by the Formation of a Tungsten Acid/Polymer Hybrid In Situ. *Angew. Chem. Int. Ed.* **2013**, *52*, 13638-13641.
67. Alhajri, N. S.; Yoshida, H.; Anjum, D. H.; Garcia-Esparza, A. T.; Kubota, J.; Domen, K.; Takahashi, K. Synthesis of Tantalum Carbide and Nitride Nanoparticles Using a

- Reactive Mesoporous Template for Electrochemical Hydrogen Evolution. *J. Mater. Chem. A* **2013**, *1*, 12606-12616.
68. Cao, B.; Veith, G. M.; Neufeind, J. C.; Adzic, R. R.; Khalifah, P. G. Mixed Close-Packed Cobalt Molybdenum Nitrides as Non-noble Metal Electrocatalysts for the Hydrogen Evolution Reaction. *J. Am. Chem. Soc.* **2013**, *135*, 19186-19192.
69. Chen, W. F.; Sasaki, K.; Ma, C.; Frenkel, A. I.; Marinkovic, N.; Muckerman, J. T.; Zhu, Y.; Adzic, R. R. Hydrogen-Evolution Catalysts Based on Non-Noble Metal Nickel-Molybdenum Nitride Nanosheets. *Angew. Chem. Int. Ed.* **2012**, *51*, 6131-6135.

# Chapter 3

## 2D Nanocomposite of g-C<sub>3</sub>N<sub>4</sub> and TiN Embedded N-Doped Graphene for Photoelectrochemical Reduction of Water using Sunlight

---

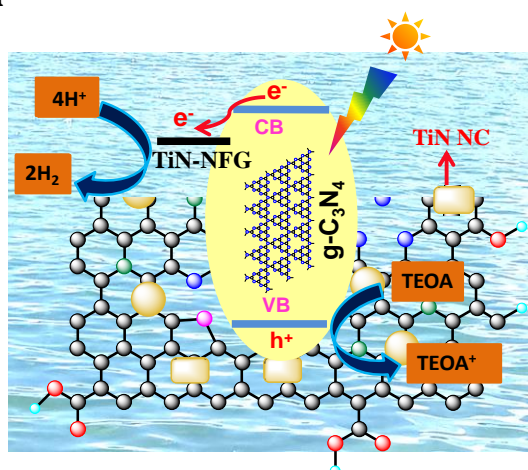
The following paper has been published based on the work documented in this chapter.

Shanker, G. S.; Bhosale, R.; Ogale, S.; Nag, A. 2D Nanocomposite of g-C<sub>3</sub>N<sub>4</sub> and TiN Embedded N-Doped Graphene for Photoelectrochemical Reduction of Water using Sunlight. *Adv. Mater. Interfaces* **2018**, *5*, 1801488. Copyright permission has been obtained for complete article from Wiley-VCH Verlag GmbH & Co.

## Summary

Photoelectrochemical (PEC) water splitting is a sustainable pathway for solar to hydrogen conversion. Graphitic g-C<sub>3</sub>N<sub>4</sub> nanosheets have the suitable band gap and band-edge energies to act as a visible-light photocatalyst for water splitting, but the fast recombination of photoexcited electron-hole pair limits the efficiency. Herein, we introduce N-doped few-layer graphene (NFG) dressed with titanium nitride (TiN-NFG) nanocrystals (NCs) as an efficient co-catalyst which improved the water reduction activity of g-C<sub>3</sub>N<sub>4</sub> nanosheet by 16 times. The 2D nanocomposite of g-C<sub>3</sub>N<sub>4</sub>:TiN-NFG has an extended interface for efficient separation of photo-excited electron-hole pair through electron transfer from g-C<sub>3</sub>N<sub>4</sub> nanosheet to TiN-NFG. The metallic electronic structure of TiN in combination with good charge conducting capability of NFG reduces the charge transfer resistance ( $R_{ct}$ ) at the electrode/electrolyte interface. Both these aspects are responsible for the enhanced PEC activity leading to a photocurrent density of  $-196 \mu\text{A}/\text{cm}^2$  at 0.11 V versus reversible hydrogen electrode (RHE) as a photocathode for the g-C<sub>3</sub>N<sub>4</sub>:TiN-NFG nanocomposite. The nanocomposite is stable, low-cost (free from noble metals), and the extent of enhancement in the PEC efficiency for reduction reaction is remarkable compared to prior literature.

## Graphical Presentation



### 3.1 Introduction

Hydrogen production via solar driven water splitting is one of the promising techniques to address the global energy demand by producing clean and sustainable fuel.<sup>1-5</sup> Numerous materials as photocatalyst are reported in this regard, out of which most of them are inorganic semiconductors such as TiO<sub>2</sub>,<sup>6</sup> WO<sub>3</sub>,<sup>7</sup> and CdS.<sup>8</sup> In recent times, graphitic carbon nitride (g-C<sub>3</sub>N<sub>4</sub>) has also emerged as an organic photocatalyst for hydrogen generation, owing to its low cost, appropriate electronic band structure, and excellent photochemical stability.<sup>1,9-10,11-12,13-14</sup> But still further improvement of efficiency and stability are required for the photocatalyst to meet the industrial requirements. To enhance the PEC activity of g-C<sub>3</sub>N<sub>4</sub> for water splitting, we report here a nanocomposite of 2D g-C<sub>3</sub>N<sub>4</sub> nanosheet photocatalyst with a 2D co-catalyst in the form of TiN NCs embedded N-doped graphene (TiN-NFG).

Hydrogen generation using pristine g-C<sub>3</sub>N<sub>4</sub> suffers from faster recombination of photogenerated charge carriers before they could participate in redox reactions occurring on the surface.<sup>3</sup> Therefore, it is required to design a composite of g-C<sub>3</sub>N<sub>4</sub> with a co-catalyst material having a suitable band alignment to facilitate charge separation (transfer) at the interface. Towards this end, hetero-junctions of g-C<sub>3</sub>N<sub>4</sub> with other semiconductors like TiO<sub>2</sub>, BiVO<sub>4</sub> and CdS<sup>15</sup> have accelerated the charge separation through built-in electric field at the interface.<sup>16</sup> Also, hetero-junctions of g-C<sub>3</sub>N<sub>4</sub> with expensive and less earth abundant noble metals (Pt, Pd and Au) and noble metal oxides (IrO<sub>2</sub> and RuO<sub>2</sub>) have been employed for water reduction and oxidation, respectively.<sup>17-18</sup> Cobalt based nanomaterials are also coupled with g-C<sub>3</sub>N<sub>4</sub> to boost the water oxidation kinetics.<sup>19-21</sup> For example Zhang et al.<sup>19</sup> reported deposition of layered Co(OH)<sub>2</sub> on polymeric C<sub>3</sub>N<sub>4</sub> which boosted the oxygen evolution reaction (OER) almost 7 times higher than pristine C<sub>3</sub>N<sub>4</sub>. In another report<sup>22</sup> CoSe<sub>2</sub> is proved to be a good co-catalyst for g-C<sub>3</sub>N<sub>4</sub> due to its lower anionic electronegativity. Also, Ni based nanomaterials like NiO<sup>23</sup> and NiS<sup>24</sup> attached with g-C<sub>3</sub>N<sub>4</sub> has shown enhancement in reduction of water.

In principle, the efficacy of charge transfer can be improved further by increasing the interfacial area per unit weight of the composite, and therefore, the possibilities of 2D co-catalyst with high surface area are also being explored. For example, Han et al.<sup>25</sup> showed that 2D/2D hetero-junction of g-C<sub>3</sub>N<sub>4</sub>/graphdiyne significantly enhances the separation of photogenerated carriers because of excellent hole transfer nature of graphdiyne at the extended interface, eventually displaying a three-fold enhancement in PEC activity. Hui et al.<sup>26</sup> reported almost ten times enhancement in PEC reduction of water to H<sub>2</sub> from the

composite of MoS<sub>2</sub> and g-C<sub>3</sub>N<sub>4</sub> at 1V versus RHE. Che et al.<sup>27</sup> fabricated a hetero-junction of g-C<sub>3</sub>N<sub>4</sub> with planar carbon ring for efficient photoexcited electron transfer with six times enhancement in photocatalytical performance. In the similar direction the PEC efficiency of g-C<sub>3</sub>N<sub>4</sub> can be achieved to greater extent if 2D carbon containing electrocatalyst is employed as a co-catalyst which not only reduces interfacial resistance but also provides lower overpotential.

In the chapter 2 of this thesis, we reported TiN-NFG as a hydrogen evolution reaction (HER) electrocatalyst.<sup>28</sup> TiN possesses a metallic band structure<sup>29-31</sup> and NFG exhibits good charge transport property. In addition, both TiN and NFG are known to provide catalytic sites for proton reduction.<sup>28, 32</sup> Along with these electronic properties, TiN-NFG is a stable, low-cost and earth-abundant (free from noble metal) material, motivating us to use it as 2D co-catalyst for g-C<sub>3</sub>N<sub>4</sub> for PEC water splitting. We have prepared the g-C<sub>3</sub>N<sub>4</sub>:TiN-NFG 2D nanocomposite demonstrating remarkable enhancement in PEC activity of g-C<sub>3</sub>N<sub>4</sub> by ~16 fold (-196  $\mu\text{A}/\text{cm}^2$  at 0.11 V versus RHE) as photocathode. As per our knowledge, such a huge increment in PEC performance of g-C<sub>3</sub>N<sub>4</sub> as photocathode is the first report of its kind.

## 3.2 Experimental Sections

### 3.2.1 Chemicals

Urea (AR, 99.0%, VETEC), distilled water, ethanol (99.9% AR, SDFCL), n-butanol (99.95%, Rankem), titanium tetrachloride (99.0%, Merck), nafion (5wt%, Sigma-Aldrich), F-doped SnO<sub>2</sub> (FTO) coated glass (~ 7 Ohm/sq, Sigma-Aldrich), sodium sulphate (99.0%, Fisher Chemicals), triethanolamine (99.0%, Sigma Aldrich), titanium nitride (nanopowder size ~20 nm, Sisco Research Pvt. Ltd.). All these chemicals are used as purchased from the sources, without any further purification.

### 3.2.2 Synthesis of Graphitic Carbon Nitride (g-C<sub>3</sub>N<sub>4</sub>) Nanosheets

g-C<sub>3</sub>N<sub>4</sub> was synthesized by pyrolysis method using urea as a precursor, following report of Liu et al.<sup>33</sup> after slight modification. Briefly, 0.17 mol (10g) of urea is placed in 50 mL alumina boat and heated to 550 °C for 2 hours in a tube furnace under N<sub>2</sub> atmosphere with heating rate of 4 °C/min. A pale yellow colored powder was obtained after cooling the furnace to room temperature, and the sample was characterized using various experimental techniques.

### 3.2.3 Synthesis of Titanium Nitride - N-Doped Few-Layer Graphene (TiN-NFG)

TiN-NFG was prepared by following the methodology discussed in the chapter 2 of this thesis. Briefly, Titanium tetrachloride (4 mmol, 438  $\mu$ L) was added to 3 mL ethanol which led to the formation of titanium ethoxide. Urea 60 mmol (3.6 g) was added slowly to the above titanium ethoxide solution for about 30 min, and was stirred for about 2 hours forming a viscous solution. This viscous solution was placed into an alumina crucible and subjected to calcination at 900 °C for 5 hours in a tube furnace under inert N<sub>2</sub> atmosphere. The ramp rate to reach 900 °C was maintained at 4° C/min. The product obtained after cooling the sample to room temperature was characterized as TiN embedded in few-layer N-doped graphene (TiN-NFG).

### 3.2.4 Synthesis of N-Doped Few-Layer Graphene (NFG)

N-doped few-layer graphene (NFG) was synthesized by following a previous report.<sup>34</sup> Initially, graphene oxide (GO) was synthesized. GO and melamine mixture in a ratio of 1:5 was mixed with 100 mL deionized water followed by ultra-sonication for 10 min to obtain a uniform mixture. Then, the resulting mixture was heated at 80 °C for 24 hours to dry the powder. The obtained mixture was calcinated at 800 °C for 4 hours under inert N<sub>2</sub> atmosphere. The ramp rate to reach 800 °C was maintained at 4 °C/min. Black colored powder was obtained after cooling the sample to room temperature.

### 3.2.5 Characterization

Powder X-ray diffraction (PXRD) patterns of all samples were obtained using a Bruker D8 Advance X-ray diffractometer equipped with Cu K $\alpha$  radiation (1.54 Å). UV-visible absorption spectra were measured using SHIMADZU UV-3600 plus UV-VIS-NIR spectrophotometer. Fourier transform infrared (FTIR) spectra measurements were performed on the pellet of samples mixed with KBr using Thermo scientific NICOLET 6700 FTIR spectrophotometer. Steady-state photoluminescence (PL) and PL decay dynamics (time-correlated single photon counting) were recorded using FLS 980 (Edinburgh Instruments). Atomic force microscopy (AFM) images were collected using Keysight atomic force microscope (model: AFM 5500) by using tapping mode technique. Transmission electron microscopy (TEM) images were taken using JEOL-JEM 2200FS 200KeV. Mott-Schottky plots of electrodes were measured in 0.5 M Na<sub>2</sub>SO<sub>4</sub> and 10 vol% tri-ethanolamine solution in dark at a frequency of 10 kHz using an AUTOLAB PGSTAT 30 using a three electrode system. Electrochemical impedance spectroscopy (EIS) experiments were performed using an AUTOLAB PGSTAT 30 from 100 kHz to 40 mHz. Electrical resistivity measurements of co-

catalysts film were obtained using a Keithley Four-probe conductivity instrument (Model 6220/6221 Current Source and Model 2182A nanovoltmeter). Field emission scanning electron microscopy (FESEM) and elemental mapping were performed using a Zeiss Ultra Plus scanning electron microscope. Surface area measurements were performed on Quantochrome Autosorb automated gas sorption analyser at 77 K. X-ray photoelectron spectroscopy (XPS) measurement were carried out using ThermoKalpha+ spectrometer using micro focused and monochromated Al K<sub>α</sub> radiation with energy 1486.6 eV.

### 3.2.6 Preparation of g-C<sub>3</sub>N<sub>4</sub>:TiN-NFG Nanocomposite Photoelectrodes

Finely grinded powders of g-C<sub>3</sub>N<sub>4</sub> nanosheets (200 mg) and different weight percentages of TiN-NFG (0%, 1%, 1.5% and 2%) were dispersed in 5 mL ethanol by ultra-sonication for about 2 hours. Ethanol was evaporated at an elevated temperature and the sample was thoroughly dried under vacuum. 100 mg of the powder was grinded (for around 1 hour) using mortar pestle. Then 600 μL n-butanol was added drop-wise (30 μL/min) to the powder and grinded continuously to make a paste. Also 60 μL nafion was added during the addition of n-butanol. Nafion improves binding between the film and the FTO glass substrate. The obtained g-C<sub>3</sub>N<sub>4</sub>:TiN-NFG nanocomposite paste was doctor bladed on cleaned FTO glass followed by annealing of the film at 250 °C for 2 hours under inert atmosphere. The area of the films was maintained at 1 cm<sup>2</sup> for all the experiments. The thicknesses of the films are in the range of ~ 0.5 to 25 μm.

### 3.2.7 Photoelectrochemical (PEC) Measurements

PEC measurements were carried out on an AUTOLAB PGSTAT 30 using a three electrode system. Different photoelectrode materials coated on FTO glass with 1 cm<sup>2</sup> area served as working electrodes, platinum as counter electrode and Ag/AgCl as reference electrode. These electrodes were placed in 0.5 M Na<sub>2</sub>SO<sub>4</sub> and 10 vol% TEOA aqueous solution purged with N<sub>2</sub>. Simulated sunlight with illumination power of 100 mW/cm<sup>2</sup> from a 400 W xenon lamp (Solar Simulator, Newport) was used for illuminations. Stability profiles were obtained in the similar PEC and electrolyte system for 5 hours at 0.1 V versus RHE. Due to the limitation of solar simulator it was kept off for half hour after every one and half hour of illumination and data was acquired. The Incident photon to current efficiency (IPCE) data were measured using a Newport IPCE system over the range of 300 - 600 nm.



To calculate the faradaic efficiency of different photoelectrodes and to confirm that the photocurrents observed in PEC cell are actually due to water splitting, we constructed a sealed and inert two electrode PEC system. It was evacuated for half an hour followed by purging with nitrogen for another half an hour. The cell was kept in dark initially for 30 minutes before exposing to solar simulator. The evolved H<sub>2</sub> were collected after regular intervals of 10 minutes from anodic and cathodic compartment of cell respectively, through a tightly sealed septum. The amount of H<sub>2</sub> generated in the system were detected and quantified by head space gas analysis with an Agilent 7890A series gas chromatography equipped with a 5 Å molecular sieve column and Thermal Conductivity Detector (TCD).

### 3.3 Results and Discussion

#### 3.3.1 Preparation of g-C<sub>3</sub>N<sub>4</sub>:TiN-NFG Nanocomposite

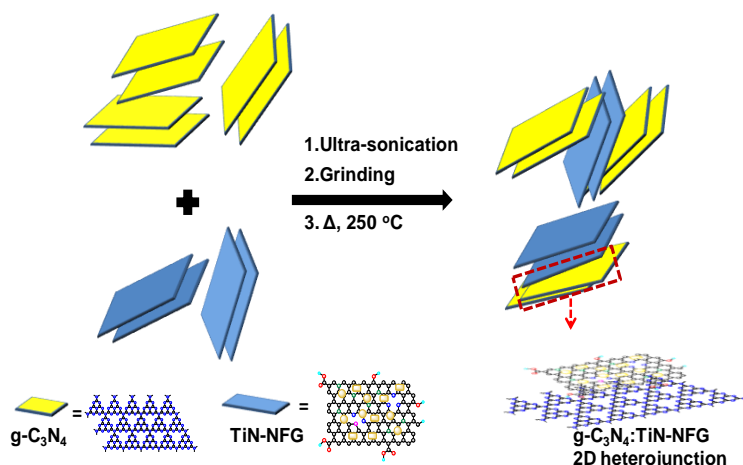


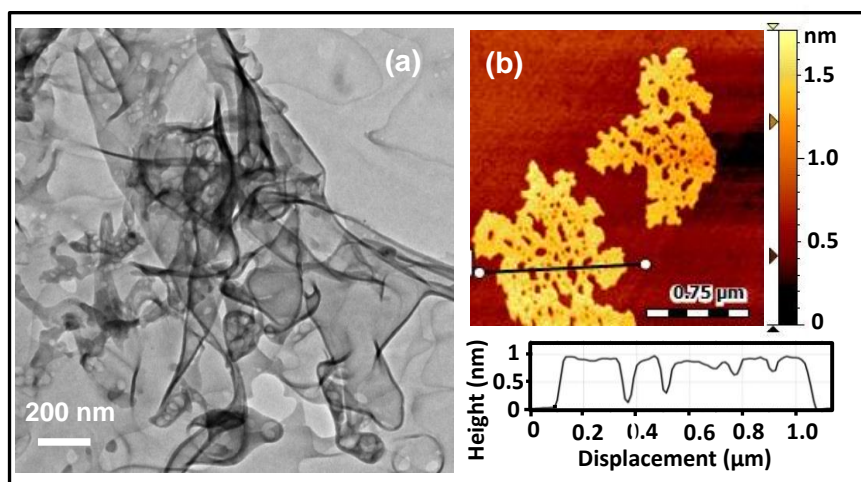
**Figure 3.1:** The schematic illustration of the formation of g-C<sub>3</sub>N<sub>4</sub>:TiN-NFG 2D nanocomposite.

Both 2D g-C<sub>3</sub>N<sub>4</sub> nanosheet photocatalyst and 2D TiN-NFG co-catalyst are prepared separately following previously reported protocols.<sup>28, 33</sup> Synthesis of g-C<sub>3</sub>N<sub>4</sub>:TiN-NFG nanocomposite has been schematically shown in Figure 3.1. Briefly, fine powders of g-C<sub>3</sub>N<sub>4</sub> and TiN-NFG were dispersed by sonicating in ethanol, followed by drying. Powder of this mixture was grinded thoroughly in the presence of small amount of n-butanol and nafion to make the paste. Photoelectrodes of g-C<sub>3</sub>N<sub>4</sub>:TiN-NFG 2D nanocomposites were then formed by doctor blading the paste on fluorine doped tin oxide (FTO) coated glass, followed by annealing at 250 °C for 2 hours under inert atmosphere. Different amounts (1%, 1.5% and 2 wt%) of the TiN-NFG co-catalyst were loaded on g-C<sub>3</sub>N<sub>4</sub> nanosheets. As discussed later,

1.5% loading provides the best PEC performance, and therefore, all the figures in this chapter showing data of g-C<sub>3</sub>N<sub>4</sub>:TiN-NFG nanocomposite correspond to this 1.5% loading.

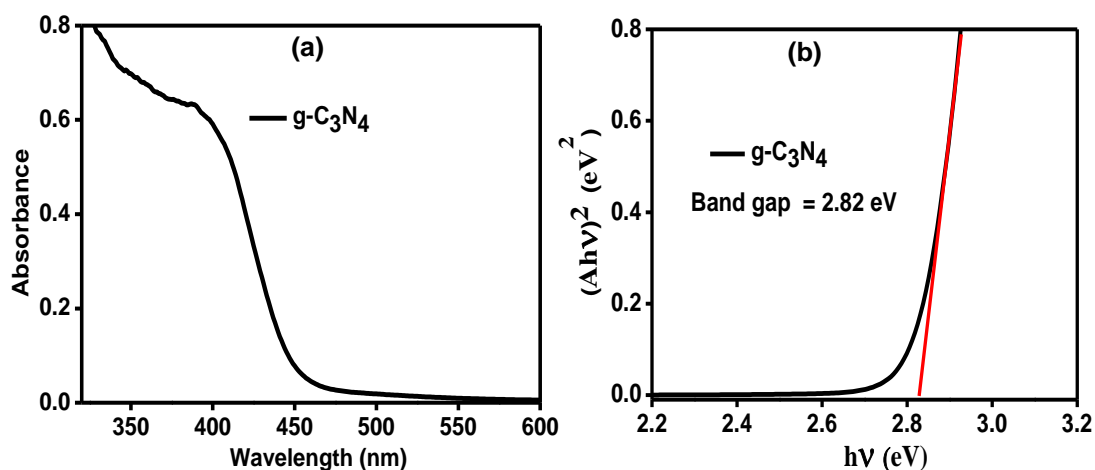
### 3.3.2 Microscopic and Structural Analysis of g-C<sub>3</sub>N<sub>4</sub>:TiN-NFG Nanocomposite

To view the microscopic morphology of synthesized samples, first, we discuss briefly about the g-C<sub>3</sub>N<sub>4</sub> nanosheets (photocatalyst) and co-catalyst TiN-NFG. TEM image showed in Figure 3.2a displays the ultrathin 2D nanosheets of g-C<sub>3</sub>N<sub>4</sub> which exhibit porous nature. Atomic force microscopy (AFM) in Figure 3.2b shows 2-3 layers (~1 nm height) of g-C<sub>3</sub>N<sub>4</sub> along with its porous nature. UV-visible absorption spectrum of g-C<sub>3</sub>N<sub>4</sub> nanosheets shown in Figure 3.3, suggests a band gap of 2.82 eV (439 nm), capable of absorbing a fraction of solar light. All these results suggest the formation of g-C<sub>3</sub>N<sub>4</sub> nanosheets similar to.<sup>35</sup>

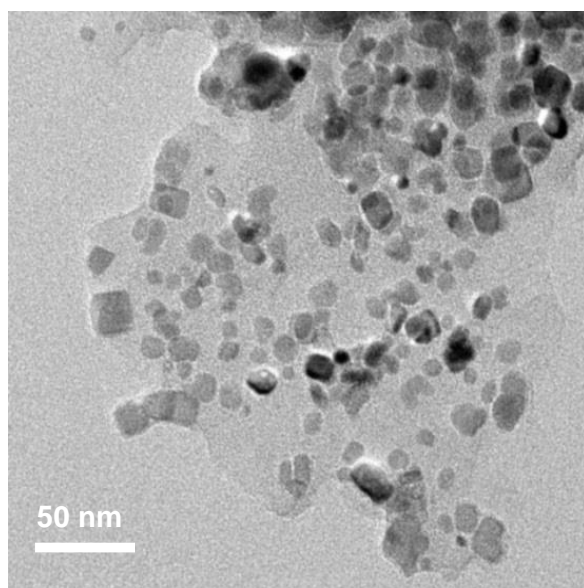


**Figure 3.2:** (a) TEM image of g-C<sub>3</sub>N<sub>4</sub> nanosheet, and (b) AFM image (top panel) and its corresponding height profile (bottom panel) of g-C<sub>3</sub>N<sub>4</sub> nanosheet. Height profile represents the height along the black line drawn in the AFM image, after considering the background height as zero.

After g-C<sub>3</sub>N<sub>4</sub> nanosheet, we discuss briefly about TiN-NFG. Figure 3.4 shows TEM image of TiN-NFG co-catalyst where TiN NCs with size ~14 nm were embedded in ultrathin NFG nanosheets. Detailed characterization of this TiN-NFG sample has been shown in the chapter 2 of this thesis. Strong chemical interaction between the TiN and NFG was established where the thickness of NFG layers were found to be ~1.5 nm (chapter 2).<sup>28</sup>



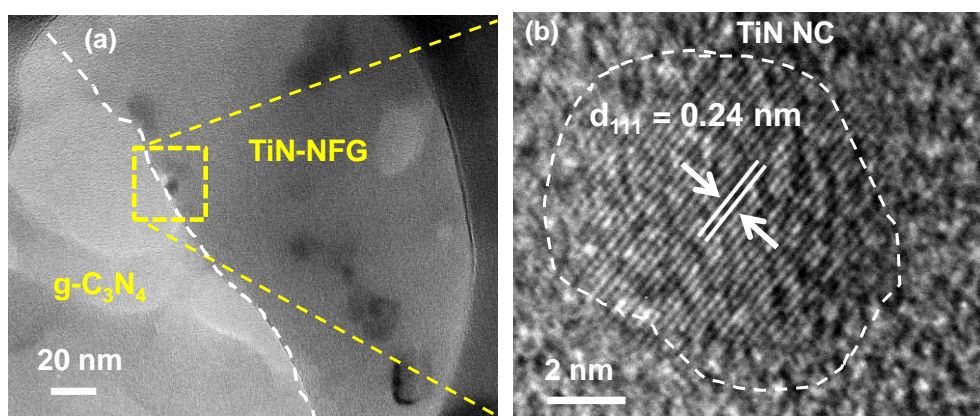
**Figure 3.3:** (a) UV-visible absorption spectrum of g-C<sub>3</sub>N<sub>4</sub> nanosheet obtained from corresponding diffuse reflectance spectrum by using Kubelka-Munk equation.<sup>36</sup> (b) Tauc plot<sup>37</sup> obtained from the absorption spectrum by considering direct bandgap.



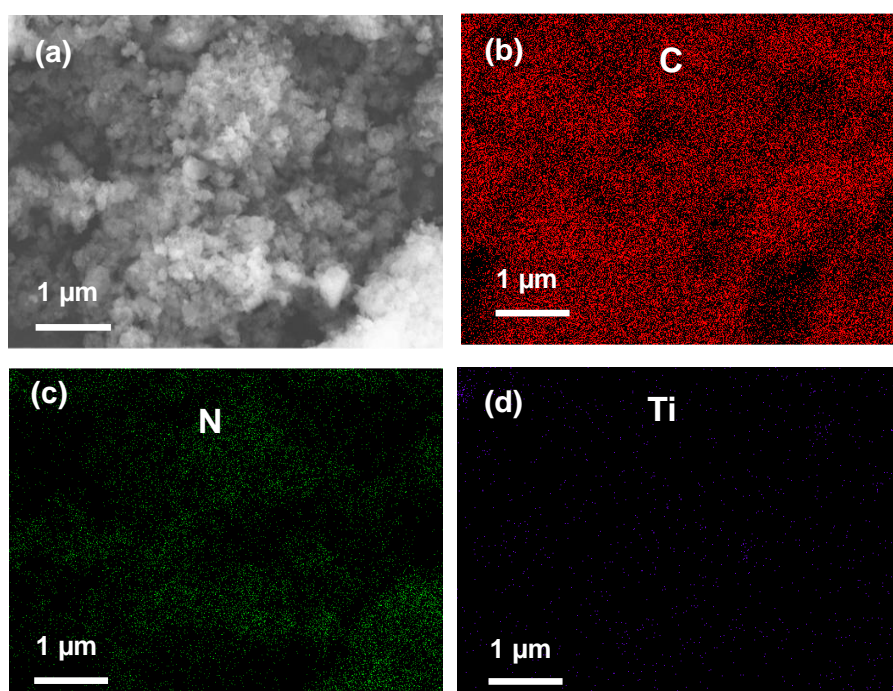
**Figure 3.4:** TEM image of TiN-NFG nanocomposite.

Figure 3.5a shows the TEM image of g-C<sub>3</sub>N<sub>4</sub>:TiN-NFG nanocomposite where overlapping of g-C<sub>3</sub>N<sub>4</sub> nanosheet with TiN-NFG nanosheet is observed, maintaining the 2D sheet like morphology. Figure 3.5b is the enlarged image of interface between g-C<sub>3</sub>N<sub>4</sub> nanosheet and TiN-NFG where d-spacing of 0.24 nm corresponding to (111) plane of cubic phase of TiN NC is observed. Further, to know the distribution of elements in g-C<sub>3</sub>N<sub>4</sub>:TiN-NFG nanocomposite we have done elemental mapping study using Energy dispersive X-ray spectroscopy (EDS). Elemental mapping of nanocomposite g-C<sub>3</sub>N<sub>4</sub>:TiN-NFG (Figure 3.6)

shows uniform distribution of elements (C, N and Ti) in the structure. Formation of such a layered hetero-junction between the two components of 2D photoelectrocatalyst is expected to be beneficial as it provides increased contact area for efficient charge transfer.<sup>38</sup>



**Figure 3.5:** TEM image of (a) g-C<sub>3</sub>N<sub>4</sub>:TiN-NFG nanocomposites, and (b) high resolution (HRTEM) image of g-C<sub>3</sub>N<sub>4</sub>:TiN-NFG of an enlarged portion (roughly indicated by square) from the image in (b).



**Figure 3.6:** FESEM image of (a) g-C<sub>3</sub>N<sub>4</sub>:TiN-NFG nanocomposite and the corresponding elemental mapping from EDS (b) carbon, (c) nitrogen and (d) titanium.

After microscopy analysis, to study the structural aspects of g-C<sub>3</sub>N<sub>4</sub>:TiN-NFG nanocomposite we used the PXRD technique. The PXRD pattern of g-C<sub>3</sub>N<sub>4</sub> nanosheets (Figure 3.7) shows a broad peak at 27.5° corresponding to interlayer stacking distance of aromatic moiety.<sup>39</sup> The

broadness of the peak suggests 2-3 layers of g-C<sub>3</sub>N<sub>4</sub> consistent with the TEM and AFM images (Figure 3.2). The PXRD pattern of TiN-NFG is dominated by TiN NCs with sharper peaks, along with a broad peak for NFG component at  $2\theta \sim 24.5^\circ$ , similar to ref.<sup>28</sup> The PXRD pattern of g-C<sub>3</sub>N<sub>4</sub>:TiN-NFG nanocomposite shows contributions from both g-C<sub>3</sub>N<sub>4</sub> and TiN-NFG, but contribution from TiN-NFG is small due to its low (1.5 wt%) loading amount. These PXRD results confirm the formation of g-C<sub>3</sub>N<sub>4</sub>:TiN-NFG nanocomposite, and no other impurity phase is observed. The PXRD patterns of the nanocomposites with different loading amounts of TiN-NFG 1.5 wt % loading co-catalyst are shown in Figure 3.8.

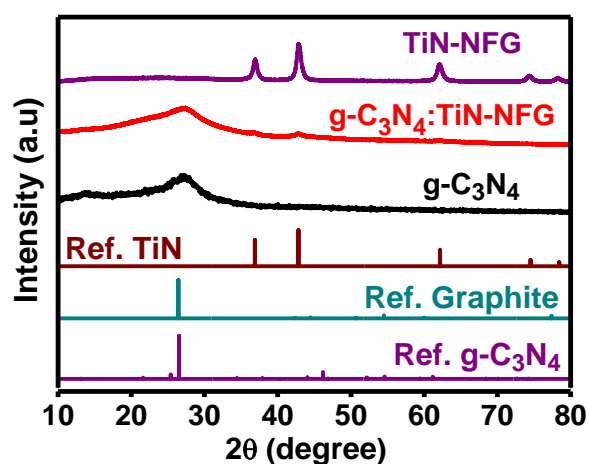


**Figure 3.7:** (a) PXRD patterns of g-C<sub>3</sub>N<sub>4</sub>, g-C<sub>3</sub>N<sub>4</sub>:TiN-NFG (1.5 wt% loading) and TiN-NFG along with reference data for bulk samples.

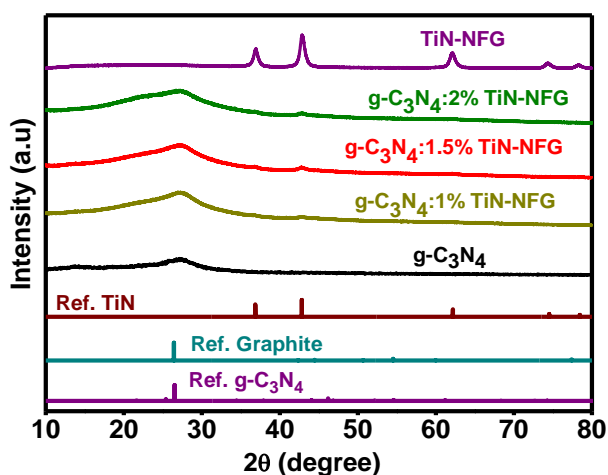


**Figure 3.8:** PXRD pattern of pristine g-C<sub>3</sub>N<sub>4</sub> nanosheet, TiN-NFG nanosheet, and g-C<sub>3</sub>N<sub>4</sub>:TiN-NFG nanocomposite with different loading (wt%) of TiN-NFG in the composite. Also, reference patterns for bulk g-C<sub>3</sub>N<sub>4</sub>, graphite and TiN are shown for comparison.



### 3.3.3 Finding of possible interaction between g-C<sub>3</sub>N<sub>4</sub> and TiN-NFG in g-C<sub>3</sub>N<sub>4</sub>:TiN-NFG nanocomposite

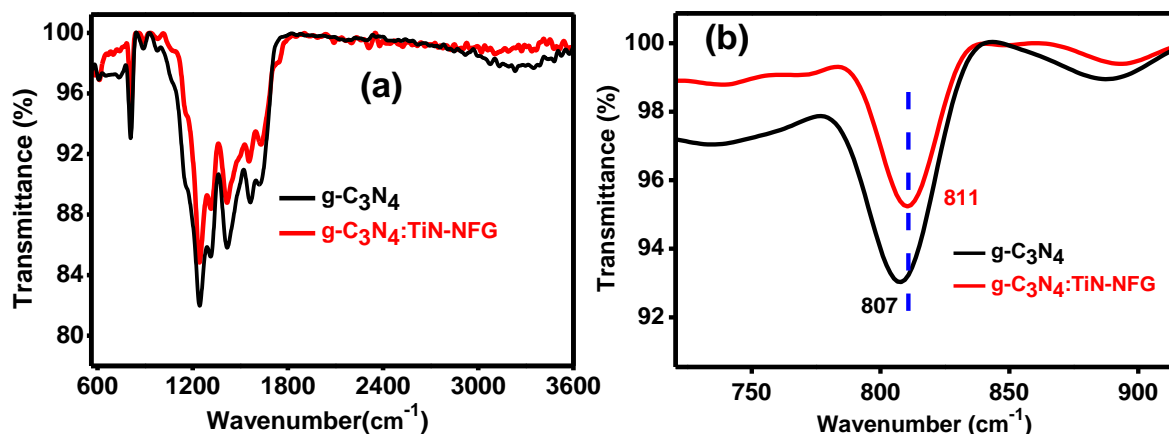


**Figure 3.9:** (a) FTIR spectra of g-C<sub>3</sub>N<sub>4</sub> and g-C<sub>3</sub>N<sub>4</sub>:TiN-NFG nanocomposite. (b) Enlarged region (720 nm to 920 nm) of spectra (a).

To find the possible interaction between g-C<sub>3</sub>N<sub>4</sub> nanosheets and TiN-NFG in g-C<sub>3</sub>N<sub>4</sub>:TiN-NFG nanocomposite we used FTIR, XPS and PL spectroscopy. Figure 3.9 compares the FTIR spectrum of pristine g-C<sub>3</sub>N<sub>4</sub> nanosheets with that of g-C<sub>3</sub>N<sub>4</sub>:TiN-NFG nanocomposite. Both the samples exhibit stretching vibrations in the region of 1230-1630 cm<sup>-1</sup> which correspond to CN heterocycles, the sharp band at ~ 808 cm<sup>-1</sup> which corresponds to the out of plane bending of -NH of the s-triazine unit, and the broad band at 3000-3600 cm<sup>-1</sup> corresponds to -NH stretching frequencies. All these spectral features correspond to g-C<sub>3</sub>N<sub>4</sub>,<sup>40</sup> without observing any major change due to the low loading amount (1.5 wt%) of co-catalyst. However, a small suppression of transmittance around 3000-3600 cm<sup>-1</sup> corresponding to amine groups, and a minor shift in breathing mode of s-triazine units from 807 cm<sup>-1</sup> to 811 cm<sup>-1</sup> is observed for g-C<sub>3</sub>N<sub>4</sub>:TiN-NFG nanocomposite compared to g-C<sub>3</sub>N<sub>4</sub>. These results suggest possibility of covalent interactions between g-C<sub>3</sub>N<sub>4</sub> and TiN-NFG in the nanocomposite.<sup>41-42</sup>

Comparison of XPS data (Figure 3.10) of pristine g-C<sub>3</sub>N<sub>4</sub> and g-C<sub>3</sub>N<sub>4</sub>:TiN-NFG nanocomposite suggest no major change because of the low (1.5 wt%) loading amount of TiN-NFG. C 1s spectra in Figure 3.10c exhibit two peaks at 288.3 and 284.7 eV corresponding to C-N and C-C bonds.<sup>25</sup> Small increase in the relative intensity of C-N related peak in the nanocomposite might be correlated with new C-N interactions between g-C<sub>3</sub>N<sub>4</sub> and TiN-NFG.

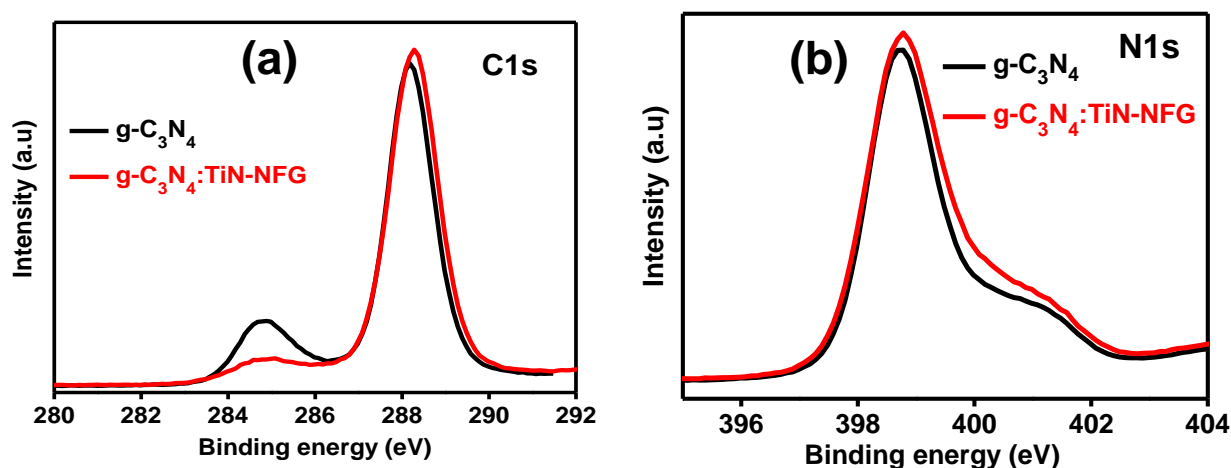


**Figure 3.10:** XPS data of (a) C 1s and (b) N 1s data of pristine g-C<sub>3</sub>N<sub>4</sub> and g-C<sub>3</sub>N<sub>4</sub>:TiN-NFG nanocomposites.

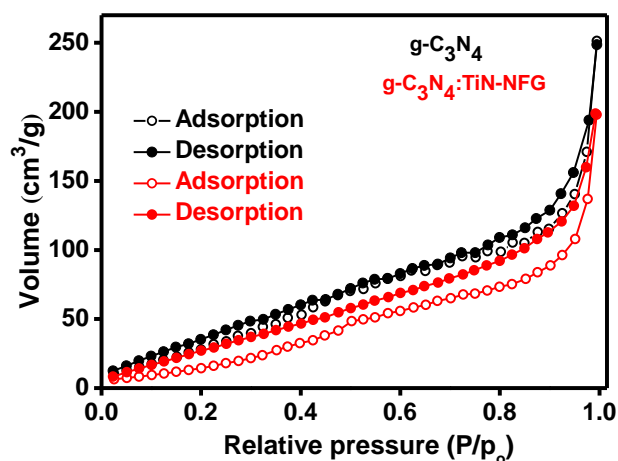


**Figure 3.11:** N<sub>2</sub> adsorption-desorption isotherms data for g-C<sub>3</sub>N<sub>4</sub> and g-C<sub>3</sub>N<sub>4</sub>:TiN-NFG powder samples at 77 K.

Formation of nanocomposite may reduce the surface area compared to that of g-C<sub>3</sub>N<sub>4</sub> nanosheets. But higher surface area is beneficial for PEC reduction of water. Therefore, to check the effect of composite formation on surface area, we measured Brunauer-Emmett-Teller (BET) specific surface area from N<sub>2</sub> adsorption-desorption isotherms shown in the Figure 3.11. g-C<sub>3</sub>N<sub>4</sub> nanosheets showed surface area of 150 m<sup>2</sup>/g whereas the composite showed decreased surface area of 80 m<sup>2</sup>/g. The decrease in surface area in the nanocomposite agrees with probable covalent type interactions between g-C<sub>3</sub>N<sub>4</sub> and TiN-NFG discussed above.

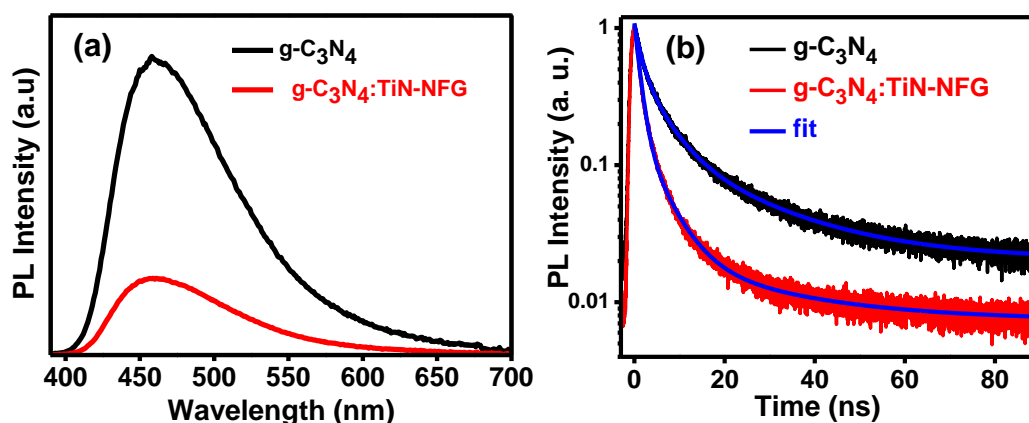


**Figure 3.12:** (a) Comparison of PL spectra and (b) PL decay dynamics of g-C<sub>3</sub>N<sub>4</sub> nanosheet and g-C<sub>3</sub>N<sub>4</sub>:TiN-NFG nanocomposite films after excitation at 340 nm. For PL decay measurements, the emission wavelengths are fixed at their respective PL peak position, and data are fitted with a tri-exponential decay.

To understand the nature of electronic interaction between g-C<sub>3</sub>N<sub>4</sub> and TiN-NFG components of the g-C<sub>3</sub>N<sub>4</sub>:TiN-NFG nanocomposite, we employed the techniques of PL, Mott-Schottky and EIS. These measurements were done on the films of respective samples. Figure 3.12a shows that both g-C<sub>3</sub>N<sub>4</sub> nanosheets and g-C<sub>3</sub>N<sub>4</sub>:TiN-NFG nanocomposites exhibit PL peaks at 460 nm (2.7 eV), which is the characteristic of band to band transition of g-C<sub>3</sub>N<sub>4</sub>.<sup>43-44</sup> But the PL intensity got significantly decreased for the nanocomposite as compared to pristine g-C<sub>3</sub>N<sub>4</sub> nanosheet. Furthermore, PL decay (Figure 3.12b) becomes significantly faster for the nanocomposite. The decay plots are fitted using tri-exponential decay function, and the best-fit parameters are given in Table 3.1. We attribute the lifetime of ~ 1 ns for faster non-radiative decay channels, and Table 3.1 shows that the contribution of this non-radiative decay increases from 49% for g-C<sub>3</sub>N<sub>4</sub> nanosheets to 82% for g-C<sub>3</sub>N<sub>4</sub>:TiN-NFG nanocomposite. Such an increase in non-radiative decay suggests that the interface between g-C<sub>3</sub>N<sub>4</sub> and TiN-NFG in the nanocomposite provides a new channel for non-radiative decay, decreasing the PL efficiency of the g-C<sub>3</sub>N<sub>4</sub>. Previous report<sup>38</sup> has suggested the possibility of photo-excited electron transfer from g-C<sub>3</sub>N<sub>4</sub> nanosheet to NFG, and such possibility of electron transfer might be present in the case of g-C<sub>3</sub>N<sub>4</sub>:TiN-NFG nanocomposite, providing the additional non-radiative pathway for PL decay.



**Table 3.1:** The best fit parameters (with 95% confidence limit) of PL decay profiles shown in Figure 3.12b. The fitting is done using a tri-exponential decay, where  $a_1$ ,  $a_2$  and  $a_3$  are percentage contributions of lifetime  $\tau_1$ ,  $\tau_2$ , and  $\tau_3$  respectively.

Sample	$\tau_1$ (ns)	$a_1$ (%)	$\tau_2$ (ns)	$a_2$ (%)	$\tau_3$ (ns)	$a_3$ (%)
g-C <sub>3</sub> N <sub>4</sub>	1.5	49	5.3	40	20.6	11
g-C <sub>3</sub> N <sub>4</sub> :TiN-NFG	1.2	82	5.0	17	25.0	1

To verify the possibility of charge transfer from g-C<sub>3</sub>N<sub>4</sub> to TiN-NFG, we estimated the flat band potential ( $V_{fb}$ ) values corresponding to the conduction band minimum, by employing electrochemical Mott-Schottky experiments (Figure 3.13a). The intercept on x-axis of Figure 3.13a determines  $V_{fb}$  values for g-C<sub>3</sub>N<sub>4</sub> nanosheet and TiN-NFG as -1.48 V and -1.20 V versus Ag/AgCl (-0.87 V and -0.59 V versus RHE) at pH = 7, respectively, similar to prior reports.<sup>45-46</sup> The observed band gap of g-C<sub>3</sub>N<sub>4</sub> nanosheets from UV-visible absorption spectrum (Figure 3.3) is 2.82 eV. Thus, from the Mott-Schottky and absorption plots, the energy for valance band maximum of g-C<sub>3</sub>N<sub>4</sub> nanosheet is found to be 1.34 V versus Ag/AgCl (1.95 V versus RHE) at pH = 7. Figure 3.13b summarizes the obtained band edge energies, and also compares with potentials for reduction and oxidation of water. These energy levels show that electron transfer from g-C<sub>3</sub>N<sub>4</sub> to TiN-NFG is thermodynamically favourable. Such electron transfer can explain the PL quenching of g-C<sub>3</sub>N<sub>4</sub>:TiN-NFG nanocomposite, discussed above.

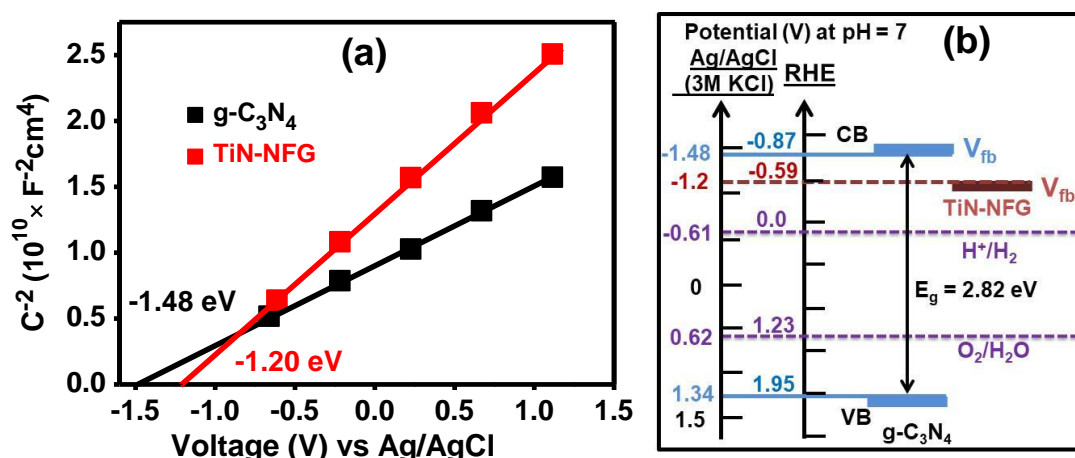


**Figure 3.13:** (a) Mott-Schottky plots, and corresponding (b) band alignment structure of g-C<sub>3</sub>N<sub>4</sub> and TiN-NFG.

As a consequence of such electron transfer, electron will reside into the conduction band of TiN-NFG co-catalyst, and hole will reside in the valence band of g-C<sub>3</sub>N<sub>4</sub>, suppressing the electron-hole recombination after photo-excitation. Such electron-hole separation is advantageous for PEC activity, but the efficiency of PEC process will also depend on charge transfer resistance ( $R_{ct}$ ) at electrode/electrolyte interface.

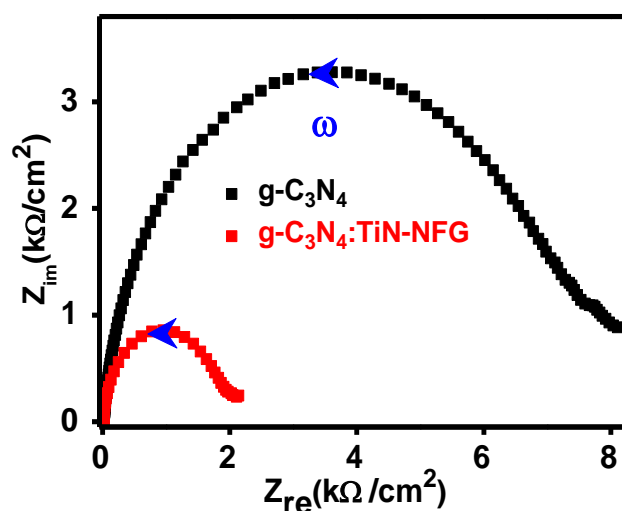


**Figure 3.14:** Nyquist plots for g-C<sub>3</sub>N<sub>4</sub> and g-C<sub>3</sub>N<sub>4</sub>:TiN-NFG nanocomposite in the frequency ( $\omega$ ) range of 100 kHz to 40 mHz.

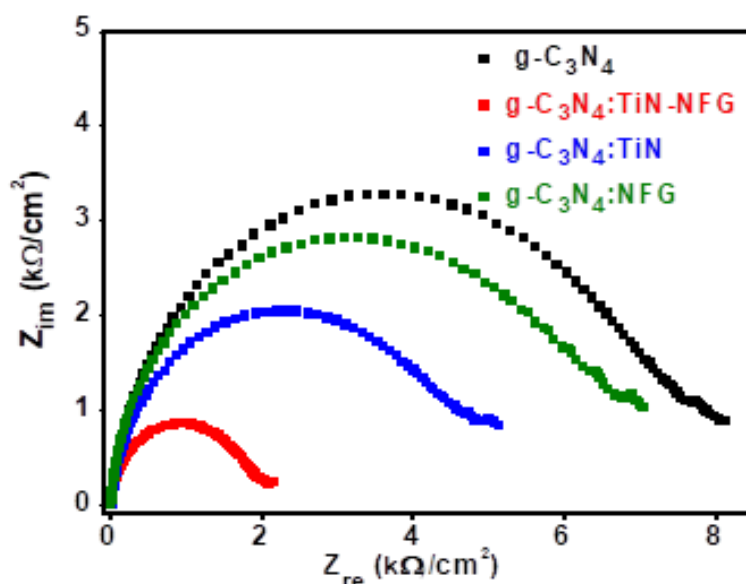


**Figure 3.15:** Nyquist plots of g-C<sub>3</sub>N<sub>4</sub>, g-C<sub>3</sub>N<sub>4</sub>:TiN, g-C<sub>3</sub>N<sub>4</sub>:NFG and g-C<sub>3</sub>N<sub>4</sub>:TiN-NFG photoelectrodes. Loading of co-catalysts are 1.5 wt% for all the composites. Frequency range 100 kHz to 40 mHz.

We measured EIS to compare  $R_{ct}$  of both pristine g-C<sub>3</sub>N<sub>4</sub> nanosheets and g-C<sub>3</sub>N<sub>4</sub>:TiN-NFG nanocomposite electrodes in 40 mL aqueous electrolyte system containing 0.5 M Na<sub>2</sub>SO<sub>4</sub> and 10 vol.% triethanolamine (TEOA). Nyquist plots given in Figure 3.14 exhibit semi-circle arcs.  $R_{ct}$  value for g-C<sub>3</sub>N<sub>4</sub>:TiN-NFG nanocomposite is 2000 ohm/cm<sup>2</sup>, which is 4 times lower than that of g-C<sub>3</sub>N<sub>4</sub> electrodes (8000 ohm/cm<sup>2</sup>). These results suggest that the co-catalyst TiN-NFG reduces  $R_{ct}$  at electrode/electrolyte interface, in addition to the previously discussed electron-hole separation from photo-excited g-C<sub>3</sub>N<sub>4</sub> nanosheet.

For control measurements, we loaded similar amount of individual TiN and NFG as co-catalyst on g-C<sub>3</sub>N<sub>4</sub>, but Figure 3.15 shows that the  $R_{ct}$  is significantly lower for TiN-NFG co-catalyst, among all the samples. This superior performance of TiN-NFG co-catalyst is attributed to the combination of metallic electronic structure of TiN and good charge transport property of NFG, resulting into lower electrical resistivity of TiN-NFG (see Table 3.2).

**Table 3.2:** Electrical resistivity of TiN-NFG, TiN, and NFG co-catalysts. Resistivity measurements were carried out on films of all co-catalysts.

Sample	Electrical resistivity (ohm cm) at 300K
TiN-NFG	0.3
TiN	11000
NFG	10

### 3.3.4 Photoelectrochemical (PEC) Water Splitting Activity of g-C<sub>3</sub>N<sub>4</sub>:TiN-NFG Nanocomposite

The above results motivated us to examine the PEC water splitting activity of g-C<sub>3</sub>N<sub>4</sub>:TiN-NFG nanocomposite compared to that of g-C<sub>3</sub>N<sub>4</sub> nanosheets. First, we see the surface morphology of g-C<sub>3</sub>N<sub>4</sub>:TiN-NFG nanocomposite photoelectrodes using FESEM. FESEM image of photoelectrode indicates curled like sheets of g-C<sub>3</sub>N<sub>4</sub> and thickness was estimated to be ~ 12 μm (Figure 3.16). After that, a three-electrode system with Ag/AgCl reference electrode, Pt counter electrode, and the photoelectrocatalyst samples coated on FTO glass as working photoelectrode was used in 40 mL aqueous electrolyte solution containing 0.5 M

Na<sub>2</sub>SO<sub>4</sub> and 10 vol.% TEOA. The photoelectrode was illuminated with a solar simulator with a power density of 100 mW/cm<sup>2</sup> under 1sun.

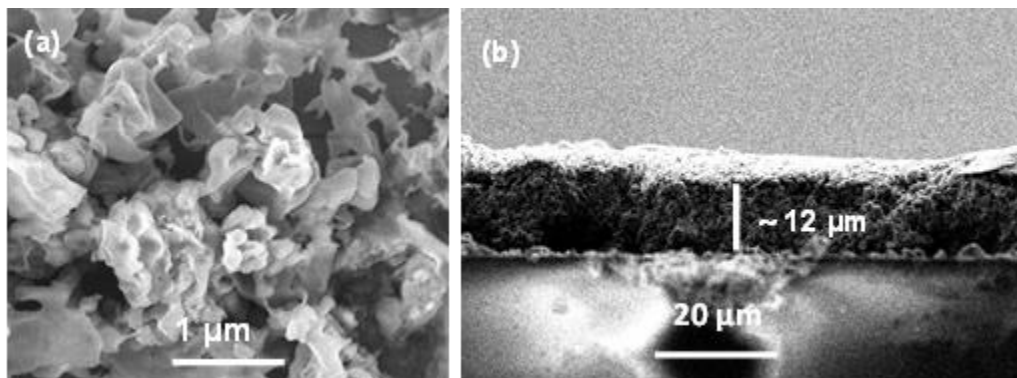


**Figure 3.16:** FESEM images show (a) morphology and (b) thickness of g-C<sub>3</sub>N<sub>4</sub>:TiN-NFG nanocomposite on fluorine doped tin oxide (FTO) coated glass.

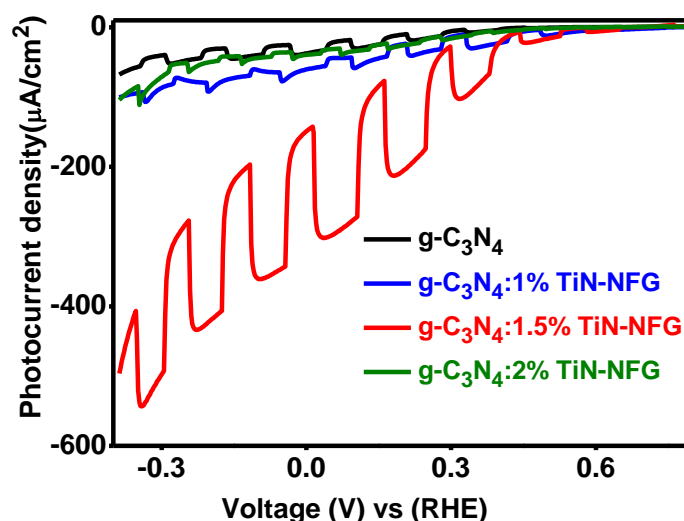


**Figure 3.17:** Linear sweep voltammetry (LSV) data of g-C<sub>3</sub>N<sub>4</sub> nanosheet and g-C<sub>3</sub>N<sub>4</sub>:TiN-NFG nanocomposites photoelectrodes with different wt% loading of TiN-NFG co-catalysts.

First we optimize the loading of co-catalyst TiN-NFG in the nanocomposite and also optimize the thickness of photoelectrodes. Linear sweep voltammetry (LSV) curves under on-off illumination for different loading amounts of TiN-NFG co-catalyst in g-C<sub>3</sub>N<sub>4</sub>:TiN-NFG nanocomposite is given in Figure 3.17. The photocurrent density is enhanced for all the loading values, but 1.5% loading shows the highest photocurrent density. Therefore, g-C<sub>3</sub>N<sub>4</sub>:TiN-NFG nanocomposite with 1.5wt% loading of TiN-NFG is studied in detail for the

PEC activity. Then, we also optimized the photoelectrode thickness to ~12  $\mu\text{m}$  by measuring the photocurrent density versus electrode thickness as shown in Figure 3.18.

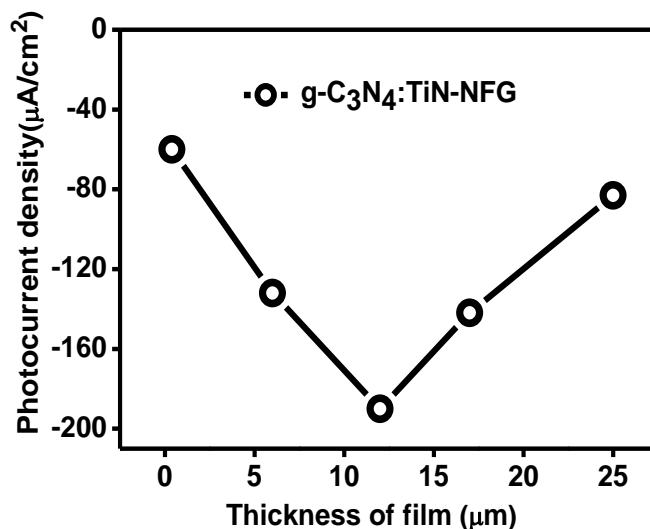


**Figure 3.18:** Photocurrent density versus thickness profile of g-C<sub>3</sub>N<sub>4</sub>:TiN-NFG nanocomposite electrode at 0.11 V versus RHE.

Now we thoroughly discuss the PEC activity of the optimized nanocomposite photoelectrode with 1.5 wt% loading of TiN-NFG and ~12  $\mu\text{m}$  thickness. LSV plots given in Figure 3.19a and b show that the pristine g-C<sub>3</sub>N<sub>4</sub> nanosheet has an onset potential at 0.36 V versus RHE for the reduction of protons whereas the g-C<sub>3</sub>N<sub>4</sub>:TiN-NFG nanocomposite exhibits much more positive onset potential at 0.61 V versus RHE. This positive shift in the onset potential indicates improved catalytic reductive nature of g-C<sub>3</sub>N<sub>4</sub> nanosheet after coupling with TiN-NFG.

Transient photocurrents versus time plots are obtained to evaluate the PEC activity with repeated on/off illumination cycles, as presented in Figure 3.19c and d. Even at 0.61 V versus RHE, the g-C<sub>3</sub>N<sub>4</sub>:TiN-NFG nanocomposite photoelectrode demonstrated enhanced PEC performance as compared to g-C<sub>3</sub>N<sub>4</sub> nanosheet. Interestingly, at 0.61 V versus RHE bias, the g-C<sub>3</sub>N<sub>4</sub>:TiN-NFG nanocomposite photoelectrode shows a cathodic nature with current density of  $-9.6 \mu\text{A}/\text{cm}^2$ , whereas pristine g-C<sub>3</sub>N<sub>4</sub> shows an anodic nature ( $0.2 \mu\text{A}/\text{cm}^2$ ). This is due to the fact that onset potential in g-C<sub>3</sub>N<sub>4</sub>:TiN-NFG nanocomposite photoelectrode has shifted to 0.61 V versus RHE as compared to 0.36 V versus RHE for g-C<sub>3</sub>N<sub>4</sub> nanosheets as shown in Figure 3.19b. Therefore, the chronoamperometric response and LSV data are in good agreement with each other.

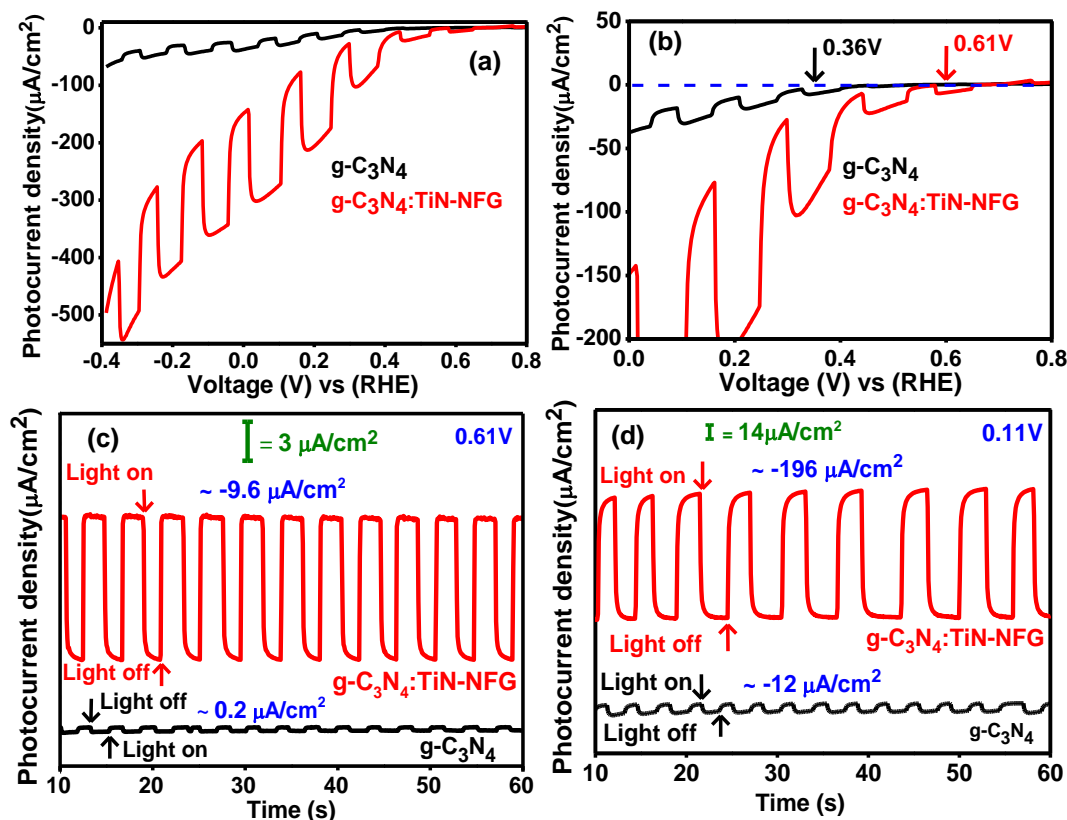


**Figure 3.19:** (a) Linear sweep voltammetry (LSV) curves for g-C<sub>3</sub>N<sub>4</sub> nanosheets and g-C<sub>3</sub>N<sub>4</sub>:TiN-NFG nanocomposite photoelectrodes. (b) Magnified view of the same LSV data indicating onset potential for water reduction to H<sub>2</sub>. Transient photocurrent density versus time plots at (c) 0.61 V, and (d) 0.11 V versus RHE of g-C<sub>3</sub>N<sub>4</sub> nanosheet and g-C<sub>3</sub>N<sub>4</sub>:TiN-NFG nanocomposite photoelectrodes.

In Figure 3.19d, we compare the PEC activity of g-C<sub>3</sub>N<sub>4</sub>:TiN-NFG nanocomposite and g-C<sub>3</sub>N<sub>4</sub> nanosheet at 0.11 V versus RHE. As a photocathode, g-C<sub>3</sub>N<sub>4</sub>:TiN-NFG nanocomposite displays the photocurrent density of -196 μA/cm<sup>2</sup> at 0.11 V versus RHE, which is almost ~16 times higher than that of pristine g-C<sub>3</sub>N<sub>4</sub> nanosheet (-12 μA/cm<sup>2</sup>). It is not easy to quantitatively compare our results with prior reports because of some differences in the experimental conditions used in different reports. But to the best of our knowledge, ~16 times enhancement in reductive PEC activity of g-C<sub>3</sub>N<sub>4</sub> by using our TiN-NFG co-catalyst is the highest reported enhancement so far. Table 3.3 compares our results with a list of prior literature.

**Table 3.3:** Comparison of photoelectrocatalytic performance of g-C<sub>3</sub>N<sub>4</sub>:TiN-NFG nanocomposite photoelectrode with prior reported carbon nitride based photoelectrocatalysts.

Photoelectrocatalyst	Photocurrent density ( $\mu\text{A}/\text{cm}^2$ ) water reduction	Source (Light density)	Increase-ment	Electrolyte	Ref.
g-C <sub>3</sub> N <sub>4</sub>	~ - 12 $\mu\text{A}/\text{cm}^2$ 0.61 V versus RHE	400 W Xe lamp (100 mW/cm <sup>2</sup> )		0.5M Na <sub>2</sub> SO <sub>4</sub> 10% TEOA	Present work
g-C <sub>3</sub> N <sub>4</sub> :TiN-NFG	~ -196 $\mu\text{A}/\text{cm}^2$ 0.11 V versus RHE	400 W Xe lamp (100 mW/cm <sup>2</sup> )	16 (W <sub>Red</sub> )	0.5M Na <sub>2</sub> SO <sub>4</sub> 10% TEOA	Present work
g-C <sub>3</sub> N <sub>4</sub> /Graphdiyne (GDY)	~ - 98 $\mu\text{A}/\text{cm}^2$ 0 V versus NHE	300 W Xe lamp (100 mW/cm <sup>2</sup> )	3	0.1M Na <sub>2</sub> SO <sub>4</sub>	12
Carbon ring – C <sub>3</sub> N <sub>4</sub>	~ - 22 $\mu\text{A}/\text{cm}^2$ -0.4 V versus Ag/AgCl	300 W Xe lamp	6	0.5M Na <sub>2</sub> SO <sub>4</sub>	27
<sup>a</sup> CNNS/NGRO O/MoS <sub>2</sub>	---	150 W Xe lamp (100 mW/cm <sup>2</sup> )	3	0.01 M Na <sub>2</sub> SO <sub>4</sub>	38
13.3% MoS <sub>2</sub> /g-C <sub>3</sub> N <sub>4</sub>	-50 $\mu\text{A}/\text{cm}^2$ 1.0 V versus RHE	300 W Xe lamp ( $\lambda > 420 \text{ nm}$ )	10	0.5 M H <sub>2</sub> SO <sub>4</sub>	26

a: CNNS/NGRO /MoS<sub>2</sub> = Carbon nitride nanosheets/N-doped reduced graphene oxide/MoS<sub>2</sub>

W<sub>Red</sub> = water reduction

Four control experiments (Figure 3.20) were conducted to validate the superior performance of g-C<sub>3</sub>N<sub>4</sub>:TiN-NFG nanocomposite. In the first control experiment (Figure 3.20a) chronoamperometry of pristine TiN-NFG shows almost negligible photocurrent. This clearly indicates that the photocurrent response of -196  $\mu\text{A}/\text{cm}^2$  is from g-C<sub>3</sub>N<sub>4</sub>:TiN-NFG nanocomposite and almost no contribution is from pristine co-catalyst TiN-NFG. Second control experiments were conducted to check contribution of individual co-catalyst TiN and

NFG. LSV and chronoamperometry (at 0.61 V and 0.11 V versus RHE) of g-C<sub>3</sub>N<sub>4</sub>:TiN and g-C<sub>3</sub>N<sub>4</sub>:NFG nanocomposites are given in Figure 3.20b, c and d, respectively.

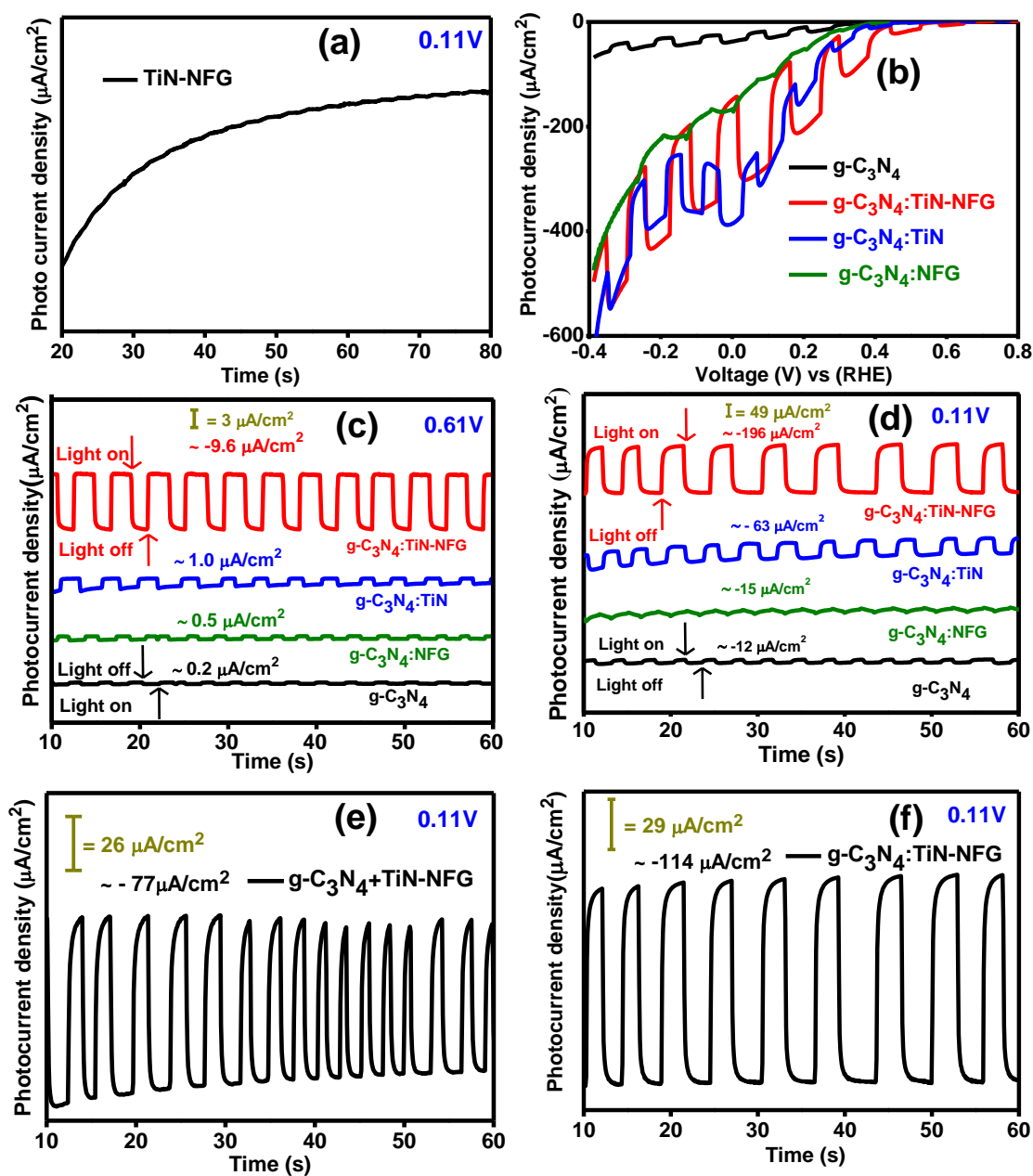


**Figure 3.20:** (a) Transient photoresponse data of TiN-NFG. (b) Linear sweep voltammetry (LSV), and (c-d) Transient photoresponse at 0.61 V and 0.11 V versus RHE data of g-C<sub>3</sub>N<sub>4</sub>, g-C<sub>3</sub>N<sub>4</sub>:NFG, g-C<sub>3</sub>N<sub>4</sub>:TiN, and g-C<sub>3</sub>N<sub>4</sub>:TiN-NFG photoelectrodes. Loading of co-catalysts are 1.5 wt% for all the composites. (e) Transient photoresponse data of physical mixture of g-C<sub>3</sub>N<sub>4</sub>+TiN-NFG in 0.5 M Na<sub>2</sub>SO<sub>4</sub> and 10 vol% TEOA electrolyte solution. Physical mixture was prepared by just mixing g-C<sub>3</sub>N<sub>4</sub> and TiN-NFG in ethanol and coated on FTO. (f) Transient photoresponse data of g-C<sub>3</sub>N<sub>4</sub>:TiN-NFG nanocomposite at 0.11 V versus RHE without TEOA.



Both g-C<sub>3</sub>N<sub>4</sub>:TiN (1  $\mu\text{A}/\text{cm}^2$ ) and g-C<sub>3</sub>N<sub>4</sub>:NFG (0.5  $\mu\text{A}/\text{cm}^2$ ) showed lower performance than g-C<sub>3</sub>N<sub>4</sub>:TiN-NFG indicating synergistic effect of TiN and NFG in co-catalyst for enhancing the g-C<sub>3</sub>N<sub>4</sub> PEC performance. In the third control experiment, co-catalyst performance of physically mixed g-C<sub>3</sub>N<sub>4</sub> and TiN-NFG is tested as shown in Figure 3.20e. This physical mixture (g-C<sub>3</sub>N<sub>4</sub> + TiN-NFG) shows photocurrent density of  $\sim 77 \mu\text{A}/\text{cm}^2$ , which is just  $\sim 6$  times higher than pristine g-C<sub>3</sub>N<sub>4</sub>, whereas g-C<sub>3</sub>N<sub>4</sub>:TiN-NFG nanocomposite shows  $\sim 16$  times enhancement. This finding again suggests that the g-C<sub>3</sub>N<sub>4</sub>:TiN-NFG has formed a hetero-junction (also evident from PL and impedance) and is not just a physical mixture. In our previous experiments, TEOA hole scavenger is employed to regenerate the photocatalyst g-C<sub>3</sub>N<sub>4</sub>. As a control measurement we evaluate the PEC activity of g-C<sub>3</sub>N<sub>4</sub>:TiN-NFG nanocomposite without adding TEOA. A photocurrent density of  $-114 \mu\text{A}/\text{cm}^2$  (Figure 3.20f) is obtained for the nanocomposite without TEOA in Na<sub>2</sub>SO<sub>4</sub> electrolyte, as opposed to  $-196 \mu\text{A}/\text{cm}^2$  photocurrent density (Figure 3.19d) in the presence of TEOA. This shows the role of TEOA in the enhancement of PEC performance but still a significant PEC activity of the nanocomposite is observed even in the absence of TEOA.

Henceforth, all the control experiments clearly signify the superiority of TiN-NFG nanocomposite as a co-catalyst for enhancement of PEC performance of g-C<sub>3</sub>N<sub>4</sub>. We attribute this huge enhancement in water splitting to both (i) large interface area between 2D photocatalyst (g-C<sub>3</sub>N<sub>4</sub>) and 2D co-catalyst (TiN-NFG) along with the desired band-alignment for efficient separation of photoexcited electron-hole pair, and (ii) lower  $R_{ct}$  at electrode/electrolyte interface owing to the higher conductivity of the co-catalyst.

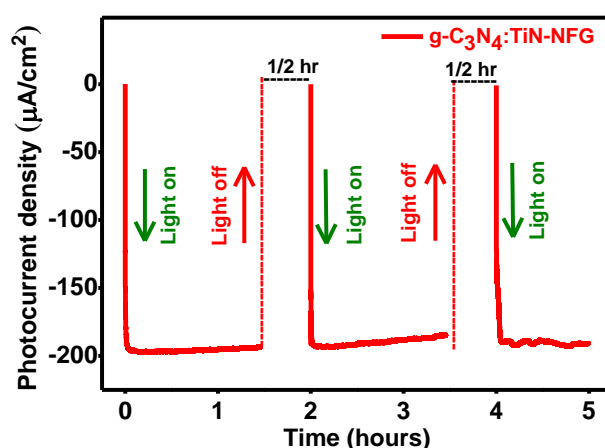


**Figure 3.21:** Stability profile of g-C<sub>3</sub>N<sub>4</sub>:TiN-NFG nanocomposite photoelectrocatalyst.

Now to evaluate the stability of g-C<sub>3</sub>N<sub>4</sub>:TiN-NFG nanocomposite, chronoamperometric experiments were carried out at 0.11 V versus RHE under the light-on and light-off mode for 5 hours. The photoelectrocatalyst maintained a photocurrent density -196  $\mu\text{A}/\text{cm}^2$  for the entire duration (Figure 3.21) of experiment, indicating good stability of the nanocomposite under light and in the electrolyte solution. Furthermore, as shown in Figure 3.22, FESEM, PXRD and EIS data before and after PEC testing is evaluated which almost showed negligible change in g-C<sub>3</sub>N<sub>4</sub>:TiN-NFG nanocomposite photoelectrode and its PEC performance. This indicates that g-C<sub>3</sub>N<sub>4</sub>:TiN-NFG nanocomposite can be useful for long term usability.

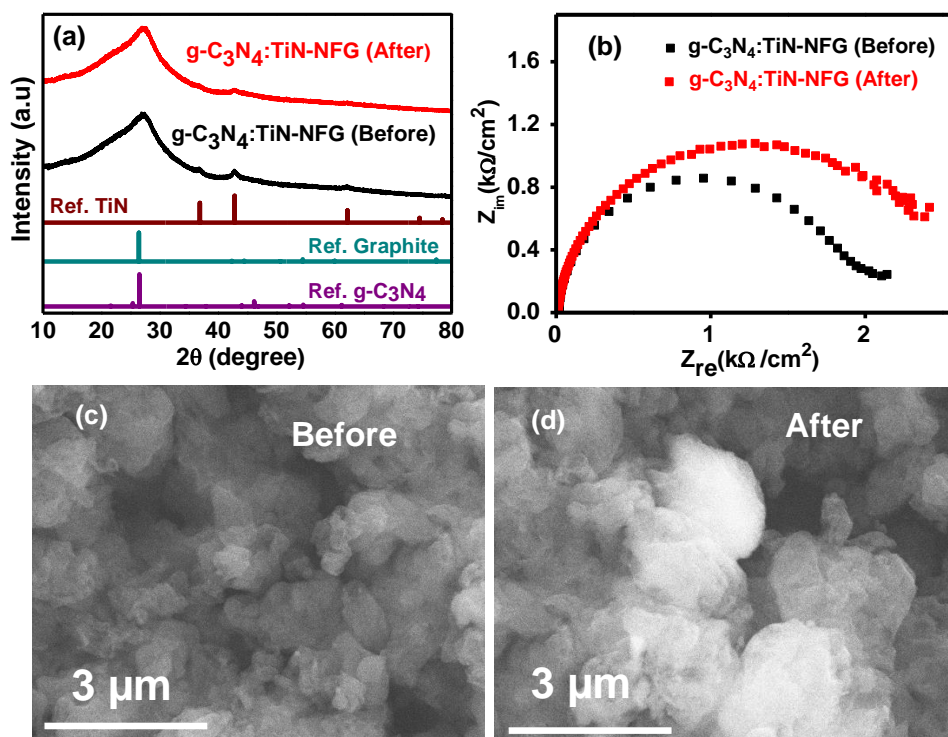


**Figure 3.22:** Comparison of (a) PXRD patterns, (b) Nyquist plots, and (c-d) FESEM images of g-C<sub>3</sub>N<sub>4</sub>:TiN-NFG nanocomposite before and after the stability test (5 hour) of photoelectrocatalytic reaction.

In order to confirm that the observed photocurrents are actually related to real PEC water splitting, we constructed a closed PEC cell and measured the evolved hydrogen with respect to time using Gas chromatography (GC). After passing 0.4 C of charges through the external circuit, 2  $\mu\text{mol}$  of hydrogen is estimated by GC and faradic efficiency of  $\sim 91\%$  for reduction of water is achieved (Figure 3.23). Thus, most of the photogenerated charges are effective in the hydrogen generation for the present system.

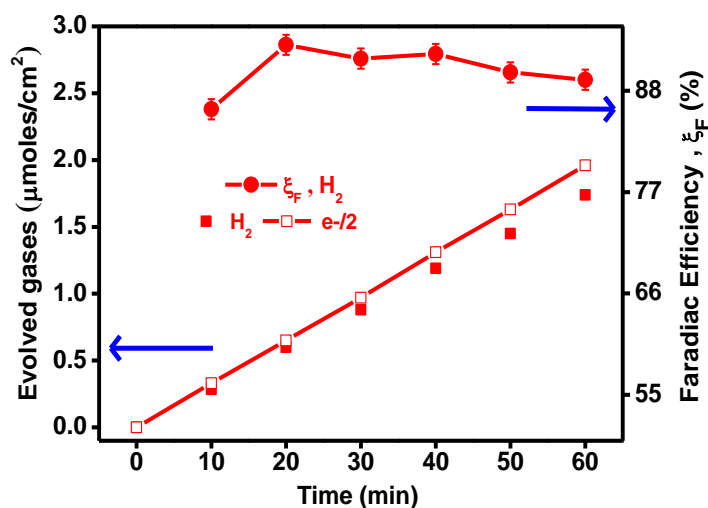


**Figure 3.23:** Experimental (red shaded circles) and calculated from photocurrent at 1.1 V (red open circles) for gas evolution rate of H<sub>2</sub>, and faraday efficiency of g-C<sub>3</sub>N<sub>4</sub>:TiN-NFG.

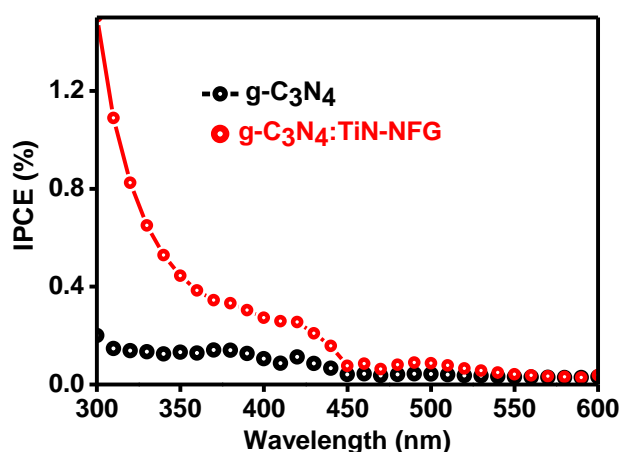


**Figure 3.24:** Incident photon to current efficiency (IPCE) data of g-C<sub>3</sub>N<sub>4</sub> and g-C<sub>3</sub>N<sub>4</sub>:TiN-NFG nanocomposite photoelectrodes at 0.61 V versus RHE.

Further, to assess quantitatively the PEC activity at different wavelengths, incident photon to current efficiency (IPCE) of g-C<sub>3</sub>N<sub>4</sub> nanosheet, and g-C<sub>3</sub>N<sub>4</sub>:TiN-NFG nanocomposite photoelectrodes are measured (Figure 3.24) at 0.61 V versus RHE. The g-C<sub>3</sub>N<sub>4</sub>:TiN-NFG nanocomposite photoelectrode presented strong photo response as compared to pristine g-C<sub>3</sub>N<sub>4</sub> nanosheet which is in accordance with UV-visible absorption spectrum (Figure 3.3). The enhanced IPCE for the nanocomposite is because of the formation of strong hetero-junction between g-C<sub>3</sub>N<sub>4</sub> and TiN-NFG.

### 3.4 Conclusions

In summary, we introduce a new 2D co-catalyst, namely, TiN-NFG nanocomposite for boosting the PEC water splitting performance of 2D g-C<sub>3</sub>N<sub>4</sub> nanosheets. The extended interface of 2D g-C<sub>3</sub>N<sub>4</sub>:TiN-NFG nanocomposite suppresses recombination of photo-excited electron-hole by separating the charge carriers. The TiN-NFG co-catalyst also reduces the  $R_{ct}$  across the electrode/electrolyte interface. As a result, excellent enhancement in the overall PEC performance is observed for the 2D g-C<sub>3</sub>N<sub>4</sub>:TiN-NFG nanocomposite. The nanocomposite shows ~16 times enhancement in the PEC activity of g-C<sub>3</sub>N<sub>4</sub> nanosheet at 0.11 V versus RHE under simulated solar illumination. The nanocomposite is stable under experimental conditions and cost-effective without involving any noble metal. The present study establishes TiN-NFG as a promising 2D co-catalyst for PEC water splitting, and needs to be explored further for other catalysts apart from g-C<sub>3</sub>N<sub>4</sub> as well.

### References

1. Wang, X.; Maeda, K.; Thomas, A.; Takanabe, K.; Xin, G.; Carlsson, J. M.; Domen, K.; Antonietti, M. A Metal-Free Polymeric Photocatalyst for Hydrogen Production from Water under Visible light. *Nat. Mater.* **2008**, *8*, 76.
2. Kelkar, S. A.; Shaikh, P. A.; Pachfule, P.; Ogale, S. B. Nanostructured Cd<sub>2</sub>SnO<sub>4</sub> as an Anergy Harvesting Photoanode for Solar Water Splitting. *Energy Environ. Sci.* **2012**, *5*, 5681-5685.
3. Arif, S.; Ashish, Y.; Meenal, D.; Sarika, K.; Ogale, S. B. Near-Field Plasmonic Functionalization of Light Harvesting Oxide-Oxide Heterojunctions for Efficient Solar Photoelectrochemical Water Splitting: The AuNP/ZnFe<sub>2</sub>O<sub>4</sub>/ZnO System. *Small* **2013**, *9*, 2091-2096.
4. Jagadeeswararao, M.; Dey, S.; Nag, A.; Rao, C. N. R. Visible Light-Induced Hydrogen Generation using Colloidal (ZnS)<sub>0.4</sub>(AgInS<sub>2</sub>)<sub>0.6</sub> Nanocrystals Capped by S<sup>2-</sup> Ions. *J. Mater. Chem. A* **2015**, *3*, 8276-8279.
5. Dongyang., W.; C., A. T.; Andrivo, R.; T., V. Comparison of Typical Photocatalytic Systems with Intrinsic Plasmonic Photocatalysts Based on Strontium Niobate for Water Splitting. *Energy Technol.* **2018**, *6*, 60-71.
6. Li, L.; Yan, J.; Wang, T.; Zhao, Z. J.; Zhang, J.; Gong, J.; Guan, N. Sub-10 nm Rutile Titanium Dioxide Nanoparticles for Efficient Visible-Light-Driven Photocatalytic Hydrogen Production. *Nat. Commun.* **2015**, *6*, 5881.

7. Junqing, Y.; Tuo, W.; Guangjun, W.; Weili, D.; Naijia, G.; Landong, L.; Jinlong, G. Tungsten Oxide Single Crystal Nanosheets for Enhanced Multichannel Solar Light Harvesting. *Adv. Mater.* **2015**, *27*, 1580-1586.
8. Li, Q.; Guo, B.; Yu, J.; Ran, J.; Zhang, B.; Yan, H.; Gong, J. R. Highly Efficient Visible-Light-Driven Photocatalytic Hydrogen Production of CdS-Cluster-Decorated Graphene Nanosheets. *J. Am. Chem. Soc.* **2011**, *133*, 10878-10884.
9. Wang, X.; Maeda, K.; Chen, X.; Takahabe, K.; Domen, K.; Hou, Y.; Fu, X.; Antonietti, M. Polymer Semiconductors for Artificial Photosynthesis: Hydrogen Evolution by Mesoporous Graphitic Carbon Nitride with Visible Light. *J. Am. Chem. Soc.* **2009**, *131*, 1680-1681.
10. Botari, T.; Huhn, W. P.; Lau, V. W. h.; Lotsch, B. V.; Blum, V. Thermodynamic Equilibria in Carbon Nitride Photocatalyst Materials and Conditions for the Existence of Graphitic Carbon Nitride g-C<sub>3</sub>N<sub>4</sub>. *Chem. Mater.* **2017**, *29*, 4445-4453.
11. Yan, J.; Li, P.; Bian, H.; Wu, H.; Liu, S. Synthesis of a Nano-Sized Hybrid C<sub>3</sub>N<sub>4</sub>/TiO<sub>2</sub> Sample for Enhanced and Steady Solar Energy Absorption and Utilization. *Sustainable Energy Fuels* **2017**, *1*, 95-102.
12. Ying-Ying, H.; Xiu-Li, L.; Shang-Feng, T.; Xue-Peng, Y.; Zhen-Wei, W.; Tong-Bu, L. Metal-Free 2D/2D Heterojunction of Graphitic Carbon Nitride/Graphdiyne for Improving the Hole Mobility of Graphitic Carbon Nitride. *Adv. Energy Mater.* **2018**, *8*, 1702992.
13. Zhang, J.; Chen, Y.; Wang, X. Two-Dimensional Covalent Carbon Nitride Nanosheets: Synthesis, Functionalization, and Applications. *Energy Environ. Sci.* **2015**, *8*, 3092-3108.
14. Zheng, Y.; Lin, L.; Wang, B.; Wang, X. Graphitic Carbon Nitride Polymers toward Sustainable Photoredox Catalysis. *Angew. Chem. Int. Ed.* **2015**, *54*, 12868-12884.
15. Tonda, S.; Kumar, S.; Gawli, Y.; Bhardwaj, M.; Ogale, S. B. g-C<sub>3</sub>N<sub>4</sub> (2D)/CdS (1D)/rGO (2D) Dual-Interface Nanocomposite for Excellent and Stable Visible Light Photocatalytic Hydrogen Generation. *Int. J. Hydrog. Energy* **2017**, *42*, 5971-5984.
16. Ong, W. J.; Tan, L. L.; Ng, Y. H.; Yong, S. T.; Chai, S. P. Graphitic Carbon Nitride (g-C<sub>3</sub>N<sub>4</sub>)-Based Photocatalysts for Artificial Photosynthesis and Environmental Remediation: Are We a Step Closer To Achieving Sustainability? *Chem. Rev.* **2016**, *116*, 7159-7329.

17. Chai, B.; Liu, C.; Yan, J.; Ren, Z.; Wang, Z. j. In-situ Synthesis of WO<sub>3</sub> Nanoplates Anchored on g-C<sub>3</sub>N<sub>4</sub> Z-Scheme Photocatalysts for Significantly Enhanced Photocatalytic Activity. *Appl. Surf. Sci.* **2018**, *448*, 1-8.
18. Zhang, G.; Lan, Z. A.; Lin, L.; Lin, S.; Wang, X. Overall Water Splitting by Pt/g-C<sub>3</sub>N<sub>4</sub> Photocatalysts without Using Sacrificial Agents. *Chem. Sci.* **2016**, *7*, 3062-3066.
19. Zhang, G.; Zang, S.; Wang, X. Layered Co(OH)<sub>2</sub> Deposited Polymeric Carbon Nitrides for Photocatalytic Water Oxidation. *ACS Catal.* **2015**, *5*, 941-947.
20. Fettkenhauer, C.; Wang, X.; Kailasam, K.; Antonietti, M.; Dontsova, D. Synthesis of Efficient Photocatalysts for Water Oxidation and Dye Degradation Reactions using CoCl<sub>2</sub> Eutectics. *J. Mater. Chem. A* **2015**, *3*, 21227-21232.
21. Zhang, G.; Huang, C.; Wang, X. Dispersing Molecular Cobalt in Graphitic Carbon Nitride Frameworks for Photocatalytic Water Oxidation. *Small* **2015**, *11*, 1215-1221.
22. Zhang, G.; Zang, S.; Lan, Z. A.; Huang, C.; Li, G.; Wang, X. Cobalt Selenide: A Versatile Cocatalyst for Photocatalytic Water Oxidation with Visible Light. *J. Mater. Chem. A* **2015**, *3*, 17946-17950.
23. Zhang, G.; Li, G.; Wang, X. Surface Modification of Carbon Nitride Polymers by Core-Shell Nickel/Nickel Oxide Cocatalysts for Hydrogen Evolution Photocatalysis. *ChemCatChem* **2015**, *7*, 2864-2870.
24. Hong, J.; Wang, Y.; Wang, Y.; Zhang, W.; Xu, R. Noble-Metal-Free NiS/C<sub>3</sub>N<sub>4</sub> for Efficient Photocatalytic Hydrogen Evolution from Water. *ChemSusChem* **2013**, *6*, 2263-2268.
25. Ying-Ying, H.; Xiu-Li, L.; Shang-Feng, T.; Xue-Peng, Y.; Zhen-Wei, W.; Tong-Bu, L. Metal-Free 2D/2D Heterojunction of Graphitic Carbon Nitride/Graphdiyne for Improving the Hole Mobility of Graphitic Carbon Nitride. *Adv. Energy Mater.* **2018**, *8*, 1702992.
26. Hui, B.; Yujin, J.; Junqing, Y.; Ping, L.; Ling, L.; Youyong, L.; Shengzhong, L. In Situ Synthesis of Few-Layered g-C<sub>3</sub>N<sub>4</sub> with Vertically Aligned MoS<sub>2</sub> Loading for Boosting Solar-to-Hydrogen Generation. *Small* **2018**, *14*, 1703003.
27. Che, W.; Cheng, W.; Yao, T.; Tang, F.; Liu, W.; Su, H.; Huang, Y.; Liu, Q.; Liu, J.; Hu, F.; Pan, Z.; Sun, Z.; Wei, S. Fast Photoelectron Transfer in (C<sub>ring</sub>) - C<sub>3</sub>N<sub>4</sub> Plane Heterostructural Nanosheets for Overall Water Splitting. *J. Am. Chem. Soc.* **2017**, *139*, 3021-3026.

28. Shanker, G. S.; Markad, G. B.; Jagadeeswararao, M.; Bansode, U.; Nag, A. Colloidal Nanocomposite of TiN and N-Doped Few-Layer Graphene for Plasmonics and Electrocatalysis. *ACS Energy Lett.* **2017**, *2*, 2251-2256.
29. Chen, J. G. Carbide and Nitride Overlayers on Early Transition Metal Surfaces: Preparation, Characterization, and Reactivities. *Chem. Rev.* **1996**, *96*, 1477-1498.
30. Zheng, P.; Zhao, J.; Zheng, J.; Ma, G.; Zhu, Z. Non-Equilibrium Partial Oxidation of TiN Surface for Efficient Visible-Light-Driven Hydrogen Production. *J. Mater. Chem.* **2012**, *22*, 12116-12120.
31. Chen, W. F.; Muckerman, J. T.; Fujita, E. Recent Developments in Transition Metal Carbides and Nitrides as Hydrogen Evolution Electrocatalysts. *Chem. Commun.* **2013**, *49*, 8896-8909.
32. Wang, H.; Maiyalagan, T.; Wang, X. Review on Recent Progress in Nitrogen-Doped Graphene: Synthesis, Characterization, and Its Potential Applications. *ACS Catal.* **2012**, *2*, 781-794.
33. Liu, J.; Zhang, T.; Wang, Z.; Dawson, G.; Chen, W. Simple Pyrolysis of Urea into Graphitic Carbon Nitride with Recyclable Adsorption and Photocatalytic Activity. *J. Mater. Chem.* **2011**, *21*, 14398-14401.
34. Singh, S. K.; Dhavale, V. M.; Kurungot, S. Surface-Tuned Co<sub>3</sub>O<sub>4</sub> Nanoparticles Dispersed on Nitrogen-Doped Graphene as an Efficient Cathode Electrocatalyst for Mechanical Rechargeable Zinc-Air Battery Application. *ACS Appl. Mater. Interfaces* **2015**, *7*, 21138-21149.
35. Yang, S.; Gong, Y.; Zhang, J.; Zhan, L.; Ma, L.; Fang, Z.; Vajtai, R.; Wang, X.; Ajayan, P. M. Exfoliated Graphitic Carbon Nitride Nanosheets as Efficient Catalysts for Hydrogen Evolution Under Visible Light. *Adv. Mater.* **2013**, *25*, 2452-2456.
36. Kubelka, P.; Munk, F. *Z. Tech. Phys.* **1931**, *12*, 593-601.
37. Tauc, J.; Grigorovici, R.; Vancu, A. Optical Properties and Electronic Structure of Amorphous Germanium. *Vancu. Phys. Status Solidi.* **1966**, *15*, 627- 637.
38. Yang, H.; Zhenhai, W.; Shumao, C.; Xiaoru, G.; Junhong, C. Constructing 2D Porous Graphitic C<sub>3</sub>N<sub>4</sub> Nanosheets/Nitrogen-Doped Graphene/Layered MoS<sub>2</sub> Ternary Nanojunction with Enhanced Photoelectrochemical Activity. *Adv. Mater.* **2013**, *25*, 6291-6297.
39. Thomas, A.; Fischer, A.; Goettmann, F.; Antonietti, M.; Muller, J. O.; Schlogl, R.; Carlsson, J. M. Graphitic Carbon Nitride Materials: Variation of Structure and

- Morphology and Their use as Metal-Free Catalysts. *J. Mater. Chem.* **2008**, 18, 4893-4908.
40. Lazauskas, A.; Baltrusaitis, J.; Puodžiukynas, L.; Andrulevičius, M.; Bagdžiūnas, G.; Volyniuk, D.; Meškiniš, Š.; Niaura, G.; Tamulevičius, T.; Jankauskaitė, V. Characterization of Urea Derived Polymeric Carbon Nitride and Resultant Thermally Vacuum Deposited Amorphous Thin Films: Structural, Chemical and photophysical Properties. *Carbon* **2016**, 107, 415-425.
41. Peng, G.; Volokh, M.; Tzadikov, J.; Sun, J.; Shalom, M. Carbon Nitride/Reduced Graphene Oxide Film with Enhanced Electron Diffusion Length: An Efficient Photo-Electrochemical Cell for Hydrogen Generation. *Adv. Energy Mater.* **2018**, 8, 1800566.
42. Hou, Y.; Wen, Z.; Cui, S.; Guo, X.; Chen, J. Constructing 2D Porous Graphitic C<sub>3</sub>N<sub>4</sub> Nanosheets/Nitrogen-Doped Graphene/Layered MoS<sub>2</sub> Ternary Nanojunction with Enhanced Photoelectrochemical Activity. *Adv. Mater.* **2013**, 25, 6291-6297.
43. Min, Y.; Qi, X. F.; Xu, Q.; Chen, Y. Enhanced Reactive Oxygen Species on a Phosphate Modified C<sub>3</sub>N<sub>4</sub>/Graphene Photocatalyst for Pollutant Degradation. *CrystEngComm* **2014**, 16, 1287-1295.
44. Tong, J.; Zhang, L.; Li, F.; Li, M.; Cao, S. An Efficient Top-Down Approach for the Fabrication of Large-Aspect-Ratio g-C<sub>3</sub>N<sub>4</sub> Nanosheets with Enhanced Photocatalytic Activities. *Phys. Chem. Chem. Phys.* **2015**, 17, 23532-23537.
45. Vilela, F.; Zhang, K.; Antonietti, M. Conjugated Porous Polymers for Energy Applications. *Energy Environ. Sci.* **2012**, 5, 7819-7832.
46. Cui, Y.; Ding, Z.; Liu, P.; Antonietti, M.; Fu, X.; Wang, X. Metal-Free Activation of H<sub>2</sub>O<sub>2</sub> by g-C<sub>3</sub>N<sub>4</sub> under Visible Light Irradiation for the Degradation of Organic Pollutants. *Phys. Chem. Chem. Phys.* **2012**, 14, 1455-1462.



## Chapter 4

### **Plasmonic Properties of Sn-Doped In<sub>2</sub>O<sub>3</sub> (ITO) Nanocrystals and Their Co-catalytic Activity with g-C<sub>3</sub>N<sub>4</sub> Nanosheets for Photoelectrochemical Reduction of Water**

---

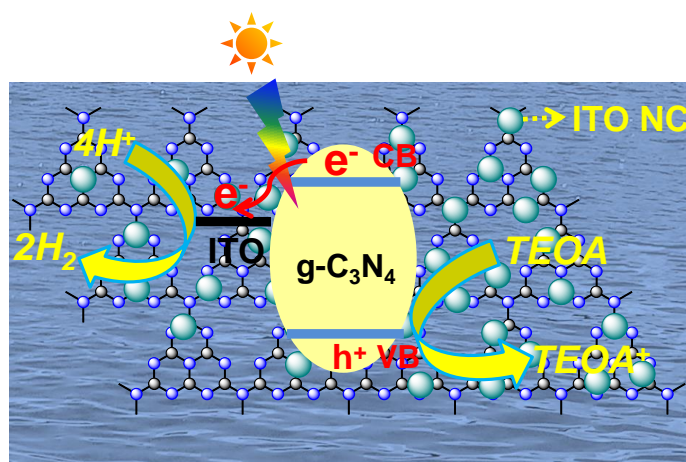
The following paper has been published based on the work documented in this chapter.

Shanker, G. S.; Tandon, B.; Shibata, T.; Chattopadhyay, S.; Nag, A. Doping Controls Plasmonics, Electrical Conductivity, and Carrier Mediated Magnetic Coupling in Fe and Sn Codoped In<sub>2</sub>O<sub>3</sub> Nanocrystals: Local Structure is the Key. *Chem. Mater.* **2015**, *27*, 892-900.  
Copyright permission has been obtained for the article from American Chemical Society.

## Summary

A typical graphitic carbon nitride (g- $\text{C}_3\text{N}_4$ ) nanosheet has brought much attention in the research area of photocatalytic water splitting. However, its photocatalytic activity is restrained due to its fast recombination of photo generated electron-hole pairs. Here, we introduce a popularly known plasmonic material which is Sn-doped  $\text{In}_2\text{O}_3$  (ITO) nanocrystals (NCs) as a co-catalyst due to its high electrical conductivity and metallic electrons. In this report, we made g- $\text{C}_3\text{N}_4$ :ITO nanocomposite photoelectrode for an efficient photoelectrochemical (PEC) reduction of water. In the first step, we studied the origin of generation of free electron in ITO NCs by monitoring the evolution of plasmonic band with reaction conditions. Then, the g- $\text{C}_3\text{N}_4$ :ITO nanocomposites were prepared and studied using various experimental techniques. g- $\text{C}_3\text{N}_4$ :ITO nanocomposite photoelectrode showed decrease ( $\sim 2.5$  times) of interfacial charge transfer resistance at electrode/electrolyte interface when compared with pristine g- $\text{C}_3\text{N}_4$  nanosheet. Our g- $\text{C}_3\text{N}_4$ :ITO nanocomposite photoelectrode showed the photocurrent density of  $-70 \mu\text{A}/\text{cm}^2$  for reduction of water to  $\text{H}_2$ , whereas for the pristine g- $\text{C}_3\text{N}_4$  nanosheet photoelectrode showed  $-12 \mu\text{A}/\text{cm}^2$  at  $0.11 \text{ V}$  versus reversible hydrogen electrode (RHE). Photocurrent density is increased by  $\sim 6$  times after the introduction of ITO NCs as a co-catalyst with g- $\text{C}_3\text{N}_4$  nanosheets. The present PEC activity of ITO NCs is reasonably high for reduction of water compared to prior literature on carbon nitride based photoelectrocatalyst.

## Graphical Presentation



## 4.1 Introduction

The requirement of clean and renewable energy is essential for future demand. One of the efficient way to produce hydrogen fuel from sun light is through the photocatalytic water splitting.<sup>1</sup> In this regard, researchers have investigated numerous photocatalysts. Among them, the most notable were inorganic semiconductors such as CdS, Cu<sub>2</sub>O and BiVO<sub>4</sub>.<sup>2</sup> These metal based semiconductors showed good photocatalytic efficiency, but suffer from stability under light illumination. On the other hand, metal free semiconductors, namely graphene oxide,<sup>3</sup> conjugated ploymers<sup>4</sup> and porous carbon nitrides<sup>5-6</sup> emerged as alternative due to their suitable electronic band structure.<sup>7</sup> In this category, carbon nitride gained much interest due to longterm photostability, ease of synthesis, and environmentally benign in nature. However, the photocatalytic activity of carbon nitride is limited by its fast recombination rate and low mobility of photogenerated charge carriers.<sup>6</sup> In order to improve the photocatalytic efficiency of carbon nitride, new structural designs have been introduced. Such hybrid structure expedites the charge transfer kinetics and reduces the recombination rates of photo induced carriers.

In this regard, researchers have discovered different type of design via construction of heterojunction between graphitic carbon nitride (g-C<sub>3</sub>N<sub>4</sub>) and various co-catalysts. For example, noble metals (Pt, Pd and Au) and noble metal oxides (IrO<sub>2</sub> and RuO<sub>2</sub>) used as a co-catalyst by construction of heterojunction with g-C<sub>3</sub>N<sub>4</sub> for both water reduction and oxidation, respectively.<sup>8</sup> It is well known that these noble metal based materials are expensive and low earth abundant. To overcome these problem, various alternative semiconductor materials have been emerged to replace expensive noble metal based materials such as TiO<sub>2</sub>, BiVO<sub>4</sub> and CdS to enhance interfacial charge transfer processes.<sup>9</sup> However, poor charge transfer at co-catalyst and water interface suppresses the photoelectrocatalytic activity. Furthermore, recently, photoelctrocatalytic activity has been improved by introducing the 2D carbon based materials as a co-catalyst. Ying-Ying et al improved the hole transfer kinetics of g-C<sub>3</sub>N<sub>4</sub> after designing the heterojunction of g-C<sub>3</sub>N<sub>4</sub>/graphdiyne.<sup>10</sup> Che et al fabricated 2D/2D heterojunction of carbon ring (C<sub>ring</sub>) - g-C<sub>3</sub>N<sub>4</sub> nanosheet photocatalyst.<sup>11</sup> In the chapter - 3 we showed superior co-catalyst activity of TiN- N-doped few-layer graphene (TiN-NFG) forming 2D/2D heterojunction between TiN-NFG and g-C<sub>3</sub>N<sub>4</sub> nanosheet. Motivated by these results, we thought to explore co-catalytic activity of ITO NCs by forming heterojunction with g-C<sub>3</sub>N<sub>4</sub> nanosheet. The reason for selection is the ITO NCs have necessary free electron density, like TiN in chapter - 3, and can be prepared easily by

employing colloidal synthesis at ~220 °C. Interestingly, the free electron density can be easily monitored by observing the intense localized surface plasmon resonance (LSPR) in near infrared region. In this chapter, first we discuss the mechanistic insights for generation of free electrons in ITO NCs, and then nanocomposites of g-C<sub>3</sub>N<sub>4</sub>:ITO (2%) were used for photoelectrocatalytic (PEC) water splitting. However, there is possibility to further improve the PEC water splitting activity by introduction of plasmonic materials as co-catalyst such as ITO NCs due to their high electrical conductivity and metallic electrons.

## 4.2 Experimental Sections

### 4.2.1 Chemicals

Indium (III) acetylacetonate (sigma-aldrich, purity  $\geq$  99.9%), tin (IV) bis(acetylacetonate) dichloride (sigma-aldrich purity  $\geq$ 99.9%), oleylamine (Sigma-Aldrich, purity 70%), tetrachloroethylene (Sigma-Aldrich, anhydrous, purity  $\geq$  99%), methanol (AR, S D Fine-chem. Ltd), hexane (AR, S D Fine Chem. Ltd), toluene (Rankem, purity 99.5% ), urea (AR, 99.0 %, VETEC), distilled water, ethanol (99.9% AR, SDFCL), n-butanol (99.95%, Rankem), nafion (5 wt%, Aldrich), sodium sulphate (99.0%, Fisher Chemicals), triethanolamine (99.0%, Sigma Aldrich), F-doped SnO<sub>2</sub> (FTO) coated glass (~7 ohm/sq, Sigma-Aldrich). No further purification was carried out in any chemical prior to use.

### 4.2.2 Synthesis of Graphitic Carbon Nitride (g-C<sub>3</sub>N<sub>4</sub>) Nanosheets

g-C<sub>3</sub>N<sub>4</sub> was synthesized by pyrolysis method using urea as a precursor, following report of Liu et al after slight modification of.<sup>12</sup> Briefly, 0.17 mol (10 g) of urea was placed in 50 mL alumina boat and heated to 550 °C for 2 hours in a tube furnace under N<sub>2</sub> atmosphere with heating rate of 4 °C/min. A pale yellow colored powder was obtained after cooling the furnace to room temperature, and the sample was characterized in detail using various experimental techniques which was shown in chapter 3 of this thesis.

### 4.2.3 Synthesis of Sn-Doped In<sub>2</sub>O<sub>3</sub> (ITO) NCs

Colloidal Sn-doped In<sub>2</sub>O<sub>3</sub> NCs were synthesized following report.<sup>13</sup> To prepare 10% Sn-doped In<sub>2</sub>O<sub>3</sub> NCs, 0.24 mmol indium (III) acetylacetonate and 0.03 mmol tin (IV) bis(acetylacetonate) dichloride were mixed with 10 mL oleylamine in a 50 mL three-necked round bottom flask. First the reaction mixture was subjected to N<sub>2</sub> atmosphere and vacuum alternatively for 30 minutes at room temperature followed by degassing at high vacuum for

30 min at 100 °C. The temperature of the reaction mixture was gradually increased to 220 °C under N<sub>2</sub> gas atmosphere and kept undisturbed for 5 hours. The solution was cooled to room temperature and then adequate amount (~30 mL) of methanol was added as a non-solvent to precipitate NCs followed by centrifugation at 5000 rpm for 5 min. The obtained NCs were redispersed in toluene and were precipitated again using methanol, and the washing process repeated twice.

#### 4.2.4 Characterization

PXRD patterns of all samples were obtained using a Bruker D8 Advance X-ray diffractometer equipped with Cu K $\alpha$  radiation (1.54 Å). UV-vis-NIR absorption spectra were measured using SHIMADZU UV-3600 plus UV-VIS-NIR spectrophotometer. Steady-state PL data were recorded using FLS 980 (Edinburgh Instruments). Transmission electron microscopy (TEM) images were taken using JEOL-JEM 2200FS 200KeV. Field emission scanning electron microscopy (FESEM) images, energy dispersive X-ray analysis (EDAX) and elemental mapping data were obtained using a Zeiss Ultra Plus scanning electron microscope. Electrical resistivity measurements of ITO NC Pellets were obtained by using a Keithley Four-probe conductivity instrument (Model 6220/6221 Current Source and Model 2182A nanovoltmeter). Mott-Schottky plots of electrodes were measured in 0.5 M Na<sub>2</sub>SO<sub>4</sub> and 10 vol% tri-ethanolamine solution in dark at a frequency of 10 kHz using an AUTOLAB PGSTAT 30 using a three electrode system. Electrochemical impedance spectroscopy (EIS) experiments were performed using an AUTOLAB PGSTAT 30 from 100 kHz to 40 mHz.

#### 4.2.5 Preparation of g-C<sub>3</sub>N<sub>4</sub>:ITO nanocomposite photoelectrodes

Finely grinded powders of g-C<sub>3</sub>N<sub>4</sub> (100 mg) nanosheets and different weight percentages of ITO NCs (0%, 1%, 2% and 4%) were dispersed in 5 mL ethanol by ultra-sonication for about 2 hours. Ethanol was evaporated at an elevated temperature and the sample was thoroughly dried under vacuum. 100 mg of the powder was grinded (for around 1 hour) using mortar pestle. Then 600  $\mu$ L n-butanol was added drop-wise (30  $\mu$ L/min) to the powder and grinded continuously to make a paste. Also 60  $\mu$ L nafion was added during the addition of n-butanol. Nafion improves binding between the film and the FTO glass substrate. The obtained g-C<sub>3</sub>N<sub>4</sub>:ITO NCs nanocomposite paste is doctor bladed on cleaned FTO glass followed by annealing of the films at 250 °C for 2 hours under inert atmosphere. The area of the films was

maintained to 1 cm<sup>2</sup> for all the experiments. The thickness of the films was estimated to ~12 μm.

#### 4.2.6 Photoelectrochemical (PEC) Measurements

PEC measurements were carried out on AUTOLAB PGSTAT 30 using a three electrode system. Different photoelectrode materials coated on FTO glass with 1 cm<sup>2</sup> area served as working electrodes, platinum as counter electrode and Ag/AgCl as reference electrode. These electrodes are placed in 0.5 M Na<sub>2</sub>SO<sub>4</sub> and 10 vol% TEOA aqueous solution purged with N<sub>2</sub>. Simulated sunlight with illumination power of 100 mW/cm<sup>2</sup> from a 400 W xenon lamp (Solar Simulator, Newport) is used for illuminations.

### 4.3 Results and Discussion

#### 4.3.1 Mechanistic Insights about the Generation of Free Electrons in Colloidal Sn-Doped In<sub>2</sub>O<sub>3</sub> NCs

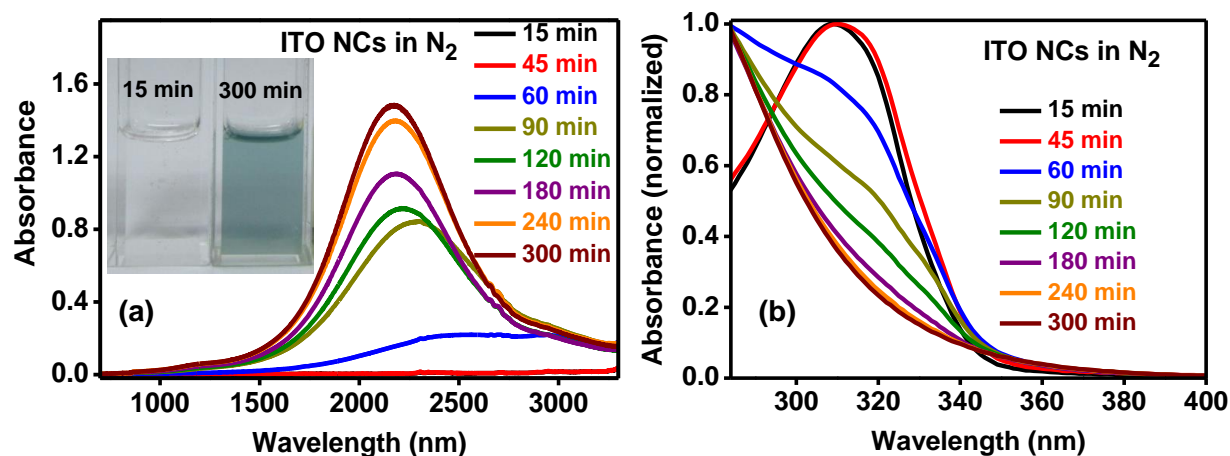
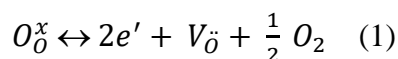


**Figure 4.1:** Variation of (a) LSPR band, and (b) excitonic transition with time of reaction for colloidal ITO NCs carried under N<sub>2</sub> atmosphere.

Synthesis details of ITO NCs have been given in the experimental section (section 4.2.3). To understand the mechanism of generation of free electron, thereby understanding the evolution of LSPR band, we have studied ITO NC at different stages of reaction. Figure 4.1a and b show the UV-visible-NIR absorption data of ITO NCs prepared under N<sub>2</sub> atmosphere at different reaction times. The absorption edge in the UV region (Figure 4.1b) corresponds to the optical gap of the semiconductor, and the NIR absorption (Figure 4.1a) is due to the LSPR band of free electrons. Clearly, the LSPR band is absent for reaction time up to 45 min. LSPR band appears at 60 min and then shifts towards shorter wavelength along with

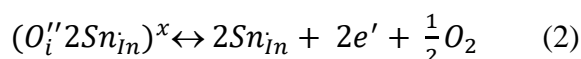
increasing absorbance as the reaction proceeds. Correspondingly, the tail of LSPR band absorbs red-light, imparting the complementary blue color to the reaction mixture after 60 min, and the color became more intense with increasing reaction time (inset of Figure 4.1a). According to the Drude model, the LSPR band is expected to shift towards shorter wavelength and become more intense (higher absorbance) with an increase in free electron density.<sup>14</sup> Therefore, it can be concluded that the free electrons starts appearing slowly during the course of reaction. The influence of this slow release of free electrons is also observed in the optical gap of NCs in the UV region (Figure 4.1b). As the reaction time increases, the sharp excitonic feature bleaches because the generated free electrons screen the Coulomb attraction between electron-hole pair.<sup>15-16</sup> Also, the generation of free electrons in the conduction band typically widens the optical gap of ITO NCs because of Burstein-Moss effect,<sup>14, 17</sup> and such a widening of optical gap is also observed (Figure 4.1b) with longer reaction time after 60 min.

What is the mechanism of this slow generation of free electrons in our NCs? In order to address this question, let us first discuss the mechanism of free electron generation in bulk Sn-doped In<sub>2</sub>O<sub>3</sub>. One oxygen vacancy can give rise to two electrons following equation 1.<sup>18</sup>



Where,  $O_O^x$  represents a neutral oxygen on an oxygen site;  $V_{\ddot{O}}$  represents a vacancy with charge of +2 on an oxygen site and  $e'$  represents an electron with charge -1. However, the amount of oxygen vacancies is typically low (< 0.5%). So far, colloidal synthesis of In<sub>2</sub>O<sub>3</sub> NCs has not lead to the formation of enough free electrons from oxygen vacancies, and therefore LSPR band has not been observed from In<sub>2</sub>O<sub>3</sub> NCs.

On the other hand, each Sn<sup>4+</sup> provides one free electron in the conduction band of bulk Sn-doped In<sub>2</sub>O<sub>3</sub> with doping level up to 5-10% following equation 2.<sup>19</sup>



Where  $Sn_{In}$  represent a positively charged Sn on an In site (basically substitution of In<sup>3+</sup> with Sn<sup>4+</sup> leads to 1+ charge in the crystal), and  $O_i''$  represent an interstitial oxygen with -2 charge. Typically, one interstitial oxygen is accompanied by two Sn<sup>4+</sup> ions substituting two In<sup>3+</sup> ions, maintaining the charge neutrality, which subsequently can get reduced following equation 2. At higher levels of Sn doping, the neutral  $(O_i'' 2Sn_{In})^x$  centers can undergo clustering

forming a more stable product which does not get reduced following equation 2, and therefore, decreases the effective free electron concentration.<sup>20</sup>

In our NCs, the slow generation of free electron can be because of multiple reasons such as (i) slow rate of formation of NCs, or (ii) even though the host NC is formed instantaneously, the rate of Sn doping can be slower, or (iii) slower reduction of active Sn dopant following equation 2.

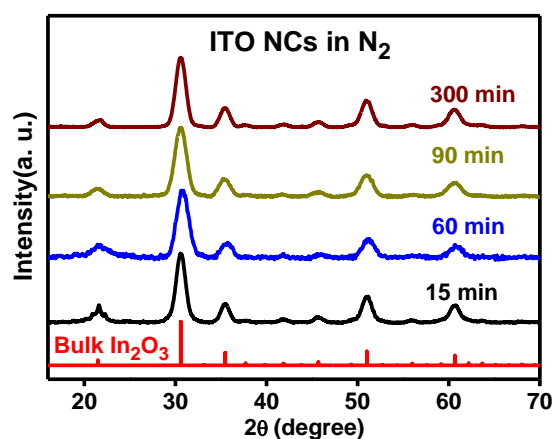


**Figure 4.2:** XRD patterns of ITO NCs isolated after different reaction times.

Let us discuss the first possibility, i.e., whether the slow formation rate of NCs is responsible for slow generation of free electron or not. Figure 4.2 shows similar XRD patterns for all NCs throughout the synthesis starting from 15 min to 300 min, which matches with the cubic bixbyite structure of  $\text{In}_2\text{O}_3$  (JCPDS no. 88-2160, space group  $Ia3$ ).

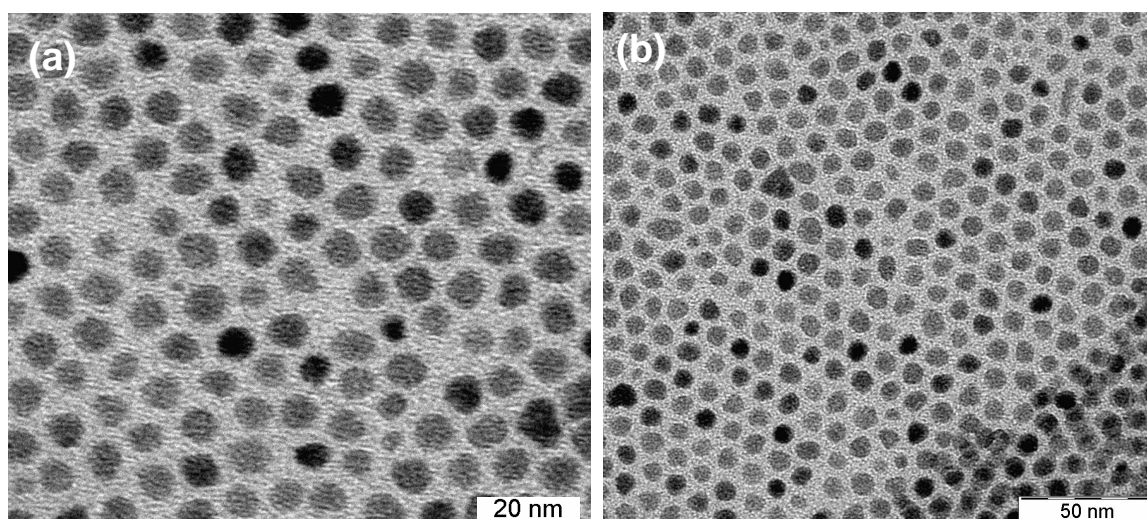


**Figure 4.3:** TEM image of (a) ITO NCs carried under  $\text{N}_2$  atmosphere isolated after 60 min, and (b) after 300 min.



TEM image in Figure 4.3a shows the average diameter of NCs is 6.5 nm after 60 min of reaction, and the size remains similar even after 300 min (Figure 4.3b). So, growth of host NCs is already over by 60 min of reaction and the release of free electrons after 60 minutes is not due to slow NC growth.

Now we verify the second possibility, i.e., whether slow incorporation of Sn in already formed NCs is responsible for slow generation of free electron or not. EDAX data exhibit a similar Sn content of 8.1 and 9.4 % for both samples obtained after 60 and 300 minutes of reactions. Similarly, ICP-OES (inductively coupled plasma-optical emission spectroscopy) shows 9.3 and 10.1 % Sn for samples obtained after 60 and 300 minutes of reactions. It is to be noted that such elemental analysis cannot distinguish between dopant ions on the surface of NCs and lattice substituted dopants at the core of NCs. However, Lounis et al.<sup>21</sup> recently demonstrated that the surface bound Sn dopants exhibit narrower LSPR spectrum compared to Sn doped into the core of  $\text{In}_2\text{O}_3$  NC lattice. Figure 4.1a does not show any broadening of LSPR peak with increasing reaction time, therefore suggesting that the diffusion of dopant ions from surface towards the core of NCs is not a plausible reason for the emergence of LSPR band with reaction time. Therefore, slower or inhomogeneous Sn incorporation is also not the cause of slow release of free electrons.

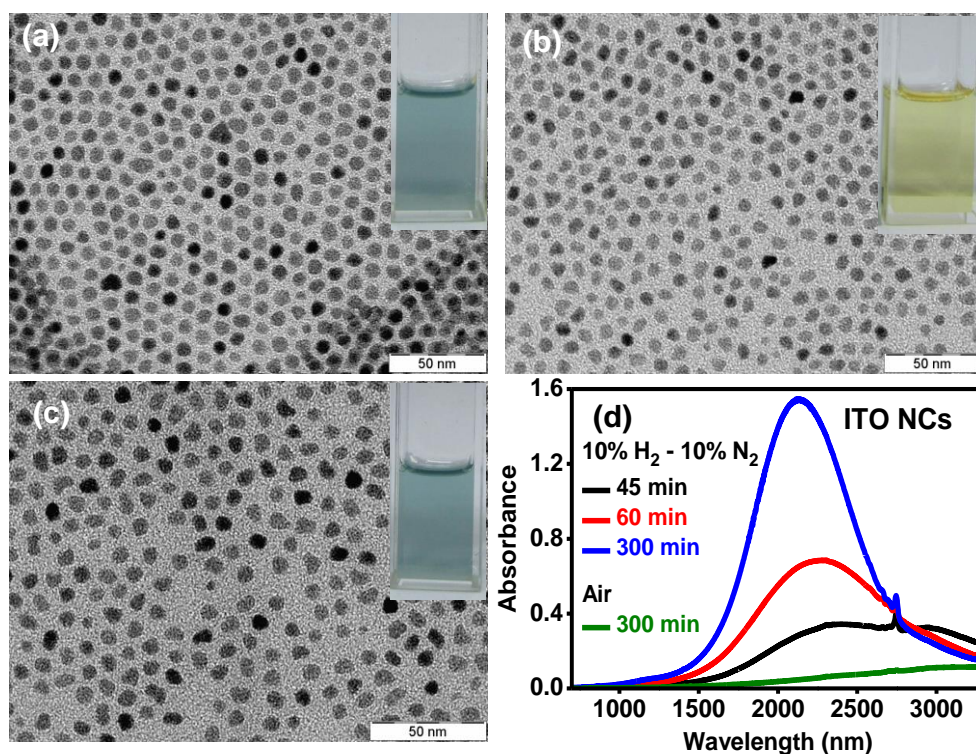


**Figure 4.4:** TEM images of ITO NCs after 300 min of reaction in different reaction environments. (a) Under  $\text{N}_2$  gas, (b) in air, and (c) under a gas mixture of 10%  $\text{H}_2$  and 90%  $\text{N}_2$ . Insets show the color of corresponding NC dispersions.

To verify the third possibility, i.e., slow reduction of active Sn dopant following equation 2, we carried out the colloidal synthesis with different oxygen partial pressure: in air, under N<sub>2</sub> gas, and under reducing (90% N<sub>2</sub> and 10% H<sub>2</sub>) gas. Such a change in reaction environment neither changes the NC size (TEM images in Figure 4.4a-c), nor the extent of Sn doping (~10%) obtained from EDAX and ICP-OES. Figure 4.3d shows that the LSPR band is almost absent for ITO NCs when the reaction is carried out in air. Consequently, the color of the NC prepared in air is also not blue (inset to Figure 4.4b). On the other hand, with reducing conditions (90% N<sub>2</sub> and 10% H<sub>2</sub>), LSPR band appears in about 45 min (Figure 4.4d) of reaction time, which is quicker compared to 60 min required to observe LSPR for reactions carried out under N<sub>2</sub> (Figure 4.4d). Evidently, a lower partial pressure of oxygen during the synthesis favors the reduction of active Sn dopant following equation 2. The slow release of free carriers during colloidal synthesis is because of the slow reduction process shown in equation 2. It is to be noted that such reduction in bulk Sn-doped In<sub>2</sub>O<sub>3</sub> also takes many hours at an elevated temperature.<sup>19</sup>

#### 4.3.2 Electrical Conductivity

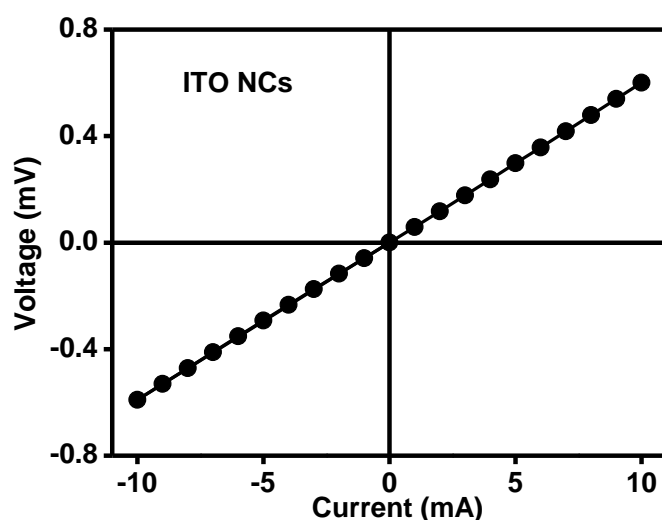


**Figure 4.5:** Voltage vs current plots for ITO NCs after making pellets. Symbols were experimental data, and line was just guide to eye.

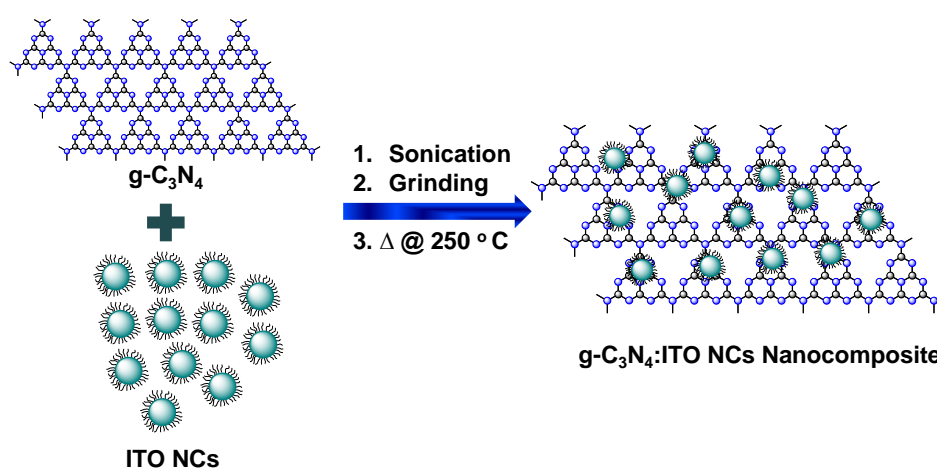
LSPR data show a reasonably high metallic free electron concentration in our ITO NCs, which is desired for PEC reduction of water. Same free electron will also give rise to electrical conductivity. To verify that, we measured electrical resistivity of the pellets of ITO NCs. Figure 4.5 shows four-probe electrical conductivity measurements on ~ 1 mm thick

pellets of ITO NCs. Linear voltage (V) vs current (I) plot was observed for ITO NCs. Interestingly, slope of the plot signify the resistance following the Ohm's law. In spite of having large contribution from grain boundaries of NCs, that hinder charge transport, the obtained conductivity value for ITO NCs was 35 S/cm.

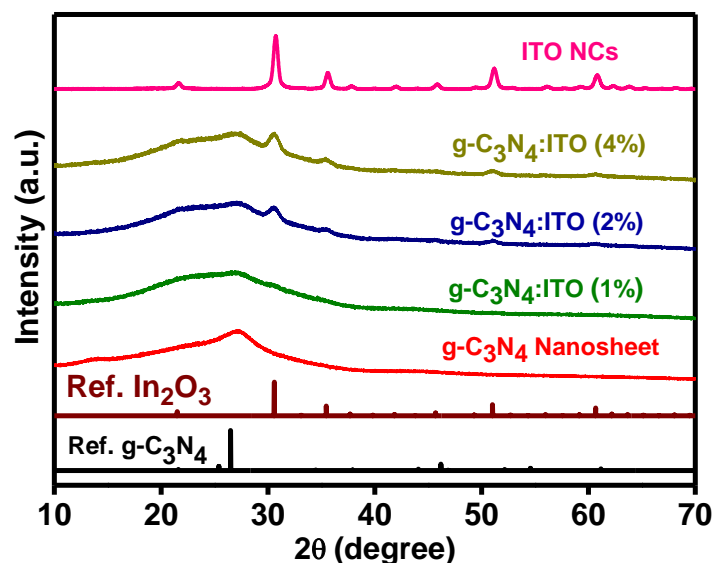
Owing to this high electrical conductivity ( $\sim 35$  S/cm) and metallic electrons of ITO NCs we got motivated to use ITO NCs as a co-catalyst with photocatalyst  $\text{g-C}_3\text{N}_4$  nanosheet (photo absorber) in PEC water splitting. The NC size of Sn-doped  $\text{In}_2\text{O}_3$  will facilitate formation of nano heterojunction with  $\text{g-C}_3\text{N}_4$  nanosheet.

### 4.3.3 Preparation of $\text{g-C}_3\text{N}_4$ :ITO Nanocomposite

$\text{g-C}_3\text{N}_4$  nanosheets were synthesized by pyrolysis method using urea as a precursor, following prior report.<sup>12</sup> Detailed characterization of  $\text{g-C}_3\text{N}_4$  nanosheets was given in the chapter 3 of this thesis. Nanocomposites of  $\text{g-C}_3\text{N}_4$ :ITO nanocomposite photoelectrocatalysts were fabricated by mixing different ratios of  $\text{g-C}_3\text{N}_4$  nanosheet and ITO NCs. After the preparation of uniform paste of  $\text{g-C}_3\text{N}_4$  nanosheet and ITO NCs, photoelectrocatalyst samples were doctor bladed on fluorine doped tin oxide (FTO) glass and then annealed at 250 °C for 2 hours. Details of fabrication method have been given in the experimental section (section 4.2.5). Figure 4.6 shows the schematic representation of the formation of  $\text{g-C}_3\text{N}_4$ :ITO nanocomposite.



**Figure 4.6:** The schematic illustration of the formation of  $\text{g-C}_3\text{N}_4$ :ITO nanocomposite.



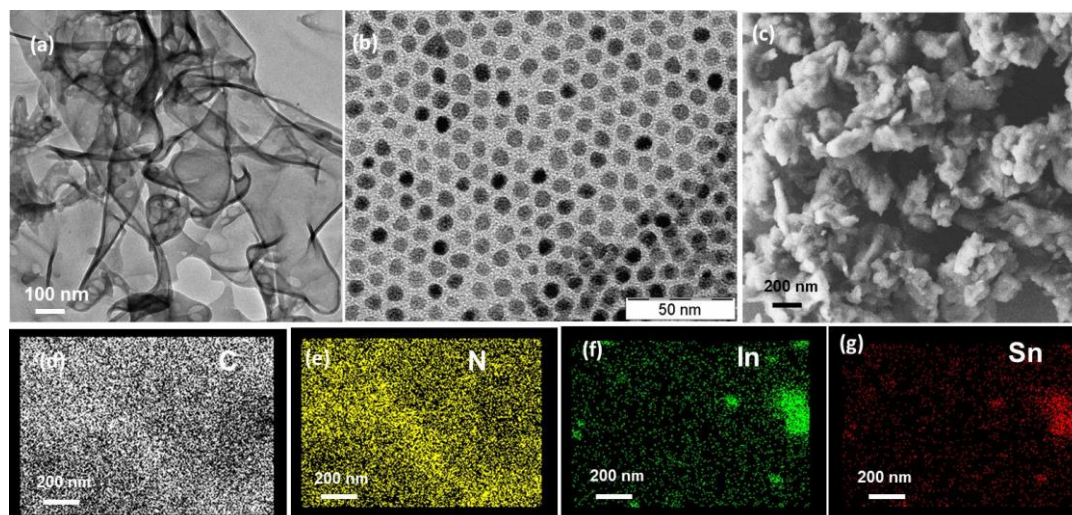
**Figure 4.7:** PXRD pattern of  $\text{g-C}_3\text{N}_4$  nanosheet, ITO NCs and  $\text{g-C}_3\text{N}_4$ :ITO nanocomposite with different loading amount (wt%) of ITO NCs in the composite. Also, reference patterns for bulk  $\text{g-C}_3\text{N}_4$ , and ITO are shown for comparison.

Figure 4.7 shows the PXRD patterns of  $\text{g-C}_3\text{N}_4$  nanosheet,  $\text{g-C}_3\text{N}_4$ :ITO nanocomposite photoelectrocatalysts with different ratio of ITO and ITO NCs. The diffraction peaks of ITO NCs in photoelectrocatalysts are of low intensity due to its low (0 to 4%) loading amount. These XRD results suggest the formation of  $\text{g-C}_3\text{N}_4$ :ITO nanocomposites, and no other impurity phase was observed. However, these XRD results do not confirm the interaction between ITO NCs and  $\text{g-C}_3\text{N}_4$  nanosheet in the nanocomposite. This issue will be discussed later in this chapter. Among all different ratios, the nanocomposites with 2 wt% ITO NCs exhibits best PEC performance. Therefore, this composition  $\text{g-C}_3\text{N}_4$ :ITO (2 wt%) of nanocomposites will be discussed in detail. Further, we discuss the efficiency of photoelectrocatalytic activity of  $\text{g-C}_3\text{N}_4$ :ITO (2%) nanocomposite and  $\text{g-C}_3\text{N}_4$  nanosheet in this chapter.

#### 4.3.4 Microscopic Analysis of $\text{g-C}_3\text{N}_4$ Nanosheet and $\text{g-C}_3\text{N}_4$ :ITO (2%) Nanocomposite

TEM image showed in Figure 4.8a displays the ultrathin 2D nanosheets of  $\text{g-C}_3\text{N}_4$  nanosheet which exhibit porous nature. Figure 4.8b shows TEM image of ITO NCs (co-catalyst) with average size  $\sim 6.5$  nm. FESEM image (Figures 4.8c) shows the  $\text{g-C}_3\text{N}_4$ :ITO (2%) nanocomposites, in which it is very difficult to observe ITO NCs due to small size ( $\sim 6.5$  nm).

The elemental mapping of  $g\text{-C}_3\text{N}_4\text{:ITO}$  (2%) nanocomposite (Figure 4.8d-f) shows the uniform distribution of elements (C, N, In and Sn) in the structure. Finding of such uniform distribution of ITO NCs and  $g\text{-C}_3\text{N}_4$  nanosheets in the nanocomposite is expected to be beneficial for efficient charge transfer.



**Figure 4.8:** TEM images of (a)  $g\text{-C}_3\text{N}_4$  nanosheet and (b) ITO NCs. FESEM image of (c)  $g\text{-C}_3\text{N}_4\text{:ITO}$  (2%) nanocomposite, and the corresponding elemental mapping from EDAX (d) carbon, (e) nitrogen, (f) indium, and (g) tin.

#### 4.3.5 Properties of $g\text{-C}_3\text{N}_4$ Nanosheet and $g\text{-C}_3\text{N}_4\text{:ITO}$ (2%) Nanocomposite

UV-vis absorption spectrum of  $g\text{-C}_3\text{N}_4$  nanosheet is shown in Figure 4.9a. The band gap of  $g\text{-C}_3\text{N}_4$  nanosheet calculated to be 2.82 eV (439 nm) using tauc plot, and is shown in Figure 4.9b. This band gap suggests that  $g\text{-C}_3\text{N}_4$  nanosheet capable of absorb small amount of solar light. The obtained band gap is in agreement with prior report.<sup>22</sup>

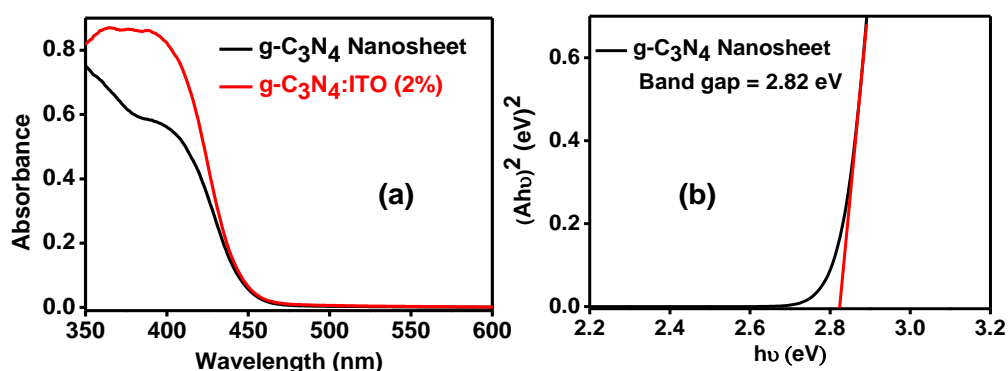


**Figure 4.9:** (a) UV-visible absorption spectra of  $g\text{-C}_3\text{N}_4$  nanosheet and  $g\text{-C}_3\text{N}_4\text{:ITO}$  (2%) nanocomposite obtained from diffuse reflectance spectrum by using Kubelka-Munk equation.<sup>23</sup> (b) Tauc<sup>24</sup> plot obtained from the absorption spectrum by considering direct bandgap.



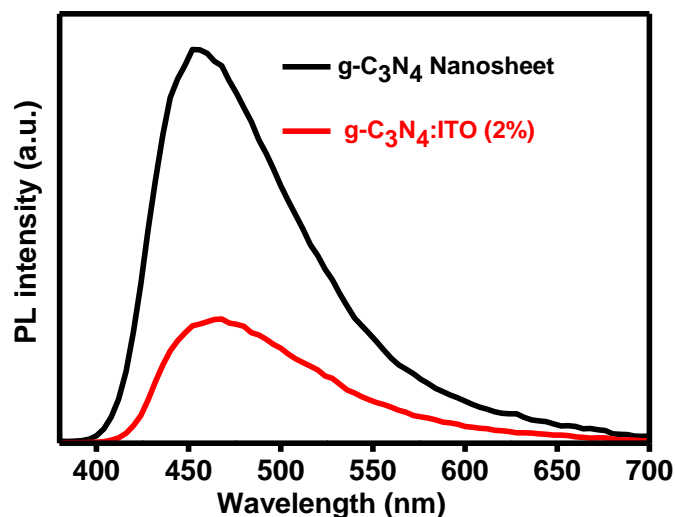


**Figure 4.10:** Comparison of PL spectra of  $\text{g-C}_3\text{N}_4$  nanosheet and  $\text{g-C}_3\text{N}_4:\text{ITO}$  (2%) nanocomposites.

In the case of nanocomposite, to understand the nature of electronic interaction between  $\text{g-C}_3\text{N}_4$  nanosheet and ITO NCs components, we employed the techniques of photoluminescence (PL) spectroscopy, Mott-Schottky measurements and electrochemical impedance spectroscopy (EIS). These measurements were done on the films of respective samples. Figure 4.10 shows both  $\text{g-C}_3\text{N}_4$  nanosheet and  $\text{g-C}_3\text{N}_4:\text{ITO}$  (2%) nanocomposite exhibit PL peaks at 460 nm (2.7 eV), which is the characteristic of band to band transition of  $\text{g-C}_3\text{N}_4$  nanosheet.<sup>25-26</sup> But the PL intensity got significantly decreased for the nanocomposite as compared to  $\text{g-C}_3\text{N}_4$  nanosheet. The decrease in PL intensity suggested the possibility of photo-excited electron transfer from  $\text{g-C}_3\text{N}_4$  nanosheet to ITO NCs this electron transfer can be one among many possibilities suppress the PL intensity. Additional experiments required to verify this possibility.

To analyse the possibility of charge transfer process from  $\text{g-C}_3\text{N}_4$  nanosheet to ITO NCs, we estimated the flat band potential ( $V_{\text{fb}}$ ) values corresponding to the conduction band minimum, by employing electrochemical Mott-Schottky experiments (Figure 4.11a). The intercept on x-axis of Figure 4.11a determines  $V_{\text{fb}}$  values for  $\text{g-C}_3\text{N}_4$  nanosheet and ITO NCs as -1.46 V and -1.26 V vs Ag/AgCl (-0.85 V and -0.65 V vs RHE) at pH = 7, respectively, similar to prior reports.<sup>27-28</sup> The observed band gap of  $\text{g-C}_3\text{N}_4$  nanosheet from UV-visible absorption spectrum (Figure 4.9) was 2.82 eV. Thus, from the Mott-Schottky and absorption plots, the energy for valance band maximum of  $\text{g-C}_3\text{N}_4$  nanosheet is found to be 1.36 V vs Ag/AgCl (1.97 V vs RHE) at pH = 7. Figure 4.11b summarizes the obtained band edge energies, and also compares with potentials for reduction and oxidation of water. These energy levels show

that electron transfer from g-C<sub>3</sub>N<sub>4</sub> nanosheet to ITO NCs is thermodynamically favourable. Such electron transfer can explain the decrease of PL intensity in the g-C<sub>3</sub>N<sub>4</sub>:ITO (2%) nanocomposite, discussed earlier. g-C<sub>3</sub>N<sub>4</sub> nanosheet with band gap 2.82 eV in the composite primarily absorbs solar light, creating electron hole - pair in g-C<sub>3</sub>N<sub>4</sub> nanosheet. As consequence of electron transfer from g-C<sub>3</sub>N<sub>4</sub> nanosheet to ITO NCs in nanocomposite, the recombination of electron - hole pair suppressed, decreases the PL efficiency. If this electron transfer is responsible for suppression of PL efficiency, then it should also enhances the PEC activity of the nanocomposite compared to pristine g-C<sub>3</sub>N<sub>4</sub> nanosheet.

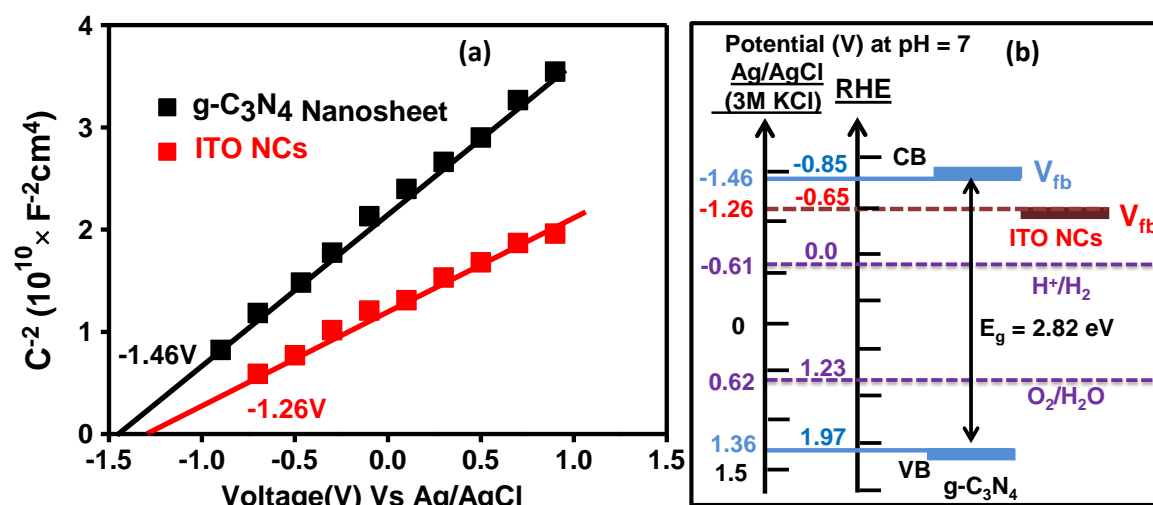


**Figure 4.11:** (a) Mott-Schottky plots, and (b) band alignment structure of g-C<sub>3</sub>N<sub>4</sub> nanosheet and ITO NCs.

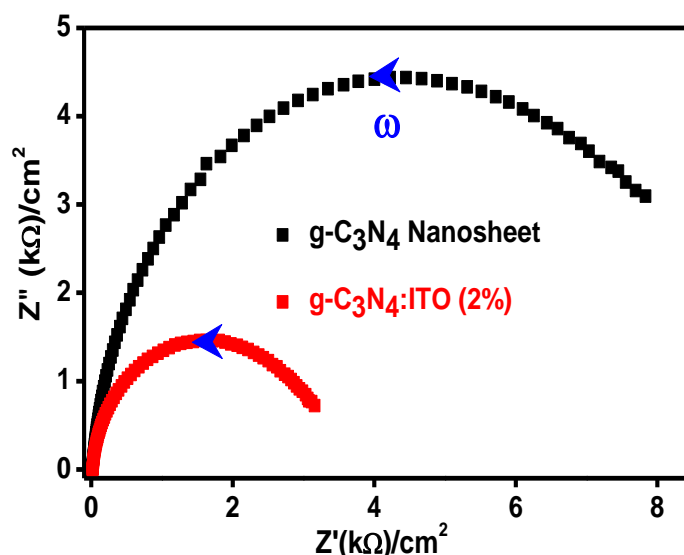


**Figure 4.12:** Nyquist plots for g-C<sub>3</sub>N<sub>4</sub> nanosheet and g-C<sub>3</sub>N<sub>4</sub>:ITO (2%) nanocomposite in frequency ( $\omega$ ) range of 100 kHz to 40 mHz.

The efficiency of PEC process will also depend on charge transfer resistance ( $R_{ct}$ ) at electrode/electrolyte interface. We measured EIS to compare  $R_{ct}$  of both pristine  $\text{g-C}_3\text{N}_4$  nanosheet and  $\text{g-C}_3\text{N}_4\text{:ITO}$  (2%) nanocomposite electrodes in 40 mL of aqueous electrolyte system containing 0.5 M  $\text{Na}_2\text{SO}_4$  and 10 vol.% triethanolamine (TEOA). Nyquist plots given in Figure 4.12 exhibit semi-circle arcs for both samples.  $R_{ct}$  value for  $\text{g-C}_3\text{N}_4\text{:ITO}$  (2%) nanocomposite is 3180  $\text{ohm/cm}^2$ , which is  $\sim 2.4$  times lower than that of  $\text{g-C}_3\text{N}_4$  nanosheet electrodes (7800  $\text{ohm/cm}^2$ ). These results suggest that the co-catalyst (ITO NCs) reduces  $R_{ct}$  at electrode/electrolyte interface, in addition to the previously discussed electron-hole separation from photo-excited  $\text{g-C}_3\text{N}_4$  nanosheet which is due to probably high electrical conductivity (35 S/cm) of co-catalyst (ITO NCs).

The above results encouraged us to examine the PEC water splitting activity of  $\text{g-C}_3\text{N}_4\text{:ITO}$  (2%) nanocomposite compared to that of  $\text{g-C}_3\text{N}_4$  nanosheet. A three-electrode system with Ag/AgCl reference electrode, Pt counter electrode, and the photoelectrocatalyst samples coated on FTO glass as working photoelectrode was used in 40 mL aqueous electrolyte solution containing 0.5 M  $\text{Na}_2\text{SO}_4$  and 10 vol.% TEOA. The photoelectrode was illuminated with a solar simulator with a power density of 100  $\text{mW/cm}^2$  under 1sun.

#### 4.3.6 Photoelectrochemical Activity of $\text{g-C}_3\text{N}_4\text{:ITO}$ (2%) Nanocomposite

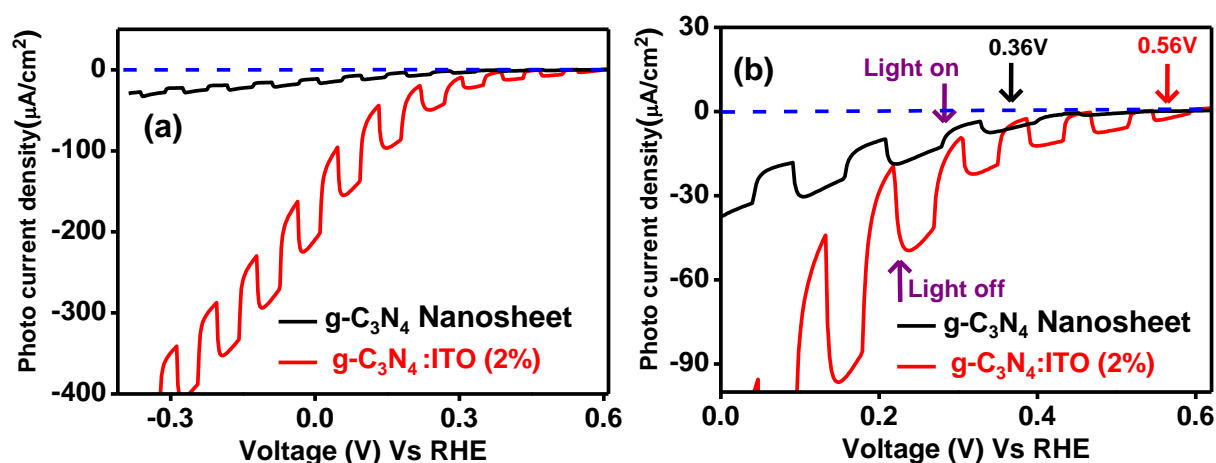


**Figure 4.13:** (a) Linear sweep voltammetry (LSV) curves for  $\text{g-C}_3\text{N}_4$  nanosheet and  $\text{g-C}_3\text{N}_4\text{:ITO}$  (2%) nanocomposite photoelectrodes. (b) Magnified view of the same LSV data indicating onset potential for reduction of water to  $\text{H}_2$ .

Linear sweep voltammetry (LSV) curves under on-off illumination for  $\text{g-C}_3\text{N}_4$  nanosheet and  $\text{g-C}_3\text{N}_4\text{:ITO}$  (2%) nanocomposites are given in Figure 4.13a. The photocurrent density is enhanced for the nanocomposite compared to pristine  $\text{g-C}_3\text{N}_4$  nanosheet. We measured the



photocurrent density of the nanocomposites with different loading of ITO NCs. Among these, 2 wt% loading shows the highest photocurrent density. Therefore, g-C<sub>3</sub>N<sub>4</sub>:ITO (2%) nanocomposite with 2 wt% loading of ITO NCs was studied in detail for the PEC activity. LSV plots given in Figure 4.13b show that the pristine g-C<sub>3</sub>N<sub>4</sub> has an onset potential at 0.36 V versus RHE for the reduction of protons whereas the g-C<sub>3</sub>N<sub>4</sub>:ITO (2%) nanocomposite exhibits much more positive onset potential at 0.56 V versus RHE. This positive shift in the onset potential indicates improved catalytic reductive nature of g-C<sub>3</sub>N<sub>4</sub> nanosheet after coupling with ITO NCs in the nanocomposite.

Transient photocurrents versus time plots were obtained to evaluate the PEC activity with repeated on/off illumination cycles, as presented in Figure 4.14a. Even at 0.56 V versus RHE, the g-C<sub>3</sub>N<sub>4</sub>:ITO (2%) nanocomposite photoelectrode demonstrated enhanced PEC performance as compared to pristine g-C<sub>3</sub>N<sub>4</sub> nanosheet. Interestingly, at 0.56 V versus RHE bias, the g-C<sub>3</sub>N<sub>4</sub>:ITO (2%) nanocomposite photoelectrode shows a cathodic nature with current density of -6  $\mu\text{A}/\text{cm}^2$ , whereas pristine g-C<sub>3</sub>N<sub>4</sub> nanosheets shows an anodic nature (0.2  $\mu\text{A}/\text{cm}^2$ ). This is due to the fact that onset potential in g-C<sub>3</sub>N<sub>4</sub>:ITO (2%) nanocomposite photoelectrode has shifted to 0.56 V versus RHE as compared to 0.36 V versus RHE for g-C<sub>3</sub>N<sub>4</sub> nanosheet, as shown in Figure 4.14a. Therefore, the chronoamperometric response and LSV data are in good agreement with each other.

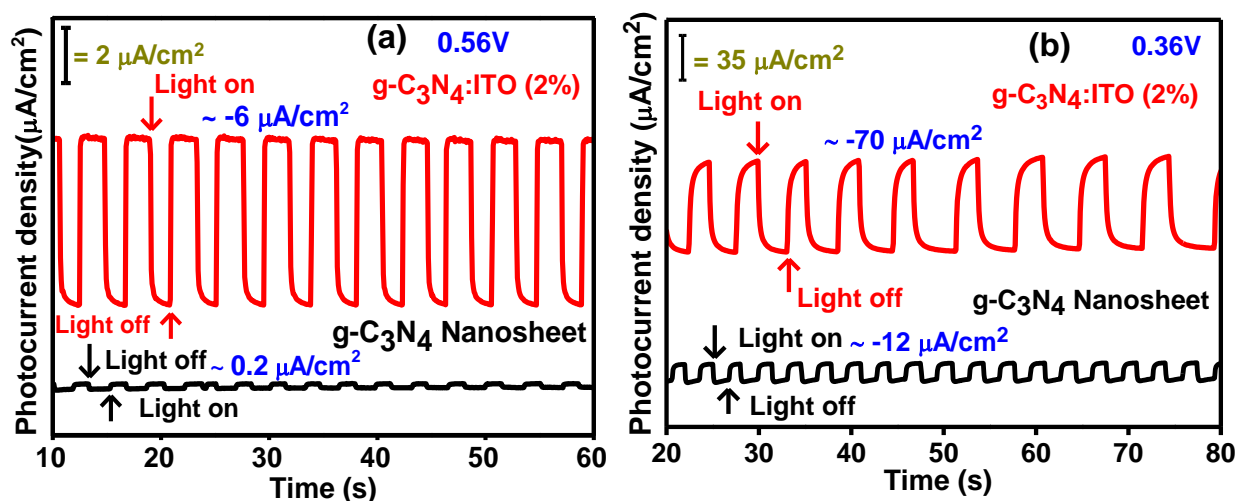


**Figure 4.14:** Transient photocurrent density versus time plots at (a) 0.56 V, and (d) 0.11 V versus RHE of g-C<sub>3</sub>N<sub>4</sub> nanosheet and -C<sub>3</sub>N<sub>4</sub>:ITO (2%) nanocomposite photoelectrodes.

In Figure 4.14b, we compare the PEC activity of g-C<sub>3</sub>N<sub>4</sub>:ITO (2%) nanocomposite and g-C<sub>3</sub>N<sub>4</sub> nanosheet at 0.11 V versus RHE. As a photocathode, g-C<sub>3</sub>N<sub>4</sub>: ITO (2%) nanocomposite

displays the photocurrent density of  $-70 \mu\text{A}/\text{cm}^2$  at 0.11 V versus RHE, which is  $\sim 6$  times higher than that of pristine g-C<sub>3</sub>N<sub>4</sub> nanosheet ( $-12 \mu\text{A}/\text{cm}^2$ ). It is not easy to quantitatively compare our results with prior reports because of some differences in the experimental conditions used in different reports. Table 4.1 compares our results with a list of prior reported carbon nitride based photoelectrocatalysts along with experimental condition. The  $\sim 6$  times enhancement in PEC activity of g-C<sub>3</sub>N<sub>4</sub> nanosheet by using our ITO NCs co-catalyst is a reasonable value in comparison with prior literature of carbon nitride based photoelectrocatalysts. But this  $\sim 6$  times enhancement by ITO NCs co-catalyst is lower than  $\sim 16$  times enhancement by TiN - N-doped graphene co-catalyst discussed in chapter 3.

**Table 4.1:** Comparison of photoelectrocatalytic performance of g-C<sub>3</sub>N<sub>4</sub>:ITO (2%) nanocomposite photoelectrode with prior reported carbon nitride based photoelectrocatalysts.

Photoelectrocatalyst	Photocurrent density ( $\mu\text{A}/\text{cm}^2$ ) Water reduction	Source (Light density)	Increase by	Electrolyte	Ref.
g-C <sub>3</sub> N <sub>4</sub> :ITO NCs	$\sim -70 \mu\text{A}/\text{cm}^2$ 0.11 V vs RHE	400 W Xe lamp (100 mW/cm <sup>2</sup> )	6	0.5M Na <sub>2</sub> SO <sub>4</sub> 10% TEOA	Present work
g-C <sub>3</sub> N <sub>4</sub> : TiN-NFG	$\sim -196 \mu\text{A}/\text{cm}^2$ 0.11 V vs RHE	400 W Xe lamp (100 mW/cm <sup>2</sup> )	16	0.5M Na <sub>2</sub> SO <sub>4</sub> 10% TEOA	Chapter 3
g-C <sub>3</sub> N <sub>4</sub> / Graphdiyne (GDY)	$\sim -98 \mu\text{A}/\text{cm}^2$ 0 V vs NHE	300 W Xe lamp (100 mW/cm <sup>2</sup> )	3	0.1M Na <sub>2</sub> SO <sub>4</sub>	<sup>29</sup>
Carbon ring – C <sub>3</sub> N <sub>4</sub>	$\sim -22 \mu\text{A}/\text{cm}^2$ -0.4 V vs Ag/AgCl	300 W Xe lamp	6	0.5M Na <sub>2</sub> SO <sub>4</sub>	<sup>11</sup>
<sup>a</sup> CNNS/NRGO/MoS <sub>2</sub>	---	150 W Xe lamp (100 mW/cm <sup>2</sup> )	3	0.01 M Na <sub>2</sub> SO <sub>4</sub>	<sup>30</sup>
13.3% MoS <sub>2</sub> /g-C <sub>3</sub> N <sub>4</sub>	$-50 \mu\text{A}/\text{cm}^2$ 1.0 V vs RHE	300 W Xe lamp ( $\lambda > 420 \text{ nm}$ )	10	0.5 M H <sub>2</sub> SO <sub>4</sub>	<sup>31</sup>

a: TiN - N-doped graphene

b: CNNS/NRGO/MoS<sub>2</sub> = Carbon nitride nanosheets/N-doped reduced graphene oxide/MoS<sub>2</sub>

## 4.4 Conclusions

ITO NCs were prepared showing LSPR band in the NIR region, suggesting metallic free electrons in ITO NCs. Mechanistic origin of generation of free electron in ITO NCs during our synthesis was studied. We find that equation 2 is critical for generation of free electron, and reaction conditions that facilitate the reaction of  $(O_i''2Sn_{in})^x$  complex generates free electron. These free electrons can also promote electrical conductivity required for co-catalytic application in PEC reduction of water. We have introduced ITO NCs as co-catalyst with g-C<sub>3</sub>N<sub>4</sub> nanosheets for the evaluation of photoelectrocatalytic reduction of water. The ITO NCs co-catalyst suppressed the PL intensity of g-C<sub>3</sub>N<sub>4</sub> nanosheets and also reduced the R<sub>ct</sub> at electrode/electrolyte interface. As a result, the enhancement in the PEC performance is observed for the g-C<sub>3</sub>N<sub>4</sub>:ITO (2%) nanocomposite. The nanocomposite shows ~6 times enhancement in the PEC activity of g-C<sub>3</sub>N<sub>4</sub> nanosheet at 0.11 V vs RHE under simulated solar light illumination. The obtained photocurrent densities are reasonable numbers as compared to other C<sub>3</sub>N<sub>4</sub> nanosheet based photoelectrocatalysts. Further modification in design of photoelectrocatalyst is necessary to improve the efficiency of PEC reduction of water.

## References

1. Zou, X.; Zhang, Y. Noble Metal-Free Hydrogen Evolution Catalysts for Water Splitting. *Chem. Soc. Rev.* **2015**, *44*, 5148-5180.
2. Osterloh, F. E. Inorganic Nanostructures for Photoelectrochemical and Photocatalytic Water Splitting. *Chem. Soc. Rev.* **2013**, *42*, 2294-2320.
3. Yeh, T. F.; Syu, J. M.; Cheng, C.; Chang, T. H.; Teng, H. Graphite Oxide as a Photocatalyst for Hydrogen Production from Water. *Adv. Funct. Mater.* **2010**, *20*, 2255-2262.
4. Wang, L.; Wan, Y.; Ding, Y.; Wu, S.; Zhang, Y.; Zhang, X.; Zhang, G.; Xiong, Y.; Wu, X.; Yang, J.; Xu, H. Conjugated Microporous Polymer Nanosheets for Overall Water Splitting Using Visible Light. *Adv. Mater.* **2017**, *29*, 1702428.
5. Wang, X.; Maeda, K.; Chen, X.; Takanabe, K.; Domen, K.; Hou, Y.; Fu, X.; Antonietti, M. Polymer Semiconductors for Artificial Photosynthesis: Hydrogen Evolution by Mesoporous Graphitic Carbon Nitride with Visible Light. *J. Am. Chem. Soc.* **2009**, *131*, 1680-1681.

6. Wang, J.; Zhang, C.; Shen, Y.; Zhou, Z.; Yu, J.; Li, Y.; Wei, W.; Liu, S.; Zhang, Y. Environment-Friendly Preparation of Porous Graphite-Phase Polymeric Carbon Nitride Using Calcium Carbonate as Templates, and Enhanced Photoelectrochemical Activity. *J. Mater. Chem. A* **2015**, *3*, 5126-5131.
7. Guo, Y.; Li, J.; Yuan, Y.; Li, L.; Zhang, M.; Zhou, C.; Lin, Z. A Rapid Microwave-Assisted Thermolysis Route to Highly Crystalline Carbon Nitrides for Efficient Hydrogen Generation. *Angew. Chem. Int. Ed.* **2016**, *55*, 14693-14697.
8. Wen, J.; Xie, J.; Chen, X.; Li, X. A Review on g-C<sub>3</sub>N<sub>4</sub>-Based Photocatalysts. *Appl. Surf. Sci.* **2017**, *391*, 72-123.
9. Ong, W. J.; Tan, L. L.; Ng, Y. H.; Yong, S. T.; Chai, S. P. Graphitic Carbon Nitride (g-C<sub>3</sub>N<sub>4</sub>)-Based Photocatalysts for Artificial Photosynthesis and Environmental Remediation: Are We a Step Closer To Achieving Sustainability? *Chem. Rev.* **2016**, *116*, 7159-7329.
10. Ying-Ying, H.; Xiu-Li, L.; Shang-Feng, T.; Xue-Peng, Y.; Zhen-Wei, W.; Tong-Bu, L. Metal-Free 2D/2D Heterojunction of Graphitic Carbon Nitride/Graphdiyne for Improving the Hole Mobility of Graphitic Carbon Nitride. *Adv. Energy Mater.* **2018**, *8*, 1702992.
11. Che, W.; Cheng, W.; Yao, T.; Tang, F.; Liu, W.; Su, H.; Huang, Y.; Liu, Q.; Liu, J.; Hu, F.; Pan, Z.; Sun, Z.; Wei, S. Fast Photoelectron Transfer in (Cring) - C<sub>3</sub>N<sub>4</sub> Plane Heterostructural Nanosheets for Overall Water Splitting. *J. Am. Chem. Soc.* **2017**, *139*, 3021-3026.
12. Liu, J.; Zhang, T.; Wang, Z.; Dawson, G.; Chen, W. Simple Pyrolysis of Urea into Graphitic Carbon Nitride with Recyclable Adsorption and Photocatalytic Activity. *J. Mater. Chem.* **2011**, *21*, 14398-14401.
13. Tandon, B.; Shanker, G. S.; Nag, A. Multifunctional Sn- and Fe-Codoped In<sub>2</sub>O<sub>3</sub> Colloidal Nanocrystals: Plasmonics and Magnetism. *J. Phys. Chem. Lett.* **2014**, *5*, 2306-2311.
14. Wang, T.; Radovanovic, P. V. Free Electron Concentration in Colloidal Indium Tin Oxide Nanocrystals Determined by Their Size and Structure. *J. Phys. Chem. C* **2011**, *115*, 406-413.
15. Shim, M.; Guyot-Sionnest, P. Organic-capped ZnO nanocrystals: Synthesis and n-Type Character. *J. Am. Chem. Soc.* **2001**, *123*, 11651-11654.

16. Faucheaux, J. A.; Jain, K. Plasmons in Photocharged ZnO Nanocrystals Revealing the Nature of Charge Dynamics. *J. Phys. Chem. Lett.* **2013**, *4*, 3024-3030.
17. Gilstrap, R. A.; Capozzi, C. J.; Carson, C. G.; Gerhardt, R. A.; Summers, C. J. Synthesis of a Non-agglomerated Indium Tin Oxide Nanoparticle Dispersion. *Adv. Mater.* **2008**, *20*, 4163.
18. Gonzalez, G. B. Investigating the Defect Structures in Transparent Conducting Oxides Using X-ray and Neutron Scattering Techniques. *Materials* **2012**, *5*, 818-850.
19. Frank, G.; Kostlin, H. Electrical-Properties and Defect Model of Tin-Doped Indium Oxide Layers. *Appl. Phys. A. Mater. Sci. Process.* **1982**, *27*, 197-206.
20. Warschkow, O.; Ellis, D. E.; Gonzalez, G. B.; Mason, T. O. Defect Cluster Aggregation and Nonreducibility in Tin-Doped Indium Oxide. *J. Am. Ceram. Soc.* **2003**, *86*, 1707-1711.
21. Lounis, S. D.; Runnerstrom, E. L.; Bergerud, A.; Nordlund, D.; Milliron, D. J. Influence of Dopant Distribution on the Plasmonic Properties of Indium Tin Oxide Nanocrystals. *J. Am. Chem. Soc.* **2014**, *136*, 7110-7116.
22. Yang, S.; Gong, Y.; Zhang, J.; Zhan, L.; Ma, L.; Fang, Z.; Vajtai, R.; Wang, X.; Ajayan, P. M. Exfoliated Graphitic Carbon Nitride Nanosheets as Efficient Catalysts for Hydrogen Evolution Under Visible Light. *Adv. Mater.* **2013**, *25*, 2452-2456.
23. Kubelka, P.; Munk, F. *Z. Tech. Phys.* **1931**, *12*, 593-601.
24. Tauc, J.; Grigorovici, R.; Vancu, A. Optical Properties and Electronic Structure of Amorphous Germanium. *Vancu, Phys. Status Solidi.* **1966**, *15*, 627- 637.
25. Min, Y.; Qi, X. F.; Xu, Q.; Chen, Y. Enhanced Reactive Oxygen Species on a Phosphate Modified C<sub>3</sub>N<sub>4</sub>/Graphene Photocatalyst for Pollutant Degradation. *CrystEngComm* **2014**, *16*, 1287-1295.
26. Tong, J.; Zhang, L.; Li, F.; Li, M.; Cao, S. An Efficient Top-Down Approach for the Fabrication of Large-Aspect-Ratio g-C<sub>3</sub>N<sub>4</sub> Nanosheets with Enhanced Photocatalytic Activities. *Phys. Chem. Chem. Phys.* **2015**, *17*, 23532-23537.
27. Vilela, F.; Zhang, K.; Antonietti, M. Conjugated Porous Polymers for Energy Applications. *Energy Environ. Sci.* **2012**, *5*, 7819-7832.
28. Cui, Y.; Ding, Z.; Liu, P.; Antonietti, M.; Fu, X.; Wang, X. Metal-Free Activation of H<sub>2</sub>O<sub>2</sub> by g-C<sub>3</sub>N<sub>4</sub> under Visible Light Irradiation for the Degradation of Organic Pollutants. *Phys. Chem. Chem. Phys.* **2012**, *14*, 1455-1462.

29. Ying-Ying, H.; Xiu-Li, L.; Shang-Feng, T.; Xue-Peng, Y.; Zhen-Wei, W.; Tong-Bu, L. Metal-Free 2D/2D Heterojunction of Graphitic Carbon Nitride/Graphdiyne for Improving the Hole Mobility of Graphitic Carbon Nitride. *Adv. Energy Mater.* **2018**, *8*, 1702992.
30. Yang, H.; Zhenhai, W.; Shumao, C.; Xiaoru, G.; Junhong, C. Constructing 2D Porous Graphitic C<sub>3</sub>N<sub>4</sub> Nanosheets/Nitrogen-Doped Graphene/Layered MoS<sub>2</sub> Ternary Nanojunction with Enhanced Photoelectrochemical Activity. *Adv. Mater.* **2013**, *25*, 6291-6297.
31. Hui, B.; Yujin, J.; Junqing, Y.; Ping, L.; Ling, L.; Youyong, L.; Shengzhong, L. In Situ Synthesis of Few-Layered g-C<sub>3</sub>N<sub>4</sub> with Vertically Aligned MoS<sub>2</sub> Loading for Boosting Solar-to-Hydrogen Generation. *Small* **2018**, *14*, 1703003.



## Chapter 5

# Electronic Grade and Flexible Semiconductor Film Employing Oriented Attachment of Colloidal Ligand- Free PbS and PbSe Nanocrystals at Room Temperature

---

The following paper has been published based on the work documented in this chapter.

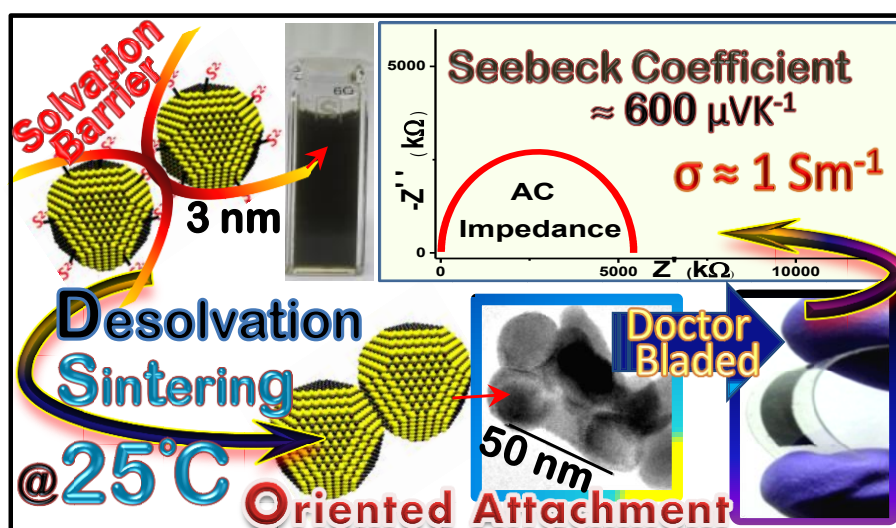
Shanker, G. S.; Swarnkar, A.; Chatterjee, A.; Chakraborty, S.; Phukan, M.; Parveen, N.; Biswas, K.; Nag, A. Electronic Grade and Flexible Semiconductor Film Employing Oriented Attachment of Colloidal Ligand-Free PbS and PbSe Nanocrystals at Room Temperature. *Nanoscale* **2015**, *7*, 9204-9214. This chapter is reproduced from our above mentioned article already published in *Nanoscale* after acknowledging Royal Society of Chemistry.



## Summary

Electronic grade semiconductor films have been achieved via sintering of solution processed PbS and PbSe nanocrystals at room temperature. Prior attempts to achieve similar films required sintering of nanocrystals at higher temperature ( $>350\text{ }^{\circ}\text{C}$ ), which inhibits processing of such films on flexible polymer substrate, and also expensive. We reduced the sintering temperature by employing two important strategies: (i) use of ligand-free nanocrystals, and (ii) oriented attachment of nanocrystals. Colloidal ligand-free PbS and PbSe nanocrystals were synthesized at  $70\text{ }^{\circ}\text{C}$  with high yield ( $\sim 70\%$ ). However, these nanocrystals start to agglomerate with time in formamide solvent and upon removal of the solvation energy, nanocrystals undergo oriented attachment forming larger elongated crystals. PbS and PbSe nanocrystal films made on both glass and flexible substrate at room temperature, exhibit Ohmic behavior with optimum DC conductivity  $0.03\text{ S/m}$  and  $0.08\text{ S/m}$  respectively. Mild annealing of the films at  $150\text{ }^{\circ}\text{C}$  increases the conductivity values to  $1.1\text{ S/m}$  and  $137\text{ S/m}$  for PbS and PbSe nanocrystal films, respectively. AC impedance was measured to distinguish the contributions from grain and grain boundary to the charge transport mechanism. Charge transport properties remain similar after repeated bending of the film on a flexible polymer substrate.

## Graphical Presentation



## 5.1 Introduction

Solution processibility of organic materials, inorganic semiconductor (SC) nanocrystals (NCs), and molecular inorganic complexes offers easy and efficient fabrication of SC films with potential to reduce the cost of commercial SC devices,<sup>1-5,6,7</sup> and also the possibility to achieve mechanically flexible devices.<sup>8-9</sup> Soluble organometallic compounds and hydrazinium chalcogenidometallates were used as precursors to grow SC films in the recent past.<sup>10-11</sup> Films of these precursors were decomposed at an elevated temperature forming thin film of a desired inorganic SC. Typically, a large weight loss (> 25%) is observed during the decomposition of precursors, generating cracks in the film. On the other hand, colloidal SC NCs are typically capped with insulating organic ligands that inhibit charge transport in NC film.<sup>12</sup> Various types of surface chemistry modifications have significantly improved the charge transport of NC film, where NCs retain their crystallite size but get electronically connected.<sup>12-16</sup> However, the grain boundary effect still remains detrimental for charge transport. Sintering of such NC film has already been found to increase the crystallite size, and thereby reducing the vexing problem of grain boundary.

Gur et al. demonstrated that the solution processed CdSe and CdTe nanorods could be sintered at 400 °C to form CdSe/CdTe bi-layer films for solar cell applications.<sup>3</sup> Jasieniak et al.<sup>17</sup> and Panthani et al.<sup>18</sup> sintered CdTe NC precursors at ~350 °C to grow CdTe films for solar cell applications. Guo et al.<sup>19</sup> and Harvey et al.<sup>20</sup> sintered copper-zinc-tin-chalcogenide (CZTS) and copper-indium-gallium-selenide (CIGS) NCs at ~500 °C. Jiang et al. demonstrated that the solid state reaction between the inorganic NCs and its inorganic capping ligand (molecular metal chalcogenide) led SC films with desired composition.<sup>21</sup> Here, the film composed of NCs and ligands was again annealed at ~500 °C to obtain a dense SC film. Clearly, sintering of NCs to achieve functional SC film is an active area of research, where NCs were annealed at temperatures >350 °C. However, such high temperature annealing is not suitable to grow thin films on a flexible polymer substrate that can be bent or twisted. Reduction of the annealing temperature below 150 °C will allow growth of SC films on mechanically flexible and light-weighted polymer substrates. In addition, the lowering of annealing/sintering temperature invariably reduces the cost associated with film growth.

The requirement of high annealing temperature for sintering of NCs into a thin film suggests the requirement of higher activation energy for the process of NC fusion yielding larger crystals. Can we facilitate the fusion process of NCs at room temperature? To address this question, we employed two strategies: (i) use of ligand-free NCs,<sup>22-23</sup> and (ii) exploring the

possibility of oriented attachment amongst NCs.<sup>24-26</sup> Bulky capping ligands on NC hinder reactions between adjacent NCs; however, such capping ligands decompose after annealing at higher temperatures causing weight loss/discontinuity in the film, and therefore, can also reduce the crystallite size. Our approach of using ligand-free NCs will overcome both these problems associated with surface ligands. Li et al. demonstrated that NC could fuse and grow much easily when two fusing NCs were oriented in a particular favorable crystallographic direction, a phenomenon known as oriented attachment.<sup>26</sup> Consequently, we targeted PbS and PbSe NCs which have the tendency to undergo oriented attachment.<sup>27-29</sup>

## 5.2 Experimental Sections

### 5.2.1 Chemicals

Lead (II) nitrate (99%, Aldrich), formamide (99%, Fluka analytical), ammonium sulphide (40 - 48 wt % solution in water, Aldrich), sodium selenide (99.8%, Alfa Aesar), acetonitrile (dry, S D fine chem Ltd), ethanol (99.9%, AR, S D fine chem Ltd), n-butanol (Analytical reagent, Rankem), sodium chloride (AR, Rankem), colloidal silver liquid (TED PELLA, INC), polyethylene terephthalate (PET substrate, Aldrich). All the chemicals were used without any further purification.

### 5.2.2 Synthesis of Ligand-Free PbS NCs

A solution containing 10 mL formamide (FA) and 0.1 mmol (33.12 mg) of  $\text{Pb}(\text{NO}_3)_2$  was degassed under  $\text{N}_2$  atmosphere at 70 °C for 15 min in a 50 mL three necked round bottom flask. Then aqueous solution (40 to 48 wt%) of  $(\text{NH}_4)_2\text{S}$  (150 $\mu\text{L}$ ) was diluted in 1 mL FA and swiftly injected to the  $\text{Pb}^{2+}$  solution. The reaction was continued for another 15 minutes. The obtained NC dispersion was directly used for solution processed measurements and for solid state measurements, the NC dispersion was precipitated by addition of adequate amount of acetonitrile, followed by centrifugation (5 min at 5000 rpm) and dried at room temperature under vacuum.

### 5.2.3 Synthesis of Ligand-Free PbSe NCs

Colloidal PbSe NCs were prepared inside a  $\text{N}_2$  filled glove box. A solution containing 0.1 mmol  $\text{PbCl}_2$  in 10 ml FA was heated up to 70 °C for 15 min. In a different vial, 0.2 mmol  $\text{Na}_2\text{Se}$  was dissolved in 1 mL FA and added to the  $\text{Pb}^{2+}$  solution drop wise. Washing of PbSe NCs were similar to that of PbS NCs.  $\text{PbCl}_2$  precursor was prepared by mixing aqueous

solution of  $\text{Pb}(\text{NO}_3)_2$  (0.015 mol in 10 mL water) with that of NaCl (0.030 mol in 10 mL water). The NaCl solution was added drop wise to  $\text{Pb}(\text{NO}_3)_2$  solution at room temperature under mild stirring condition, and continued for 30 min. The precipitate was filtered using Buchner funnel and washed with water thrice.  $\text{PbCl}_2$  precipitates were white in color and characterized by powder x-ray diffraction (PXRD).

#### 5.2.4 Characterization

UV-visible-NIR absorption spectra were recorded using a lambda-45 UV/vis spectrometer. Steady state photoluminescence (PL) was measured using FLS 980 (EDINBURGH Instruments). PXRD data were recorded using a Bruker D8 Advanced X-ray diffractometer using  $\text{Cu K}\alpha$  radiation (1.54 Å).  $\zeta$ -potential and dynamic light scattering (DLS) data were obtained using Nano-ZS90 from Malvern Instruments, U.K. Transmission electron microscopy (TEM) images were obtained using JEOL JEM 2100 F field emission transmission electron microscope at 200 kV. Field emission scanning electron microscopy (FESEM) experiments were carried out using Zeiss Ultra Plus scanning electron microscope. Thickness of films was measured using Veeco Dektar 150 surface profiler.

#### 5.2.5 Deposition of NC Film

Dried PbS NCs (100 mg) powder was grinded using mortar and pestle to make fine homogeneous powder. n-butanol (20  $\mu\text{L}$ ) was added drop wise to the powder and grinded further to make a thick paste. This process of adding n-butanol (20  $\mu\text{L}$ ) while grinding was repeated 15 times to get a homogeneous paste. The obtained NC paste was doctor bladed on cleaned glass as well as PET substrate. The area of the rectangular NC film was kept around 8 mm  $\times$  4 mm, however, films with different dimensions were also made. The films were prepared in ambient conditions. Some of the NC films were annealed at 150 °C for 30 min inside a  $\text{N}_2$  filled glove box. The same procedure was followed for making PbSe films.

#### 5.2.6 DC and AC Electrical Measurements

The Four probe DC resistivity measurements were performed with co-linear four individually spring loaded probes. Colloidal silver liquid was used to make contacts on NC films. The probes were separated by a distance 1.7 mm, with probe diameter 1 mm. Current for all the measurements was supplied by Model6220/6221 Current Source and the voltage was obtained by 2182A NANO VOLTMETER. The calculated conductivity values were

obtained by passing current (I) through the outer two probes and measuring the voltage (V) across the inner two probes. The resistivity of NCs films was calculated by using the following equation<sup>30</sup>

$$\rho_s = \frac{V}{I} C \text{ and } \rho = \rho_s \omega$$

where,  $\rho_s$  is sheet resistance, C is correction factor,  $\omega$  is thickness of film and  $\rho$  is resistivity. AC impedance was measured in two-probe geometry by using computer enabled PARSTAT 2273 potentiostat/galvanostat, along the film on both glass and PET substrate. Colloidal silver liquid was used to make contacts between the film and two spring-loaded gold electrodes were used as probes. The distance between probes was 1.5 mm. The AC perturbing voltage was kept at 500 mV in the frequency range of 2 MHz to 100 Hz. The measured data were fitted in ZSimpWin 3.2 electrochemical impedance modeling software.

## 5.3 Results and Discussion

### 5.3.1 Colloidal Ligand-Free PbS NCs

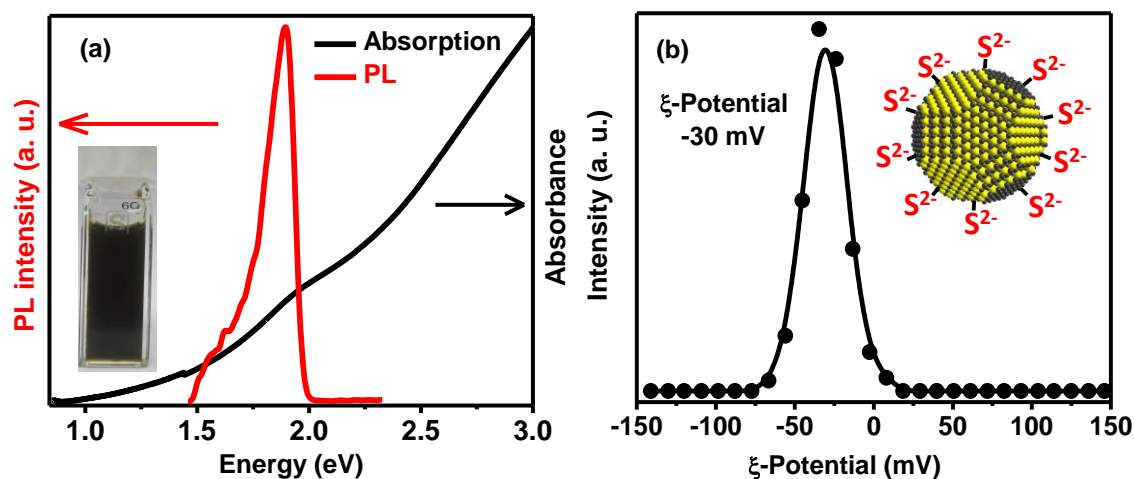


**Figure 5.1:** (a) UV-vis-NIR absorption and PL spectra of ligand-free PbS NCs dispersed in FA. The inset shows photograph of colloidal dispersion of ligand-free PbS NCs in FA. (b)  $\zeta$ -potential of ligand-free PbS NCs dispersed in FA. Inset shows a model of ligand-free PbS NC with excess  $S^{2-}$  ( $S^{\delta-}$ ) on surface.

Ligand-free colloidal PbS and PbSe NCs were prepared employing a simple single-step reaction. The yield of the reaction is  $\sim 70\%$ , and does not involve any expensive organic capping ligand. Furthermore, the reaction is carried out at a low temperature ( $70^\circ\text{C}$ ) and can be scaled up. All these aspects make our colloidal synthesis of NCs easily reproducible and

cost-effective. These NCs do not exhibit very narrow size distribution, a parameter that is not critical in the present case because these NCs are only precursor for growing electronically active SC films with larger crystallite size. After the synthesis, we have characterized the NCs using various experimental techniques as follows.

UV-vis-NIR absorption spectrum in Figure 5.1a shows lowest energy excitonic feature at 1.98 eV (626 nm) for colloidal PbS NCs dispersed in FA. The absorption feature is highly blue shifted compared to the bulk PbS because of the quantum confinement effect.<sup>31</sup> The size of colloidal PbS NCs is calculated to be 2.5 nm using the size vs optical gap relation,<sup>31</sup> assuming that the NCs are spherical. The absorption data cannot suggest the shape of the NCs; however, they definitely suggest that the dimensions (at least one dimension) of PbS NCs are around a few nm. These PbS NCs exhibit excitonic emission, as shown by the PL spectrum in Figure 5.1a. The observation of excitonic PL suggests lower defect density in our ligand-free PbS NCs.

The solution is colloidal stable for about a day, after which the NCs precipitate out. A digital image of the colloidal dispersion of PbS NCs in FA is shown in the inset of Figure 5.1a. Figure 5.1b shows the  $\zeta$ -potential value of -30 mV for the as synthesized PbS NCs in FA. This negative  $\zeta$ -potential establishes -ve charge on the NC surface, as schematically shown in the inset of Figure 5.1b. This negative charge arises from the excess  $S^{2-}$  ( $S^{\delta-}$ ) ions on the NC surface. These negatively charged NCs repel each other electrostatically, forming a colloidal solution in a polar solvent like FA. The counter ion  $NH_4^+$  has a poor affinity towards the  $S^{2-}$  ions on the NC surface and remains solvated by the polar FA molecules.

### 5.3.2 Larger NCs at Room Temperature through Oriented Attachment

When less polar acetonitrile was added to the NC dispersion in FA, the NCs precipitate out. Acetonitrile is well-known non-solvent for precipitating/washing of various kinds of NCs dispersed in FA.<sup>22, 32-33</sup> However, unlike all prior cases with NCs of CdSe, CdS, ZnS, ZnSe,<sup>32</sup> our precipitated PbS NC could not be re-dispersed into a pure FA solvent. More surprisingly, the PXRD pattern (Figure 5.2a) of these PbS NC precipitates shows sharp peaks corresponding to mean crystallite size  $\sim$  27 nm, following the Scherrer equation.<sup>34</sup> The TEM image (Figure 5.2b) of the PbS precipitate shows elongated NCs with average length 53 nm and width 23 nm. The band gap of the PbS NC precipitate drastically decreases to 0.39 eV (Figure 5.3) compared to that (1.98 eV) of colloidal NCs before precipitation. The obtained band gap of PbS NC precipitate correspond to that of the bulk PbS, confirming the crystallite

size is  $> 18$  nm, which is the value for Bohr excitonic radius of PbS.<sup>31</sup> Unambiguously, the crystallite size of PbS NCs in the precipitate is about an order of magnitude larger compared to that of the colloidal (prior to the precipitation) NCs, which was obtained by UV-vis-NIR spectrum.

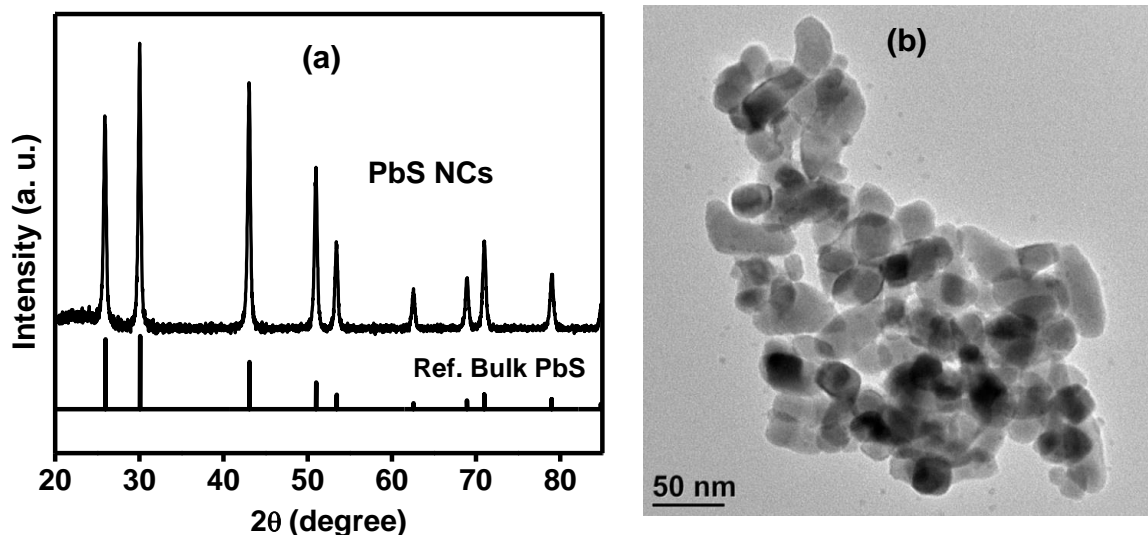


**Figure 5.2:** (a) PXRD pattern and (b) TEM image of ligand-free PbS NC precipitate.

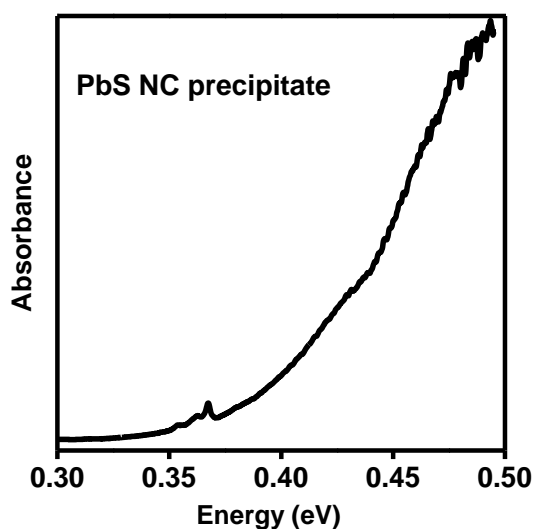


**Figure 5.3:** Infra-red absorption spectrum of PbS NCs precipitate.

\*Declaration: Spectra of Figure 5.3 and 5.15 were recorded by Dr. Kanishka Biswas research group at JNCASR, Bangalore.

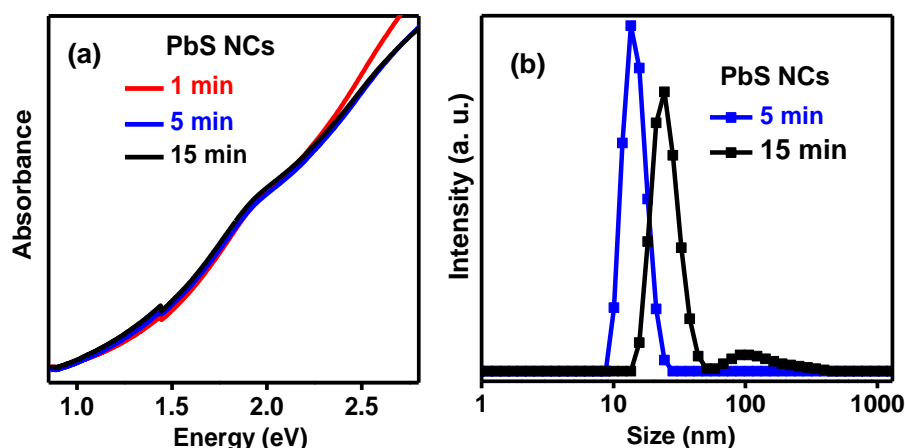


**Figure 5.4:** Synthesis of ligand-free colloidal PbS NCs was stopped immediately after the injection of  $S^{2-}$  precursor into the  $Pb^{2+}$  solution. The solution was then cooled and maintained at room temperature. (a) UV-vis-NIR and (b) DLS data were measured using the same sample of PbS NCs at different times.

To understand the post-synthetic changes in the colloidal NCs, we obtained the DLS and UV-vis-NIR absorption spectra of colloidal NCs in FA after the reaction was over. The reaction mixture was isolated immediately after the injection of  $S^{2-}$  precursor into the  $Pb^{2+}$  precursor solution in FA maintained at 70 °C. The solution was immediately cooled to room temperature, and was analyzed at different time intervals. The DLS data (not shown here) do not show any particle with size greater than 5 nm after 1 min. UV-vis-NIR absorption data (Figure 5.4a) show the excitonic feature of PbS NCs corresponding to size of 2.5 nm. These results suggest that NCs are already formed but not agglomerated after 1 min. However, as the time increases, DLS (Figure 5.4b) shows a systematic increase in hydrodynamic size: 14 nm after 5 min, and 25 nm (along with a smaller fraction of 105 nm) after 15 min. This larger hydrodynamic radius obtained from DLS represents the size of the agglomerated structure containing many NCs, and does not necessarily mean that the size of a given NC has increased with time. In fact, the excitonic feature in both the absorption (Figure 5.4a) and PL (Figure 5.5) does not change with time, confirming that the crystallite size of a NC does not change with time; however, multiple NCs get agglomerated with time. An increase in the absorption tail at energies lower than the optical gap is also observed (Figure 5.4a) with time, which again indicates the increasing tendency of the agglomeration of NCs with time. All these data suggest that the NCs undergo agglomeration with time, increasing the DLS size and absorption tail, whereas the crystallite size remains unchanged even after agglomeration; thus, the optical gap is not altered. Moreover, the colloidal solution remains stable after



agglomeration, suggesting a possible solvation effect, where solvent molecules can penetrate through the porous agglomerated structure of NCs.<sup>35</sup> With further increase in time, agglomeration increases yielding a DLS peak >100 nm (not shown here) after many hours, eventually followed by the precipitation of NCs.

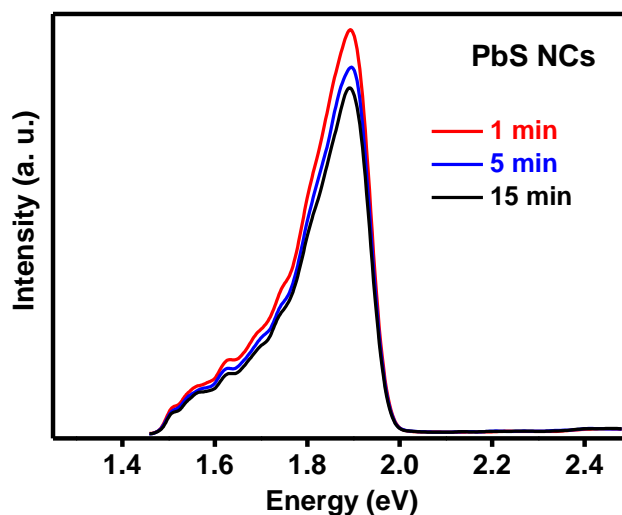


**Figure 5.5:** PL spectra for same sample (used in Figure 5.4) of ligand-free PbS NCs in FA at different time after stopping the reaction immediately after injecting  $S^{2-}$  solution in  $Pb^{2+}$  solution.

Although the NCs agglomerated in FA solvent without increasing the crystallite size, the addition of a non-solvent drastically increases the crystallite size (Figure 5.2). A typical growth model,<sup>36</sup> including Ostwald ripening cannot explain the sudden increase in crystal size after addition of non-solvent. On the other hand, PbS and PbSe NCs are known to possess dipole moment along different crystallographic directions, leading to oriented attachment of NCs.<sup>27</sup> The observed agglomeration of PbS NCs in FA, followed by formation of larger NCs after removal of FA could possibly be explained by the dipole moment of PbS NCs. Dipole moment leads to agglomeration of NCs in FA, which has high dielectric constant and can provide solvation energy, inhibiting fusion of NCs. When FA molecules (solvation energy) are removed from the agglomerated structure, NCs within the agglomerated structure get fused to each other forming a larger crystallite. A similar effect of solvent polarity has been observed earlier for the fusion of  $SnO_2$  NCs via oriented attachment where the dipole-dipole attraction between NCs was found to be inversely proportional to the dielectric constant of the solvent.<sup>37-38</sup>

The fact that the removal of solvent molecules immediately leads to the formation of larger crystals, makes it difficult for us to collect TEM images of smaller NCs before precipitation. Consequently, we analyzed high resolution TEM (HRTEM) images only after precipitation of NCs. Figure 5.6a shows fusion of multiple NCs. We concentrate on two junctions I and II between NCs (indicated in Figure 5.6a) to investigate the possibility of oriented attachment. Figure 5.6b shows a HRTEM image closer view of junctions I and II. Clearly, junction I shows oriented attachment perpendicular to  $\{111\}$  facets of the adjacent NCs, having interplanar distance  $3.42 \text{ \AA}$ . The fast Fourier transform (FFT) pattern of Junction I in Figure 5.6d shows single crystalline nature along with diffused reciprocal spots along  $\{111\}$  ( i.e.,  $(-1-1-1)$  and  $(11-1)$  ) signifying lattice defects/dislocations at the interface of the NCs undergoing attachment, which is in agreement with the HRTEM image showing oriented attachment along  $\langle 111 \rangle$  direction of the NCs.

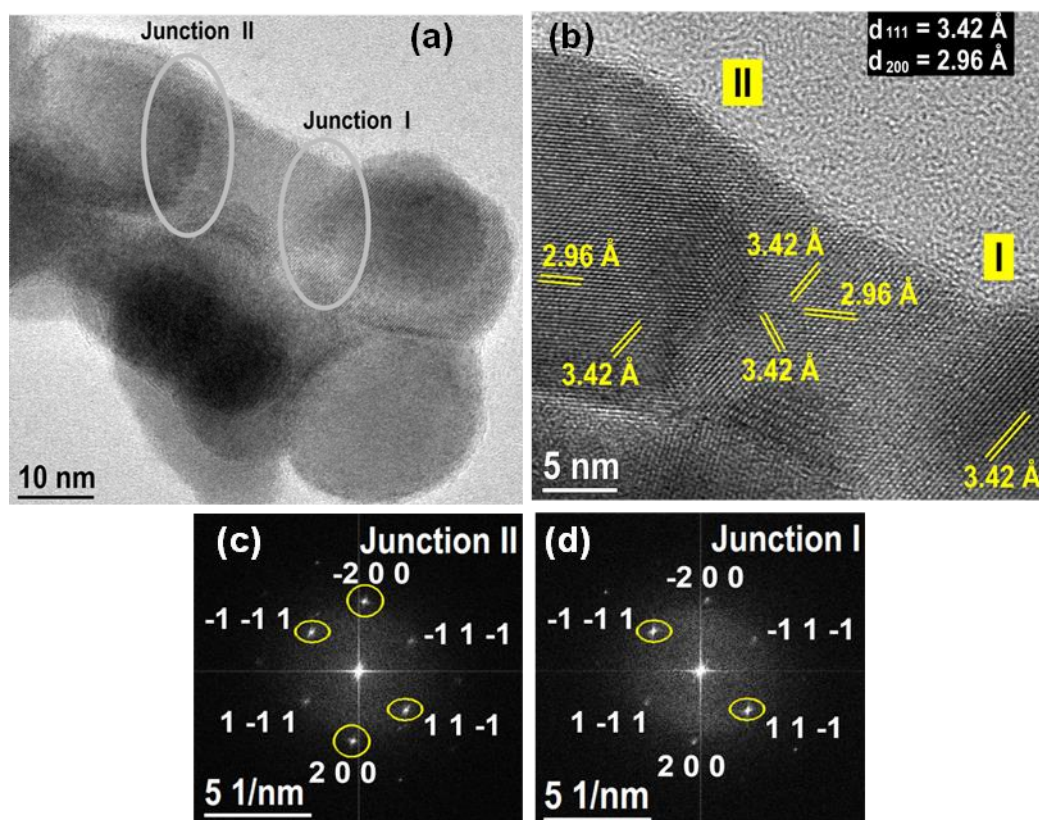


**Figure 5.6:** (a) and (b) show HRTEM images of a part of ligand-free NC precipitate. (c) and (d) show FFT patterns of junctions II and I respectively. These junctions are interfaces between fusing NCs as indicated in (a) and (b).

Junction II (Figure 5.6b) again shows oriented attachment perpendicular to  $\{111\}$  facets. In addition, the  $\{200\}$  facets with interplanar distance  $2.96 \text{ \AA}$  undergo lateral oriented attachment at the junction. Pacholski.<sup>39</sup> and Li et al.<sup>26</sup> demonstrated similar oriented attachment both lateral (and twin-related) and perpendicular to the participating lattice planes. Figure 5.6c shows FFT pattern of junction II having diffused reciprocal spots for  $\{111\}$  ( i. e.,  $(-1-11)$  and  $(11-1)$ ) and  $\{200\}$  ( i.e.,  $(200)$  and  $(-200)$ ) facets, suggesting the participation of  $\{111\}$  and  $\{200\}$  facets in the oriented attachment.

Figure 5.7 shows another set of NCs undergoing oriented attachment. Here, the oriented attachment takes place perpendicular to  $\{200\}$  (analogous to  $\{100\}$  as well) facets. The FFT pattern of junction III (inset in Figure 5.7b) shows single crystalline pattern with diffused reciprocal spots for  $\{200\}$  (i.e.,  $(200)$  and  $(-200)$ ) facets, suggesting oriented attachment along  $\{200\}$  facets. We observe oriented attachment perpendicular to both  $\{200\}$  (analogous to  $\{100\}$ ) (Figure 5.7) and  $\{111\}$  (Figure 5.6) facets. It is to be noted that the magnitude of dipole moment is known to be high along both  $\langle 100 \rangle$  and  $\langle 111 \rangle$  directions of PbS and PbSe with rock salt structure.<sup>27</sup> Therefore, our observation of oriented attachments along these directions again suggests the dipole-dipole interaction between NCs as a probable cause for the oriented attachment.

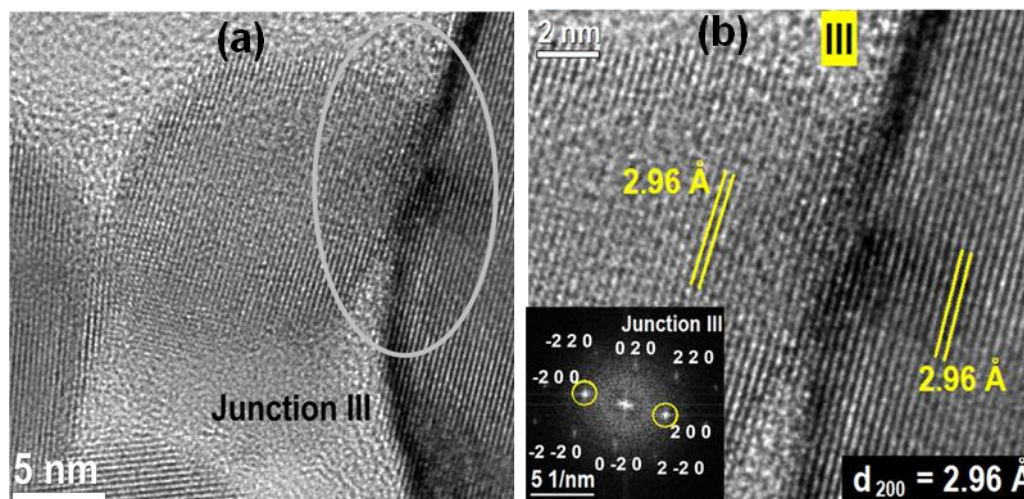


**Figure 5.7:** (a) and (b) show HRTEM images of another part (different from Figure 5.6) of the same ligand-free NC precipitate. Inset of (b) is FFT patterns of junctions III indicated in (a) and (b).

Such oriented attachment requires easy movement of NCs, which is allowed in a colloidal dispersion, where dipole-dipole interaction is strong enough to orient adjacent NCs in a

preferred crystallographic direction. Unlike colloidal dispersion, the movement of NCs gets restricted in a film. Therefore, the removal of organic ligands from the surface of PbS NCs, which were already casted into a film, yielded a film of ligand-free PbS NCs, but did not undergo oriented attachment to form larger NCs.<sup>40</sup> In recent times, the oriented attachment has been controlled in different ways achieving 1D, 2D and 3D fused structures of PbS and PbSe NCs.<sup>41-42</sup> In our case, we have uncontrolled (both perpendicular and lateral) oriented attachment of PbS NCs giving larger elongated NCs. It should be noted that we could not capture the TEM images for smaller NCs that are present in solution because the removal of solvents leads to the formation of larger NCs.

### 5.3.3 DC and AC Electrical Properties of PbS NC Film

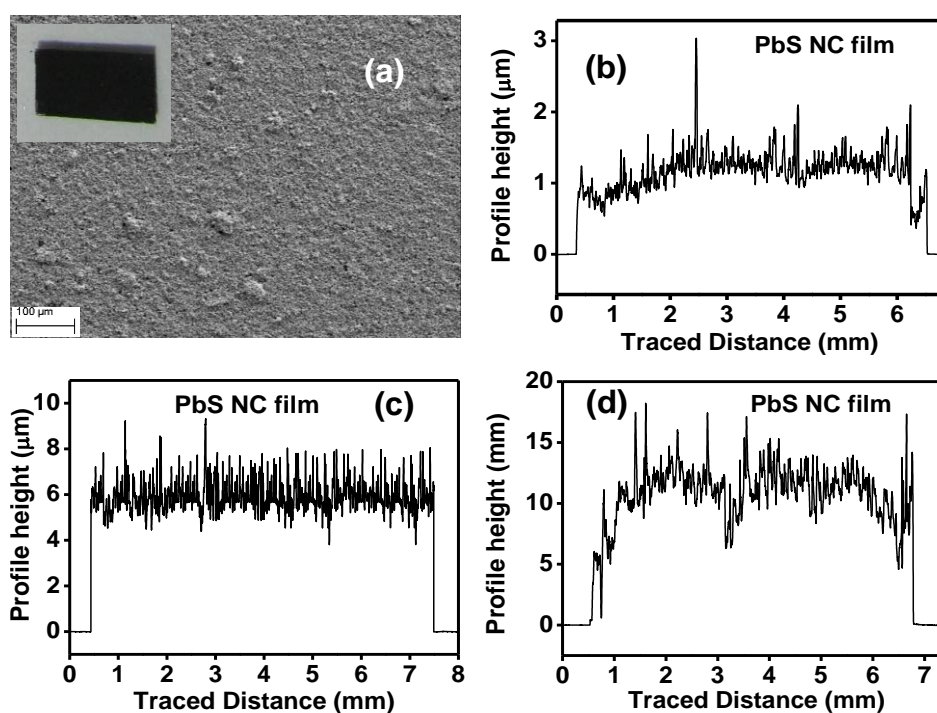


**Figure 5.8:** (a) FESEM image of a large area of PbS NC film on a glass substrate processed at room temperature. Inset shows photograph of a typical PbS film on glass. (b) Surface profilometry of three different PbS films showing the control over film thickness in the range of 1 to 15 μm.

Films of precipitated PbS NCs were prepared on both glass and flexible PET substrate by employing doctor-blading technique. The inset to Figure 5.8a shows a digital image of a PbS NC film on glass substrate. The FESEM image of the film in Figure 5.8a shows homogenous film morphology with no unwanted pin-holes. Thickness of the film can be controlled



between 1 to 15  $\mu\text{m}$  (see Figure 5.8b-d). The FESEM image in Figure 5.9 suggests a crystallite size of  $\sim 50\text{ nm}$  in the film, in agreement with TEM results in Figure 5.2b.

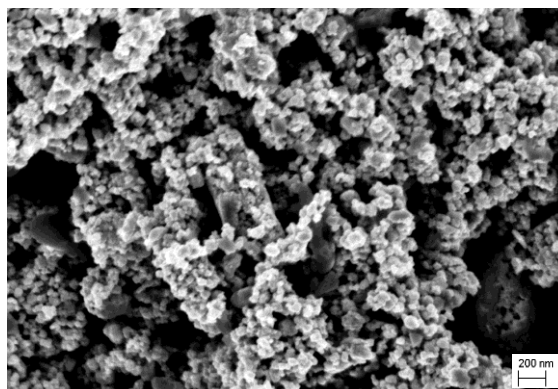


**Figure 5.9:** FESEM image of PbS NC film on glass substrate processed at room temperature.

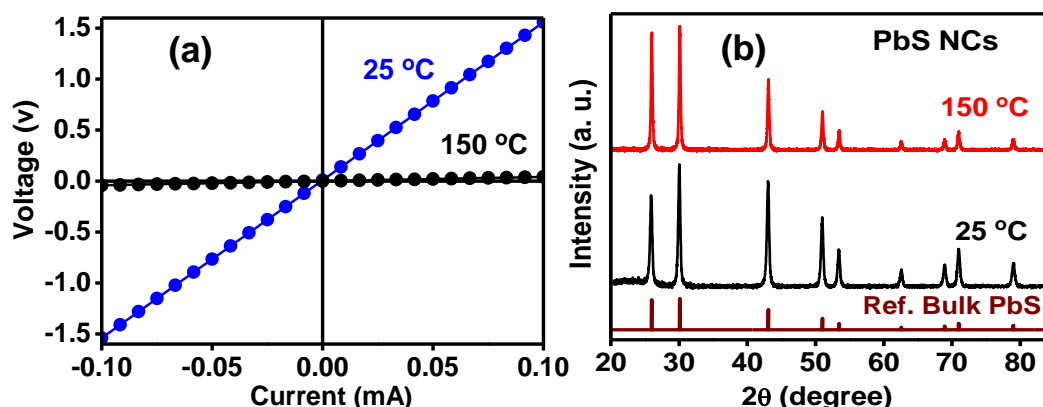


**Figure 5.10:** (a) Four probe I vs V plots of PbS NC films on glass substrate processed at 25  $^{\circ}\text{C}$  and 150  $^{\circ}\text{C}$ , both the measurements were done at room temperature. (b) PXRD patterns of PbS NC films processed at 25  $^{\circ}\text{C}$  and 150  $^{\circ}\text{C}$ .

Four-probe DC electrical conductivity measurements (Figure 5.10a) on the PbS NC films on glass substrate show ohmic behavior of current (I) vs voltage (V) with conductivity of 0.03 S/m for the film processed at room temperature. Upon annealing the film at 150  $^{\circ}\text{C}$  for 30 min, the conductivity increased to 1.1 S/m. The width of the XRD peaks (Figure 5.10b) decreases further after annealing, suggesting an increase in crystallite size with annealing. The obtained electrical conductivities are comparable to that of PbS films obtained by other expensive techniques that employ high temperatures and vacuum.<sup>43</sup> Sharp and intense XRD peaks of our NC film suggest better crystallinity of our NCs compared to typical films made by chemical bath deposition at low temperature.<sup>44-46</sup>

Electrical properties of a polycrystalline film such as our PbS NC film depend upon both inter- and intra-granular resistance. A typical DC measurement cannot differentiate between such inter- and intra-NC contributions to electrical conductivity. To obtain a better understanding about resistance and capacitance arising from both within NC (intra-granular) and grain boundaries (inter-granular), we carried out AC impedance measurements over a wide frequency range (2 MHz to 100 Hz). Impedance,  $\hat{Z}$  is a vector quantity and can be expressed as a complex number  $\hat{Z} = Z' - iZ''$  where  $Z'$  is the real part (resistive),  $Z''$  is the imaginary part (reactive) and  $i = \sqrt{-1}$ .<sup>47</sup> Figure 5.11a shows Nyquist plot for PbS NC films on glass substrate, where the imaginary component,  $Z''$  is plotted on Y-axis with negative sign vs real component,  $Z'$  on X-axis. Shape of the Nyquist plot is a single semicircle, a characteristic of polycrystalline film where the grain boundary dominates the electrical impedance.<sup>48-49,42</sup> The experimental data (symbols) could be fitted (red line) well using a simple  $R_b(R_{gb}C_{gb})$  electrical model (inset to Figure 5.11a),<sup>48-49</sup> where  $R_b$  and  $R_{gb}$  correspond to resistances due to bulk and grain boundary, respectively, and  $C_{gb}$  is the capacitance across grain boundaries.

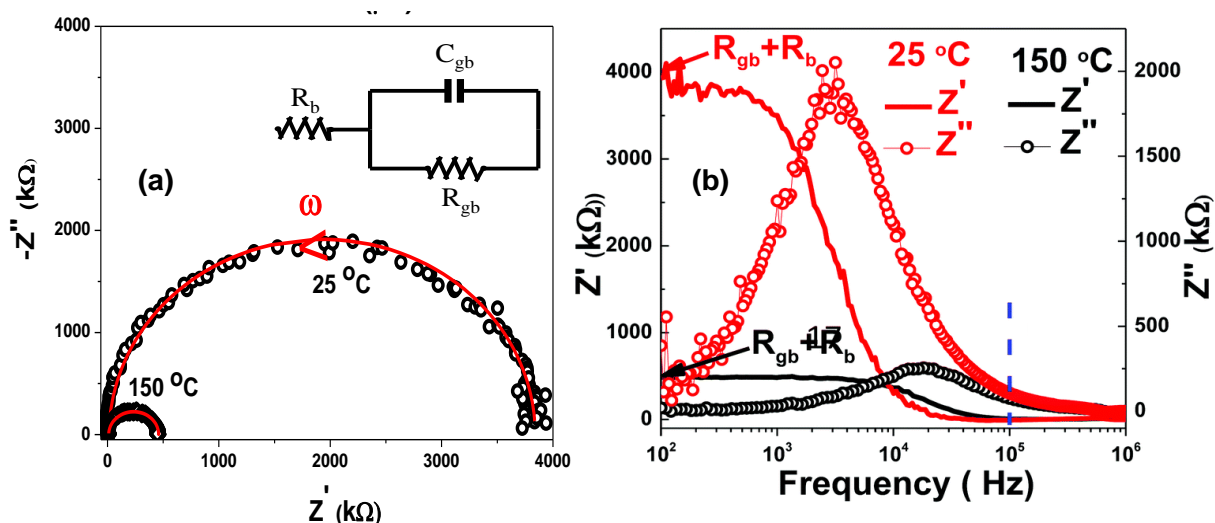


**Figure 5.11:** (a) Nyquist plots and (b) spectroscopic plot of ligand-free PbS NC films obtained from two-probe AC impedance measurements. Films were processed at 25 °C and 150 °C, but both the impedance measurements were done at room temperature. Inset in Figure 5.11a shows a schematic electric circuit diagram of charge conduction in PbS NC film.

The semicircular shape of the Nyquist plot is due to  $R_{gb}$  parallel to  $C_{gb}$ . The radius of the semicircle would be  $R_{gb}/2$ , and centred at  $R_{gb}/2$  if  $R_b = 0$ . The addition of  $R_b$  in series just shifts the curve to a higher  $Z'$  value by the small quantity of  $R_b$ . The values of  $R_{gb}$  and  $C_{gb}$

obtained from the fitting for the PbS film on glass substrate and processed at room temperature are 3.84 M $\Omega$  and 14.2 pF. The value of the capacitance matches well with the capacitance due to grain boundary present in a typical polycrystalline film.<sup>50</sup> When the film was annealed at 150 °C, radius of the semicircle decreased significantly, suggesting the decrease in R<sub>gb</sub> upon annealing the film, without any considerable change in the R<sub>b</sub>. The best fit parameter values of R<sub>gb</sub> and C<sub>gb</sub> for the PbS film on glass substrate and annealed at 150 °C are 0.45 M $\Omega$  and 20.7 pF.

Spectroscopic plot, presented in Figure 5.11b, is another way of presenting impedance as a function of frequency where we can separate the Z' and Z'', and can analyse their dependency at different ranges of frequency. There is no considerable change in the value of Z' and Z'' at high frequency (> 10<sup>5</sup> Hz) indicated by vertical blue-dashed line, whereas at lower frequency (<10<sup>5</sup> Hz) Z' and Z'' decreases significantly after annealing the film at 150 °C. The high and low frequency regime electrical responses typically correspond to grain and grain boundary respectively.<sup>42</sup> Therefore the observed change in charge conduction (Z' and Z'') at low frequency is attributed to change in the characteristic of grain boundary upon annealing the film. On the other hand, the value of the capacitance also increased after annealing the film suggesting that the inter-granular regions narrowed upon annealing the film.<sup>42</sup> Moreover, the electrical relaxation time,  $\tau$ , which is the product of R<sub>gb</sub> and C<sub>gb</sub>, and equal to  $(\omega_{max})^{-1}$ , was also reduced to 5.7 times after annealing the film at 150 °C, where  $\omega_{max}$  is the angular frequency of maximum loss in an RC circuit.<sup>42</sup> The decrease in R<sub>gb</sub> and  $\tau$  along with an increase in C<sub>gb</sub> after annealing the film is because of improved electrical connectivity between adjacent NCs (grains) via removal of defects from the interface of connected NCs ensuring better fusion of NCs.

We have also casted similar films of PbS NCs on flexible PET substrates. The film processing was done at room temperature. The I vs V plots were obtained from four probe DC resistivity measurements, shown in Figure 5.12a establishes ohmic behavior with conductivity 0.02 S/m. The film on the PET substrate can be bent as shown in the inset of Figure 5.12b. The film was repeatedly bent for 50 times to a curvature radius of 1.1 cm, and the electrical measurements were repeated. The DC conductivity decreases to 0.015 S/m after bending the film for 50 times, compared to 0.02 S/m before bending. AC impedance data in Figure 5.12b for the PbS NC film on PET show semicircular Nyquist plots similar to those in Figure 5.11a. The radius of the semicircle increased after bending the film repeatedly for 50 times. Both plots, before and after bending the film, can be fitted with R<sub>b</sub>(R<sub>gb</sub>C<sub>gb</sub>) electrical

model. The best fit values of  $R_{gb}$  are 5.42 M $\Omega$  and 10.72 M $\Omega$  before and after bending the film, respectively, keeping  $C_{gb}$  largely unaltered  $\sim$ 21 pF. Importantly, the film still exhibits high electrical conductivity even after repeated bending experiments, suggesting the suitability of our PbS NC film for integration in flexible electronic devices. It is to be noted that, often the films made from traditional SCs generates cracks upon bending resulting into a drastic (over many orders of magnitude) decrease in electrical conductivity.<sup>51</sup> The sustained electrical conductivity of the NC film after bending the film is because of the smaller size of our NC compared to bending curvature of the film, and therefore, the bending related strain is not strongly felt by NC grains and grain boundaries.

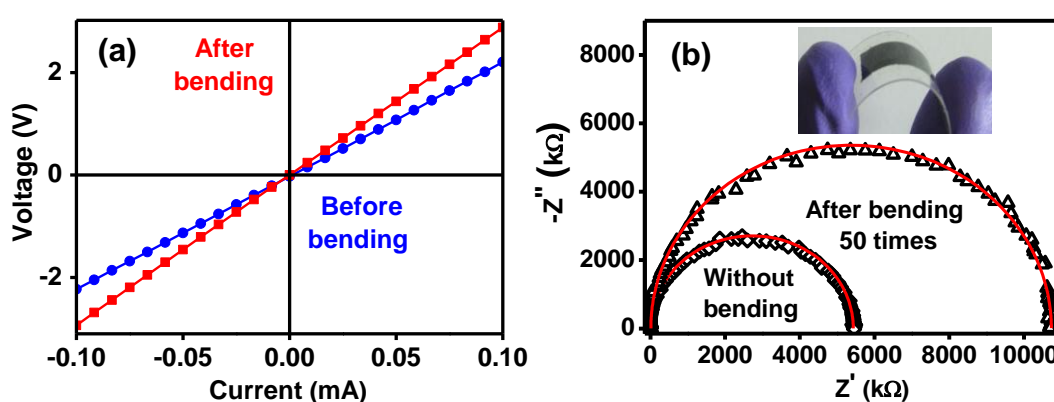


**Figure 5.12:** (a) Comparison of four-probe DC I vs V plots, and (b) corresponding Nyquist plots (two-probe AC impedance data) of ligand-free PbS NC films on a flexible PET substrate before and after bending the film for 50 times. Inset in figure 5.12b shows the photograph of the flexible film on PET.

\*Declaration: In this chapter, Impedance study was carried out by Abhishek Swarnkar, who was integrated Ph.D. student in our group.

### 5.3.4 PbSe NCs

Colloidal ligand-free PbSe NCs were also prepared in a manner similar to the synthesis of ligand-free PbS NCs, but by using  $\text{Na}_2\text{Se}$  and  $\text{PbCl}_2$  as sources of  $\text{Se}^{2-}$  and  $\text{Pb}^{2+}$  ions, respectively. UV-vis-NIR absorption spectrum in Figure 5.13a shows a shoulder for excitonic absorption at 1.7 eV, which correspond to a PbSe NCs with diameter of 3.4 nm diameter, assuming spherical shape.<sup>31</sup> PbSe NCs dispersed in FA show a  $\zeta$ -potential value (Figure 5.13b) of -44 mV, suggesting negatively charged NC surface, therefore, providing colloidal stability via electrostatic repulsion among similarly charged PbSe NCs. The NCs precipitate



upon addition of non-solvent acetonitrile, and the precipitate could not be redispersed in FA.

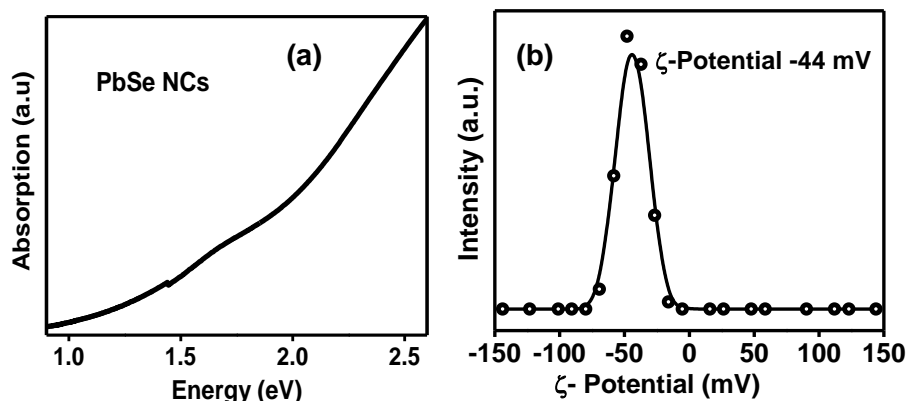


**Figure 5.13:** (a) UV-vis-NIR absorption spectrum and (b)  $\zeta$ -potential of ligand-free PbSe NCs dispersed in FA. In the (b) open circles represents the experimental data and the solid line is a guide to eye.

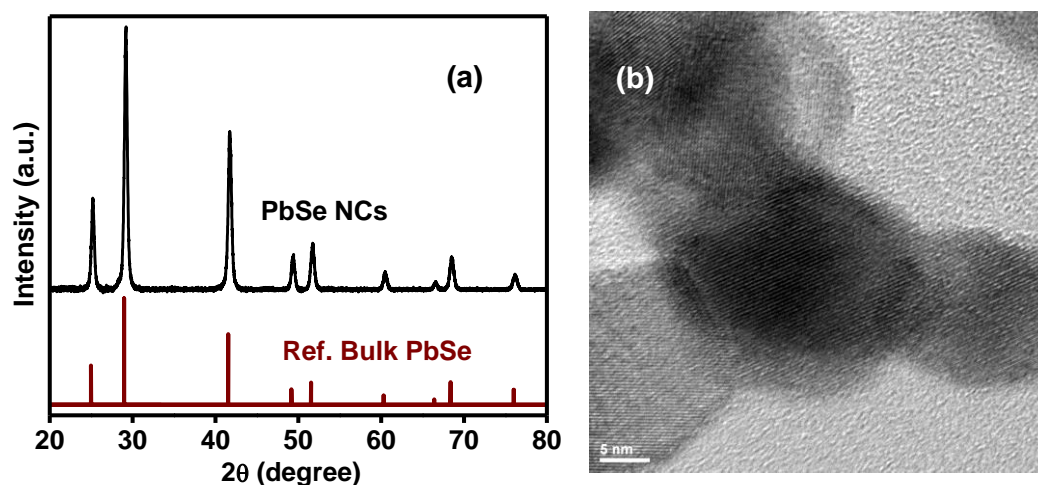


**Figure 5.14:** (a) PXRD pattern and (b) HRTEM image of PbSe NCs after precipitation.

The PXRD pattern of the precipitate (Figure 5.14a) shows PbSe NCs of size  $\sim 19$  nm with rock-salt crystal structure. TEM image in Figure 5.14b shows fusion of small PbSe NCs forming larger PbSe NCs. Figure 5.15 shows 0.28 eV (4429 nm) band gap for PbSe NC precipitate similar to bulk PbSe. All these observations for PbSe NCs are qualitatively similar to those of PbS NCs discussed above. Removal of the solvation energy during the precipitation leads to fusion of NCs.

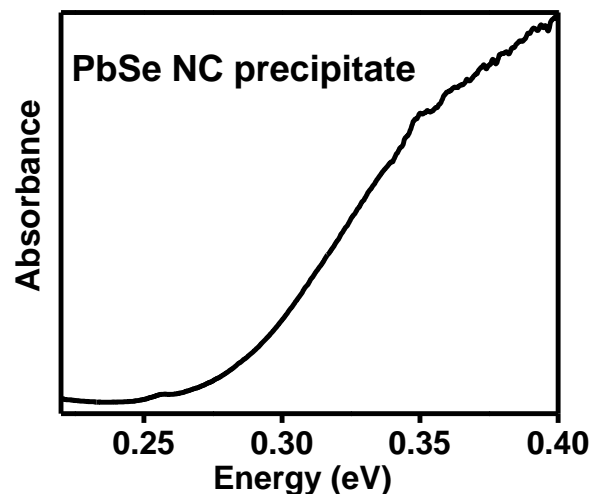


**Figure 5.15:** Infra-red absorption spectrum of PbSe NC precipitate.

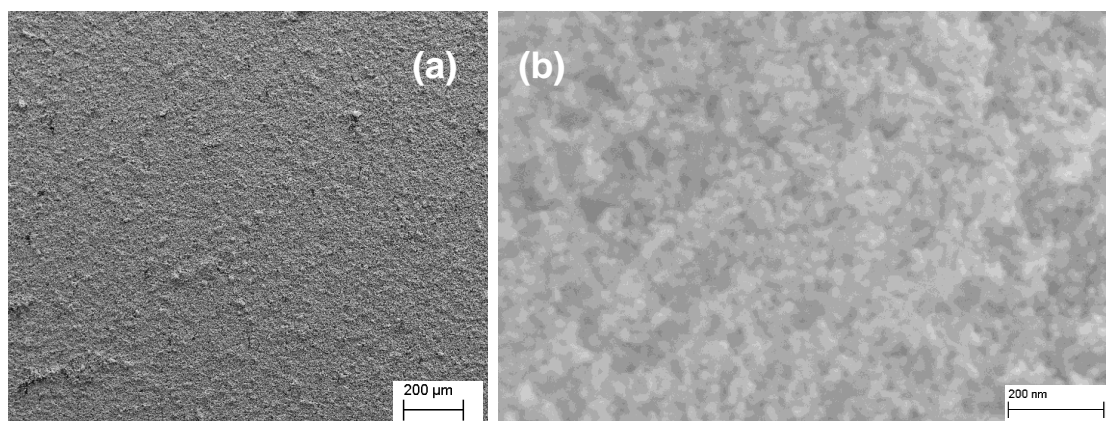


**Figure 5.16:** (a) FESEM image of a large area of PbSe NC film on glass, and (b) FESEM image of PbSe NC film on glass substrate, both the films processed at room temperature.

Thin films of PbSe NC precipitates can be prepared on both glass and flexible PET substrate with thickness in the range of 1 to 15  $\mu\text{m}$  using doctor blading technique. Figure 5.16a shows FESEM image of a representative PbSe film on glass showing homogeneous film morphology without any pin-holes. Figure 5.16b shows higher magnification FESEM image exhibiting elongated NCs with diameter  $\sim 20$  nm.

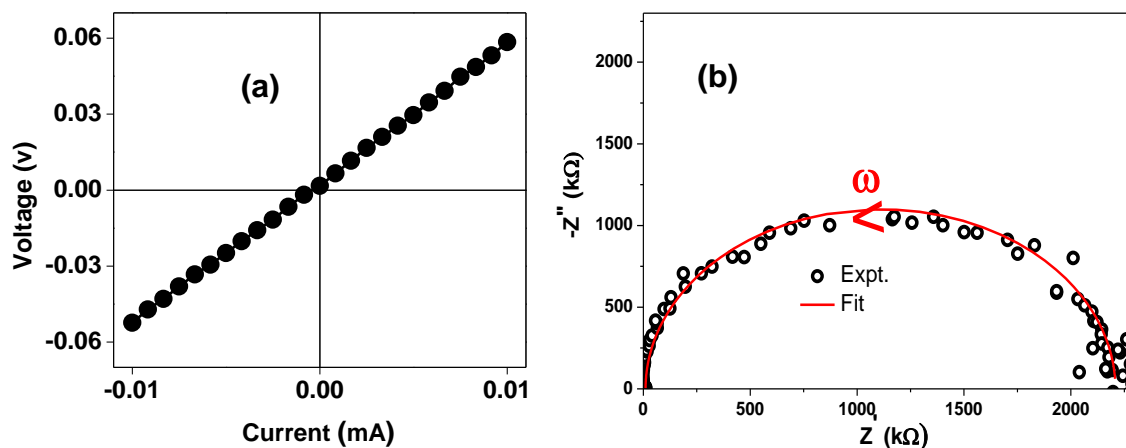


**Figure 5.17:** (a) Four probe DC I vs V plot, and (b) Nyquist plot (two-probe AC impedance data) of ligand-free PbSe NC film on glass processed at room temperature.

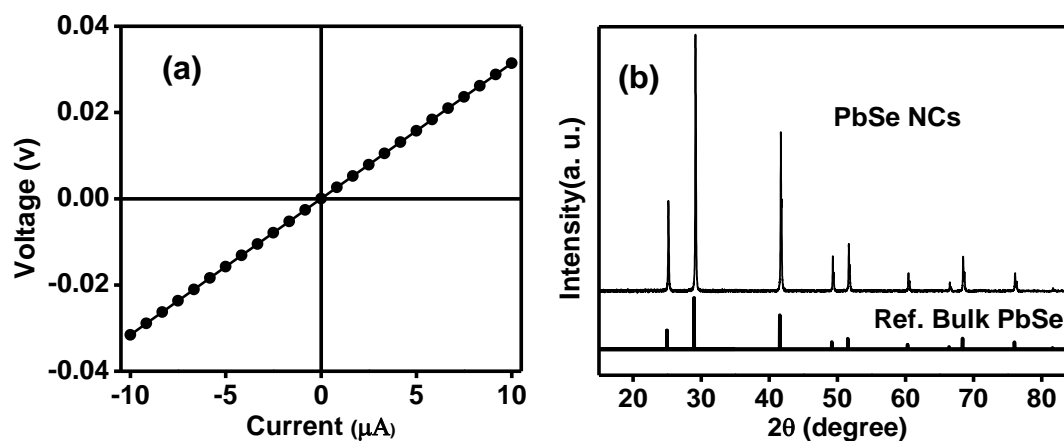


**Figure 5.18:** (a) Four-probe Current (I) vs voltage (V) plot for PbSe NC film on glass substrate after annealing at 150  $^{\circ}$ C. Electrical measurement was done at room temperature. (b) The PXRD pattern of PbSe NC film after annealing at 150  $^{\circ}$ C.

Four probe DC I vs V plot in the Figure 5.17a shows ohmic behaviour, for the PbSe film processed at room temperature with conductivity 0.08 S/m. After annealing the film at 150  $^{\circ}$ C, the conductivity drastically increases to 137 S/m (Figure 5.18a). The PXRD pattern (Figure 5.18b) shows increase in crystallite size via narrowing of PbSe peaks after annealing at 150  $^{\circ}$ C, which explains the reason for increase in conductivity after annealing. Two-probe AC impedance data for PbSe NC film shown in the form of Nyquist plot (Figure 5.17b) shows a single semicircular shape with  $R_{gb} = 2.20$  M $\Omega$  and  $C_{gb} = 20.4$  pF. A comparison of electrical data shows PbSe NC films are electronically more conducting compared to PbS NC films, similar to their bulk counterparts. Electrical conductivity of our PbSe NC films are comparable to PbSe films prepared at higher temperature using expensive methodologies.<sup>43</sup>

## 5.4 Conclusions

We developed a strategy to prepare electronic grade SC thin film using colloidal ligand-free PbS and PbSe NCs at room temperature. The processing at room temperature allows us to prepare films on flexible substrate, and the charge transport properties do not deteriorate much with repeated bending of the film. Therefore, lowering of film processing temperature allows us to get flexible SC film, and also reduces the cost of film deposition. We reduced the sintering temperature of NCs by employing two strategies: (i) preparing ligand-free colloidal PbS and PbSe NCs, (ii) oriented attachment of NCs. Ligand-free NCs do not have insulating organic ligands on the surface, therefore can provide more conducting and crack-free inorganic SC film without any further heat/chemical treatment. On the other hand, dipole moment of PbS and PbSe NCs encourages oriented attachment of NCs, therefore, reducing the activation energy of the fusion of NCs, which is forming single-crystalline larger sized crystals even at room temperature. The organic-free surface of NCs also probably supports the easier fusion of NCs. Colloidal NCs undergo oriented attachment immediately after removing the polar solvent FA during the irreversible precipitation process. DC I vs V plots of PbS and PbSe NC films exhibit linear ohmic behavior with electrical conductivities 0.03 S/m and 0.08 S/m respectively after processing the film at room temperature. The electrical conductivity increase to 1.1 S/m and 137 S/m for PbS and PbSe respectively, after annealing the film on glass substrate at 150 °C. AC impedance data show dominance of grain boundary exhibiting a single semicircular Nyquist plots. Both the oriented attachment and organic-free colloidal NCs are generic phenomena for a variety of NC systems. Therefore, the developed strategy can possibly be extended to a variety NC systems including doped NCs and also hetero-structured NCs, achieving electronic grade and flexible films of functional SC. Such variation of complex compositions along with high crystallinity is difficult to achieve by employing other low-temperature film growth technique such as chemical bath deposition.

## References

1. Mitzi, D. B.; Kosbar, L. L.; Murray, C. E.; Copel, M.; Afzali, A. High-Mobility Ultrathin Semiconducting Films Prepared by Spin Coating. *Nature* **2004**, *428*, 299-303.
2. Shaheen, S. E.; Ginley, D. S.; Jabbour, G. E. Organic-Based Photovoltaics Toward Low-cost Power Generation. *MRS Bull.* **2005**, *30*, 10-19.

- Gur, I.; Fromer, N. A.; Geier, M. L.; Alivisatos, A. P. Air-Stable All-Inorganic Nanocrystal Solar Cells Processed from Solution. *Science* **2005**, *310*, 462-465.
- Milliron, D. J.; Mitzi, D. B.; Cope, M.; Murray, C. E. Solution-Processed Metal Chalcogenide Films for p-Type Transistors. *Chem. Mater.* **2006**, *18*, 587-590.
- Panthani, M. G.; Korgel, B. A., Nanocrystals for Electronics. *Annu. Rev. Chem. Biomol. Eng.* **2012**, *3*, 287-311.
- Jara, D. H.; Yoon, S.; Stampelcoskie, K. G.; Kamat, P. V. Size-Dependent Photovoltaic Performance of CuInS<sub>2</sub> Quantum Dot-Sensitized Solar Cells *Chem. Mater.* **2014**, *26*, 7221-7228.
- Chesman, A. S. R.; Duffy, N. W.; Martucci, A.; Tozi, L. D. O.; Singh, T. B.; Jasieniak, J. J. Solution-Processed CdS Thin Films from a Single-Source Precursor *J. Mater. Chem. C* **2014**, *2*, 3247-3253
- Cairns, D. R.; Crawford, G. P. Electromechanical Properties of Transparent Conducting Substrates for Flexible Electronic Displays. *Proc. IEEE* **2005**, *93*, 1451-1458.
- Kim, D. K.; Lai, Y. M.; Vemulkar, T. R.; Kagan, C. R. Flexible, Low-Voltage, and Low-Hysteresis PbSe Nanowire Field-Effect Transistors. *ACS Nano* **2011**, *5*, 10074-10083.
- Castro, S. L.; Bailey, S. G.; Raffaele, R. P.; Banger, K. K.; Hepp, A. F. Nanocrystalline Chalcopyrite Materials (CuInS<sub>2</sub> and CuInSe<sub>2</sub>) via Low-Temperature Pyrolysis of Molecular Single-Source Precursors. *Chem. Mater.* **2003**, *15*, 3142-3147.
- Liu, W.; Mitzi, D. B.; Yuan, M.; Kellock, A. J.; Chey, S. J.; Gunawan, O. 12% Efficiency CuIn(Se,S)<sub>2</sub> Photovoltaic Device Prepared Using a Hydrazine Solution Process. *Chem. Mater.* **2010**, *22*, 1010-1014.
- Talapin, D. V.; Lee, J.-S.; Kovalenko, M. V.; Shevchenko, E. V. Prospects of Colloidal Nanocrystals for Electronic and Optoelectronic Applications. *Chem. Rev.* **2010**, *110*, 389-458.
- Baumgardner, W. J.; Whitham, K.; Hanrath, T. Confined-but-Connected Quantum Solids via Controlled Ligand Displacement. *Nano Lett.* **2013**, *13*, 3225-3231.
- Oh, S. J.; Berry, N. E.; Choi, J.-H.; Gaulding, E. A.; Lin, H.; Paik, T.; Diroll, B. T.; Muramoto, S.; Murray, C. B.; Kagan, C. R. Designing High-Performance PbS and PbSe Nanocrystal Electronic Devices through Stepwise, Post-Synthesis, Colloidal Atomic Layer Deposition. *Nano Lett.* **2014**, *14*, 1559-1566.

15. Oh, S. J.; Wang, Z.; Berry, N. E.; Choi, J. H.; Zhao, T.; Gauding, E. A.; Paik, T.; Lai, Y.; Murray, C. B.; Kagan, C. R. Engineering Charge Injection and Charge Transport for High Performance PbSe Nanocrystal Thin Film Devices and Circuits. *Nano Lett.* **2014**, *14*, 6210-6216.
16. Nag, A.; Zhang, H.; Janke, E.; Talapin Dmitri, V. Inorganic Surface Ligands for Colloidal Nanomaterials. *Z. Phys. Chem.* **2015**, *229*, 85-107.
17. Jasieniak, J.; MacDonald, B. I.; Watkins, S. E.; Mulvaney, P. Solution-Processed Sintered Nanocrystal Solar Cells via Layer-by-Layer Assembly. *Nano Lett.* **2011**, *11*, 2856-2864.
18. Panthani, M. G.; Kurley, J. M.; Crisp, R. W.; Dietz, T. C.; Ezzyat, T.; Luther, J. M.; Talapin, D. V. High Efficiency Solution Processed Sintered CdTe Nanocrystal Solar Cells: The Role of Interfaces. *Nano Lett.* **2014**, *14*, 670-675.
19. Guo, Q.; Ford, G. M.; Yang, W. C.; Walker, B. C.; Stach, E. A.; Hillhouse, H. W.; Agrawal, R. Fabrication of 7.2% Efficient CZTSSe Solar Cells Using CZTS Nanocrystals. *J. Am. Chem. Soc.* **2010**, *132*, 17384-17386.
20. Harvey, T. B.; Mori, I.; Stolle, C. J.; Bogart, T. D.; Ostrowski, D. P.; Glaz, M. S.; Du, J.; Perniki, D. R.; Akhavan, V. A.; Kesrouani, H.; Bout, D. A. V.; Korgel, B. A. Copper Indium Gallium Selenide (CIGS) Photovoltaic Devices Made Using Multistep Selenization of Nanocrystal Films. *ACS Appl. Mater. Interfaces* **2013**, *5*, 9134-9140.
21. Jiang, C. Y.; Lee, J. S.; Talapin, D. V. Soluble Precursors for  $\text{CuInSe}_2$ ,  $\text{CuIn}_{(1-x)}\text{Ga}_{(x)}\text{Se}_2$ , and  $\text{Cu}_2\text{ZnSn}(\text{S},\text{Se})_4$  Based on Colloidal Nanocrystals and Molecular Metal Chalcogenide Surface Ligands. *J. Am. Chem. Soc.* **2012**, *134*, 5010-5013.
22. Kadlag, K. P.; Rao, M. J.; Nag, A. Ligand-Free, Colloidal, and Luminescent Metal Sulfide Nanocrystals. *J. Phys. Chem. Lett.* **2013**, *4*, 1676-1681.
23. Kadlag, K. P.; Patil, P.; Rao, M. J.; Datta, S.; Nag, A. Luminescence and Solar cell from Ligand-Free Colloidal  $\text{AgInS}_2$  Nanocrystals. *CrystEngcomm* **2014**, *16*, 3605-3612.
24. Tang, Z.; Kotov, N. A.; Giersig, M. Spontaneous Organization of Single CdTe Nanoparticles into Luminescent Nanowires. *Science* **2002**, *297*, 237-240.
25. Zhang, Q.; Liu, S. J.; Yu, S. H. Recent Advances in Oriented Attachment Growth and Synthesis of Functional Materials: Concept, Evidence, Mechanism, and Future. *J. Mater. Chem.* **2009**, *19*, 191-207.

26. Li, D.; Nielsen, M. H.; Lee, J. R. I.; Frandsen, C.; Banfield, J. F.; De Yoreo, J. J. Direction-Specific Interactions Control Crystal Growth by Oriented Attachment. *Science* **2012**, *336*, 1014-1018.
27. Cho, K. S.; Talapin, D. V.; Gaschler, W.; Murray, C. B. Designing PbSe Nanowires and Nanorings Through Oriented Attachment of Nanoparticles. *J. Am. Chem. Soc.* **2005**, *127*, 7140-7147.
28. Schliehe, C.; Juarez, B. H.; Pelletier, M.; Jander, S.; Greshnykh, D.; Nagel, M.; Meyer, A.; Foerster, S.; Kornowski, A.; Klinke, C.; Weller, H. Ultrathin PbS Sheets by Two-Dimensional Oriented Attachment. *Science* **2010**, *329*, 550-553.
29. Acharya, S.; Das, B.; Thupakula, U.; Ariga, K.; Sarma, D. D.; Israelachvili, J.; Golan, Y. A Bottom-Up Approach toward Fabrication of Ultrathin PbS Sheets. *Nano Lett.* **2013**, *13*, 409-415.
30. Smits, F. M. Measurement of Sheet Resistivities with the Four-Point Probe. *The Bell System Technical Journal*, May **1958**.
31. Kang, I.; Wise, F. W. Electronic Structure and Optical Properties of PbS and PbSe Quantum dots. *J. Opt. Soc. Am. B. Opt. Phys.* **1997**, *14*, 1632-1646.
32. Nag, A.; Kovalenko, M. V.; Lee, J. S.; Liu, W. Y.; Spokoyny, B.; Talapin, D. V. Metal-free Inorganic Ligands for Colloidal Nanocrystals:  $S^{2-}$ ,  $HS^-$ ,  $Se^{2-}$ ,  $HSe^-$ ,  $Te^{2-}$ ,  $HTe^-$ ,  $TeS_3^{2-}$ ,  $OH^-$ , and  $NH_2^-$  as Surface Ligands. *J. Am. Chem. Soc.* **2011**, *133*, 10612-10620.
33. Swarnkar, A.; Shanker, G. S.; Nag, A. Organic-Free Colloidal Semiconductor Nanocrystals as Luminescent Sensors for Metal Ions and Nitroaromatic Explosives. *Chem. commun.* **2014**, *50*, 4743-4746.
34. West, A. R. Solid State Chemistry and its Applications, John Wiley and Sons, Student edn, **1998**, ch. 5.
35. Dey, S.; Das, B.; Voggu, R.; Nag, A.; Sarma, D. D.; Rao, C. N. R. Interaction of CdSe and ZnO Nanocrystals with Electron-Donor and Acceptor Molecules. *Chem. Phys. Lett.* **2013**, *556*, 200-206.
36. Viswanatha, R.; Amenitsch, H.; Sarma, D. D. Growth Kinetics of ZnO Nanocrystals: A Few Surprises. *J. Am. Chem. Soc.* **2007**, *129*, 4470-4475.
37. Sinyagin, A. Y.; Belov, A.; Tang, Z. N.; Kotov, N. A. Monte Carlo Computer Simulation of Chain Formation from Nanoparticles. *J. Phys. Chem. B* **2006**, *110*, 7500-7507.

38. Xu, X. X.; Zhuang, J.; Wang, X. SnO<sub>2</sub> Quantum Dots and Quantum Wires: Controllable Synthesis, Self-Assembled 2D Architectures, and Gas-Sensing Properties. *J. Am. Chem. Soc.* **2008**, *130*, 12527-12535.
39. Pacholski, C.; Kornowski, A.; Weller, H. Self-Assembly of ZnO: From Nanodots, to Nanorods. *Angew. Chem. Int. Ed.* **2002**, *41*, 1188.
40. Zhang, H.; Hu, B.; Sun, L.; Hovden, R.; Wise, F. W.; Muller, D. A.; Robinson, R. D. Surfactant Ligand Removal and Rational Fabrication of Inorganically Connected Quantum Dots. *Nano Lett.* **2011**, *11*, 5356-5361.
41. Boneschanscher, M. P.; Evers, W. H.; Geuchies, J. J.; Altantzis, T.; Goris, B.; Rabouw, F. T.; van Rossum, S. A. P.; van der Zant, H. S. J.; Siebbeles, L. D. A.; Van Tendeloo, G.; Swart, I.; Hilhorst, J.; Petukhov, A. V.; Bals, S.; Vanmaekelbergh, D. Long-range Orientation and Atomic Attachment of Nanocrystals in 2D Honeycomb Superlattices. *Science* **2014**, *344*, 1377-1380.
42. Sashchiuk, A.; Amirav, L.; Bashouti, M.; Krueger, M.; Sivan, U.; Lifshitz, E. PbSe Nanocrystal Assemblies: Synthesis and Structural, Optical, and Electrical Characterization. *Nano Lett.* **2004**, *4*, 159-165.
43. Fardy, M.; Hochbaum, A. I.; Goldberger, J.; Zhang, M. M.; Yang, P. D. Synthesis and Thermoelectrical Characterization of Lead Chalcogenide Nanowires. *Adv. Mater.* **2007**, *19*, 3047.
44. Kotadiya, N. B.; Kothari, A. J.; Tiwari, D.; Chaudhuri, T. K. Photoconducting Nanocrystalline Lead Sulphide Thin Films Obtained by Chemical Bath Deposition. *Appl. Phys. A: Mater. Sci. Process.* **2012**, *108*, 819-824.
45. Grozdanov, I.; Najdoski, M.; Dey, S. K. A Simple Solution Growth Technique for PbSe Thin Films. *Mater. Lett.* **1999**, *38*, 28-32.
46. Sarkar, S. K.; Kababya, S.; Vega, S.; Cohen, H.; Woicik, J. C.; Frenkel, A. I.; Hodes, G. Effects of Solution pH and Surface Chemistry on the Postdeposition Growth of Chemical Bath Deposited PbSe Nanocrystalline Films. *Chem. Mater.* **2007**, *19*, 879-888.
47. Sinclair, D. C. Characterization of Electro-Materials using AC Impedance Spectroscopy. *Bol. Soc. Esp. Cerám. Vidrio*, **1995**, *34*, 55-65.
48. Ponce, M. A.; Castro, M. S.; Aldao, C. M. Influence of Oxygen Adsorption and Diffusion on the Overlapping of Intergranular Potential Barriers in SnO<sub>2</sub> Thick Films. *Mater. Sci. Eng. B.* **2004**, *111*, 14-19.



49. Ponce, M. A.; Parra, R.; Savu, R.; Joanni, E.; Bueno, P. R.; Cilense, M.; Varela, J. A.; Castro, M. S. Impedance Spectroscopy Analysis of TiO<sub>2</sub> Thin Film Gas Sensors Obtained from Water-Based Anatase Colloids. *Sens. Actuator. B. Chem.* **2009**, *139* 2, 447-452.
50. Irvine, J. T. S.; Sinclair, D. C.; West, A. R. Electroceramics: Characterization by Impedance Spectroscopy. *Adv. Mater.* **1990**, *2*, 132.
51. Hu, L. B.; Kim, H. S.; Lee, J. Y.; Peumans, P.; Cui, Y. Scalable Coating and Properties of Transparent, Flexible, Silver Nanowire Electrodes. *ACS Nano* **2010**, *4*, 2955-2963.

# **Thesis Summary and Future Outlook**

## Thesis Summary

Production of a hydrogen fuel using clean and renewable energy sources has been realized to reduce the burden of conventional fossil fuel consumption process. Consequently, production of hydrogen through water splitting by employing electrocatalysis, and photoelectrocatalysis experimental techniques has received great attention.

Towards this end, recently, TiN has been received great attention in the research filed of electrocatalysis and photoelectrocatalysis for the production of hydrogen due to unique properties such as metallic electronic structure,<sup>1</sup> high electrical conductivity<sup>2</sup> and good corrosion resistance.<sup>3</sup> Owing to these properties, TiN nanocrystals (NCs) encouraged us to utilize them as catalysts. High surface volume ratio of NCs can provide large number of active sites which is beneficial for the catalysis. But at the same time, the film of these NCs exhibit poor charge transport compared to their bulk counterparts which is a disadvantage in the case of catalysis. Improving the charge transport of NC films by following different approaches and ascertainment of efficiency of these catalysts in electrocatalysis and photoelectrocatalysis for hydrogen production is the major part of this thesis.

This thesis discusses, the synthesis of colloidal TiN - N-doped few-layer graphene (TiN-NFG) nanocomposite starting from molecular precursors. This nanocomposite exhibited stable chemically bound interface between TiN and NFG providing colloidal stability, and enhanced charge transfer across the interface. Colloidal nanocomposite exhibited properties like metallic electrons showing localized surface plasmon resonance (LSPR), large surface area (270 m<sup>2</sup>/g), and electrical resistivity of 0.3 ohm cm which are important properties for an efficient catalyst in electrocatalysis. Owing to these properties, dye sensitized solar cell (DSSC) prepared using TiN-NFG counter electrode resulted into high power conversion efficiency of 8.9 %. The nanocomposite also exhibit stable electrocatalytic hydrogen evolution reaction (HER) with reasonably low overpotential of 161 mV at 10 mA/cm<sup>2</sup> current density. Overall, our TiN-NFG nanocomposite is an alternative of expensive noble metals like Pt, for electrocatalytic applications.

It is realized that the electrocatalyst can help to increase photoelectrochemical (PEC) water splitting efficiency of photocatalyst. Due to promising electrocatalytic activity of our TiN-NFG nanocomposite, we studied the co-catalyst efficiency of TiN-NFG with g-C<sub>3</sub>N<sub>4</sub> nanosheet (photo absorber) for PEC reduction of water using solar light. 2D/2D hetero-junction has been constructed between g-C<sub>3</sub>N<sub>4</sub> nanosheets and TiN-NFG nanocomposite. 2D g-C<sub>3</sub>N<sub>4</sub>:TiN-NFG nanocomposite have been reduced the recombination of photo-induced

electron-hole through the separation of the charge carriers as well as decreased the charge transfer resistance ( $R_{ct}$ ) across the electrode/electrolyte interface. Probably, due to these properties, the nanocomposite displayed ~16 times increment in PEC activity of g-C<sub>3</sub>N<sub>4</sub> nanosheet at 0.11 V versus reversible hydrogen electrode (RHE) under solar light illumination. The nanocomposites exhibited stability for long time (~8 hours) under experimental conditions and cost-effective without consisting of any expensive noble metals. This study establishes TiN-NFG as a promising 2D co-catalyst for PEC water splitting.

We explored other material namely Sn-doped In<sub>2</sub>O<sub>3</sub> (ITO) NCs because of metallic free electron similar to TiN. Origin of LSPR from ITO NCs and their efficiency as co-catalyst in PEC water splitting was studied by making g-C<sub>3</sub>N<sub>4</sub>:ITO (2%) nanocomposite. Making a composite of NCs with charge transporting NFG is a good strategy for catalytic purposes discussed above. But to get an electronic grade film of semiconductor, we prepared thin film of pure PbS or PbSe. Colloidal ligand-free PbS and PbSe NCs fuse to each other because of oriented attachment of NCs, upon removal of the solvent at room temperature. This fusion of NCs improves charge transport in NC solids, resulting into formation of electronic grade semiconductor film at room temperature. PbS and PbSe NC films exhibit electrical conductivities 0.03 S/cm and 0.08 S/cm, respectively, after processing the film at room temperature. The electrical conductivity increased by 2 - 3 orders of magnitude after mild annealing of the film on glass substrate at 150 °C. This low temperature processing is also good for casting semiconductor film on flexible substrate.

## **Future Direction**

### **Novel Metal Nitride (TaN, HfN and MoN) based Electrocatalysts or Co-catalysts for Hydrogen Production**

Scientists are putting enormous efforts to develop catalyst materials which show comparable catalytic activity similar to noble metal catalysts. In this journey, identifying new catalyst materials for the production of hydrogen through electrocatalysis and photoelectrocatalysis is important. HER<sup>4-7</sup> and PEC water splitting<sup>8</sup> are two major processes that require catalysts. In addition to efficient activity comparable to noble metal catalysts, a new catalyst should have low-cost and high durability under the experimental conditions. In this context, TiN- N-doped few-layer graphene (TiN-NFG) nanocomposite as catalyst for HER. The HER activity of TiN-NFG is reasonably good but still inferior to Pt. Interestingly, we developed a new

synthesis strategy where chemically bound interface has been established between TiN and NFG.

Recently, Abghoui et al.<sup>9</sup> predicted the free energies ( $\Delta_{GH}$ ) for adsorption of hydrogen and activation energies for the evolution of hydrogen on the (100) facet of different metal nitride using density functional theory (DFT). Figure 1a and b show the  $\Delta_{GH}$  value for 1H adsorption and 2H adsorption atoms on different metal nitride catalyst surface such as Ti, Sc, Y, Ta, Mo and Hf as well as Pt, Au and Mo metals. Among of all, TaN, HfN and MoN have exhibited remarkable  $\Delta_{GH}$  values closer to zero for both adsorption of 1H or 2H after the Pt metal. Particularly, TaN has exhibited low  $\Delta_{GH}$  value (0.092 eV) for adsorption of hydrogen and activation energy (84 mV) for the evolution of hydrogen in comparison of all the above mentioned metal nitrides. On the other hand, according to report,<sup>9</sup> TiN has showed a large positive  $\Delta_{GH}$  value compared to TaN, HfN and MoN. These results suggest that metal nitrides like TaN, HfN and MoN show superior free energy for hydrogen adsorption and low activation energies for hydrogen evolution compare to TiN. Therefore, TaN, MoN and HfN are expected to be better catalysts compared to TiN.

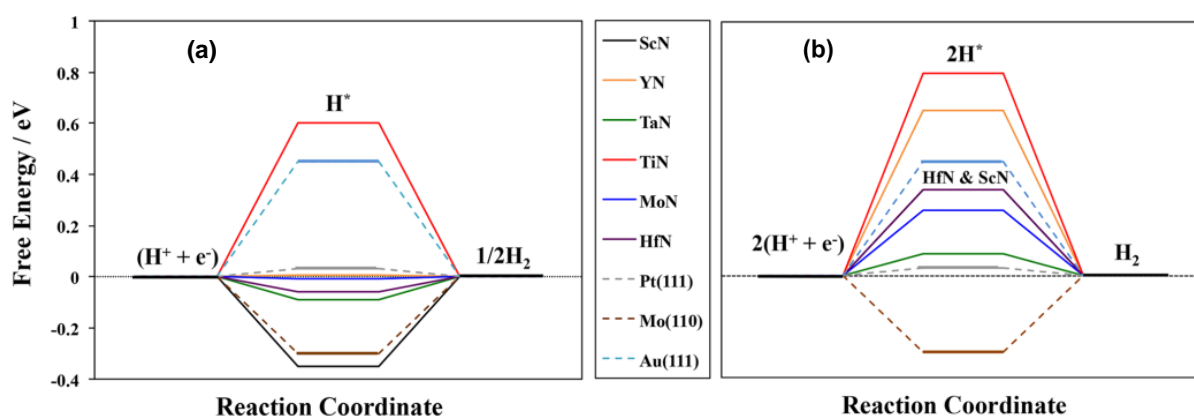


**Figure 1:** (a) and (b) show the depicted free energy ( $\Delta_{GH}$ ) versus reaction coordinate plots on different metal nitride (100) facet of rock salt structure for 1H and 2H adsorption, respectively. Reprinted with permission from ref.<sup>9</sup> Copyright 2017, American Chemical Society.

Making the nanocrystal of these nitrides will increase the number of active sites due to high surface to volume ratio. But charge transport is the major issue in the case of nanocrystal films. To overcome this problem, our synthetic methodology for synthesis of nanocomposites of metal nitride and graphene like material will be helpful. Therefore, we will like to prepare nanocomposite of TaN - graphene like material following our synthesis method. In addition

to intrinsic thermodynamic parameters shown in Figure 1, TaN - graphene nanocomposite will combine high surface area and charge transport, required to catalyze a HER reaction. We will also explore nanocomposites of HfN and MoN with graphene for HER reaction. These novel nanocomposites can then also be explored as co-catalyst in PEC water reduction.

## References

1. Lee, T.; Delley, B.; Stampfl, C.; Soon, A. Environment-Dependent Nanomorphology of TiN: The Influence of Surface Vacancies. *Nanoscale* **2012**, *4*, 5183-5188.
2. Yasuhiro, I.; Hiroji, M.; Koichi, A.; Tokio, M. Structure and Electrical Properties of Titanium Nitride Films. *Jpn. J. Appl. Phys.* **1978**, *17*, 85.
3. Han, Y.; Yue, X.; Jin, Y.; Huang, X.; Shen, P. K. Hydrogen Evolution Reaction in Acidic Media on Single-Crystalline Titanium Nitride Nanowires as an Efficient Non-Noble Metal Electrocatalyst. *J. Mater. Chem. A* **2016**, *4*, 3673-3677.
4. Popczun, E. J.; Read, C. G.; Roske, C. W.; Lewis, N. S.; Schaak, R. E. Highly Active Electrocatalysis of the Hydrogen Evolution Reaction by Cobalt Phosphide Nanoparticles. *Angew. Chem. Int. Ed.* **2014**, *53*, 5427-5430.
5. Li, H.; Tsai, C.; Koh, A. L.; Cai, L.; Contryman, A. W.; Fragapane, A. H.; Zhao, J.; Han, H. S.; Manoharan, H. C.; Abild-Pedersen, F.; Nørskov, J. K.; Zheng, X. Activating and Optimizing MoS<sub>2</sub> Basal Planes for Hydrogen Evolution Through the Formation of Strained Sulphur Vacancies. *Nat. Mater.* **2015**, *15*, 48.
6. Xie, J.; Zhang, J.; Li, S.; Grote, F.; Zhang, X.; Zhang, H.; Wang, R.; Lei, Y.; Pan, B.; Xie, Y. Controllable Disorder Engineering in Oxygen-Incorporated MoS<sub>2</sub> Ultrathin Nanosheets for Efficient Hydrogen Evolution. *J. Am. Chem. Soc.* **2013**, *135*, 17881-17888.
7. Popczun, E. J.; McKone, J. R.; Read, C. G.; Biacchi, A. J.; Wiltrout, A. M.; Lewis, N. S.; Schaak, R. E. Nanostructured Nickel Phosphide as an Electrocatalyst for the Hydrogen Evolution Reaction. *J. Am. Chem. Soc.* **2013**, *135*, 9267-9270.
8. Han, N.; Liu, P.; Jiang, J.; Ai, L.; Shao, Z.; Liu, S. Recent Advances in Nanostructured Metal Nitrides for Water Splitting. *J. Mater. Chem. A* **2018**, *6*, 19912-19933.
9. Abghoui, Y.; Skúlason, E. Hydrogen Evolution Reaction Catalyzed by Transition-Metal Nitrides. *J. Phys. Chem. C* **2017**, *121*, 24036-24045.

## List of Publications

### Included in Thesis

1. **Shanker, G. S.**; Bhosale, R.; Ogale, S.; Nag, A. 2D Nanocomposite of g-C<sub>3</sub>N<sub>4</sub> and TiN Embedded N-Doped Graphene for Photoelectrochemical Reduction of Water using Sunlight. *Adv. Mater. Interfaces* **2018**, *5*, 1801488.
2. **Shanker, G. S.**; Markad, G. B.; Rao, M. J.; Bansode, U.; Nag, A. Colloidal Nanocomposite of TiN and N-Doped Few-Layer Graphene for Plasmonics and Electrocatalysis. *ACS Energy Lett.* **2017**, *2*, 2251-2256.
3. **Shanker, G. S.**; Tandon, B.; Shibata, T.; Chattopadhyay, S.; Nag, A. Doping Controls Plasmonics, Electrical Conductivity, and Carrier Mediated Magnetic Coupling in Fe and Sn Co-Doped In<sub>2</sub>O<sub>3</sub> Nanocrystals: Local Structure Is the Key. *Chem. Mater.* **2015**, *27*, 892-900.
4. **Shanker, G. S.**; Swarnkar, A.; Chatterjee, A.; Chakraborty, S.; Phukan, M.; Parveen, N.; Biswas, K.; Nag, A. Electronic Grade and Flexible Semiconductor Film Employing Oriented Attachment of Colloidal Ligand-Free PbS and PbSe Nanocrystals at Room Temperature. *Nanoscale*, **2015**, *7*, 9204-9214.

### Not Included in Thesis

5. Swarnkar, A.; **Shanker, G. S.**; Nag, A. Organic-Free Colloidal Semiconductor Nanocrystals as Luminescent Sensors for Metal Ions and Nitro-Aromatic Explosives. *Chem. Commun.*, **2014**, *50*, 4743-4746.
6. Tandon, B.; **Shanker, G. S.**; Nag, A. Multifunctional Sn and Fe Co-Doped In<sub>2</sub>O<sub>3</sub> Colloidal Nanocrystals: Plasmonics and Magnetism. *J. Phys. Chem. Lett.* **2014**, *5*, 2306-2311.
7. Naphade, R.; Nagane, S.; **Shanker, G. S.**; Fernandes, R.; Kothari, D.; Zhou, Y.; Pature, N. P.; Ogale, S. Hybrid Perovskite Quantum Nanostructures Synthesized by Electrospray Antisolvent - Solvent Extraction and Intercalation. *ACS Appl. Mater. Interfaces*, **2016**, *8*, 854-861.
8. Haque, A.; Ravi, V. K.; **Shanker, G. S.**; Sarkar, I.; Nag, A.; Santra, P. K. Internal Heterostructure of Anion-Exchanged Cesium Lead Halide Nanocubes. *J. Phys. Chem. C* **2018**, *122*, 13399-13406.

**RightsLink®**[Home](#)[Create Account](#)[Help](#)**ACS Publications**  
Most Trusted. Most Cited. Most Read.**Title:** Colloidal Nanocomposite of TiN and N-Doped Few-Layer Graphene for Plasmonics and Electrocatalysis**Author:** G. Shiva Shanker, Ganesh B. Markad, Metikoti Jagadeeswararao, et al**Publication:** ACS Energy Letters**Publisher:** American Chemical Society**Date:** Oct 1, 2017

Copyright © 2017, American Chemical Society

**LOGIN**

If you're a **copyright.com** user, you can login to RightsLink using your copyright.com credentials. Already a **RightsLink** user or want to [learn more?](#)

**PERMISSION/LICENSE IS GRANTED FOR YOUR ORDER AT NO CHARGE**

This type of permission/license, instead of the standard Terms & Conditions, is sent to you because no fee is being charged for your order. Please note the following:

- Permission is granted for your request in both print and electronic formats, and translations.
- If figures and/or tables were requested, they may be adapted or used in part.
- Please print this page for your records and send a copy of it to your publisher/graduate school.
- Appropriate credit for the requested material should be given as follows: "Reprinted (adapted) with permission from (COMPLETE REFERENCE CITATION). Copyright (YEAR) American Chemical Society." Insert appropriate information in place of the capitalized words.
- One-time permission is granted only for the use specified in your request. No additional uses are granted (such as derivative works or other editions). For any other uses, please submit a new request.

[BACK](#)[CLOSE WINDOW](#)

Copyright © 2018 [Copyright Clearance Center, Inc.](#) All Rights Reserved. [Privacy statement.](#) [Terms and Conditions.](#) Comments? We would like to hear from you. E-mail us at [customercare@copyright.com](mailto:customercare@copyright.com)





# RightsLink®

[Home](#)
[Account Info](#)
[Help](#)


**Title:** 2D Nanocomposite of g-C<sub>3</sub>N<sub>4</sub> and TiN Embedded N-Doped Graphene for Photoelectrochemical Reduction of Water Using Sunlight

**Author:** Angshuman Nag, Satishchandra Ogale, Reshma Bhosale, et al

**Publication:** Advanced Materials Interfaces

**Publisher:** John Wiley and Sons

**Date:** Nov 14, 2018

Copyright © 2018, John Wiley and Sons

Logged in as:  
Golla Shiva Shanker  
IISER

[LOGOUT](#)

## Order Completed

Thank you for your order.

This Agreement between IISER -- Golla Shiva Shanker ("You") and John Wiley and Sons ("John Wiley and Sons") consists of your license details and the terms and conditions provided by John Wiley and Sons and Copyright Clearance Center.

Your confirmation email will contain your order number for future reference.

### [printable details](#)

License Number	4497931260037
License date	Dec 28, 2018
Licensed Content Publisher	John Wiley and Sons
Licensed Content Publication	Advanced Materials Interfaces
Licensed Content Title	2D Nanocomposite of g-C <sub>3</sub> N <sub>4</sub> and TiN Embedded N-Doped Graphene for Photoelectrochemical Reduction of Water Using Sunlight
Licensed Content Author	Angshuman Nag, Satishchandra Ogale, Reshma Bhosale, et al
Licensed Content Date	Nov 14, 2018
Licensed Content Volume	5
Licensed Content Issue	24
Licensed Content Pages	8
Type of use	Dissertation/Thesis
Requestor type	Author of this Wiley article
Format	Print and electronic
Portion	Full article
Will you be translating?	No
Title of your thesis / dissertation	Designing Nanocrystal Interfaces to Improve Charge Transport for Photo- and Electro-Catalytic Solar Energy Applications
Expected completion date	May 2019
Expected size (number of pages)	8
Requestor Location	IISER IISER PUNE  PUNE, 411008 India Attn: IISER
Publisher Tax ID	EU826007151
Total	0.00 USD

**RightsLink®**[Home](#)[Create Account](#)[Help](#)ACS Publications  
Most Trusted. Most Cited. Most Read.**Title:** Doping Controls Plasmonics, Electrical Conductivity, and Carrier-Mediated Magnetic Coupling in Fe and Sn Codoped In<sub>2</sub>O<sub>3</sub> Nanocrystals: Local Structure Is the Key**Author:** G. Shiva Shanker, Bharat Tandon, Tomohiro Shibata, et al**Publication:** Chemistry of Materials**Publisher:** American Chemical Society**Date:** Feb 1, 2015

Copyright © 2015, American Chemical Society

**LOGIN**

If you're a [copyright.com user](#), you can login to RightsLink using your [copyright.com credentials](#). Already a [RightsLink user](#) or want to [learn more?](#)

**PERMISSION/LICENSE IS GRANTED FOR YOUR ORDER AT NO CHARGE**

This type of permission/license, instead of the standard Terms & Conditions, is sent to you because no fee is being charged for your order. Please note the following:

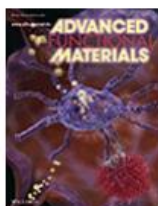
- Permission is granted for your request in both print and electronic formats, and translations.
- If figures and/or tables were requested, they may be adapted or used in part.
- Please print this page for your records and send a copy of it to your publisher/graduate school.
- Appropriate credit for the requested material should be given as follows: "Reprinted (adapted) with permission from (COMPLETE REFERENCE CITATION). Copyright (YEAR) American Chemical Society." Insert appropriate information in place of the capitalized words.
- One-time permission is granted only for the use specified in your request. No additional uses are granted (such as derivative works or other editions). For any other uses, please submit a new request.

[BACK](#)[CLOSE WINDOW](#)

Copyright © 2018 [Copyright Clearance Center, Inc.](#) All Rights Reserved. [Privacy statement](#). [Terms and Conditions](#).  
Comments? We would like to hear from you. E-mail us at [customer@copyright.com](mailto:customer@copyright.com)



# RightsLink®

[Home](#)
[Account Info](#)
[Help](#)


**Title:** Heterostructures for Electrochemical Hydrogen Evolution Reaction: A Review

**Author:** Guoqiang Zhao, Kun Rui, Shi Xue Dou, et al

**Publication:** Advanced Functional Materials

**Publisher:** John Wiley and Sons

**Date:** Aug 16, 2018

Logged in as:  
Golla Shiva Shanker  
IISER

Account #:  
3001385920

[LOGOUT](#)

Copyright © 2018, John Wiley and Sons

## Order Completed

Thank you for your order.

This Agreement between IISER -- Golla Shiva Shanker ("You") and John Wiley and Sons ("John Wiley and Sons") consists of your license details and the terms and conditions provided by John Wiley and Sons and Copyright Clearance Center.

Your confirmation email will contain your order number for future reference.

### [printable details](#)

License Number	4498000267017
License date	Dec 29, 2018
Licensed Content Publisher	John Wiley and Sons
Licensed Content Publication	Advanced Functional Materials
Licensed Content Title	Heterostructures for Electrochemical Hydrogen Evolution Reaction: A Review
Licensed Content Author	Guoqiang Zhao, Kun Rui, Shi Xue Dou, et al
Licensed Content Date	Aug 16, 2018
Licensed Content Volume	28
Licensed Content Issue	43
Licensed Content Pages	26
Type of use	Dissertation/Thesis
Requestor type	University/Academic
Format	Print and electronic
Portion	Figure/table
Number of figures/tables	1
Original Wiley figure/table number(s)	Figure 1
Will you be translating?	No
Title of your thesis / dissertation	Designing Nanocrystal Interfaces to Improve Charge Transport for Photo- and Electro-Catalytic Solar Energy Applications
Expected completion date	May 2019
Expected size (number of pages)	8
Requestor Location	IISER IISER PUNE  PUNE, 411008 India Attn: IISER
Publisher Tax ID	EU826007151
Total	0.00 USD

<https://s100.copyright.com/AppDispatchServlet>

1/2



Shiv Shankar <shivshankar@students.iiserpune.ac.in>



### Copyright.com Order Confirmation

no-reply@copyright.com <no-reply@copyright.com>  
To: shivshankar@students.iiserpune.ac.in

Sat, Dec 29, 2018 at 11:00 AM

**Do Not Reply Directly to This Email**

To ensure that you continue to receive our emails,  
please add [copyright@marketing.copyright.com](mailto:copyright@marketing.copyright.com) to your address book.

<b>Thank You for Your Order with Copyright Clearance Center</b>	
<p><b>Dear Golla Shiva Shanker,</b></p> <p>Thank you for placing your order with Copyright Clearance Center.</p> <p>Order Summary: Order Date: 12/29/2018 Confirmation Number: 11777830 Items in order: 1 Order Total: \$ 0.00</p> <p>To view or print your order details or terms and conditions, click the following link and log in: <a href="#">Order link</a></p> <p>Need additional permissions? <a href="#">Go here.</a></p> <p>How was your experience? <a href="#">Click here to give us feedback.</a></p>	
<p>If you need assistance, please visit our online help (<a href="http://www.copyright.com/help">www.copyright.com/help</a>).</p> <p>Please do not reply to this message. This e-mail address is not monitored for responses.</p> <p><b>Toll Free: +1.855.239.3415</b> <b>Local: +1.978.646.2600</b> <b><a href="mailto:info@copyright.com">info@copyright.com</a></b> <b><a href="http://www.copyright.com">www.copyright.com</a></b></p>	

Please visit [Copyright Clearance Center](http://www.copyright.com) for more information.

**RightsLink®**[Home](#)[Create Account](#)[Help](#)**ACS Publications**  
Most Trusted. Most Cited. Most Read.**Title:** Hydrogen Evolution Reaction Catalyzed by Transition-Metal Nitrides**Author:** Younes Abghoui, Egill Skúlason**Publication:** The Journal of Physical Chemistry C**Publisher:** American Chemical Society**Date:** Nov 1, 2017

Copyright © 2017, American Chemical Society

**LOGIN**

If you're a [copyright.com](#) user, you can login to RightsLink using your [copyright.com](#) credentials. Already a [RightsLink](#) user or want to [learn more?](#)

**PERMISSION/LICENSE IS GRANTED FOR YOUR ORDER AT NO CHARGE**

This type of permission/license, instead of the standard Terms & Conditions, is sent to you because no fee is being charged for your order. Please note the following:

- Permission is granted for your request in both print and electronic formats, and translations.
- If figures and/or tables were requested, they may be adapted or used in part.
- Please print this page for your records and send a copy of it to your publisher/graduate school.
- Appropriate credit for the requested material should be given as follows: "Reprinted (adapted) with permission from (COMPLETE REFERENCE CITATION). Copyright (YEAR) American Chemical Society." Insert appropriate information in place of the capitalized words.
- One-time permission is granted only for the use specified in your request. No additional uses are granted (such as derivative works or other editions). For any other uses, please submit a new request.

If credit is given to another source for the material you requested, permission must be obtained from that source.

[BACK](#)[CLOSE WINDOW](#)

Copyright © 2018 [Copyright Clearance Center, Inc.](#) All Rights Reserved. [Privacy statement.](#) [Terms and Conditions.](#) Comments? We would like to hear from you. E-mail us at [customer@copyright.com](mailto:customer@copyright.com)



# RightsLink®

[Home](#)
[Account Info](#)
[Help](#)


**Title:** Recent advancements in semiconductor materials for photoelectrochemical water splitting for hydrogen production using visible light

Logged in as:  
Golla Shiva Shanker  
IISER  
Account #:  
3001385920

**Author:** Sushil Kumar Saraswat,Dylan D. Rodene,Ram B. Gupta

[LOGOUT](#)

**Publication:** Renewable and Sustainable Energy Reviews

**Publisher:** Elsevier

**Date:** June 2018

© 2018 Elsevier Ltd. All rights reserved.

## Order Completed

Thank you for your order.

This Agreement between IISER -- Golla Shiva Shanker ("You") and Elsevier ("Elsevier") consists of your license details and the terms and conditions provided by Elsevier and Copyright Clearance Center.

Your confirmation email will contain your order number for future reference.

### [printable details](#)

License Number	4498070748196
License date	Dec 29, 2018
Licensed Content Publisher	Elsevier
Licensed Content Publication	Renewable and Sustainable Energy Reviews
Licensed Content Title	Recent advancements in semiconductor materials for photoelectrochemical water splitting for hydrogen production using visible light
Licensed Content Author	Sushil Kumar Saraswat,Dylan D. Rodene,Ram B. Gupta
Licensed Content Date	Jun 1, 2018
Licensed Content Volume	89
Licensed Content Issue	n/a
Licensed Content Pages	21
Type of Use	reuse in a thesis/dissertation
Portion	figures/tables/illustrations
Number of figures/tables/illustrations	1
Format	both print and electronic
Are you the author of this Elsevier article?	No
Will you be translating?	No
Original figure numbers	Figure 2A
Title of your thesis/dissertation	Designing Nanocrystal Interfaces to Improve Charge Transport for Photo- and Electro-Catalytic Solar Energy Applications
Expected completion date	May 2019
Estimated size (number of pages)	8
Requestor Location	IISER IISER PUNE  PUNE, 411008 India Attn: IISER
Publisher Tax ID	GB 494 6272 12



12/29/2018

IISER, Pune Mail - Copyright.com Order Confirmation



Shiv Shankar <shivshankar@students.iiserpune.ac.in>

## Copyright.com Order Confirmation


no-reply@copyright.com <no-reply@copyright.com>  
To: shivshankar@students.iiserpune.ac.in

Sat, Dec 29, 2018 at 11:58 AM

**Do Not Reply Directly to This Email**

To ensure that you continue to receive our emails,  
please add [copyright@marketing.copyright.com](mailto:copyright@marketing.copyright.com) to your address book.

**Thank You for Your Order with  
Copyright Clearance Center**



**Dear Golla Shiva Shanker,**

Thank you for placing your order with Copyright Clearance Center.

**Order Summary:**  
Order Date: 12/29/2018  
Confirmation Number: 11777838  
Items in order: 5  
Order Total: \$ 0.00

To view or print your order details or terms and conditions,  
click the following link and log in: [Order link](#)

Need additional permissions? [Go here.](#)

How was your experience? [Click here to give us feedback.](#)

---

If you need assistance, please visit our online help ([www.copyright.com/help](http://www.copyright.com/help)).

Please do not reply to this message. This e-mail address is not monitored for responses.

**Toll Free: +1.855.239.3415**  
**Local: +1.978.646.2600**  
[info@copyright.com](mailto:info@copyright.com)  
[www.copyright.com](http://www.copyright.com)

Please visit [Copyright Clearance Center](http://www.copyright.com) for more information.

<https://mail.google.com/mail/u/0?ik=c49df98dff&view=pt&search=all&permmsgid=msg-f%3A1621166557676388520&simpl=msg-f%3A162116655...> 1/2

12/29/2018

IISER, Pune Mail - Copyright.com Order Confirmation



Shiv Shankar <shivshankar@students.iiserpune.ac.in>

## Copyright.com Order Confirmation


no-reply@copyright.com <no-reply@copyright.com>  
To: shivshankar@students.iiserpune.ac.in

Sat, Dec 29, 2018 at 12:06 PM

**Do Not Reply Directly to This Email**

To ensure that you continue to receive our emails,  
please add [copyright@marketing.copyright.com](mailto:copyright@marketing.copyright.com) to your address book.

**Thank You for Your Order with  
Copyright Clearance Center**



**Dear Golla Shiva Shanker,**

Thank you for placing your order with Copyright Clearance Center.

**Order Summary:**  
Order Date: 12/29/2018  
Confirmation Number: 11777841  
Items in order: 1  
Order Total: \$ 0.00

To view or print your order details or terms and conditions,  
click the following link and log in: [Order link](#)

Need additional permissions? [Go here.](#)

How was your experience? [Click here to give us feedback.](#)

---

If you need assistance, please visit our online help ([www.copyright.com/help](http://www.copyright.com/help)).

Please do not reply to this message. This e-mail address is not monitored for responses.

**Toll Free: +1.855.239.3415**  
**Local: +1.978.646.2600**  
[info@copyright.com](mailto:info@copyright.com)  
[www.copyright.com](http://www.copyright.com)

Please visit [Copyright Clearance Center](http://www.copyright.com) for more information.

<https://mail.google.com/mail/u/0?ik=c49df98dff&view=pt&search=all&permmsgid=msg-f%3A1621167089663419986&simpl=msg-f%3A162116708...> 1/2



12/29/2018

IISER, Pune Mail - Copyright.com Order Confirmation



Shiv Shankar <shivshankar@students.iiserpune.ac.in>

## Copyright.com Order Confirmation


no-reply@copyright.com <no-reply@copyright.com>  
To: shivshankar@students.iiserpune.ac.in

Sat, Dec 29, 2018 at 12:13 PM

**Do Not Reply Directly to This Email**

To ensure that you continue to receive our emails,  
please add [copyright@marketing.copyright.com](mailto:copyright@marketing.copyright.com) to your address book.

**Thank You for Your Order with  
Copyright Clearance Center**



**Dear Golla Shiva Shanker,**

Thank you for placing your order with Copyright Clearance Center.

Order Summary:  
Order Date: 12/29/2018  
Confirmation Number: 11777845  
Items in order: 1  
Order Total: \$ 0.00

To view or print your order details or terms and conditions,  
click the following link and log in: [Order link](#)

Need additional permissions? [Go here.](#)

How was your experience? [Click here to give us feedback.](#)

---

If you need assistance, please visit our online help ([www.copyright.com/help](http://www.copyright.com/help)).

Please do not reply to this message. This e-mail address is not monitored for responses.

**Toll Free: +1.855.239.3415**  
**Local: +1.978.646.2600**  
**[info@copyright.com](mailto:info@copyright.com)**  
**[www.copyright.com](http://www.copyright.com)**

Please visit [Copyright Clearance Center](http://www.copyright.com) for more information.

<https://mail.google.com/mail/u/0?ik=c49df98dff&view=pt&search=all&permmsgid=msg-f%3A1621167509994403236&simpl=msg-f%3A162116750...> 1/2

12/29/2018

IISER, Pune Mail - Copyright.com Order Confirmation



Shiv Shankar <shivshankar@students.iiserpune.ac.in>

## Copyright.com Order Confirmation


no-reply@copyright.com <no-reply@copyright.com>  
To: shivshankar@students.iiserpune.ac.in

Sat, Dec 29, 2018 at 12:32 PM

**Do Not Reply Directly to This Email**

To ensure that you continue to receive our emails,  
please add [copyright@marketing.copyright.com](mailto:copyright@marketing.copyright.com) to your address book.

**Thank You for Your Order with  
Copyright Clearance Center**



**Dear Golla Shiva Shanker,**

Thank you for placing your order with Copyright Clearance Center.

Order Summary:  
Order Date: 12/29/2018  
Confirmation Number: 11777864  
Items in order: 1  
Order Total: \$ 0.00

To view or print your order details or terms and conditions,  
click the following link and log in: [Order link](#)

Need additional permissions? [Go here.](#)

How was your experience? [Click here to give us feedback.](#)

---

If you need assistance, please visit our online help ([www.copyright.com/help](http://www.copyright.com/help)).

Please do not reply to this message. This e-mail address is not monitored for responses.

**Toll Free: +1.855.239.3415**  
**Local: +1.978.646.2600**  
[info@copyright.com](mailto:info@copyright.com)  
[www.copyright.com](http://www.copyright.com)

Please visit [Copyright Clearance Center](http://www.copyright.com) for more information.

<https://mail.google.com/mail/u/0?ik=c49df98dff&view=pt&search=all&permmsgid=msg-f%3A1621168682456530867&simpl=msg-f%3A162116868...> 1/2



# RightsLink®

[Home](#)
[Account Info](#)
[Help](#)


**Title:** Formation Mechanisms of Uniform Nanocrystals via Hot-Injection and Heat-Up Methods

**Author:** Soon Gu Kwon, Taeghwan Hyeon

**Publication:** Small

**Publisher:** John Wiley and Sons

**Date:** Aug 1, 2011

Logged in as:  
Golla Shiva Shanker  
IISER

Account #:  
3001385920

[LOGOUT](#)

Copyright © 2011, John Wiley and Sons

## Order Completed

Thank you for your order.

This Agreement between IISER -- Golla Shiva Shanker ("You") and John Wiley and Sons ("John Wiley and Sons") consists of your license details and the terms and conditions provided by John Wiley and Sons and Copyright Clearance Center.

Your confirmation email will contain your order number for future reference.

### [printable details](#)

License Number	4499151313867
License date	Dec 31, 2018
Licensed Content Publisher	John Wiley and Sons
Licensed Content Publication	Small
Licensed Content Title	Formation Mechanisms of Uniform Nanocrystals via Hot-Injection and Heat-Up Methods
Licensed Content Author	Soon Gu Kwon, Taeghwan Hyeon
Licensed Content Date	Aug 1, 2011
Licensed Content Volume	7
Licensed Content Issue	19
Licensed Content Pages	18
Type of use	Dissertation/Thesis
Requestor type	University/Academic
Format	Print and electronic
Portion	Figure/table
Number of figures/tables	1
Original Wiley figure/table number(s)	Figure
Will you be translating?	No
Title of your thesis / dissertation	Designing Nanocrystal Interfaces to Improve Charge Transport for Photo- and Electro-Catalytic Solar Energy Applications
Expected completion date	May 2019
Expected size (number of pages)	8
Requestor Location	IISER IISER PUNE  PUNE, 411008 India Attn: IISER
Publisher Tax ID	EU826007151
Total	0.00 USD

**RightsLink®**[Home](#)[Create Account](#)[Help](#)**ACS Publications**  
Most Trusted. Most Cited. Most Read.**Title:** Hydrogen Evolution Reaction Catalyzed by Transition-Metal Nitrides**Author:** Younes Abghoui, Egill Skúlason**Publication:** The Journal of Physical Chemistry C**Publisher:** American Chemical Society**Date:** Nov 1, 2017

Copyright © 2017, American Chemical Society

**LOGIN**

If you're a **copyright.com** user, you can login to RightsLink using your copyright.com credentials. Already a **RightsLink** user or want to [learn more?](#)

**PERMISSION/LICENSE IS GRANTED FOR YOUR ORDER AT NO CHARGE**

This type of permission/license, instead of the standard Terms & Conditions, is sent to you because no fee is being charged for your order. Please note the following:

- Permission is granted for your request in both print and electronic formats, and translations.
- If figures and/or tables were requested, they may be adapted or used in part.
- Please print this page for your records and send a copy of it to your publisher/graduate school.
- Appropriate credit for the requested material should be given as follows: "Reprinted (adapted) with permission from (COMPLETE REFERENCE CITATION). Copyright (YEAR) American Chemical Society." Insert appropriate information in place of the capitalized words.
- One-time permission is granted only for the use specified in your request. No additional uses are granted (such as derivative works or other editions). For any other uses, please submit a new request.

If credit is given to another source for the material you requested, permission must be obtained from that source.

[BACK](#)[CLOSE WINDOW](#)

Copyright © 2018 [Copyright Clearance Center, Inc.](#) All Rights Reserved. [Privacy statement.](#) [Terms and Conditions.](#) Comments? We would like to hear from you. E-mail us at [customer care@copyright.com](mailto:customer care@copyright.com)